

DISS. ETH NO. 19224

Surface-chemical gradients and patterns on metal oxide substrates

A dissertation submitted to the

ETH ZURICH

for the degree of

Doctor of Sciences

(Dr. sc. ETH Zürich)

presented by

Mathias Rodenstein

Dipl. Physiker TU Dresden

born December 15, 1980

Citizen of Germany

accepted on the recommendation of

Prof. Dr. N. D. Spencer, examiner

Prof. Dr. G. Leggett, co-examiner

Dr. S. G. P. Tosatti, co-examiner

Dr. S. Zürcher, co-examiner

2010

Oberflächenchemische Gradienten sind Oberflächen, deren Funktionalität sich graduell entlang einer räumlichen Richtung ändert. Sie finden unter anderem Anwendung in Biomedizin, Tribologie und Oberflächenpolymerchemie. Auf der einen Seite können sie eine treibende Kraft für physiochemische oder biologische Prozesse präsentieren, zum Beispiel für die Bewegung von Flüssigkeiten oder Zellen. Auf der anderen Seite stellen sie eine Kombination von individuellen Oberflächen mit Varietät in Eigenschaften dar. Sie können somit benutzt werden, Phänomene wie Haptotaxis oder Chemotaxis zu studieren oder den Durchsatz durch das Parallelrastern von Oberflächen drastisch zu erhöhen. Dies kann kosteneffektiv und experimentell optimierend sein, da methodische Fehler reduziert werden.

Im Kontrast zu Oberflächengradienten können Oberflächenmuster dazu benutzt werden, um die Interaktion zweier System an ihrer Grenzschicht explizit zu kontrollieren, beispielsweise die Haftung oder die Beweglichkeit von Zellen an einer Oberfläche. Die Herstellung solcher Muster kann also dazu dienen, 2D-Beschränkungen oder spezifische Haftpunkte zu kreieren, die für Zell- oder Bakterienstudien genutzt werden können. Das Ziel dieser Arbeit war es, neue selbstordnende Chemien als valide Systeme für Oberflächengradienten zu etablieren, im Speziellen solche, die auf Catecholen und Phosphaten basieren. Dies sollte durch die Erweiterung einer simplen Zweistufen-Eintauch-Methode, basierend auf molekularer Adsorption und Ersatz, geleistet werden. Gradienten in Oberflächenbedeckung mit Perfluoroalkylen und Alkylen mit unterschiedlichen ω -Funktionalitäten wurden benutzt, um Gradienten in freier Oberflächenenergie und damit Hydrophobizität zu erzeugen. Desweiteren wurde das Herunterskalieren der räumlichen Größenordnung der Gradienten durch direkte Photolithographie erreicht. Diese wurde auch genutzt, um Muster in Oberflächenfunktionalität zu erzeugen. Beide Teile der Arbeit waren auf Metalloxide (Titanat und Niobat im speziellem) ausgerichtet, welche eine Großzahl von Anwendungen beispielsweise in Biomedizin, Solarenergieumwandlung, und Halbleiterindustrie haben. Röntgenphotoelektronenspektroskopie, Kontaktwinkelmessungen, winkelabhängige spektroskopische Ellipsometrie und Fluoreszenzmikroskopie wurden zur Oberflächencharakterisierung verwendet.

Der erste Teile der Arbeit konzentrierte sich auf die Charakterisierung homogen funktionalisierter Oberflächen. Durch die Kontrolle von Lösungskonzentrationen und Adsorptionszeiten wurden Adsorptionskinetiken ermittelt und dazu genutzt,

spezifische Eintauchprogramme zu erstellen. Diese wurden für die Herstellung von zentimeterlangen auf Alkyl-Phosphaten und Catecholen basierenden Oberflächengradienten benutzt. Im zweiten Teil wurden die Degradationskinetiken von Oberflächenschichten von PLL-*g*-PEG und PLL-*g*-PMOXA auf Titan- und Niobiumoxid unter photokatalytisch induzierter UV-Degradation ermittelt. Diese Methode wurde angewendet, um Strukturen und Gradienten in Proteinresistenz auf Millimeter- und Mikrometerskalen zu fabrizieren. Erste Applikationen wurden für Experimente im Bereich Zelladhäsion und -proliferation gefunden, welche genutzt wurden, um Vergleichsstudien zwischen PLL-*g*-PEG and PLL-*g*-PMOXA als Antifoulingpolymere zu erstellen.

Surface-chemical gradients are surfaces whose functionality changes gradually along a spatial direction. They find applications in biomedicine, tribology, and surface-polymer chemistry, amongst other fields. On the one hand, they can present a driving force for physiochemical or biological processes, for example the motion of liquids or cells. On the other hand, they pose the combination of individual surfaces with a variety of properties. They can thus be used to study phenomena such as haptotaxis and chemotaxis or highly increase experimental throughput by allowing surfaces to be screened for different properties in parallel. This can be cost-effective and experimentally optimizing by reducing the potential for methodological errors. In contrast to surface-chemical gradients, distinct surface-chemical patterns can be used to explicitly restrict or control interactions between two systems at their 2D interface, for example the attachment and motility of cells on a surface. The fabrication of such patterns can thus be used to create 2D confinements or specific attachment sites which can be used to study cell and bacterial adhesion and proliferation behaviors.

The aim of this thesis was to establish certain self-assembly chemistries, in particular those based on phosphates or catechols, as valid systems for the fabrication of surface-chemical gradients. This was to be achieved by extending the applicability of a two-step immersion method based on controlled molecular adsorption and replacement. Surface-coverage gradients in alkyl and perfluoro-alkyl with different ω -functionality were used to yield gradients in free surface energy and thus hydrophobicity. Furthermore, the downscaling of gradients' length-scales was achieved by investigating and utilizing direct photocatalytically assisted photolithography which was also used to generate patterns in surface functionality. Both parts of the work were focused on metal oxide substrates (titanium dioxide and niobium pentoxide in particular), which have a plethora of applications in biomedicine, solar energy conversion, and the semiconductor industry, for example. X-ray photoelectron spectroscopy, contact-angle measurements, variable-angle spectroscopic ellipsometry, and fluorescence microscopy were used to characterize and analyze the surface-chemical gradients and patterns.

The first part of the thesis focused on the characterization of homogeneously functionalized surfaces. By controlling solution concentration and substrate immersion times, adsorption kinetics were established and used to design appropriate gradual

immersion program resulting in the fabrication of cm-long phosphate- and catechol-based surface-chemical gradients on metal oxide surfaces. In a second part, the degradation kinetics of adlayers of PLL-*g*-PEG and PLL-*g*-PMOXA on titanium and niobium oxide substrates by photocatalytically assisted UV degradation were established and used to fabricate both surface-functional patterns and gradients of protein resistance on millimeter and micrometer scales.

First applications of so-generated surfaces were found with the study of cell adhesion and proliferation on modified metal oxide substrates leading to comparative studies between PLL-*g*-PEG and PLL-*g*-PMOXA as antifouling polymers.

Contents

Contents	viii
1 Introduction	xiii
1.1 General Introduction	1
1.2 Aims of this thesis	2
1.3 Structure of thesis (chapters)	3
2 Theoretical background	5
2.1 Substrates	9
2.1.1 Metal oxides: titanium dioxide (TiO_2) and niobium pentoxide (Nb_2O_5)	10
2.1.2 Silicon dioxide (SiO_2)	13
2.1.3 Chromium/Chromium oxide (Cr/CrOx)	14
2.2 Homogeneous coatings	14
2.2.1 Surface adlayers (SADs)	14
2.2.2 Self-assembled monolayers (SAMs)	15
2.2.3 Phosph(on)ates	17
2.2.4 Catechols	18
2.2.5 Polyelectrolytes	19
2.3 Heterogeneous surface functionalizations	22
2.3.1 Mixed surface functionalizations	22
2.3.2 Surface-chemical gradients	23
2.3.3 Patterned surfaces	23
2.4 Modification of surface adlayers	25
2.4.1 Decomposition and modification under irradiation	25

2.4.2	Substitution and backfilling of (sub)monolayers	26
2.5	Analytical techniques	27
2.5.1	X-ray photoelectron spectroscopy (XPS)	27
2.5.2	Fluorescence microscopy (FM)	29
2.5.3	Variable-angle spectroscopic ellipsometry (VASE)	30
2.5.3.1	Cauchy-layer	30
2.5.3.2	Metal-oxide (MO) layer	31
2.5.4	Contact angle goniometer (CA)	32
2.5.5	Micro droplet density (MDD)	32
2.5.6	X-ray diffraction (XRD)	33
3	Surface preparation and analysis: materials, protocols, and ana-	
	lytical methods	35
3.1	Instruments	36
3.1.1	X-ray Photoelectron Spectroscopy (XPS)	36
3.1.2	Variable Spectroscopic Ellipsometry (VASE)	37
3.1.3	X-ray Diffraction (XRD)	37
3.1.4	Fluorescence Microscopy (FM)	38
3.1.5	Water Contact Angles (sCA)	38
3.1.6	Microdroplet Density MDD	38
3.1.7	Linear motion drive (LMD) for surface-chemical gradients by immersion	39
3.1.8	UV setup for direct UV photolithography	40
3.2	Substrates	40
3.2.1	Titanium dioxide (TiO ₂), niobium pentoxide (Nb ₂ O ₅)	41
3.2.2	Silicon dioxide (SiO ₂)	47
3.2.3	Chromium with native oxide layer (Cr/CrOx)	47
3.3	Chemicals and solutions	47
3.3.1	Solvents	47
3.3.2	Alkyl phosphates, catechol derivatives	49
3.3.3	Polyelectrolytes	49
3.4	Protein solutions	50
3.5	Protocols for surface preparation	50

3.5.1	Adsorption of adlayers/monolayers	50
3.5.1.1	Adsorption protocols for alkyl phosphates	50
3.5.1.2	Adsorption protocols for catechols	51
3.5.1.3	Protocols for PLL-based polymers	51
3.5.2	Determination of adsorption kinetics and protocols for gradients by immersion (LMD)	51
3.5.3	Protocols for direct UV photolithography	51
3.5.4	Protocols for protein adsorption tests	52
4	Characterization of homogeneously functionalized surfaces	53
4.1	Catechols (PFAND and ND)	54
4.1.1	Homogeneous adlayer, adsorption kinetics (on TiO ₂)	54
4.1.1.1	Stability/degradation of catechol SADs under X-ray exposure	63
4.1.1.2	Stability/Degradation of catechol SAMs under deep-UV exposure	68
4.1.1.3	Considerations for VASE measurements of (PFA)ND adlayers	69
4.1.2	Adsorption on Cr/CrOx	71
4.2	Polyelectrolytes	76
4.2.1	Homogeneous layers	76
4.2.2	Degradation under X-ray	76
4.2.3	Degradation under deep-UV	85
4.3	Alkyl phosphates	90
4.4	Conclusion	93
5	Surface-chemical gradients by immersion	95
5.1	Catechol-based	99
5.1.1	PFAND and ND self-assembly kinetics	100
5.1.2	PFAND and PFAND-ND gradients on TiO ₂	106
5.2	Phosphate-based	112
5.2.1	DDPO4 self-assembly kinetics	113
5.2.2	Phosphate-based surface-chemical gradients by LMD	121

5.3	Conclusion for phosphate- and catechol-based SAM molecules: adsorption kinetics and surface-chemical gradients by LMD	125
6	Surface adlayer modification through deep-UV	129
6.1	Degradation kinetics	132
6.2	Patterning	136
6.2.1	PLLs	138
6.2.2	PFAND	139
6.2.3	Backfilled patterns	140
6.3	Conclusion	141
7	Conclusions and Outlook	143
7.1	Conclusions	144
7.2	Applications	146
7.2.1	Surface-chemical gradients by direct UV-photolithography . .	147
7.2.2	Controlled localization of cellular adhesion	149
7.3	Outlook	151
	Bibliography	155
	Curriculum Vitae	183

CHAPTER 1 

Introduction

Art is always and everywhere
the secret confession, and at the
same time the immortal
movement of its time.

Karl Marx

1.1 General Introduction

Targeted surface modification is a powerful tool to endow the interface between an object and its surrounding with properties not exhibited by its bulk material. A great variety of such modifications is commonly performed on various length scales and for multitudes of purposes: Superhydrophobic surfaces with self-cleaning properties can be used on windows and digital displays to reduce staining and smudging. [1, 2] Surfaces of medical implants are tailored to optimize acceptance by the target host [3] and increase corrosion resistance [4]. Nanoscale electronic devices are made with functional molecular monolayers to create electronic barriers or conductors [5–7].

In modern chemo- and biosensors, specifically modified surfaces translate the presence of certain chemical compounds or biological systems into electr(on)ic signals upon contact.

From the given examples it is clear that numerous fields of current research are highly dependant on surface and interface properties, ranging over several orders of magnitude and parameter spaces (e.g. temperature, surface roughness, hydrophobicity) – tribology can be named as an example. [8] A common scientific challenge is to experimentally cover any such ranges efficiently, be th of physical or chemical nature such as surface roughness or hydrophobicity, respectively. The task of doing so can be tedious if performed in individual experiments. Also, most industrial or academic research aimed at large-scale, high-throughput analysis with high accuracy eventually aspires to do so while only varying few parameters. One approach to increase throughput by parallelization is the utilization of (micro)arrays – a set of (surface) modifications in a spatially discrete manner on a single sample. [9] A slightly different and potentially even more promising approach is the substitution of discrete sample sets with continuous spectra of (surface) properties – so called gradients: on the sample surface a continuous range of (at least) one surface parameter is varied along a spatial dimension. Such gradients have been developed as 1-D, 2-D systems and are described in the literature. [10, 11] The particular case of surface-chemical gradients constitutes samples with ranges of chemical functionality. [10, 11] Additionally to the aforementioned advantage of high-throughput screening, surface-chemical gradients can also function as biomimetic systems with particular interfacial properties that are experimentally inaccessible by homogeneous sampling, e.g. chemotaxis of cells

and bacteria on surfaces [12, 13] or guided movement of liquids as a delivery system on (dynamic) gradients on the submicro- to millimeter scales. [14–16]

During the past two decades, several chemical systems and technical approaches for the fabrication of surface gradients in general and surface-chemical gradients in particular have been developed. [10, 11] Examples of chemistries comprise thiols on noble metals, [17, 18] silanes on silica, [14] PLL-based block copolymers on metal oxides. [19–21] Gradients of metals can be achieved using physical vapor deposition (PVD), of metal oxides with chemical vapor deposition (CVD). [22]

1.2 Aims of this thesis

The motivation of this thesis is to extend the realm of surface-chemical gradients with respect to applicable chemistries – in particular phosphate- and catechol-based self-assembled monolayers (SAMs) on metal oxides, fabrication techniques [23–27] (linear motion drive (LMD) [18, 28] immersion and direct UV photolithography (DUP) [29, 30]) as well as scalability. The work is focused on the adaptation of established methods with regard to fabrication of tailorable hydrophobic-hydrophilic and charged surface on metal oxide [23, 31] as well as providing low-cost approaches to the fabrication of patterned anti-fouling polymeric surfaces, which can be easily implemented in laboratories lacking surface science expertise and costly surface modification equipments such as UV lithography setups. [32] The relevance of such gradients, their scalability, and reproducibility on metal oxides can be seen in studies concerning the interaction of proteins (conformation, binding strength) and cells (attachment, proliferation, motility) with surfaces depending on the degree of hydrophobicity [33, 34] and surface charge [34, 35]. Ever since surface gradients were introduced about three decades ago, various challenges have been faced regarding their: [14, 36]

1. reproducibility
2. stability
3. applicability
4. versatility

With respect to these four points, this thesis details the fabrication and stability of phosphate- and catechol-based (hydrophobicity) gradients in order to illustrate a promising, recently established route to both types of (metal oxide) surface functionalization. [7,27] Furthermore, direct UV photolithography enhanced by photocatalytically active substrates such as TiO_2 and Nb_2O_5 is shown to be a very useful, easily applicable, yet low-budget method for fabricating structures in surface adlayers as well as surface-chemical gradients. [37–39]

1.3 Structure of thesis (chapters)

Chapter 2:

General introduction to theory and literature on the analytical methods and (surface-)chemistries that were applied in this work.

Chapter 3:

Framework and outline of approaches taken.

Chapter 4:

Characterization of homogeneous surfaces, i.e. adsorption kinetics, characterization of surface adlayers with respect to chemical/elemental composition, thickness and functionality.

Chapter 5:

Surface-chemical gradients by immersion. Correlation between spatial position, surface coverage, chemical state and functionality along gradients.

Chapter 6:

Surface-chemical structures by deep UV. Characterization of degradation kinetics and final structural composition of UV treated surface adlayers.

Chapter 7:

Outlook for future work.

CHAPTER 2

Theoretical background

If the facts don't fit the theory,
change the facts.

Albert Einstein

This chapter outlines the various theoretical backgrounds fundamental to the results presented: chemical and physical properties of substrates (TiO_2 , Nb_2O_5 , SiO_2 , Au), surface modifiers (catechol and phosphate derivatives, poly (L-lysine)-based polymers), as well as principles of surface-adlayer modification (UV lithography, X-ray induced degradation, linear-motion-drive immersion) and analytical techniques (X-ray Photoelectron Spectroscopy (XPS), Variable Angle Spectroscopic Ellipsometry (VASE), static water Contact Angle (sCA), and X-ray Diffraction (XRD)).

Within the scope of this work only a few surface modification techniques were employed. Beyond these, various well established surface modification methods are listed with specific examples and references in Table 2.1. The list is not comprehensive and distinguishes between physical and chemical methods even though some methods such as electrochemical and photochemical ones cannot be assigned exclusively.

Examples of surface properties that can be tailored by surface functionalization and their relevance are listed in Table 2.2.

Surfaces of semiconductor materials such as GaAs are wet-etched in order to optimize photoluminescence by tailoring surface states and thus decreasing surface recombination rates. [56] Surfaces of metal oxides such as Al_2O_3 can be specifically roughened by combinations of mechanical abrasion and chemical polishing to tailor surface roughness. Kunzler et al. demonstrated the effects of surface roughness on cell (adhesion) behavior for osteoblasts (RCO) and fibroblasts (HGF): [70] Al_2O_3 roughness gradients [47] were replicated and coated with titanium, then exposed to cell cultures, permitting the study of response of mentioned cell types to different surface roughness – essential to osteointegration for example. The choice of any modification method and functionalization essentially depend on the desired final application, e.g. optimization of absorption spectra of solar cells, reduction or inhibition of abrasion of gears, and integration of medical implants in the human body.

Furthermore, combinatorial effects are often encountered and desired. For example, the degree of hydrophobicity of a surface depends on the surface chemistry but also on surface roughness and micrometer-scale structure. [73]

Table 2.1: Examples and applications of surface modifications

Type	Method	Variations	Examples
Physical	sputtering	deposition	TiO ₂ coatings [40, 41]
	irradiation	destructive light, X-ray, α -, β -, γ -, plasma, e ⁻	TiO ₂ depth profiling [42, 43] SAM modification [44–46]
	mechanical abrasion	grinding, particle blasting	tailoring surface roughness [47]
	magnetization	optical, magnetic, electrical	ferroelectric domain orientation [48]
	adsorption of surface adlayers	self-assembled monolayers, polymer adsorption	thiols on Au [49, 50], phosphates on metal oxides [51], silanes on SiO ₂ [52, 53]
Chemical	surface polymerization	photopolymerization	polypyrrole on metals [54]
	oxidation, reduction	electrochemical oxidation	oxidizing metal surfaces [55]
	chemical etching	wet-etching	surface etching of semiconductor [56]
	polishing	electro-chemical	tailoring surface roughness [47]

Table 2.2: Examples of tailorable surface properties

Functionalization	Surface interaction with	Relevance	References
lipo-/hydrophilicity	oils/water	self-cleaning, protein and cell adhesion	[1, 2, 57]
protein resistance or specific adhesion	cells and bacterial adhesion	implants, medical devices such as surgical equipment	[31, 58, 59]
work function	electromagnetic radiation	solar cells, optical transducers, LEDs	[60–62]
band gap	light	solar cells, photocatalysis	[63, 64]
reflectivity	light	shielding from or filtering of light	[65]
color	light	foods, diodes, paints	[65–67]
surface charge	charge(d) systems	adhesion, localization of nanoparticles	[33, 35, 68]
surface roughness	liquids and organisms	degree of cell and bacterial adhesion, self-cleaning	[2, 57, 69, 70]
friction	mechanics	machinery, e.g. clock mechanisms	[71, 72]

2.1 Substrates

The materials that served as main types of substrates throughout this work were sputtered oxides of titanium and niobium, namely titanium dioxide (TiO_2) and niobium pentoxide (Nb_2O_5). Both materials belong to a group of metal oxides and semiconductors (amongst others: ZnO , CuO , Fe_2O_3) which possess remarkable properties as photocatalysts and optoelectronic components. [3, 74–82] TiO_2 and Nb_2O_5 occur naturally as native oxide layers on the surfaces (upon exposure to air or generally oxygenic environments) of their corresponding metals, which constitute basic materials for example for bone implants [59, 83] because of their inherent light weight combined with mechanical strength. TiO_2 forms surface layers with thicknesses of only a few nanometers under ambient conditions, highly increasing the corrosion resistance of Ti-based materials. [84] Such layers can be altered with regard to thickness and crystallinity to strongly influence optical, chemical, and mechanical properties. [84–88] Additionally, much research is focused on TiO_2 itself as a very promising alternative and enhancement for SiO_2 in solar cells and other electro-optical devices because of its abundance on earth and high absorption of (UV-)light. [76, 89, 90] Nb_2O_5 has also been under scientific investigation because of its similar photocatalytic activity under UV in comparison to TiO_2 . Cui et al. showed that mixed $\text{Nb}_2\text{O}_5/\text{TiO}_2$ layers showed an increase of photocatalytic activity (determined by decomposition of 1,4-dichlorobenzene (DCB)) by 100% over pure TiO_2 samples due to increased (surface) acidity. Thus, Nb_2O_5 was also chosen as a substrate for a considerable number of experiments presented in this work (see Table 2.3 for comparison of the two materials).

For comparison experiments and to emphasize particularities/benefits of TiO_2 and Nb_2O_5 as substrates for the investigated surface functionalizations regarding affinity for adlayer formation and efficiency during surface adlayer photodegradation (see sections on adlayers stabilities), silicon dioxide (SiO_2) and chromium with its native oxide layer (Cr/CrOx) were included as substrates. Furthermore, any extension of the studies undertaken in the course of this work to these materials is reasonable since Si based materials are used for their unique and readily adjustable semiconductor properties. Because of the ever-growing desire for higher computational performance, electronic elements and circuits have undergone continuous

efforts of downscaling. Successful downscaling, however, has reached limits mostly because the nanoscale physical properties, such as the electronic band structures (essential for the functionality of transistors, for example) differ considerably from those of bulk materials. It is here that molecular-self-assembly-based production processes are thought to present promising paths to overcome current size restrictions and also facilitate production processes, making it evermore desirable to explore new surface chemistries for semiconductors, metals, and metal oxides. [5, 91]

2.1.1 Metal oxides: titanium dioxide (TiO_2) and niobium pentoxide (Nb_2O_5)

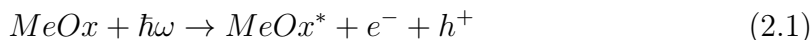
Besides their occurrence as native oxide layers of titanium and niobium, TiO_2 and Nb_2O_5 and mixtures thereof can be grown artificially – chemically and physically – for example by sublimation, [1] sol-gel processes, [43] soft-solution methods, [92] and magnetron sputtering [41]. [84, 93, 94] Depending on the technological conditions during film growth [95], such as pressure and temperature, the formed oxides are amorphous or of one of the various crystal phases [96–98]. The main naturally occurring phases of TiO_2 are anatase, rutile [99], and brookite [100], rutile being the most thermodynamically and thus most common form because amorphous TiO_2 as well as anatase and brookite can be converted to it upon heating. [95] The most common forms of Nb_2O_5 are TT-, T-, M-, and H- Nb_2O_5 (named after their different crystal structures). [98, 101] Some properties of the materials are outlined in Table 2.3, and are highly dependant on crystal structure, particle size, and doping.

Applications of the metals and their oxides in medicine and other fields, as surface coatings, corrosion protection, insulation, coloring, or as cleaning agents demand tailoring of hardness and band gap structure to achieve for example mechanical stability or good absorbance of sunlight by doping and surface modification. [79, 82]

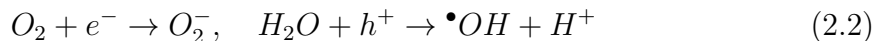
The refractive indices and direct band gaps of TiO_2 and Nb_2O_5 are in the same range (3.0 - 3.4 eV), as outlined in Table 2.3, displaying a maximum in their absorption optical spectrum in the UV (thin films are transparent for visible light). The band gap as well as the refractive index, however, are strongly influenced by the crystal structure [95], doping [102, 103], oxidation state [95], and physical shape (e.g. mesoporosity) [104, 105]. Additionally, it is known that for the case of TiO_2

the crystal phase/structure and degree of hydroxylation determine the adsorption behavior of adsorbates (e.g. catechols [106, 107]). Nevertheless, a general affinity of TiO_2 and Nb_2O_5 for surface adlayers based on phosph(on)ate [108], catechols [27], and PLL-based polymers [31], amongst others, has been established in the literature.

The aforementioned photocatalytic activity of TiO_2 and Nb_2O_5 upon exposure to UV is based on light with (with energy $E = \hbar\omega$) in the range of the metal oxide's band gap being absorbed, and generating electron-hole pairs (e^- - h^+). These cause redox reactions with molecules/radicals whose redox potentials are close to the band edges of the metal oxides. [82, 134, 135] These pairs in return can interact with molecules such as O_2 and create radicals. Such radicals, i.e. superoxide ($\text{O}_2^{-\bullet}$), can potentially degrade a vast number of hazardous organic compounds into nonhazardous products. [82, 136] The creation of the radicals at the surface of the metal oxides (MeOx) can be expressed as follows:



The e^- - h^+ pairs create oxygen-derived radicals such as superoxide and hydroxyl radicals in the presence of H_2O and O_2 [82]:



The radicals in return oxidize or reduce organic adsorbates (proximity to the photocatalyst surface increases probability of reaction) thus leading to their degradation, ultimately resulting in H_2O , CO_2 and (volatile) organic byproducts, essentially cleaning the surface. [137, 138] The intensity and efficiency of the photocatalytic activity and the spectral range depend on the crystalline structure of the metal oxides as well as present dopants. [104, 139, 140] Nitrogen-doped TiO_2 , for example, has been shown to exhibit photocatalytic activity in the visible light range of the spectrum, enhancing its applicability as a cleaning agent or in solar cells under sun light. [139]

Further research regarding TiO_2 is derived from the use of titanium alloys as medical implants. Here, it is thus important to

1) study interfaces of Ti/TiO_2 with biological systems such as proteins, cells, and bacteria

Table 2.3: Overview of properties of TiO_2 and Nb_2O_5 (and SiO_2 for comparison)

Property	TiO_2	Nb_2O_5	SiO_2
refractive index (at λ)	2.30-2.75 (at $\lambda = 633 \text{ nm}$) [109, 110]	2.2-2.6 [94]; 2.1-2.4 (at $\lambda = 633 \text{ nm}$) [111]	≈ 1.46 [112, 113]
band gap E_g (eV)	3.03 - 3.39 [109, 114, 115]	3.0-3.3 [94, 104]	1.1-1.6 (Si) [116, 117]; 5-9 (SiO_2) [118, 119]
potential adsorbates	polycationic polymers [31, 120, 121], $-\text{PO}_3/4$ [26, 58, 122], catechols [27], silanes [123, 124], $-\text{COOH}$	polycationic polymers [120, 121, 125, 126], $-\text{PO}_3/4$ [51]	sil(ox)anes [52, 127], PLL-based polymers [120, 128]
photocatalysis	[82, 129-131]	[104, 131, 132]	in conjunction with TiO_2 [133]

2) be able to modify the implant surfaces according to application requirements (e.g. osteointegration).

Biocompatibility of a material or more generally an object describes physiological responses triggered in biological systems when in contact with the material, e.g. immune reactions. For example, implants have to be accepted by the host system which in some cases means certain types of tissue must be able and prone to attach to the surface (osteointegration) while in other cases this has to be strictly avoided (e.g. stents).

2.1.2 Silicon dioxide (SiO_2)

Table 2.3 lists physical and chemical properties of Si/SiO₂ surfaces. The diverse developments in the semiconductor industry, mainly focused on silicon-based materials such as silicon nitride and silicon oxides, lead to extensive research regarding surface chemical, electronic and optical properties, such as surface charge, band gap, work function, refractive index, and electromagnetic absorption behavior of these materials. The band gaps of silicon and silicon oxide, depending on crystallinity and bulk porosity, lie in the ranges of 1.1-1.6 eV [116,117] and 5-9 eV [116,117], respectively (see Table 2.3). Hence, bulk forms of both materials are not suitable for UV-induced photocatalysis – silicon’s band gap is smaller than the necessary redox potentials (for example $\text{OH}^- = \bullet\text{OH} + e^-$; $E^0 = -2.8 \text{ V}$ [102]) while the band gap of SiO₂ is larger than the energy of UV photons (3 - 5 eV). Thus, Si/SiO₂ can serve as a reference material during the investigation of the mechanisms and influence of substrate as part of direct UV-photolithography of adlayers from polymers and molecules that adsorb on TiO₂ or Nb₂O₅ and Si/SiO₂ surfaces. One type of polymer known to do so are cationic (co-)polymers such as PLL-*g*-PEG. [128,141]

Si/SiO₂ (e.g. glass, wafers) surfaces can be functionalized (e.g. for self-cleaning windows) with silanes. [127,142,143] Similarly to thiols on gold, studies undertaken regarding properties of surface adlayer similar to systems investigated in this work can be used for comparison with respect to adlayer properties such as surface coverage and stability.

Thirdly, silicon wafers and specially treated glass surfaces can be coated with (nanometer thin) films of TiO₂ and Nb₂O₅ yielding almost atomically flat surfaces

of the two metal oxides. Such films can be optically transparent and find application as substrate materials in optical microscopy.

2.1.3 Chromium/Chromium oxide (Cr/CrOx)

The well established affinity of chromium for pyridinium- [144] and catechol-based [145–147] molecules makes it feasible to construct self-assembly-based nano systems that tailor the work function [148], conductivity, [6] protein resistance [149], and other properties on such substrates in a manner comparable to thiol- [50, 150] or disulfide-based [49, 50, 151] systems (on gold and silver substrates). [6, 49, 50, 152, 153]

2.2 Homogeneous coatings

It is often desirable to functionalize surfaces homogeneously, e.g. as a protection against corrosion or in stacked layer-based systems. [154, 155] Several methods to achieve such coatings exist. Their objective is to create a surface layer whose physical and chemical properties do not vary (only within acceptable margins) across the surface. It is desirable that the coating spreads homogeneously by itself with as little external interference as possible.

Such coatings permit tailoring of surface properties on a bulk material without having to alter the actual bulk. Downscaling, *i.e.* minimizing coating thickness, while preserving the coatings essential properties is important in order to lower costs and optimize surface properties. Furthermore, it is crucial to exert high degrees of control over the homogeneity of the coating which can pose a challenge on the macro-, micro-, and nanoscale. Various deposition techniques such as chemical vapor deposition (CVD) [156] or physical vapor deposition (PVD) [157–160] are viable means to achieve such coatings.

2.2.1 Surface adlayers (SADs)

The epitome of minimizing coating thickness is the fabrication of adlayers with layer thickness of only one or a few molecular lengths that (strongly) adhere to the surface. Techniques such as chemical vapor deposition (CVD) [156] or physical vapor

deposition (PVD) [157–160] have been shown to allow adlayers structures to be fabricated, the functional species (polymers, fullerenes, or simply atomic species such as metals) are evaporated to form gases that condense or react to solid forms on the surface. It is difficult however to achieve sufficiently good control over the deposition process (which is usually performed under vacuum) and obtain monolayers.

An easier approach is to form the adlayers by adsorption from solutions. Polymeric adlayers, for examples, can be made by “grafting-from” or “grafting-to” when a polymer film is grown directly on a surface or the ready made polymer is adsorbed from solution. Other functional molecules, such as fullerenes, benzenes, and alkenes, can be deposited in similar fashions.

2.2.2 Self-assembled monolayers (SAMs)

One of, if not the easiest and most desirable approach is for aforementioned surface adlayers to be molecular monolayers, spontaneously formed without the need of exterior control during formation – self-assembled monolayers (SAMs). A variety of molecules and polymers have been found to do exactly that. Examples are polycationic-based polymers, alkyl-thiols, alkyl-phosph(on)ates, and alkyl-sil(ox)anes (see Table 2.4). [53, 120, 121, 161, 162] Adlayers of the latter three have also shown a high degree of intermolecular order. [25, 142, 151, 163] While various authors see this as a crucial part of the definition of SAMs, it is not considered as such in this work because no analysis with regard to intermolecular order was performed for the investigated systems. It will not be ruled out, however, for the catechol systems presented (phosphate ordering has been extensively investigated by others [26, 164]). SAMs can exhibit a high degree of order effectively forming a 2-dimensional crystalline structure. The molecules’ general molecular structure with its three major parts is sketched in Figure 2.1 :

1. functional group: a chemical unit carrying a specific/desired (surface) functionality, such as protein resistance or hydrophobicity.
2. spacer group: often alkyl chains of different length connecting the functional and anchor group and contributing to the stability and ordering of the SAM, via van der Waals’ interactions.

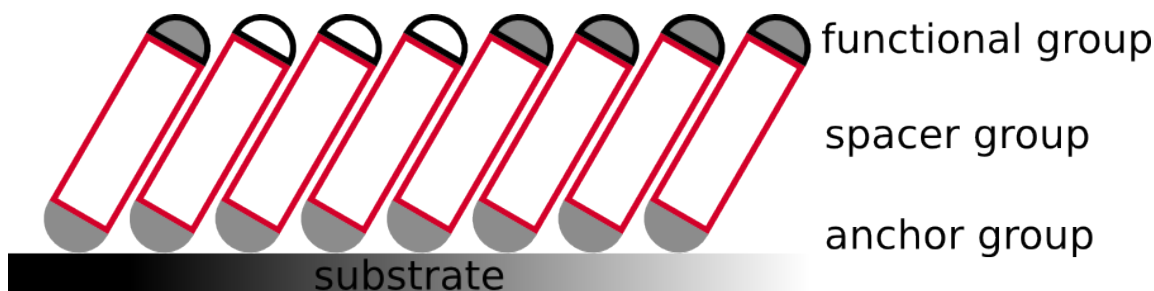


Figure 2.1: Sketch of the basic structure of (adsorbed) molecules comprising an anchor group, a spacer group, and a functional group.

Table 2.4: List of common SAM systems.

Type	Anchor group(s)	Examples of substrates	References
Thiols	-SH	noble metals (Au, Ag)	[161, 166]
Phosph(on)ates	-PO ₄ H ₂ , -PO ₃ H ₂	metal oxides (Nb ₂ O ₅ , TiO ₂ , Ta ₂ O ₅)	[23, 25, 26, 167]
Silanes	-SiCl ₃ , Si(OR) ₃	silica	[52, 53, 127]
PLL	-NH ₂	metal oxides	[141, 168, 169]
Catechols	-C ₆ H ₄ (OH) ₂	metals, oxides	[7, 27, 170]

- anchor group: a chemical unit such as -SH, -PO₄H₂, -PLL that binds to the substrate of interest. The strength and type of bond influence the stability of the SAM.

Additionally, the spacer group also serves other purposes, e.g. an optical switch mechanism through which the orientation and thus functionality of the monolayer can be altered upon irradiation with light. [165]. A listing of some of the most studied SAM systems is given in Table 2.4.

During adsorption from solution, the kinetics of layer formation and ordering are influenced by all three parts (anchor, spacer, and functional group). The role of alkyl chain length on ordering and adlayer quality has been described for thiols on Au by Nuzzo et al. [49, 151] and Bain et al. [162] and for phosphates by Spori et al. [171] Longer alkyls exhibit both higher adsorption probability and higher degree of ordering (number of CH₂ groups < 20). [53] Different degrees of fluorination also affect the formation of adlayers, as shown for alkanephosphonic acids [172] and

thiols [173,174]. Ordering and surface coverage is also influenced by the number of anchor groups per molecule. Park et al. demonstrated that layers of alkyl dithiols are less densely packed than alkyl thiols of the same length due to the larger footprint of the anchor group. [175,176] Lecollinet et al. came to similar conclusions for biphosphonates versus normal alkyl phosphonates. [177] Yet, neither makes any definite statements about any possibly increased stability of molecules with multiple anchors. These examples and others such as PLL-based polymers indicate that higher numbers of anchor groups per adlayer building block increase the binding strength to the substrate while decreasing order within the adlayer – inducing competing processes regarding (long term) adlayer stability. [153] Anchor groups with multidentate binding sites such as phosphonic acid and catechols show dependence of stability on the number of molecule-substrate bonds. Binding energies (= strength) for catechols with different conformations have been investigated by Li et al. [106] and Terranova et al. [178] by density functional theory (DFT). Conformational dependencies (e.g. alkyl chain tilt angle) for mono-, bi-, and tridentate phosphonic-titania bonds were described by Guerrero et al. [179] Furthermore, it is known that exterior conditions such as temperature, salinity, and pH of the solution highly influence behavior and particularly adsorption kinetics of polymers and alkyl derivatives. [122,125,180,181]

2.2.3 Phosph(on)ates

Phosph(on)ates are known to bind to numerous metal oxides, including Al_2O_3 , Nb_2O_5 , Ta_2O_5 , TiO_2 , and iron oxides. Their alkyl derivatives have been shown to form highly ordered and stable surface adlayers and SAMs on these substrates. [24,25,53,182] In contrast to thiol-Au chemistry, phosph(on)ates bind to substrates via their oxygen atoms, thus offering between one and three bridging atoms (mono-, bi-, and tridentate binding). These oxygen atoms can form strong P-O-substrate covalent bonds but also weaker hydrogen bridges to the substrate and neighboring molecules. The influence of mono- vs. bidentate binding to tantalum oxide and titanium dioxide has been laid out in the literature, essentially stating that predominantly bidentate configurations are observed. [25,167,172] Phosph(on)ates SAMs have been used to immobilize bioactive molecules [183], improve implant osteointegration [184], and tailor the degree of hydrophobicity of surfaces [23] amongst other

things demonstrating their versatility. Drawbacks occasionally encountered when working with phosph(on)ate-based SAM systems, however, include the long-term stability of their adlayers, e.g. in aqueous environments. One way to overcome the issues of easy removal by solvent rinsing appears to be gentle heating of adlayers after adsorption, as demonstrated by Gawalt et al. [122]

2.2.4 Catechols

Catechol (1,2-dihydroxybenzene) is a benzene ring with two hydroxyl groups in adjacent ring positions. Several catechol derivatives, such as the catecholamines dopamine and norepinephrine, fulfill important roles in nature and have found applications in medicine, e.g. as neurotoxins, indicators of metabolic activity, and components of neuronal and hormonal processes [185–188]. Beyond the medical implications, recent research on catechol derivatives derived from the chelation properties exhibited by siderophores from cyanobacteria [189,190]. It was also found that chemistries of mussel adhesion to objects involved catechol derivatives, such as the amino acid 3-(3,4-dihydroxyphenyl)-L-alanine (L-DOPA), further intensifying focus on catechols' adhesive properties. [27, 191–193] The strong bonding properties of catechols to various materials, in particular metals, have already been known for decades but are still the topic of extensive scientific investigation because of constantly growing interest in surface functionalization. [27, 170, 194] Another reason for the interest in catechols is the change in optical absorption behavior induced in surfaces upon adsorption, which can find application in optical nano devices: Xu et al. mention several effects including a large red shift in the absorption threshold of TiO₂. [195] Catechols have been found to be utilized by micro-organisms such as cyanobacteria and mussels to form strong bonds to metals. This suggests basing approaches in surface-functionalization on this observation in the form of functional surface adlayers (SADs). [180, 190] This approach is particularly intriguing because of the purely organic, and simple, yet versatile nature of catechol. Figure 2.5 shows two functional catechol derivatives: nitrodopamine (ND) and a perfluoro-alkyl nitrodopamine (PFAND). The former is eminently hydrophilic and can be (de)protonated, and thus charged by adjusting the solvent's pH. The latter's functional group is a CF₂ chain, possibly allowing the molecule to be used to render substrates hydrophobic and in-

fluence their work function in manners comparable, for example, to perfluorinated alkyl thiols and n-alkanoic acids. [148, 196, 197]

ND is a catechol with a $-(\text{CH}_2)_2\text{NH}_2$ in the 4- and an $-\text{NO}_2$ group in the 5-position. The amine group guarantees a hydrophilic character of the molecule but also allows for further functionalization, while the nitro group protects the benzene against oxidation and thus degradation and potential polymerization.

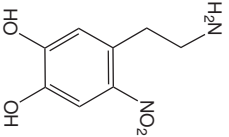
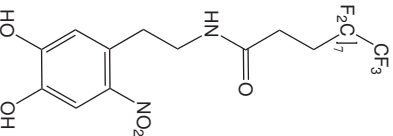
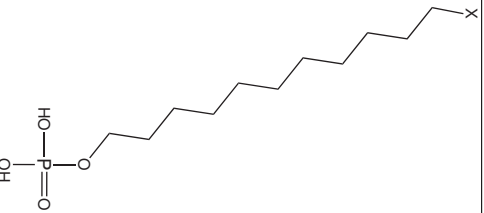
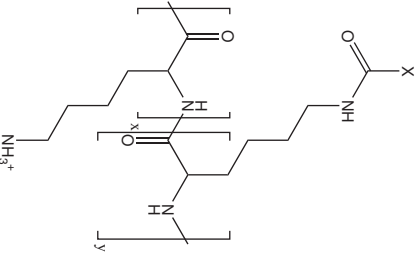
The mentioned perfluoro-alkyl nitrodopamine (PFAND) essentially is ND where a perfluoro-alkyl $\text{CF}_3-(\text{CF}_2)_7$ -tail is coupled to the amine group thus creating a molecule with strong hydrophobic character that can potentially be used to functionalize substrates via catechol adsorption.

2.2.5 Polyelectrolytes

Poly(L-lysine)-based (co-)polymers (see Table 2.5) adsorb via their (in aqueous solutions positively) charged ammonium groups onto negatively charged metal oxides including SiO_2 , TiO_2 and Nb_2O_5 . [121, 168] A prominent member of this polymer family is poly(L-lysine)-graft-poly(ethylene glycol) (PLL-*g*-PEG). Its structure, adsorption behavior, functionality and other properties have been outlined in the literature. [120, 121, 198, 199] For a long time, most interest was extensively focused on using it to render surfaces antifouling upon adsorption, including various metal oxide systems otherwise prone to cell or bacterial adhesion. More recently, it was pointed out by Lee et al. and later elaborated by Muller et al. how different architectures of PLL-*g*-PEG can improve aqueous lubrication. [199–201] How to improve stronger adsorption of the block copolymers by coupling catechols to free lysine groups was recently shown by Saxer et al. [202]

It must be noted, however, that PEG is prone to oxidation and thus degradation by oxidizing agents. This drawback has given motivation to the design of a different protein resistant polymer: Poly-2-methyl-2-oxazoline (PMOXA). [126] Initial tests have shown higher long time resistance of PLL-*g*-PMOXA against protein adsorption, as well as cellular adhesion and degradation, in comparison to PLL-*g*-PEG.

Table 2.5: Basic types of molecules used in this work.

	Nitrodopamine	Perfluoro-alkyl nitrodopamine	Alkyl phosphates	Poly(L-lysine)-based polymers
Acronyms	ND	PFAND	DDPO ₄ , OH-DDPO ₄ , COOH-UDDPO ₄	PLL- <i>g</i> -X, X=PMOXA, PEG*
Molecular formula	C ₈ H ₁₀ N ₂ O ₄	C ₁₉ H ₁₃ N ₂ O ₅ F ₁₇	X-(CH ₂) ₁₁ PO ₄ H ₂ , X=CH ₃ , OH-(CH ₂), COOH	-*
Molar mass [g/mol]	198.18	672.29	DDPO ₄ : 266.31, OH-DDPO ₄ : 282.31, COOH-UDDPO ₄ : 296.31	*
Solvent	ultra-pure H ₂ O	H ₂ O:2-propanol 2:1	n-heptane:2-propanol; H ₂ O for ammonium salts	HEPES/HEPES2 buffer*
Structure				

*(see Section 3.3)

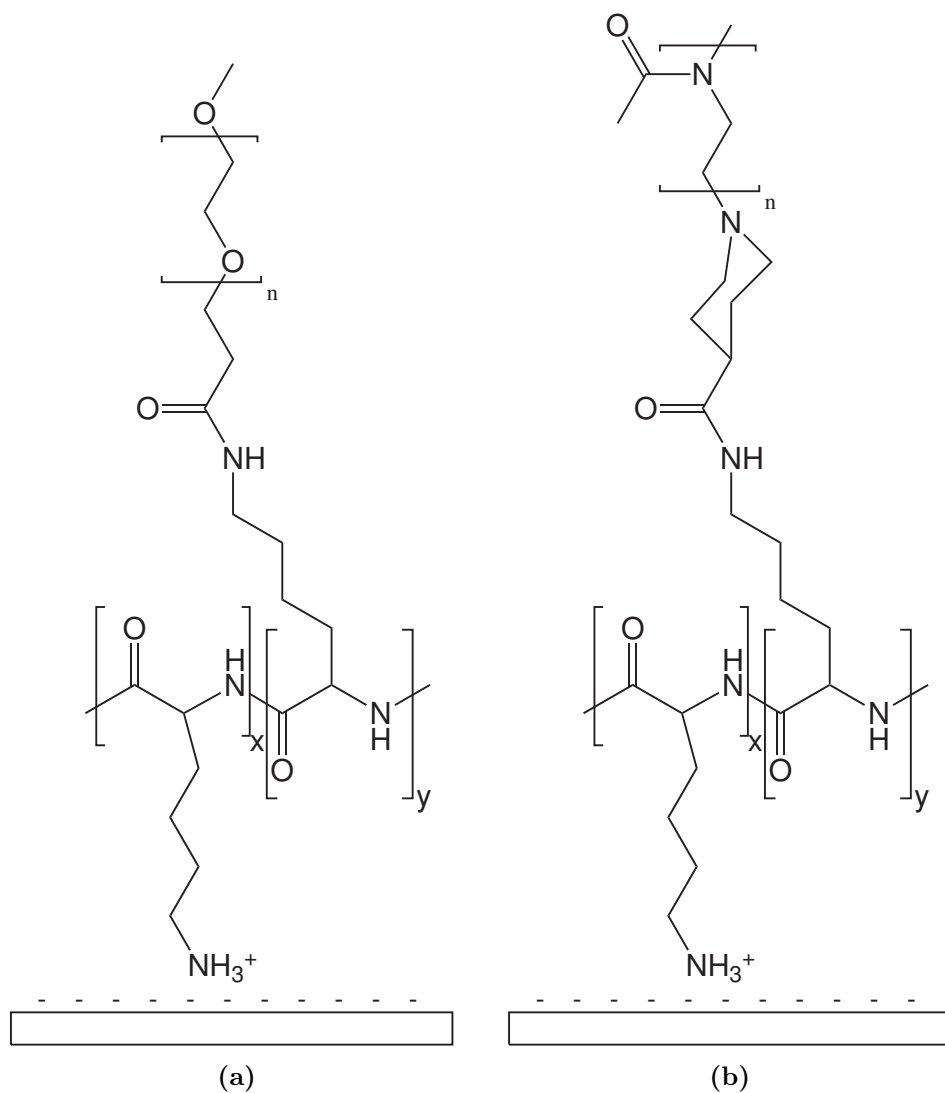


Figure 2.2: Chemical structure of (a) PLL-*g*-PEG and (b) PLL-*g*-PMOXA (when adsorbed on a negatively charged surface). The parameters “x” and “y” determine the grafting ratio, “n” the polymer’s “chain length”.

2.3 Heterogeneous surface functionalizations

Various applications require not homogeneity but heterogeneity – meaning at least two different functionalizations – of a surface adlayer in order to achieve specifically designed surface functionality.

The length scale of the heterogeneity is to be correlated to the size of the interacting entity (bacterium, water droplet, sensor probe, proteins, or dust particles) and its probing/sensing capabilities. In order to differentiate types of heterogeneity, it is important how and on what scale (average) distributions of the individual functionalities on the surface appear to the entity. If the probing system cannot spatially distinguish between the two functionalities the surface functionalization will be considered as mixed. If the spatial sensitivity of the probe is high, such that it can distinguish and locate areas with either functionality, differentiate and react differently to them, the surface is considered patterned.

2.3.1 Mixed surface functionalizations

Examples for mixed surface functionalizations include the specific adjustment of the degree of hydrophobicity by coadsorbing hydrophobic and hydrophilic SAM molecules. [23] Water droplets with a diameter of 1 mm on such a mixed hydrophilic-hydrophobic SAM “respond” with an average contact angle that mainly depends on the ratio of the two kinds of molecules but not on the intermolecular structure. [18, 23, 28] A similar approach can be taken for surface charge. In both cases, the adhesion behavior of proteins and cells is strongly influenced and can thus be used to trigger certain cellular reactions. [33, 203] Keeping the basic idea of mixed surface functionality in mind, one can tailor surface potential by combination of different alkyl chain length. [204]

Mixed adlayers allow for two things: the degree of surface functionality (e.g. free surface energy, chemical reactivity) can not only be achieved by specifically designing and synthesizing SAM molecules but also be adjusted at the (inter)molecular level upon adsorption. Specific values between two extremes (e.g. hydrophilic and hydrophobic, positively and negatively charged) can be tailored by choosing appropriate adsorption conditions for both kinds of molecules. On the other hand, two

functionalities can be bestowed upon a surface and adjusted simultaneously (e.g. hydrophilicity and charge, work function and lipophilicity) by using two differently (ω -)functionalized molecular species (e.g. acid, base, positively or negatively charged, or dipole moment) or differentiated intramolecular structures (e.g. (polymer) grafting density or alkyl chain length).

2.3.2 Surface-chemical gradients

Surface-chemical gradients constitute the pinnacle of a mixed surface-coating – the degree of a surface functionality is varied continuously from one extreme to the other along (at least) one spatial direction. Depending on the approach for functionalization, this can for example be achieved by the continuous change of the mixing ratio between two molecular species, the degree of polymerization, or increasing the length of a spacer group. When the first gradients were produced in laboratory environments by Elwing et al. [36,205] with silanes on glass, Chaudhury and Whitesides [14] with silanes on silicon wafers and Liedberg [20] with thiols on gold, it was shown how such simple gradients of chemical groups on surfaces can be used to screen interactions with proteins and detergents. Later on it became apparent, however that such surfaces also allowed other effects only accessible to surface gradient techniques, e.g. cellular chemotaxis, to be observed. [13]

With time, various fabrication techniques and applications have been developed, including liquid diffusion, density gradient, radio frequency plasma discharge methods [205], vapor diffusion [14], diffusion in a matrix [20], microfluidics [206], and immersion. [10,11] The latter is a simple dip and rinse technique used to make large scale (centimeter and above) surface-chemical gradients and has been developed by Morgenthaler et al. in our lab. [18]. Genzer et al. and Morgenthaler et al. have written extensive reviews on gradient fabrication techniques and applications. [10,11]

2.3.3 Patterned surfaces

Creating patterns of antifouling polymers on surfaces on scales beyond the size of cells, on the other hand, can create highly localized confinement areas for cells when attaching to the surface. For example, when studying cellular or more generally

biological surface interactions, it is advisable to directly compare two states of the surface, either two functionalities or a functionality vs. a reference. Not doing so by simply using homogeneous surfaces can introduce errors between experiments because of environmental conditioning. Producing surface patterns allows such studies by exposing cells, for example, to both surfaces simultaneously. Depending on the relative scales of the responsive system (cell) and pattern the reaction of the former can either be

- a) non detrimental or irrelevant - the pattern is too small to be detected,
- b) patterns is of same order of sensitivity of the cell - single cells adjust to the environment individually, or
- c) pattern is significantly larger than cell and cannot be bridged – cells behave differently depending on where they are on the pattern. Examples of specific cellular and protein adaptation to surface patterns have been given for thiols on gold [207], silanes on Si [208], PLL-based polymers [128, 141].

Besides biological applications, surface-chemical (by SAM) patterns can also be used as platforms for generating patterns in nanoparticles [30], surface polymerization [209], or chemical etching [210].

In the course of finding and characterizing platforms, chemistries, and fabrication techniques for surface patterns several methods have emerged by, e.g., using and/or combining photolithography(PL), [30] microcontact printing (μ CP), [32] Selective Molecular Assembly Patterning (SMAP), [128] Molecular Assembly Patterning by Lift-off (MAPL). [211]

For initial investigations of the direct UV patterning technique, the polyelectrolytes PLL-*g*-PEG and PLL-*g*-PMOXA (see Figure 2.2) were used because the surface patterns generated could easily be imaged using (fluorescently) labeled proteins and under fluorescence microscopy. The drawings in Figure 2.2 show the general structure of both polymers, where the given parameters “x” and “y” determine the grafting ratio (PLL units per PEG/PMOXA chain) and “n” gives the PEG/PMOXA chain length.

In all cases, it was found that the molecular weights of backbone (PLL) and side chains (PEG, PMOXA) and the degree of “catecholization” determine the adsorption kinetics, functionality, and adlayer longevity. [120, 202]

2.4 Modification of surface adlayers

2.4.1 Decomposition and modification under irradiation

When performing surface analysis it is important to be aware whether the measurement technique at hand is destructive or not. Some techniques are intrinsically destructive such as Time-of-Flight Secondary Ion Mass Spectrometry (TOF-SIMS), while others are only very rarely destructive (for very sensitive systems) and usually considered non-destructive, such as ellipsometry. In between are techniques whose level of destructiveness depends on the object to be analyzed because of the use of high-energy photon beams such as deep-UV radiation or X-rays. With respect to the stability of surface adlayers under electro-magnetic and particle irradiation, several studies have investigated alkyls and polymers. [44, 125, 212–214] Two effects can occur during the exposure of surface adlayers to light or X-rays: direct (chemical) reaction (possibly supported by photoinitiators adsorbed on the surface) and generation of secondary electrons (from the substrate) and radicals (i.e. of oxygen) which cause transformation and degradation of the surface adlayer. [215] Either process depends on the wavelength of the absorbed radiation. In the literature it has been pointed out how alkane thiols [216], silanes [33], phosphate [37] and others, can be altered and particularly oxidized by exposure to UV through the generation of oxygen radicals. [217]

Hence, two things come to mind:

1. During surface analysis, one must be aware of the degradational effects specific to the measurement technique with respect to the analyzed object.
2. Application of the degradation/transformation effect to specifically and controllably modify surface adlayers.

With regard to the first point the relevance of X-ray radiation being high-energy electro-magnetic waves causing direct (by bond scission) and indirect damage (by secondary electrons) to organic materials by radicalization of molecules must be accounted for during XPS measurements. Fluorocarbon (FC) films especially have a tendency to degradation under X-rays. Degradational mechanisms for FC films on Si have been described by Himmerlich et al. [218] The damage induced in fluorinated alkyls during XPS measurements for example has been studied by several groups,

revealing that especially CF_2 -groups are prone to X-ray-induced degradation and show several pathways of transformation. [214, 218, 219]

Thiols adsorbed on Au are known to undergo degradation induced by X-rays [220] and low-energy electrons [212, 213].

The second point concerns the possibility to create binary patterns or gradients as described above. A rather new potential enhancement of this approach is the modification and decomposition of organic adsorbates by means of (surface) photocatalysis (discussed more in detail below). UV degradation of surface adlayer systems comparable to those investigated within this work can be found in the literature:

UV light induced damage of PLL-g-PEG has been investigated and applied for patterning by Azioune et al. [221]

Self-assembled monolayers of alkylphosphonic acids, thiols, or silanes can be degraded and almost completely removed by UV. [37, 222–224]

2.4.2 Substitution and backfilling of (sub)monolayers

During coadsorption and backfilling of (partial) SAMs of two different types of molecules on one surface, several ordering and adsorption processes and parameters such as pH, alkyl chain length, and anchor group footprint size determine stability and composition of the final layer. [53, 150, 153, 225] For example Biebuyck et al. showed for disulfides and thiols of similar structure that thiols have higher adsorption probabilities than their corresponding disulfides and replace them on gold surfaces. [153] While studies by Ishida et al. established higher adsorption rates for shorter alkyl thiols, [225] Laibinis et al. stated that longer alkyl chains lead to higher adsorption probabilities [226] – shorter alkyls are replaced by longer ones. Also, coadsorption of differently ω -functionalized SAM molecules from mixed solutions show compositional differences between relative concentrations in adlayer and solution, e.g. methyl and hydroxyl terminated phosphates or thiols on gold. [23, 162, 226]

Consequently, one can adjust the relative concentrations of two SAM molecules in one solution to achieve a specific ratio when adsorbed on a surface. Secondly, an incomplete SAM with tailored surface coverage of one component can be backfilled with a second component to achieve a full SAM of mixed functionality.

2.5 Analytical techniques

Many techniques applied for the analysis of surfaces rely on optical phenomena - the interaction of a material, bulk or surface, with light. Three phenomena arise:

1. absorption
2. reflection
3. transmission

When light is absorbed, the photon energy is transformed into another form of energy: phonons, plasmons, photoelectrons, photons of different wave length, excited molecules, heat, etc. The techniques that have been developed to collect these (quasi-)particles provide different information on chemical or physical states of samples. It is for the user to decide what is of interest and which technique to use. It must be noted that, because of potentially high-energy and its absorption, some of the techniques can have destructive effects on samples. Depending on the amount of absorbed photons, the penetration depth of the radiation, and the attenuation length of the emitted radiation, the surface sensitivity can vary between sub-nanometer to micrometers.

2.5.1 X-ray photoelectron spectroscopy (XPS)

XPS as a tool for surface chemistry analysis was developed by Siegbahn et al. in the 1960s and has been well established for decades. [227, 228] Its basic principle is the photoelectric effect. [229] The absorption of high-energy photons of energy E_γ by a body causes the emission of photo-electrons. The fundamental equation is:

$$E_\gamma = E_{e^-} = E_{kin} + E_{bind} + \phi \quad (2.3)$$

where $E_\gamma = \hbar\omega$ is the photon's energy, E_{e^-} , E_{kin} , E_{bind} , and ϕ respectively the total, the kinetic, and the binding energy of the emitted electron and the spectrometer work function.

If E_γ is known and E_{kin} can be measured with a spectrometer, the binding energy (E_{bind}) of emitted electrons can be derived:

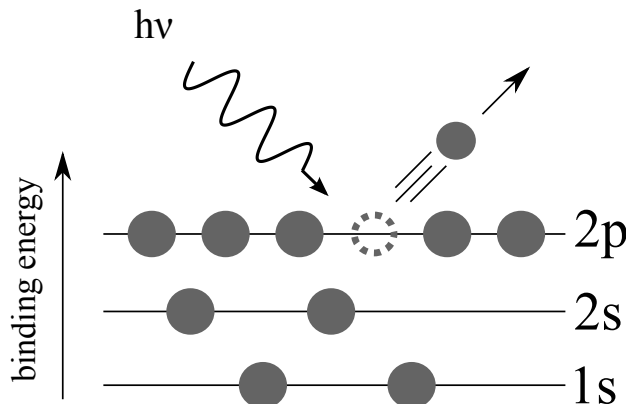


Figure 2.3: Photoelectric effect. Electrons can be ejected from atoms upon irradiation with photons (of energy $E_\gamma = h\nu$).

$$E_{\text{bind}} = E_\gamma - E_{\text{kin}} - \phi \quad (2.4)$$

A more detailed equation would be:

$$E_{\text{core}} + \Delta E_{\text{chem}} = E_\gamma - E_{\text{kin}} - \phi \quad (2.5)$$

denoting that the binding energy comprises the elemental binding energy E_{core} and a term ΔE_{chem} which is determined by the chemical state/bond of the atom. Thus, XPS allows the identification of elements present on a surface as well as their chemical state. Since the electrons that are emitted are used for identification, one must account for potential losses of kinetic energy or intensity of the electron flux brought up by elastic and inelastic collision.

The intensity I of a flux of electrons with kinetic energy E_{kin} obeys the following equation:

$$I = I_0 \times \exp\left(-\frac{d}{\lambda}\right) \quad (2.6)$$

when travelling through a material of thickness d . λ (the inelastic mean free path, IMFP) depends on E_{kin} and the material. The literature suggests several approaches for the calculation of λ . [230–232] If the electrons of interest are emitted in the very same layer as they are passing through, equation 2.6 changes to:

$$I = I_0 \times \frac{\lambda}{d} \times \left(1 - \exp\left(-\frac{d}{\lambda}\right)\right) \quad (2.7)$$

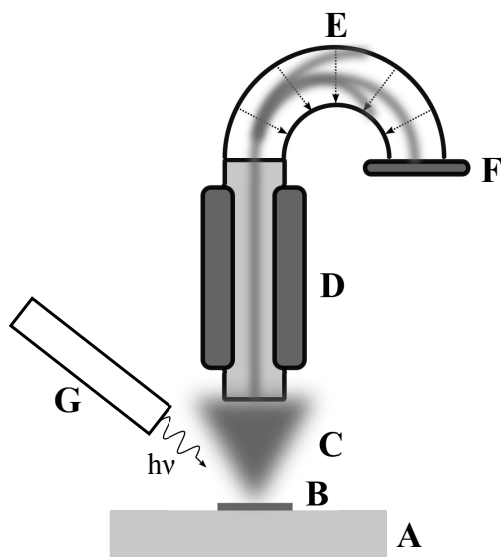


Figure 2.4: General setup for an XPS system: **A** sample holder, **B** sample, **C** electron cloud emitted from sample, **D** electro-magnetic transfer lens system for electron beam, **E** hemisphere with electrical field, **F** detector, **G** X-ray source (including crystal monochromator for monochromatic X-ray system).

The general setup of an XP spectrometer is given in Figure 2.4. A sample (B) is illuminated by an X-ray beam from a standard source (G) which is normally made of Al or Mg, emitting photons with $E_\gamma = 1486.3$ eV and 1253.4 eV, respectively. Monochromatic X-rays are obtained by diffracting the non-monochromatic X-ray beam coming from the source off a crystal monochromator (quartz).

2.5.2 Fluorescence microscopy (FM)

Fluorescence is the emission of light by a molecule after absorption of light of a lower wavelength. Fluorescence Microscopy (FM) employs fluorescent chemicals to visualize (surface) structures. Certain fluorescent molecular groups - so called markers or labels - can be linked to larger molecules, polymers, proteins, or cells. Imaging of the labeled objects is thus greatly facilitated. Cells or molecules that only adsorb in certain regions on a substrate or sample can easily be detected and mapped by FM.

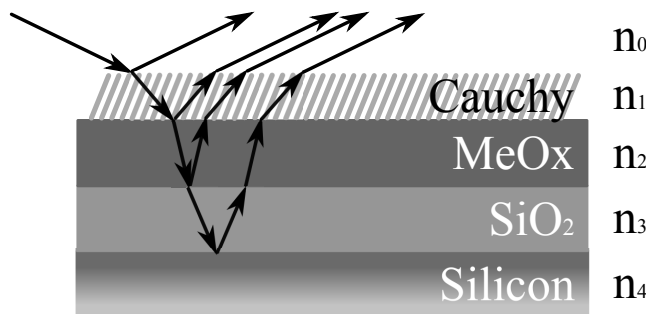


Figure 2.5: VASE model used for determining surface adlayer thickness (Cauchy layer) on MeOx coated silicon wafer.

2.5.3 Variable-angle spectroscopic ellipsometry (VASE)

The change of polarization and phase of light when reflected from a surface can be monitored and used to identify the optical properties of that surface (e.g. refractive index, optical thickness, dielectric constants). While it is possible to use a single wavelength, single incident angle light beam in ellipsometry, the quality and quantity of data are greatly improved by scanning a surface over a spectral range of light at several angles, as is done in VASE.

VASE is not a direct measurements technique. Obtained data on changes in polarization and phase of reflected light has to be fitted against a model by which layer thicknesses and optical constants for each layer are deduced. Standard data sets exist for well studied materials such as Si and SiO₂. Models exist that can be fit to reflect the properties of other materials with sufficient accuracy.

The relation between measured polarization (Ψ) and phase shift (Δ) and material properties can be given in the form of:

$$\tan(\Psi)e^{i\Delta} = \frac{r_p}{r_s} = \rho \quad (2.8)$$

2.5.3.1 Cauchy-layer

The simplest model commonly used for organic surface adlayers is purely empirical - the Cauchy layer which has the general form: [233]

Table 2.6: VASE data modeling

Layer	Model	Parameters	Thickness	Error
adlayer	Cauchy	A=1.45, B=0.01, C=0	0 - 2 nm	± 5% - 20%
TiO ₂	Tauc-Lorentz	variable	10 - 20 nm	± 0.1 nm
SiO ₂	constant	constant	2.3 nm	n.a.
Si	constant	constant	1 mm	n.a.

$$n(\lambda) = A + \frac{B}{\lambda^2} + \frac{C}{\lambda^4} \quad (2.9)$$

where n is the adlayer's refractive index. A , B , and C are fit parameters and λ is the wavelength of the incident light.

2.5.3.2 Metal-oxide (MO) layer

In order to assess the thickness of the organic adlayer layer in the four-layer model as outlined in Table 2.6 correctly, the thickness of the TiO₂ sputter coated onto the SiO₂ had to be determined first. Exemplary spectroscopic data are presented in Figure 3.3. The first part of the fitting model is a Tauc-Lorentz function for ε_2 :

$$\varepsilon_2(E) = \begin{cases} \frac{AE_0\Gamma(E-E_g)^2}{(E^2-E_0^2)^2+\Gamma^2E^2} \times \frac{1}{E}, & E > E_g \\ 0, & E \leq E_g \end{cases} \quad (2.10)$$

A represents the optical transition matrix, Γ being a broadening factor, E_g the band gap, and E_0 the peak transition energy. ε_1 is derived from ε_2 via the Kramers-Kronig integration:

$$\varepsilon_1(E') = \varepsilon_1(\infty) + \frac{2}{\pi}P \int_{E_g}^{\infty} \frac{\varepsilon_2(E)E}{E^2 - E'^2} dE \quad (2.11)$$

The Tauc-Lorentz model allows the determination of the band gap E_g of the TiO₂ and Nb₂O₅ coatings. Over the range of film thickness of 10 - 25 nm no significant difference was noted for E_g , the average being $E_g = 3.26 \pm 0.01$ eV for TiO₂ and $E_g = 3.31 \pm 0.01$ eV for Nb₂O₅, in good agreement with previous studies. [109,114,132,234]

2.5.4 Contact angle goniometer (CA)

When a drop of water (or any other liquid) is placed on a solid surface under normal laboratory conditions, the interface of the three phases (substrate, liquid, air) rapidly forms an equilibrium that depends on the interfacial energies γ_{SL} between the sample surface and water, γ_{LG} between water and air, γ_{GS} between air and the sample surface. This equilibrium is described by Young's equation:

$$0 = \gamma_{GS} - \gamma_{SL} - \gamma_{LG}\cos(\theta_C) \quad (2.12)$$

θ_C denoting the drop's contact angle. Essentially, a water droplet forms on the surface and the equilibrium leads to a measurable static contact angle (CA). Since water and air can be assumed to be constants in all experiments, measuring this CA displays a pure property of the sample surface - hydrophobicity. Amongst the surfaces known to show the highest degrees of hydrophobicity are those of polytetrafluoroethylene (PTFE) and perfluoro-alkyls. Besides surface-chemistry, physical surface structure also influences the effective contact angle. The lotus leaf displays superhydrophobicity because the hydrophobic effect of waxes are strongly increased by surface microstructures.

2.5.5 Micro droplet density (MDD)

Driving the relative humidity of an aerial environment above 100% by lowering the temperature of the substrate leads to condensation of water when it reaches the dew point. When this condensation happens on surfaces, the degree of wettability (different interfacial free energy) and physiochemical homogeneity/heterogeneity (e.g. roughness, mixed surface functionalities) of that surface determine how the water droplets forms. [235] On contaminated, polar, highly wettable surfaces, water is more likely to condense compared to the situation on clean, apolar, and flat surfaces, which show reduced wettability. [235–238] Inhomogeneities in a surface's physiochemical properties are reflected by droplet patterns. [235, 239] They can be observed and recorded using a microscope and a computer-assisted camera system. On hydrophobic surfaces, once water has started to condense, one sees the condensed droplets continuing to grow rather than new droplets nucleating at the surface. Hy-

drophilic surfaces behave in a more complicated way because condensed droplets tend to coalesce in the course of the condensation experiment. For qualitative assessment it can suffice to keep a constant temperature and thus condensation-evaporation equilibrium in order to distinguish areas of different degrees of hydrophobicity.

2.5.6 X-ray diffraction (XRD)

We consider that solids can be described as either amorphous (atoms are arranged randomly and disorderly) or crystalline (atoms are arranged in a regular pattern with a unit cell that can be used to describe the crystal). Parallel X-ray beams diffracted from a solid-state material can interfere. The interference is constructive, with maximum intensity under certain angles Θ , when the reflected beams are in phase (illustrated in Figure 2.13). [240, 241] The dimension/parameters of the unit cell being very material specific determine Θ of maximum intensity and the whole 2Θ spectrum. [240, 241] Every crystalline substance yields a pattern. [242] These patterns can be determined according to Equation 2.13 (based on Figure 2.6), where λ is the X-ray's wavelength, d the distance between neighboring atoms, and Θ the angle between incoming/scattered beam and the surface.

$$2d\sin(\Theta) = n\lambda \quad (2.13)$$

These angles depend on the crystallinity, parallel crystalline planes of the sample, and the crystal's orientation. High crystallinity causes sharp peaks, while amorphism leads to broad or no peaks. XRD serves as a high-accuracy method to identify the kind of crystalline material at hand, its crystal structure, and also its degree of crystallinity.

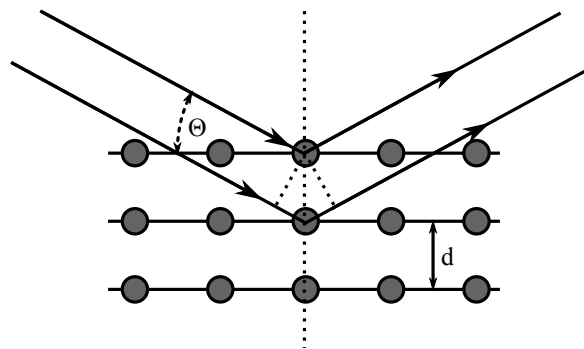


Figure 2.6: XRD principle: X-rays are scattered by atoms and interfere constructively for $2d\sin(\Theta)=n\lambda$.

CHAPTER 3

Surface preparation and analysis:
materials, protocols, and analytical
methods

In the final analysis, a drawing simply is no longer a drawing, no matter how self-sufficient its execution may be. It is a symbol, and the more profoundly the imaginary lines of projection meet higher dimensions, the better.

Paul Klee

In this chapter all details regarding experimental techniques, instruments, and protocols are presented. X-ray photoelectron spectroscopy (XPS) instruments were a Sigma2 and a PHI5000, X-ray diffraction (XRD) was carried out on a Bruker D8, and the variable spectroscopic ellipsometer (VASE) was a Woollam MF-2000F.

3.1 Instruments

3.1.1 X-ray Photoelectron Spectroscopy (XPS)

A Sigma2 instrument (Thermo Fisher Scientific, Loughborough, Great Britain) was utilized for routine XPS experiments. The Sigma2 is equipped with a UHV chamber (pressure $< 10^{-6}$ Pa during measurements). The X-ray source is a non-monochromated 300 W Al-K α source ($h\nu = 1486.6$ eV) that illuminates the sample at an angle of 54° to the surface normal. The hemispherical analyzer is mounted at 0° with respect to the surface normal, thus operating at the magic source-analyzer angle, which eliminates the need for angular-distribution correction. [227] The detector consists of seven channeltrons. The spot size of the analyzed area (large-area mode) was 400 μm , and the results therefore represent a laterally averaged chemical composition. For this setup the full width at half maximum (FWHM) of Ag 3d $_{5/2}$ is 1.4 eV using a pass energy of 25 eV. Standard measurements comprised averages over nine (for C, F, and N) or three (for Ti, Si, Nb, and O) scans for each element plus survey scans with pass energies of 25 eV and 50 eV, respectively. Energy resolution was 0.05 eV for C, F, and N and 0.1 eV for other elements. The dwell time was left at 100 ms at all times, resulting in 3-5 minutes measurement time per spot for each element, accumulating to about 30 min for a complete elemental scan of one spot.

Figure 2.4 is a sketch of the general configuration of an XPS instrument and also corresponds well to that of the Sigma2.

For XPS peak modeling of catechol adlayers, 30 (PFAND) or 10 (ND) high-resolution XPS spectra were recorded using a PHI5000 Versa Probe (ULVAC-PHI, INC., Chigasaki, Japan) on homogeneous samples. The spectrometer is equipped with a 180° spherical capacitor energy analyzer and a multi-channel detection system with 16 channels. Spectra were acquired at a base pressure of 5×10^{-8} Pa using a focused scanning monochromatic Al-K α source (1486.6 eV) with a spot size of 200

μm and 47.6 W power. The instrument was run in the FAT analyzer mode with electrons emitted at 45° to the surface normal. The pass energy used for survey scans was 187.85 eV and 46.95 eV for detail spectra at FWHM of about 0.7 eV.

For homogeneous layers only one spot per sample was measured. Gradient samples were analyzed by measuring 10 positions along the gradient with 4 mm center-to-center distance, beginning at 2 mm from the hydrophobic edge.

3.1.2 Variable Spectroscopic Ellipsometry (VASE)

VASE was used to measure surface coverage/layer thickness. A Woollam MF-2000F (WOOLLAM Co., Inc., Lincoln, Nebraska, USA) ellipsometer was utilized at the three incident angles of 65° , 70° , and 75° with respect to the surface normal, averaging 50 measurements at each point. The selected spectral range was $\lambda = 350 \text{ nm} - 750 \text{ nm}$. The calculation of the thickness of the surface layer was performed using the four-layer model (Si/SiO₂/MeOx/Cauchy) illustrated in Figure 2.5, where Si and SiO₂ were assumed to be constant for all wafers. The TiO₂ layer was fitted before adsorption, the Cauchy layer (organic layer) after adsorption with parameters $A = 1.45$, $B = 0.01$. Refractive-index variations depending on the order of the SAM (estimated to be approximately 10%) were not taken into account. The positioning of the gradient samples was adjusted manually with an estimated error of $\pm 0.5 \text{ mm}$. Due to the elliptical beam size, the measured thickness corresponds to an average over $2 \text{ mm} \times 5 \text{ mm}$ (65°) to $2 \text{ mm} \times 8 \text{ mm}$ (75°). If not stated otherwise, the error bars in VASE graphs are standard deviations from repeated experiments (three or more).

3.1.3 X-ray Diffraction (XRD)

The X-ray diffraction diagrams were measured in the reflection mode (Cu K α radiation) on a Bruker D8 diffractometer (Bruker AXS GmbH, Karlsruhe, Germany) equipped with a scintillation counter. Each sample was measured for $\approx 30 \text{ min}$ with 2θ ranging from 5° to 50° with a step size of 0.004° .

3.1.4 Fluorescence Microscopy (FM)

High-resolution fluorescence imaging was performed on a confocal laser scanning microscope (Confocal ZeissLSM 510, Carl Zeiss GmbH, Jena, Germany) using a 10 \times , 0.3 NA objective (Zeiss, Germany). All other fluorescence images were recorded on an Axioscope AX10 IMAGER M1m (Carl Zeiss GmbH, Jena, Germany) equipped with an Hg-arc medium pressure lamp and Zeiss filter #10 (17 FITC) and #7 (Rhod). Exposure time was 5 seconds at 3200 K color temperature and a gain of 2. Image post-processing was performed with ImageJ software (version 1.43, available at <http://rsbweb.nih.gov/ij>).

3.1.5 Water Contact Angles (sCA)

Static water contact angles (sCA) were measured (with a NRL C.A. goniometer, model 100-00-230, Ramé-Hart, Netcong, NJ, USA) for one-component as well as two-component homogeneous samples and gradients. The volume of the water drops for all measurements was 2 μ l. On homogeneous samples, two contact angles were measured for each spot. On gradient samples (1 \times 4 cm²) 10 spots with a center-to-center distance of 4 mm were analyzed, the first spot always being 2 mm from the hydrophobic edge.

Dynamic water contact angles (advancing (aCA) and receding (rCA)) were measured using a Krüss contact-angle-measuring system (G2/G40 2.05-D, Krüss GmbH, Germany) with a speed of 15 μ L/min.

3.1.6 Microdroplet Density MDD

Qualitative MDD measurements to visualize patterns of hydrophobic PFAND on TiO₂ 1 \times 1 cm² were performed as described by Hofer et al. [235] Briefly, the sample was placed onto a metal stage in a transparent humidity chamber. The metal stage was cooled by pumping iced water through it. The nucleation and growth of water droplets was recorded using a CCD camera (model WV-BP 310/6, Matsushita Communication Deutschland GmbH, Germany) coupled to a microscope (Carl Zeiss (Schweiz) AG, Switzerland). Images at the point of droplet nucleation were saved

for further processing. Image post-processing was performed with ImageJ software (version 1.43).

3.1.7 Linear motion drive (LMD) for surface-chemical gradients by immersion

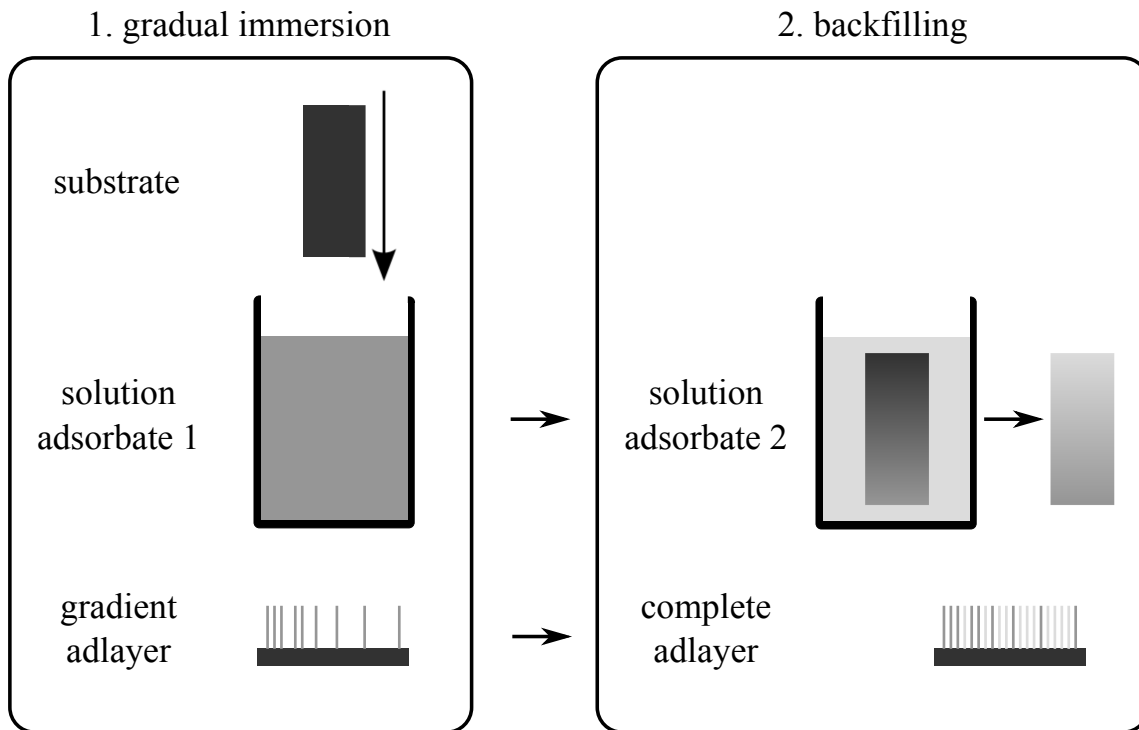


Figure 3.1: Schematic of linear motion drive (LMD) technique for fabrication of surface-chemical gradients by immersion. First step: gradual immersion of clean substrate into solution of adsorbate 1 leading to a gradient in surface density of adsorbed molecules. Second step: backfilling with adsorbate 2 (by either complete or counter gradual immersion in solution of adsorbate 2).

The principle and examples of fabricating surface-chemical gradients with the LMD have been described extensively by Morgenthaler et al. [18, 243]. Only a brief

description will be given here. One-component gradients are fabricated by immersing clean (TiO_2) substrates ($1 \times 4 \text{ cm}^2$) gradually into adsorbate solution. Adsorption kinetics in combination with a well-adjusted immersion protocol allow for the creation of well-controlled, position-dependent surface-coverage gradients. Optimization of immersion protocols is done by evaluation of adsorption kinetics. SAM systems such as phosphates, thiols and catechols (see results section) follow Langmuir-type adsorption kinetics:

$$\Theta(t) = \Theta(\infty)[1 - \exp(-ckt^a)] \quad (3.1)$$

where Θ denotes the surface coverage, c the concentration of the solution, k the rate constant of adsorption, and a a parameter determined by diffusion limitation.

If x (position of sample during LMD immersion) is given a specifically adjusted logarithmic relation to t , $\Theta(x)$ is a linear function. For all gradients presented in this work the immersion protocol was adjusted to either $\Theta(x)$ or $sCA(x)$ be linear.

3.1.8 UV setup for direct UV photolithography

All UV induced adlayer degradation (for TiO_2 and Nb_2O_5 photocatalytically enhanced) tests were performed in a home-built UV-setup: metal case ($50 \times 50 \times 20 \text{ cm}^3$) equipped with a water cooled ACE-Hanovia medium pressure 450 W quartz mercury arc lamp (type 7825-34) with characteristic peaks at 254 nm and 366 nm. Before exposure, the lamp was always left for 10 min to power up and reach constant intensity.

3.2 Substrates

Clean silicon wafers with a natural oxide layer ($\approx 2.3 \text{ nm}$) were obtained from Si-Mat Silicon Materials, Landsberg/Lech, Germany. Sputter coating with ($\approx 20 \text{ nm}$) of TiO_2 or Nb_2O_5 on such wafers was done at the PSI, Villigen, Switzerland. For homogeneous film studies, wafers were cut into pieces of $1 \times 1 \text{ cm}^2$, gradient samples $1 \times 4 \text{ cm}^2$ by Powatec GmbH, Hünenberg, Switzerland.

In order to correctly assess physical and chemical properties such as adsorption behavior, pKa values, or photocatalytic activity it is necessary to examine bare,

Table 3.1: Standard metal oxide substrate cleaning protocol.

Step	Timing	Purpose
ultrasonication in toluene	2×7 min	to remove glue residues from wafer cutting procedure
ultrasonication in 2-propanol	2×7 min	removal of physically bound contamination
UV/O ₃	> 30 min	(photocatalytically aided) UV/ozone degradation of remaining surface contamination
immersion in pure H ₂ O	until usage	preservation of clean surface

clean substrates as used during all experiments. Results of these evaluations are presented here because adsorption and chemical stability of surface adlayers as well as photocatalytic activity depend on the physical and chemical states of the substrates at hand. [134]

3.2.1 Titanium dioxide (TiO₂), niobium pentoxide (Nb₂O₅)

The standard cleaning protocol as it was applied for all metal oxide substrates is given in Table 3.1.

Freshly cleaned TiO₂ and Nb₂O₅ substrates are prone to adsorption of airborne (organic) contamination. The formation of contaminant “adlayers” on TiO₂ at different relative humidities (RH) was followed *in situ* by VASE and is shown in Figure 3.2. It is clear from the graph that a) it is vital to immerse substrates into adsorbate solution immediately after cleaning, b) that air-borne contamination continuously grows on clean/exposed TiO₂ and Nb₂O₅ if left unprotected. The surface coverage by contamination amounts to an equivalent of about 10% (55% RH) or 15% (35% RH) of a SAM (of thickness of ≈ 1.5 nm, approximate mean value for SAMs in this work). Storing UV-cleaned substrates in ultra pure H₂O proved to allow preservation of cleanliness (as assessed by XPS, see Figure 3.4) over several days. The storage and interaction between substrate and H₂O, however, might alter density or number of hydroxyl groups on the surface, important for bonds during SAM formation. Kim et al. argued that exposure of TiO₂ substrates to normal atmosphere leads to degener-

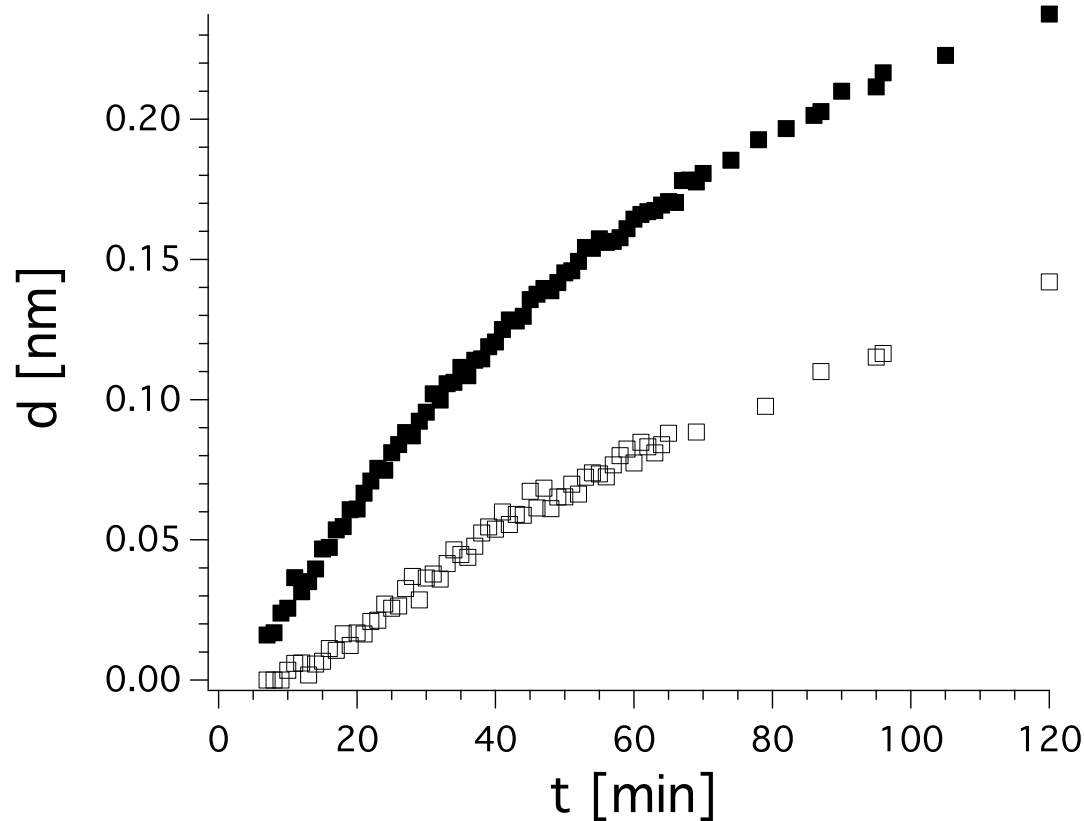


Figure 3.2: Growth of airborne contamination adlayer on freshly cleaned TiO_2 surface as assessed with VASE at relative humidity of 35% (■) and 55% (□).

ation of surface hydroxyl groups, indicated by a continuous increase in water contact angle from 0° (after plasma cleaning in their case) to 60° (after 480 h). [244] It is more likely that the continuous adsorption of adventitious carbon and other airborne contamination is the cause of the increase in adlayer thickness and hydrophobicity.

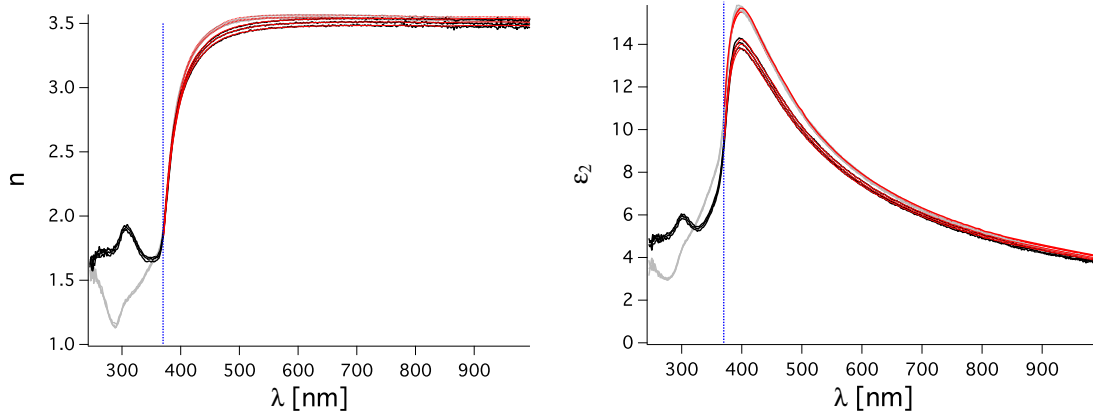


Figure 3.3: VASE spectra of clean TiO_2 (black line) on Nb_2O_5 (grey line) substrates. Red lines represent data fits (only for $\lambda > 370$ nm). Measurements were taken at incident angles of 65° , 70° , and 75° .

Table 3.2: Atomic % for clean TiO_2 and Nb_2O_5 (on Si-wafers) substrates as determined by XPS (Sigma2).

Element	clean TiO_2	clean Nb_2O_5
Carbon (1s)	6.7 ± 0.3	5.8 ± 0.3
Oxygen (1s)	62.4 ± 0.1	65.5 ± 0.2
Nitrogen (1s)	0.3 ± 0.0	0.0*
Titanium (2p)	30.5 ± 0.3	-
Niobium (3d)	-	28.7 ± 0.2

*nitrogen might be present but the peak hidden an adjacent niobium peak

XP spectra for clean TiO_2 and Nb_2O_5 surfaces obtained after applying the standard cleaning protocol outlined before are shown in Figures 3.4 and 3.5. Levels of airborne contamination are generally higher on cleaned TiO_2 than on Nb_2O_5 surfaces, as can be seen from C 1s and N 1s spectra, and from elemental atomic % as determined by XPS (Table 3.2).

Nb_2O_5 -film thickness d , refractive index $n(\lambda)$, and $\epsilon_2(\lambda)$ were determined as described above (see Section 2.5.3.2). Graphs for $n(\lambda)$, and $\epsilon_2(\lambda)$ are shown in Figure 3.3. Differences between TiO_2 and Nb_2O_5 are clearly visible for wavelengths below $\lambda = 370$ nm, resulting from different UV absorption behavior, and making it easy to

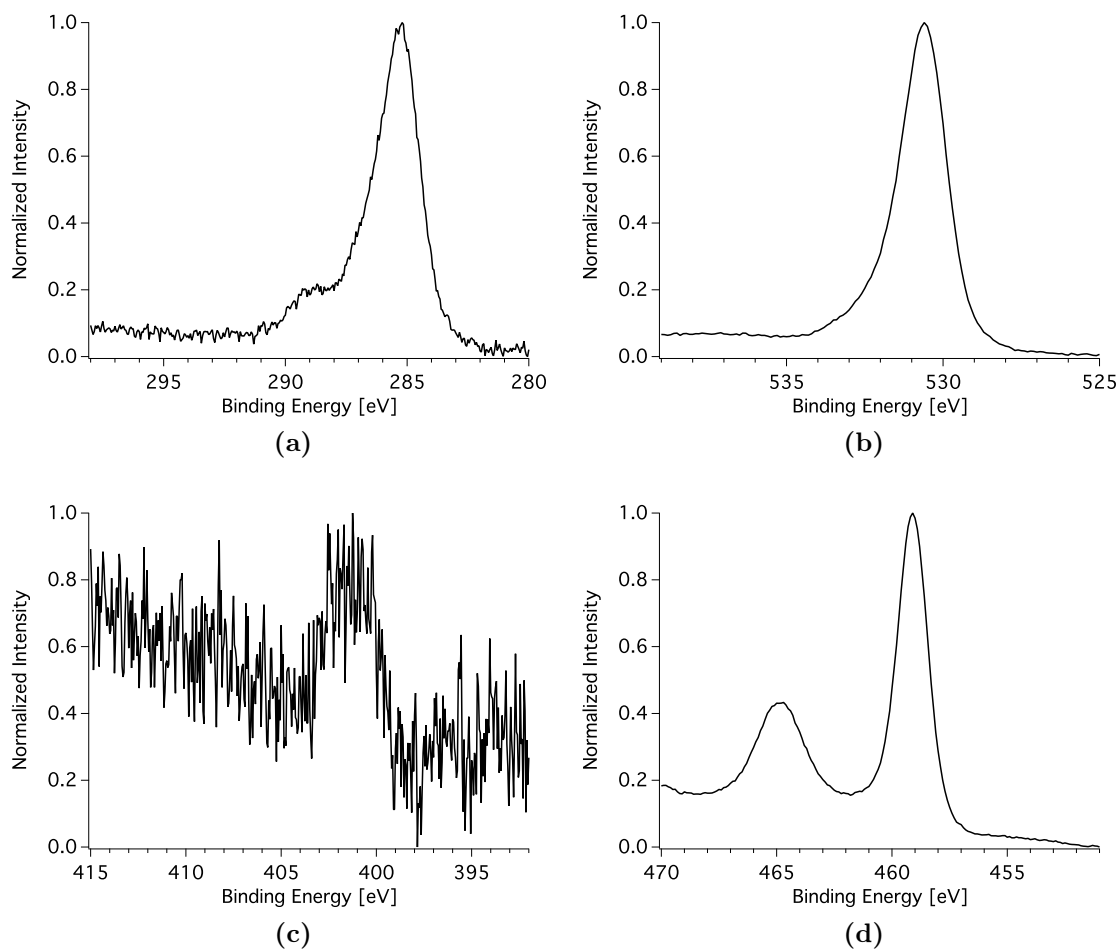


Figure 3.4: Normalized XP spectra of clean TiO_2 (≈ 20 nm on SiO_2 wafers) substrates: (a) carbon 1s, (b) oxygen 1s, (c) nitrogen 1s, (d) titanium 2p.

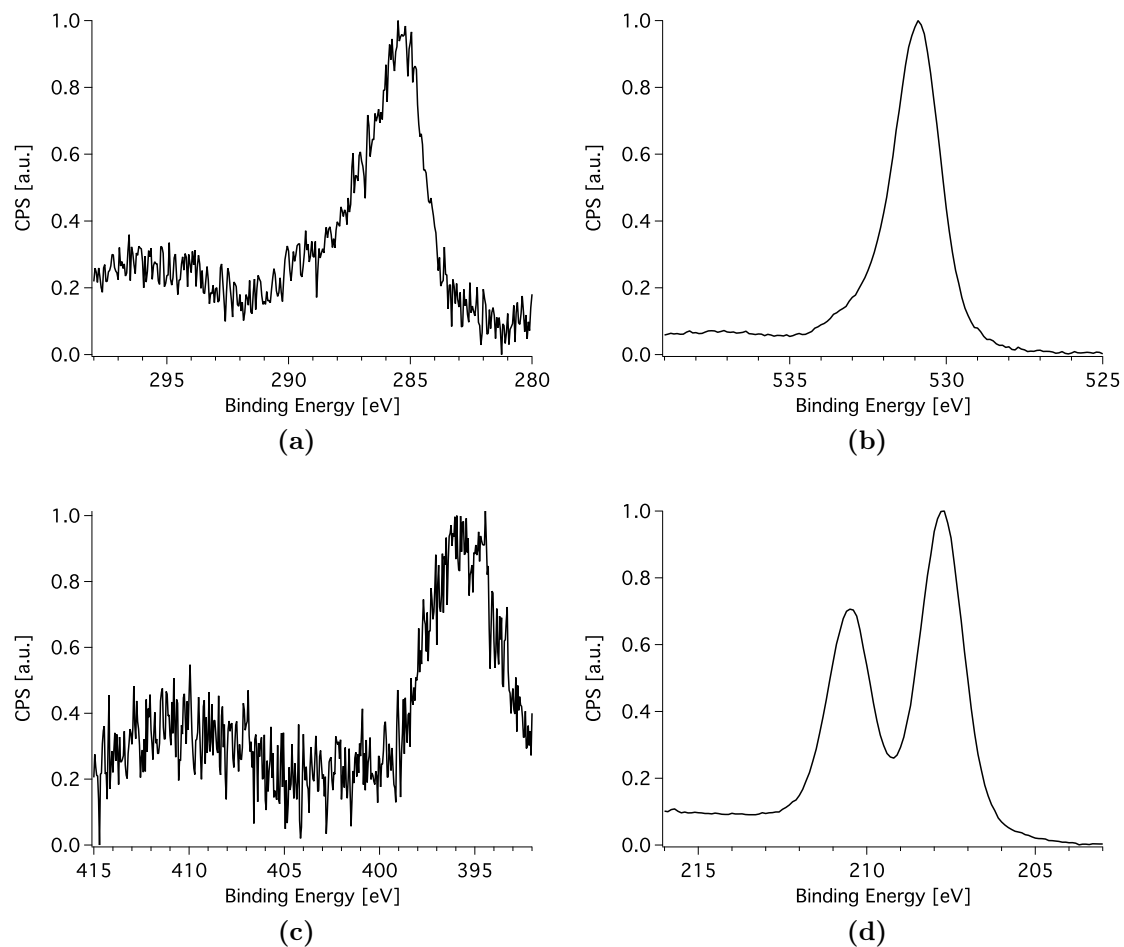


Figure 3.5: Normalized XP spectra of clean Nb_2O_5 (≈ 20 nm on SiO_2 wafers) substrates: (a) carbon 1s, (b) oxygen 1s, (c) nitrogen 1s, (d) niobium 3d.

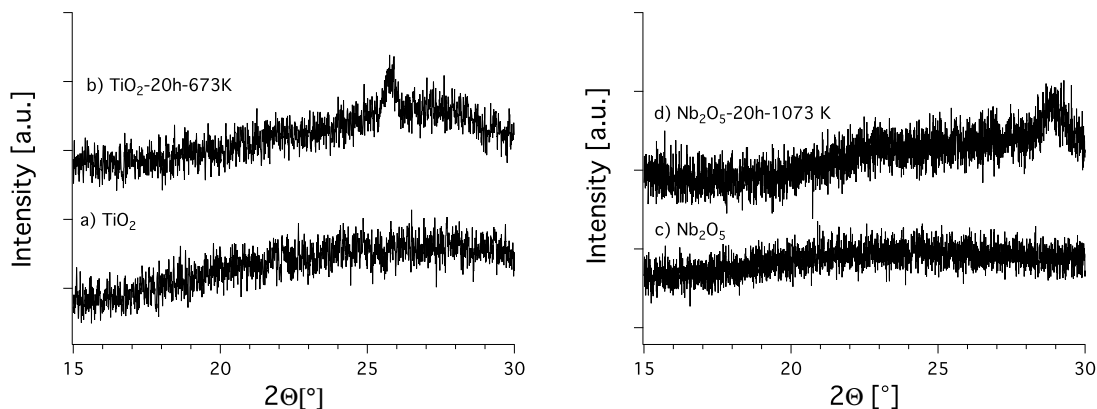


Figure 3.6: XRD patterns of cleaned TiO_2 coatings on silicon wafers (left): 20 nm TiO_2 , (b) 20 nm TiO_2 after tempering at 673K for 20 h and Nb_2O_5 coatings on silicon wafers (right): 20 nm Nb_2O_5 and (d) 20 nm Nb_2O_5 after tempering at 1073K for 20 h. In both cases tempered samples show peaks of crystalline forms (at $2\Theta = 26^\circ$ for TiO_2 and $2\Theta = 29^\circ$ for Nb_2O_5) not present before tempering.

distinguish the two substrates by means of VASE. Data fitting was usually performed for $\lambda = [370 \text{ nm}, 1000 \text{ nm}]$ where the same model (Figure 2.5) was used for TiO_2 and Nb_2O_5 .

X-ray diffraction was used to establish the crystalline structure of the TiO_2 coatings of different thicknesses on SiO_2 substrates. The patterns of 20, 60 nm TiO_2 films after cleaning are presented in Figure 3.6, a) and c). After annealing such substrates at 673 K for 20 h, peaks that are characteristic for anatase and rutile appear between $2\Theta = 25^\circ$ and 30° (see Figure 3.6, b) and d)). The comparison between spectra taken before and after tempering implies that the substrates as we used them were amorphous. The characteristic peaks for crystalline TiO_2 only appearing after annealing supports this assumption.

The Nb_2O_5 coatings on Si/ SiO_2 -wafers as used in this work were amorphous. The XRD patterns for substrates as-deposited and those annealed at 1073 K are shown in Figure 3.6, clearly indicating the transition from amorphous to crystalline structure after annealing (appearance of peak at $2\Theta = 29^\circ$). Kominami et al. investigated photocatalytic activities of different forms of Nb_2O_5 (also in comparison to TiO_2) by

photocatalytic dehydrogenation of methanol. [134] They concluded for their system that the activity of amorphous Nb_2O_5 is higher than for crystalline forms. Thus, it can be expected that the Nb_2O_5 films used for our adsorption/patterning experiments exhibit similar capabilities, fully supporting the patterning and gradient fabrication technique by direct deep-UV photolithography.

3.2.2 Silicon dioxide (SiO_2)

The cleaning protocol for SiO_2 substrates is similar to that of TiO_2 and Nb_2O_5 but oxygen plasma is used (for 2 min) instead of UV/ozone. The main reasons are the photocatalytically driven self-cleaning of TiO_2 and Nb_2O_5 under UV, which is not present for SiO_2 , and UV/ozone being a milder treatment inducing less structural change to the surface (see Section 4.2.3). [244]

3.2.3 Chromium with native oxide layer (Cr/CrOx)

Chromium surfaces were fabricated by evaporating ≈ 50 nm thick layers of the metal onto clean silicon wafers in an evaporation station (MED020 coating system, BALTEC, Balzers, Lichtenstein). Substrates were cleaned with piranha solution and rinsed intensively with water then dried with pure nitrogen before usage.

3.3 Chemicals and solutions

3.3.1 Solvents

Solvents (ethanol, 2-propanol, toluene, n-heptane) obtained from Sigma-Aldrich, Switzerland, were of analytical grade. Ultra pure water (TOC < 5 ppb, R = 18.2 $\text{M}\Omega\text{cm}$) was taken from a TKA-GenPure UV-TOC/UF (Huber & Co AG, Reinach BL, Switzerland). 4-(2-hydroxyethyl)-1-piperazineethanesulfonic acid (HEPES) and other chemicals used for buffer preparation were purchased from Fluka (Buchs, Switzerland). The buffer used for diluting polyelectrolytes was 4-(2-hydroxyethyl)

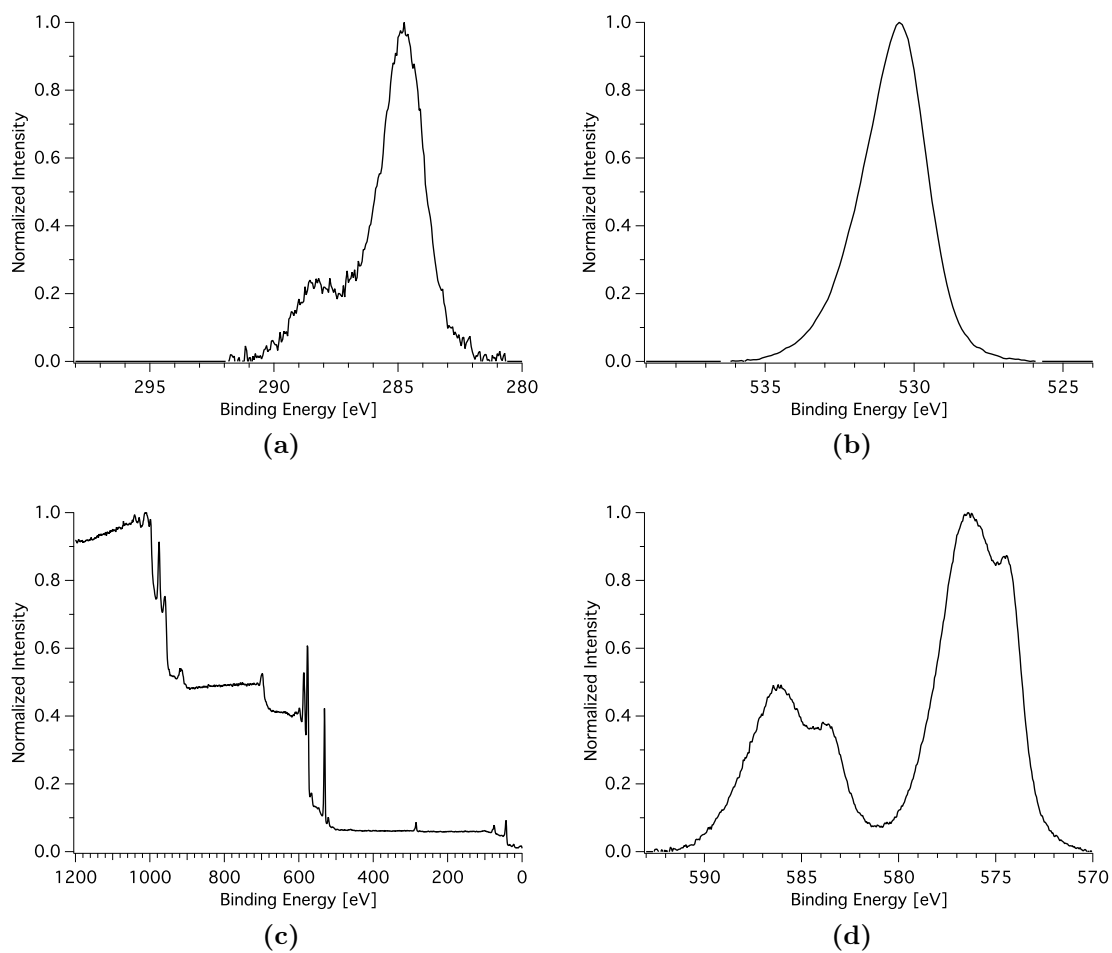


Figure 3.7: Normalized XP spectra of clean Cr/CrO_x (≈ 15 nm Cr coated on SiO₂ wafers) substrates: (a) carbon 1s, (b) oxygen 1s, (c) survey, (d) chromium 2p.

piperazine-1-ethanesulfonic acid (HEPES) solution with additional 150 mM NaCl (called HEPES2). All buffer solutions were adjusted to pH 7.4 using 6 M NaOH.

3.3.2 Alkyl phosphates, catechol derivatives

Alkyl phosphates (as described in Table 2.5: dodecyl phosphate (DDPO4), hydroxy dodecyl phosphate (OH-DDPO4), and carboxy undecyl phosphate (COOH-UDPO4) and their respective ammonium salts DDPO4(NH₄)₂, OH-DDPO4(NH₄)₂, COOH-UDPO4(NH₄)₂), perfluoro-alkyl nitrodopamine (PFAND), and nitrodopamine (ND) were obtained from SuSoS AG, Dübendorf, Switzerland. Synthesis and characterization are described in the literature. [51, 245, 246]

Pure alkyl phosphates were dissolved in 2-propanol and diluted with n-heptane to reach (n-heptane(99.2%):2-propanol(0.8%)) final solution. Ammonium salts were diluted in pure H₂O.

ND is very hydrophilic due to its hydroxyl and amine groups and therefore soluble in pure H₂O (TKA-GenPure UV-TOC/UF, Huber & Co AG, Reinach BL, Switzerland). PFAND is strongly hydrophobic because of its perfluorinated alkyl tail. It was dissolved in 2-propanol (Sigma-Aldrich, Switzerland) first and then diluted with H₂O in a 2:1 ratio of H₂O:2-propanol.

3.3.3 Polyelectrolytes

The synthesis and characterization of PLL-*g*-PEG have been described before. [121] PLL and PLL-*g*-PEG polymers were purchased from SuSoS AG, Dübendorf, Switzerland. PLL-*g*-PMOXA polymers were synthesized and characterized according to Konradi et al. [126] and provided by Bidhari Pidhatika. The architectures of the polymers (PLL-*g*-PEG: 20kDa:3.6:5kDa (“PEG5”), 20kDa:3.2:2kDa (“PEG2”), and PLL-*g*-PMOXA: 20kDa:3:4kDa (“PMOXA4”), 20kDa:3:8kDa (“PMOXA8”)) are given in Table 3.3. The pure PLL HBr salt had a molecular mass of 20 kDa. PLL-*g*-PEG and PLL-*g*-PMOXA were dissolved in HEPES 2 buffer at 1 g/l and 0.1g/l, respectively, to obtain appropriate adsorbate solutions before adsorption. Two different molecular masses of PEG and PMOXA were chosen to allow comparison of polymer stability as function of polymer chain length.

Table 3.3: Stoichiometric configurations of PLL-based polymers as used in this work.

Acronym*	m PLL [kDa]	grafting ratio g	m PEG/PMOXA [kDa]	# EG/MOXA units
PEG2	20	3.2	2	45
PEG5	20	3.6	5	120
PMOXA4	20	3	4	50
PMOXA8	20	3	8	100

*as used in this work

3.4 Protein solutions

Fibronectin/fibrinogen proteins (Sigma-Aldrich, Buchs, Switzerland) were labelled with AlexaFluor488 using an antibody labeling kit (Molecular Probes, Leiden, Netherlands). Prepared probe solutions had a concentration of 20 $\mu\text{g/ml}$.

3.5 Protocols for surface preparation

This section gives details about all protocols applied for surface functionalization.

3.5.1 Adsorption of adlayers/monolayers

3.5.1.1 Adsorption protocols for alkyl phosphates

Various concentrations of (ammonium salt derivatives of) alkyl phosphates (example of $\text{DDPO}_4\text{-NH}_3$ given in Table 2.5) were investigated with respect to adsorption kinetics and state of homogeneous adlayers on TiO_2 (using VASE and XPS) - details are given in Sections 4.3 and 5.2. [51] Homogeneous surface functionalizations were obtained by immersing clean TiO_2 substrates for 48 h in the respective 500 μM solutions. After adsorption, samples were rinsed thoroughly under running pure H_2O and immediately measured with VASE and XPS afterwards. A series of samples for static water contact angle measurements was examined separately.

3.5.1.2 Adsorption protocols for catechols

Homogeneous monolayers of nitrodopamine (ND) and perfluoro-alkyl-nitrodopamine (PFAND) were obtained by completely immersing clean TiO_2 substrates in 500 μM (ND) and 440 μM (PFAND) solutions for 48 h. ND samples were extensively rinsed under a stream of pure H_2O while PFAND samples (including gradients) were sonicated for 1 min in 2-propanol, then blow-dried under pure nitrogen. The same protocol was followed for the substrates Nb_2O_5 and Cr/CrOx.

3.5.1.3 Protocols for PLL-based polymers

PLL-*g*-PEG and PLL-*g*-PMOXA were adsorbed onto TiO_2 and Nb_2O_5 substrates from droplets of 30 - 35 μl depending on samples size for 2 hours. After adsorption, samples were extensively rinsed under a stream of pure H_2O and blown dry with pure nitrogen.

3.5.2 Determination of adsorption kinetics and protocols for gradients by immersion (LMD)

In order to adapt LMD immersion protocols for surface-chemical gradients, adsorption kinetics for phosphates and the catechol derivatives were determined by exposing clean substrates (TiO_2) to different concentrations (range: 0.5 - 500 μM) in the corresponding solvents and for different times (range: 1 min - 48 h). Samples were immediately rinsed with the appropriate solvents and dried under a flow of nitrogen (see Section 3.5.1). Assessment of obtained adlayers was done by XPS and VASE. The determined and subsequently utilized immersion protocols are detailed as part of the gradients results sections.

3.5.3 Protocols for direct UV photolithography

For all UV experiments, homogeneously coated surfaces were used.

For degradation kinetics:

SiO_2 , TiO_2 and Nb_2O_5 coated substrate were placed on a home-built sample holder, covered with a $10 \times 10 \text{ cm}^2$ quartz glass. The glass was pressed onto the

samples by tightening the sample holder screws to the point that interference patterns were visible on the sample surfaces. The holder was then placed at a distance of 10 cm from the UV lamp and exposed for 1, 2, 4, 8, 16, 64, or 256 min.

For direct UV photopatterning and UV induced surface-functional gradients:

Masks (EM 300 meshes S160) were placed between sample and quartz glass for binary patterns. Samples were exposed for 1 h at a distance of 3 cm from the UV lamp. For gradient surfaces the clear quartz glass was exchanged with one coated with a chromium coverage gradient (see gradient Section 6.2.1 for details). Samples were exposed for 20 min at a distance of 10 cm from the UV lamp. The different exposure times are based on different desired degrees of degradation - 1 h at 3 cm guaranteed complete removal, while 20 min at 10 cm was deemed suitable for gradient removal (considering the shading effect of the chromium). Immediately after exposure, samples were immersed in the appropriate solvent (2-propanol for PFAND, 1:1 Ethanol:H₂O for PLL-based polymers) for 5 min. PFAND samples were subsequently sonicated for 1 min. All samples were blow-dried after 5 min of solvent exposure.

3.5.4 Protocols for protein adsorption tests

UV patterns and gradients were exposed to labeled fibrinogen or fibronectin (depending on needs for subsequent biological experiments) for 20 min, then rinsed with ultrapure H₂O and blow-dried with N₂.

CHAPTER 4

Characterization of homogeneously functionalized surfaces

If you quietly accept and go
along no matter what your
feelings are, ultimately you
internalize what you're saying,
because it's too hard to believe
one thing and say another.

Noam Chomsky

4.1 Catechols (PFAND and ND)

4.1.1 Homogeneous adlayer, adsorption kinetics (on TiO_2)

Hydrophobic coatings with maximal surface coverage corresponding to one monomolecular layer were obtained by immersing cleaned substrates (TiO_2 and Nb_2O_5) into PFAND solutions ($440 \mu\text{M}$) for 48 hours. The layer thickness of such samples measured by VASE was $1.3 \pm 0.1 \text{ nm}$ (the length of a fully stretched PFAND molecule is $\approx 2.1 \text{ nm}$) and sCA $105 \pm 2^\circ$. Dynamic water contact angles were $110 \pm 3^\circ$ (advancing) and $75 \pm 5^\circ$ (receding). Such coatings served as references when determining X-ray degradation of the coating as a function of time (see next section 4.1.1.1). [219, 247, 248]

Homogeneous layers of ND are completely hydrophilic (sCA $< 10^\circ$) and their thickness was determined to be $0.5 \pm 0.1 \text{ nm}$ (see Table 4.1). Table 4.1 shows the surface-chemical composition (at.-%), adlayer thickness and static water contact angle for different layers assembled from a $440 \mu\text{M}$ and $500 \mu\text{M}$ solution of PFAND and ND, respectively. For the XPS data, the calculations are based on a stack model for the adlayer (see Figure 4.4), and include corrections for transmission function and IMFPs associated with the XPS measurements (utilizing Equations 2.6 and 2.7).

To discriminate substrate from overlayer oxygen all oxygen species except that of TiO_2 were assigned to the adlayer, assuming that all surface (hydroxyl) groups participate in the binding of catechol. This assumption might be an overestimation of surface coverage because not all surface hydroxyl groups are occupied. PFAND and ND are assumed to bind via the catechol group to the TiO_2 surface in two possible configurations. Figure 4.5 shows monodentate (I) and bidentate (II) configurations of ND and PFAND molecules adsorbed on TiO_2 , as described for catechol on rutile by Li et al. [106] The different binding states of the catechol's hydroxyl groups lead to changes in the electron distribution within the benzene ring and thus also in the attached nitro-group. These differences become detectable in the nitrogen XP spectra for the nitro group as a binding-energy shift. The presence of both binding modes causes the appearance of two nitrogen peaks for the NO_2 group.

Tables 4.3 and 4.2 show the analysis of PFAND and ND layers on TiO_2 as determined from high-resolution XPS (PHI5000) spectra. Figure 4.1 shows the cor-

Table 4.1: Apparent normalized atomic concentration (determined with XPS, analysis depth ≈ 10 nm), adlayer thickness (VASE) and static contact angle for homogeneous monolayers assembled from PFAND (440 μM in 1:2 propanol:H₂O) and ND (500 μM in pure H₂O) solutions after 48 h of immersion. As a comparison, the calculated values for pure PFAND and pure ND are given.

Sample		XPS apparent at.-% for layers on TiO ₂							VASE d [nm]	CA [°]
		C 1s	N 1s	O 1s	F 1s	Ti 2p				
Blank reference	substrate only	5.1	0.2	66.0	0.0	28.7		0.0	<10	
	incl. substrate	18.5	1.9	44.8	16.0	18.9		1.3 \pm 0.1	105 \pm 2	
PFAND	Overlayer excl. TiO ₂	44.5	4.6	12.4	38.5	-				
	calculated	45.7	4.7	11.6	39.5			2.1 \pm 0.1*		
ND	incl. substrate	17.6	3.0	56.2	0.0	23.2		0.5 \pm 0.1	<10	
	Overlayer excl. TiO ₂	61.8	10.5	27.7	0.0					
	Calculated	57.1	14.3	28.6	0.0			0.6 \pm 0.1*		

* calculated longest intramolecular distance (O-C of catechol vs. F in CF₃ (PFAND) and H in NH₂ (ND))

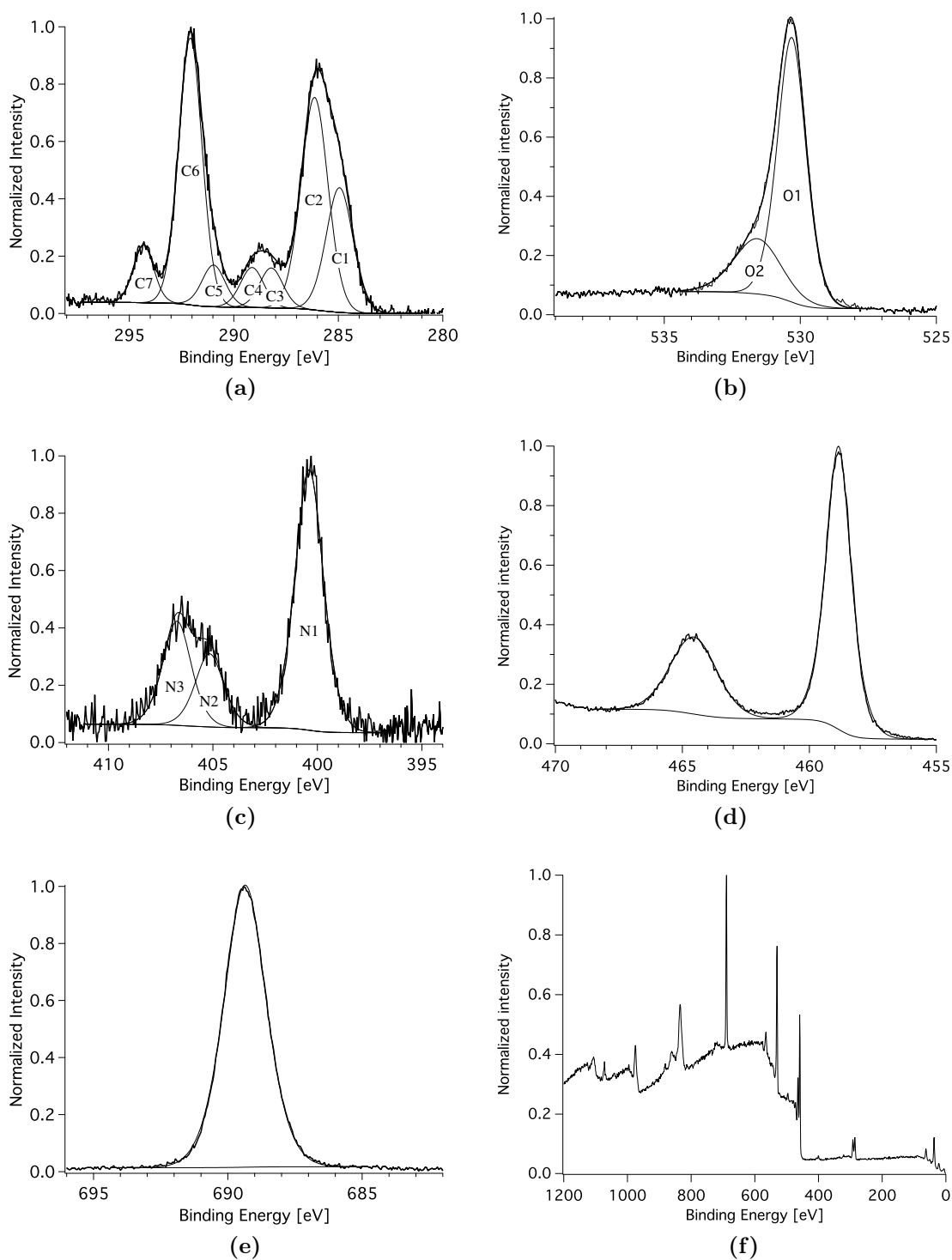


Figure 4.1: Normalized XP spectra (PHI5000) of PFAND monolayers adsorbed on TiO_2 , (a) carbon 1s, (b) oxygen 1s, (c) nitrogen 1s, (d) titanium 2p, (e) fluorine 1s, (f) survey. C 1s, N 1s, O 1s components are listed in Table 4.2.

Table 4.2: Binding energies, full width at half maximum (FWHM), assignment and measured areas for a homogeneous PFAND film on TiO₂ relative to the carbon area of the CF₃ group. Comparison between experimental and stoichiometrically calculated intramolecular ratios, measured using monochromatic (high resolution, PHI5000) or non-monochromatic X-rays (Sigma2 Probe). In case of the Sigma2 Probe, in addition to the FWHM constrains, peak positions were also constrained relative to the C-C-C component as found in the high-resolution spectra (PHI5000).

Element	Peak	Binding energy [eV] ^a	FWHM [eV] ^a	Assignment (atoms)	Area [†] relative to N _{tot} = 2 PHI5000	Sigma2
Carbon (1s)	C1	285.00	1.63 ± 0.08	C-C-C (4)	3.3 ± 0.2	2.6 ± 0.1
	C2	286.18 ± 0.02	=FWHM(C1)	C-O; C-N; C-CON; C-CF ₂ (5)	5.5 ± 0.2	4.9 ± 0.3
	C3	288.22 ± 0.03	1.35 ± 0.04	-C(=O)-N (1)	1.1 ± 0.1	0.9 ± 0.1
	C4	289.22 ± 0.04	=FWHM(C3)	-C-NO ₂ (1)	1.1 ± 0.1	0.9 ± 0.1
	C5	290.93 ± 0.08	=FWHM(C3)	C-CF ₂ -CF ₂ (1)	1.0 ± 0.1	0.9 ± 0.1
	C6	292.00 ± 0.09	=FWHM(C3)	CF ₂ -CF ₂ -CF _x (6)	5.5 ± 0.4	5.1 ± 0.2
	C7	294.24 ± 0.09	1.17 ± 0.07	CF ₂ -CF ₃ (1)	1.0 ± 0.1	1.0 ± 0.0
Nitrogen (1s)	N1	400.42 ± 0.05	1.78 ± 0.12	-C(=O)-NH ₂ (1)	1.06 ± 0.08	1.05 ± 0.07
	N2	405.09 ± 0.12	=FWHM(N1)	-C-NH ₃ ⁺ (II) (x)	0.20 ± 0.04	0.26 ± 0.04
	N3	406.56 ± 0.12	=FWHM(N1)	-C-NO ₂ (II) (1-x)	0.31 ± 0.03	0.23 ± 0.06
Fluorine (1s)		689.27 ± 0.1	1.88 ± 0.03	-CF _x (17)	18.8 ± 0.9	16.7 ± 0.8
		530.29 ± 0.05	1.27 ± 0.03	TiO ₂ (2×Ti)	19.18 ± 0.82	26.0 ± 1.6
Oxygen (1s)		531.59 ± 0.19	2.00 ± 0.23	C-O-H; C-O-Ti; -C(=O)-N	4.67 ± 0.36	3.82 ± 0.21
				-C-NO ₂ ; Ti-OH		

^aPHI5000, [†]R.S.F. corrected

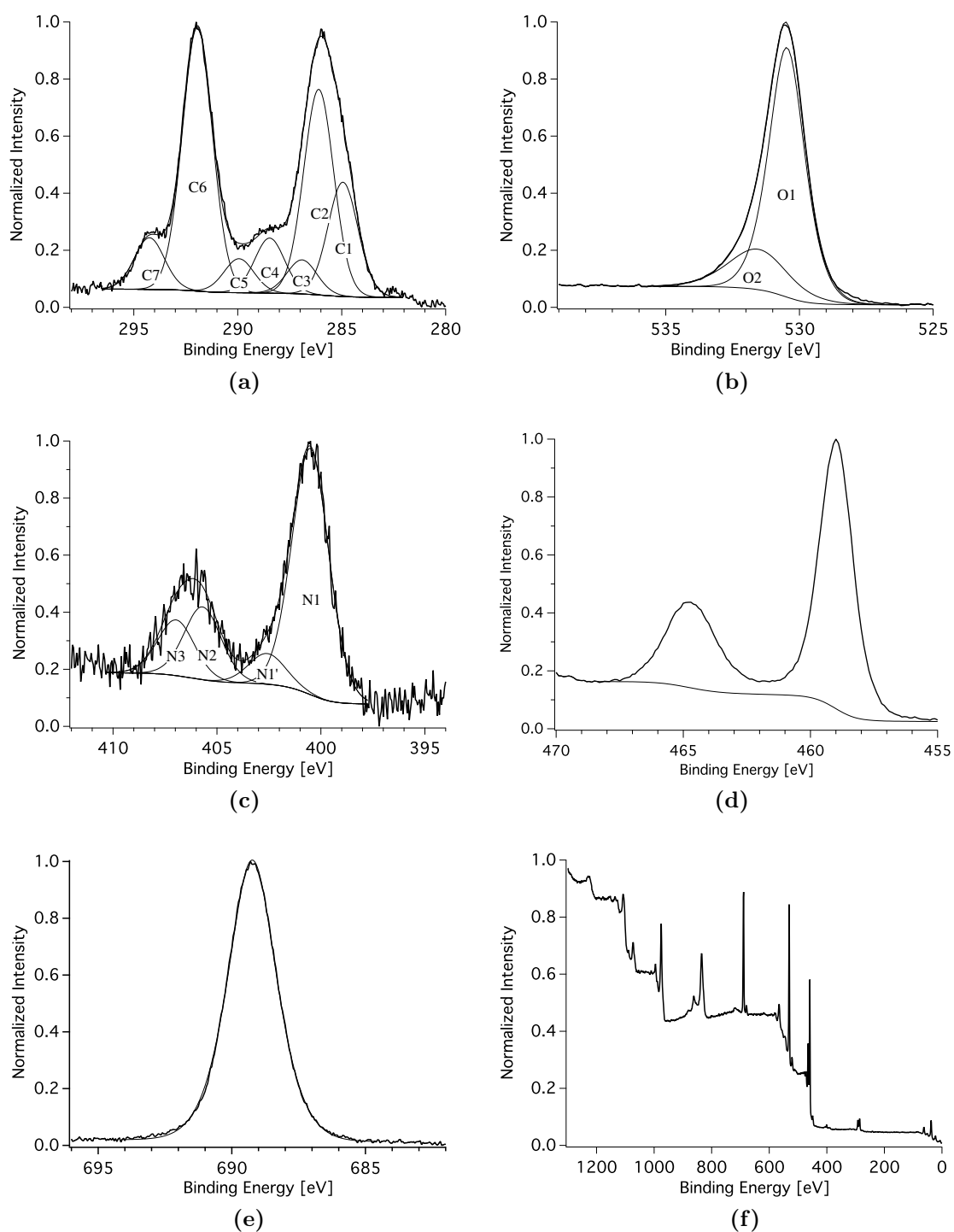


Figure 4.2: Normalized XPS (Sigma2) spectra of PFAND monolayers adsorbed on TiO_2 , (a) carbon 1s, (b) oxygen 1s, (c) nitrogen 1s, (d) titanium 2p, (e) fluorine 1s, (f) survey. C 1s, N 1s, O 1s components are listed in Table 4.2.

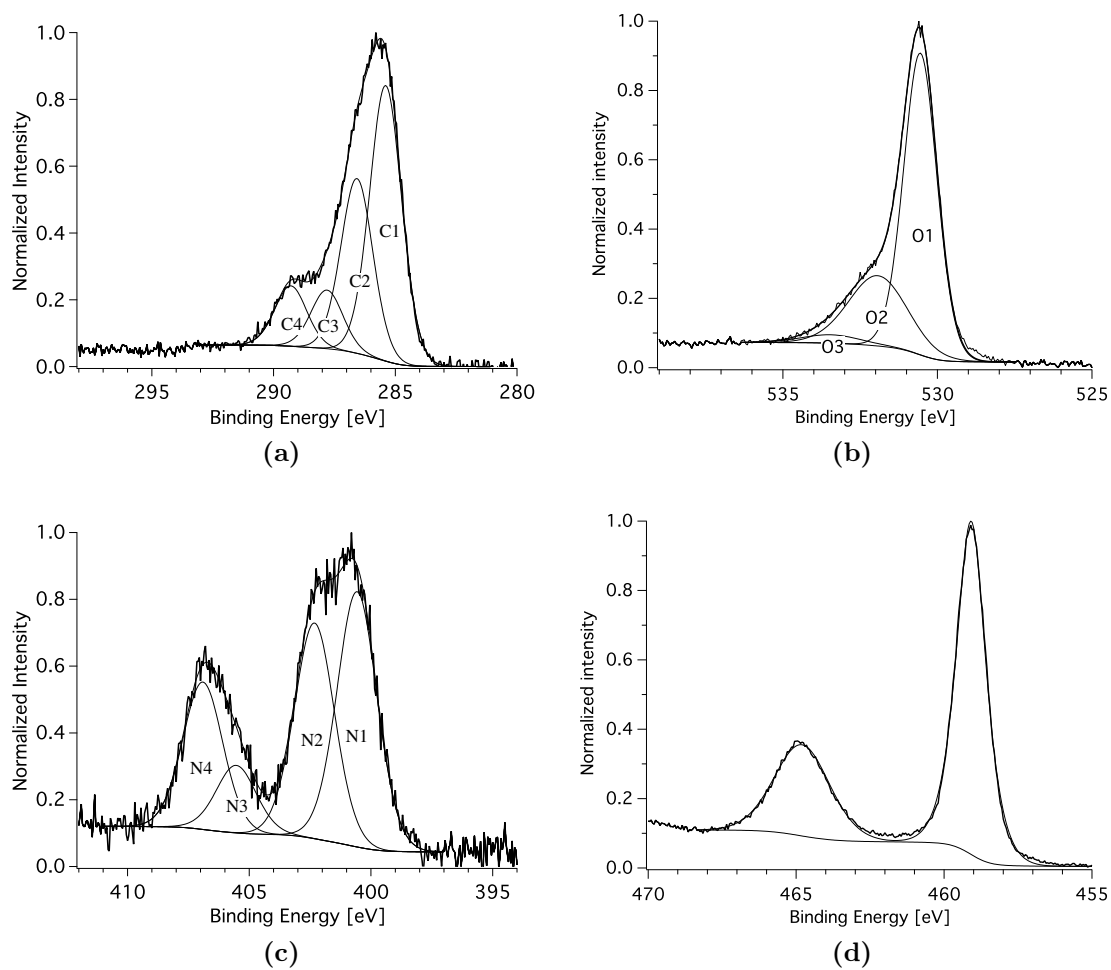


Figure 4.3: Normalized XP spectra (Versa Probe) of nitrodopamine (ND) adsorbed on TiO₂: (a) carbon 1s, (b) oxygen 1s, (c) nitrogen 1s, (d) titanium 2p with corresponding peak assignments (see Table 4.3).

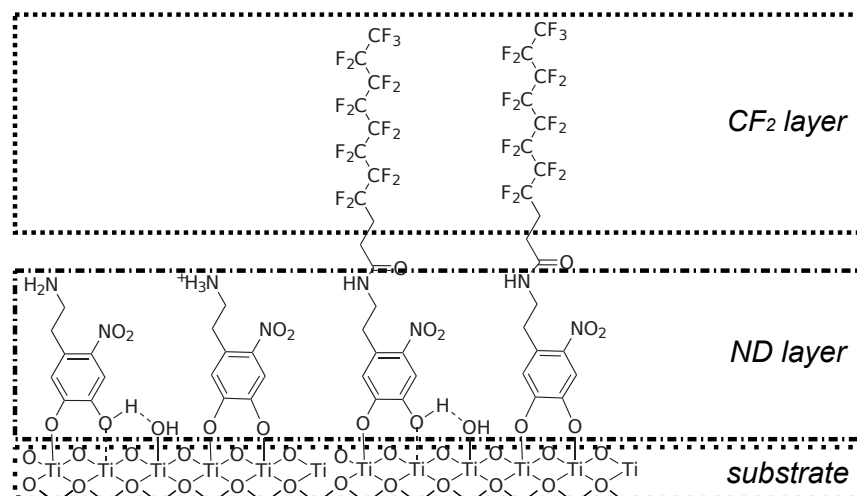


Figure 4.4: Stack layer model as used for XPS layer composition calculations: a CF_2 -layer (PFAND only) on top of a ND (catechol) layer adsorbed on the substrate (TiO_2).

responding normalized high-resolution C 1s, F 1s, N 1s, O 1s, and Ti 2p spectra of PFAND and ND on TiO_2 , respectively. The equivalent spectra as recorded on the Sigma2 are given in Figure 4.2. All identified components are marked C1-C7 and N1-N4. For C 1s: positions of the fitted components are as expected from the intra-molecular bonds of the molecules. Experimental area ratios are higher than the theoretical values, suggesting the presence of contamination. Differences between the FWHM of identified C 1s and O 1s components are due to the presence of contaminants as well as the slightly different electronic configurations or hybridization of bonds associated with a single binding energy (Tables 4.2 and 4.3). For N 1s: PFAND shows 3, ND 4 peaks although only 2 kinds of nitrogen (NO_2 , NH_2) are expected from the stoichiometry. The amine-to-nitro peak area ratio is not 1, in contrast to the molecular stoichiometry. Possible explanations for this observation are given below.

XPS data (Table 4.3 and 4.2) show good agreement between molecular stoichiometry and elemental distribution in surface adlayers. Deviations between the experimental and theoretical data are attributed to contamination. The different mechanisms by which catechols can bind to TiO_2 have been described previously. [249] Monodentate and bidentate configurations are possible (see Figure 4.5), leading to

Table 4.3: Binding energies, full width at half maximum (FWHM), assignment and measured areas for a homogeneous ND film on TiO₂ relative to the nitrogen 1s peak area. Comparison between experimental and stoichiometrically calculated intramolecular ratios, measured using monochromatic (high resolution, PHI5000) or non-monochromatic X-rays (Sigma2 Probe). In the case of the Sigma2 Probe, in addition to the FWHM constraints, peak positions were also constrained relative to the C-C-C component, as found in the high-resolution spectra (PHI5000).

Element	Peak	Binding energy [eV] ^a	FWHM [eV] ^a	Assignment (atoms)	Area ^b relative to N _{tot} = 2 PHI5000	Sigma2
Carbon (1s)	C1	285.00	1.58 ± 0.02	C-C-C (4)	5.80 ± 0.24	3.6 ± 0.3
	C2	286.19 ± 0.03	=FWHM(C1)	C-O; C-N (3)	3.56 ± 0.12	3.6 ± 0.3
	C3	287.47 ± 0.11	=FWHM(C1)	-C-NO ₂ (1-x)	1.07 ± 0.05	0.7 ± 0.1
	C4	288.90 ± 0.06	=FWHM(C1)	-C-NO ₂ (x)	1.19 ± 0.05	0.5 ± 0.1
Nitrogen (1s)	N1	400.14 ± 0.03	1.96 ± 0.03	-C-NH ₂ (1-y)	0.73 ± 0.02	0.5 ± 0.0
	N2	401.88 ± 0.03	=FWHM(N1)	-C-NH ₃ ⁺ (y)	0.62 ± 0.01	0.5 ± 0.0
	N3	405.19 ± 0.06	=FWHM(N1)	-C-NO ₂ (II) (x)	0.22 ± 0.01	0.3 ± 0.0
	N4	406.54 ± 0.04	=FWHM(N1)	-C-NO ₂ (I) (1-x)	0.43 ± 0.01	0.2 ± 0.0
Oxygen(1s)		530.14 ± 0.02	1.28 ± 0.02	TiO ₂ (2×Ti)	16.08 ± 0.49	15.7 ± 0.7
		531.47 ± 0.19	2.23 ± 0.00	C-O-H; C-O-Ti;	6.63 ± 0.31	7.5 ± 0.5
		532.95 ± 0.34	1.95 ± 0.39	-C-NO ₂ ; Ti-OH	0.90 ± 0.81	0.0 ± 0.0

^aPHI5000, ^bR.S.F. corrected

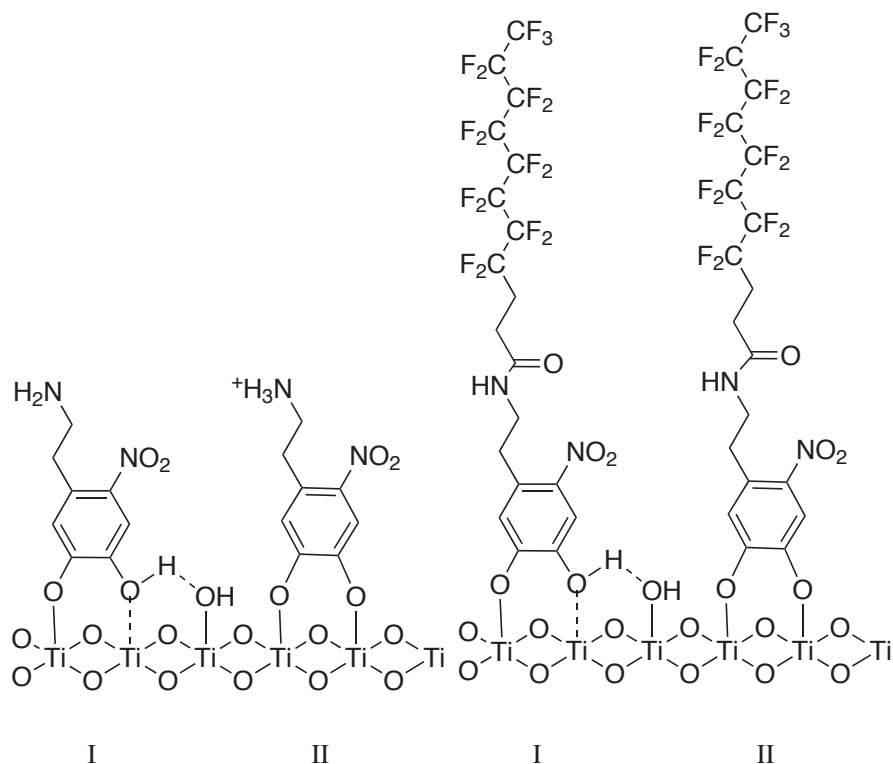


Figure 4.5: Two possible configurations of ND and PFAND when adsorbed on TiO_2 . I: monodentate binding with a hydrogen bridge to a neighboring surface hydroxide. II: bidentate binding, in which both catechol oxygens are deprotonated.

different bond strengths and electron distributions in the adsorbate (particularly the benzene). Such different electron distributions lead to the appearance of neighboring peaks for the $-\text{NO}_2$ groups in the N 1s XP spectra of PFAND and ND as shown in Figure 3. PFAND and ND show two peaks at 405.1 and 406.6 eV associated to the nitro group. The peak splitting arises from the nitro group, which is conjugated to the benzene ring and therefore sensitive to the binding state of the catechol (see Figure 2). For ND there are two peaks at 400.1 and 401.9 eV, which we attribute to partial protonation of the amine group. This splitting is not observed in the case of the amide nitrogen of PFAND at 400.4 eV (on the PHI5000), since protonation is not possible. The N 1s XPS amine/amide-to-nitro area ratio is greater than 1 for both molecules, which implies a possible reduction of NO_2 to NO_x or loss of NO_2 induced

by the X-ray radiation or emitted photo-electrons. Such an effect could also be the reason for the disappearance of the PFAND nitro peak during X-ray exposure (see next section). N 1s spectra of PFAND recorded on the Sigma2 probe show a small additional peak (N1') at about 402.5 which might also be caused by the degradation of (amide or nitro group nitrogen) PFAND under X-radiation.

4.1.1.1 Stability/degradation of catechol SADs under X-ray exposure

One must take into account potential degradation processes when measuring perfluoro-alkyl surface adlayers with XPS because of the structural changes during measurements induced by X-radiation. [214,218] Such changes lead to deviations in elemental ratios determined by XPS from the stoichiometric values. Minimizing measurement times based on consideration of degradation rates can render any additional corrections to XPS-quantification for X-ray-induced damage unnecessary. As discussed in the main text, XPS measurement times with the Sigma2 of PFAND adlayers on TiO₂ were adjusted to 30 min per spot, placing degradation effects within the normal XPS error margins.

Continuously iterated XPS measurements for up to 20 hours reveal that X-radiation degrades PFAND and, to a much lesser extent, ND adlayers on TiO₂. Figure 4.6 shows the different degradation rates of the C 1s, N 1s, and F 1s signals over time for PFAND monolayers during X-ray exposure. In particular, the amount of fluorine continuously decreases (by 60% over 20 hours) while the amounts of carbon (-7%) and nitrogen (-20%) only diminish during the first 1-4 hours but then remain constant. [214,218] Interestingly, also individual behavior of the intensities of the individual peaks in the C 1s spectrum were noticed: those associated with CF₂- and CF₃-bonds decrease, while peaks with binding energies lower than that of CF₂ increase. These changes and the degradation rates imply that X-radiation changes the structure of PFAND predominantly by disintegration of the perfluoro-alkyl functional group (scission of F-C-F bonds). The altered molecules remain on the surface. These observations, the F 1s peak position shift as shown in Figure 4.7, as well as the decrease in integrated signal intensity (Figure 4.6 and 4.8) of F 1s are also attributed to transformations of -CF₂- and -CF₃ to other CF_x-species, possibly via reactions outlined in Figure 4.9: the electromagnetic radiation produces radicals from the -

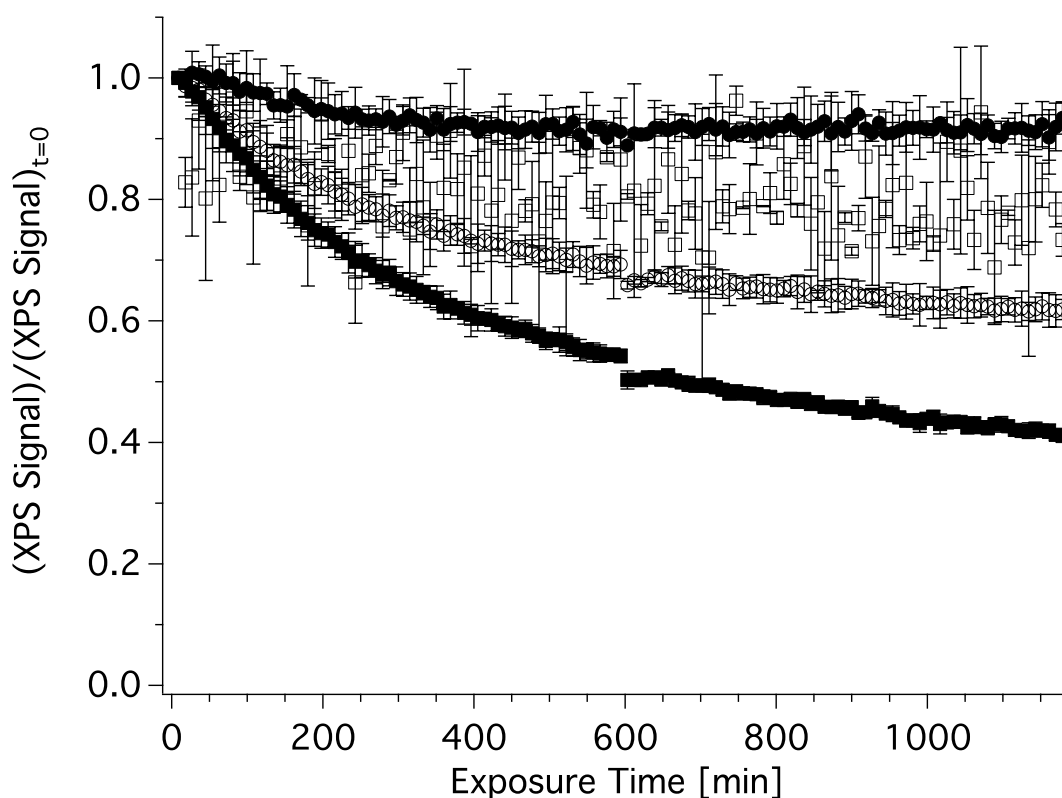


Figure 4.6: PFAND adlayers on TiO_2 degrade with time under X-ray irradiation (during XPS measurements on a Sigma2). For the first 4 hours up to 5% of the total carbon (●) disappears from the surface after which its value remains roughly constant. Fluorine (■) continuously diminishes over 20 h indicating net loss and degradation of the perfluorinated alkyl chain of PFAND. The nitrogen signal (□) is noisy but appears to decrease by about 20% over 20 h. The sum of the N 1s, C 1s, and F 1s signals (○) decreases continuously over the 20 h, illustrating X-ray induced degradation of PFAND adlayers.

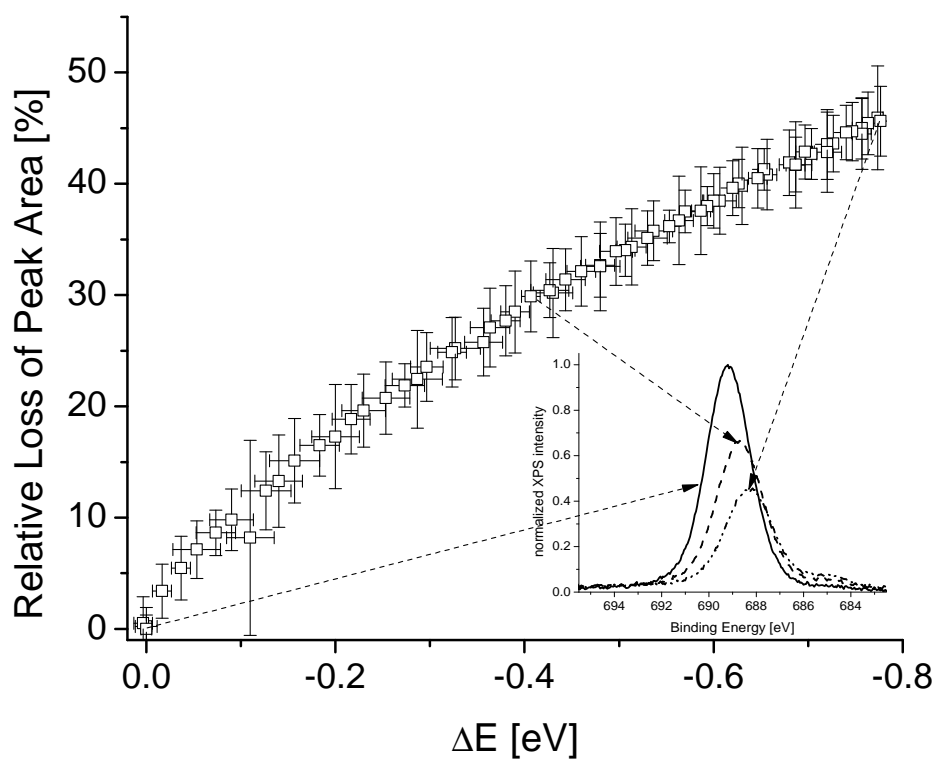


Figure 4.7: Correlation between shift (ΔE) in binding energy and decrease of total integrated area of F 1s signal in the XP spectrum for a monolayer of PFAND on TiO_2 under constant X-ray exposure for 20 hours. The insert shows three F 1s spectra (after 0, 3, and 20 hours of XPS exposure), clearly indicating the shift and reduction in intensity of the F 1s signal as a function of time.

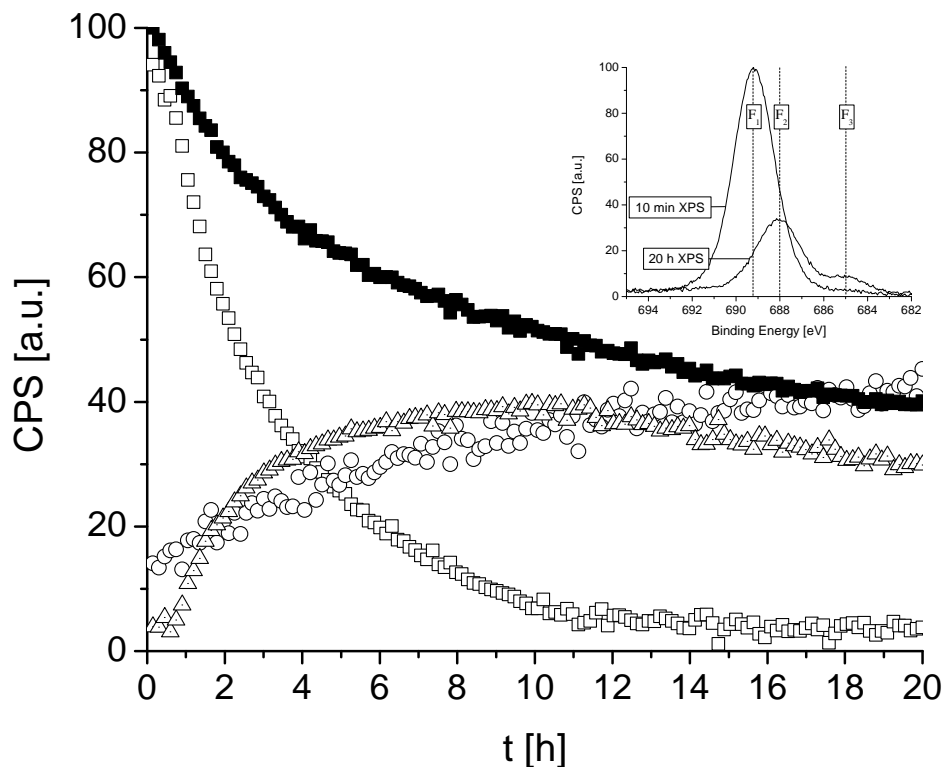


Figure 4.8: Degradation of PFAND during XPS: F 1s total signal (■), F 1s peak (CF₂) at 689.2 eV (□), F 1s peak (CF) at 688.1 eV (△), F 1s peak (×7) (unidentified F species) at 685.0 eV (○).

CF_n-components, either directly or indirectly through the generation of secondary (photo-)electrons, which in turn attack CF_n-bonds. Fluorine atoms/ions/radicals are split off leaving reduced -CF_x- behind. Figure 4.8 confirms this hypothesis: the decrease in intensity of the -CF₂- peak at 689.2 eV (F1) is accompanied by an increase of at least one other peak at 688.1 eV (F2), possibly that of -FC=CF-, over the first 10 hours. After that, both peaks decrease. Both effects are attributed to the mentioned changes in the -CF₂-CF₂- structure, although the exact reaction remains unclear. The different fluorocarbon stoichiometries lead to changes in the electron distribution/density for the fluorine and their neighboring carbon atoms. Hence, the

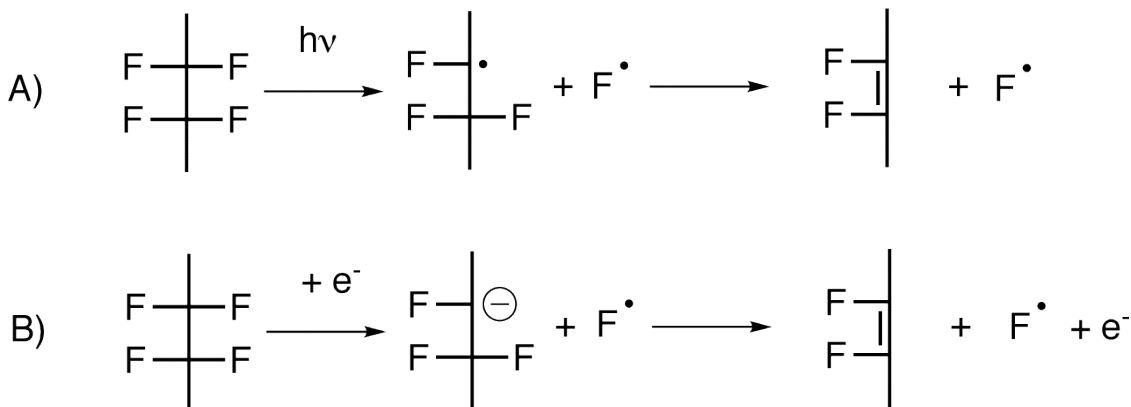


Figure 4.9: Possible degradation mechanisms. A) direct C-F bond cleavage by X-ray radiation, B) uptake of a secondary electron.

binding energies of the involved bonds are different. This explains the previously mentioned changes in the C 1s and F 1s peaks with time: those peaks associated with CF_n decrease, while others increase. The outlined determination of the degradation behavior of PFAND under X-ray exposure is necessary to ensure the accuracy of XPS quantification of its adlayers on TiO_2 . Subsequent calculations need to account for X-ray-induced damage during spectral acquisition. The approach chosen to assess the degree of degradation was to utilize the clear correlation between the shift of the binding energy and the reduction of integrated intensity of the F 1s peak (shown in Figure 4.7): actual loss of fluorine can be deduced from the position of the F 1s peak in the XP spectrum. The correlation is based on the degradation of CF_2 groups to fluorine compounds with lower binding energies, effectively reducing the area of the CF_2 peaks and increasing that of other peaks of lower binding energy in the F 1s spectrum. For the quantification of all homogeneous and gradient samples, we found that deviations of the F 1s signal position was within the error margin (0.1 eV, which would equal a maximum loss of 10% of material). Consequently, all measurements as presented in our work did not indicate sufficiently large shifts to necessitate correcting any performed quantification.

4.1.1.2 Stability/Degradation of catechol SAMs under deep-UV exposure

Because of the photocatalytic activity exhibited by TiO_2 , it is relevant to test the stability of PFAND SAMs on TiO_2 . Furthermore, it suggests itself to try patterning PFAND functionalized (TiO_2) surfaces in the same manner as done for phosphonic acids on TiO_2 [30]. In the course of this work the UV setup as described before was used to establish UV-induced degradation kinetics of PFAND- TiO_2 adlayers. The stability of PFAND as a function of UV exposure time is shown through XPS ratios (C/Ti, F/Ti, and N/Ti) in Figure 4.10 (samples were always covered by quartz glass, to be compatible with direct UV photolithography). All signals associated with PFAND decline with time until complete removal of the adlayer. The degradation proceeds faster without the quartz cover (compare Sections 4.2.3 and 6.1) because of easier diffusion of desorbed material away from the surface (already reacted radicals can be replenished faster). It is noticeable that after 1 min of UV exposure the amount of carbon (C/Ti) is about 10% higher than for the initial monolayer. This increase is possibly due to radicals remaining on the substrate surface after short exposure times. The radicalized surfaces are highly reactive and easily bind airborne contamination during sample transport. Assuming that the degradation of CF_2 -groups, similar to the representation shown in Figure 4.9, takes place through C=C formation and liberation of $\text{F}\bullet$ radicals, such radicals are likely to react with other organic species already present close to the substrate surface or directly with TiO_2 . It can be seen in F 1s XP spectra (Figure 4.11) that new fluorine species appear on the TiO_2 surface during UV exposure. For exposure times > 4 min the carbon signal also decreases in accordance with other elements present (F and N).

While Figure 4.10 indicates that the degradation kinetics for the three elements (carbon, nitrogen, and fluorine) belonging to PFAND are identical, the degradation mechanisms at hand are assumed to be based on UV photocatalytically induced (oxygen) radicals originating from TiO_2 . The complete degradation/removal is additionally confirmed by VASE measurements (see Figure 4.10) where the adlayer thickness does not significantly decrease after 1 min of UV exposure (in similarity to the XPS carbon signal) but goes to 0 within 1 h. Surfaces can thus be cleaned from PFAND adlayers and rendered hydrophilic with no remains in contrast to phosphate-based

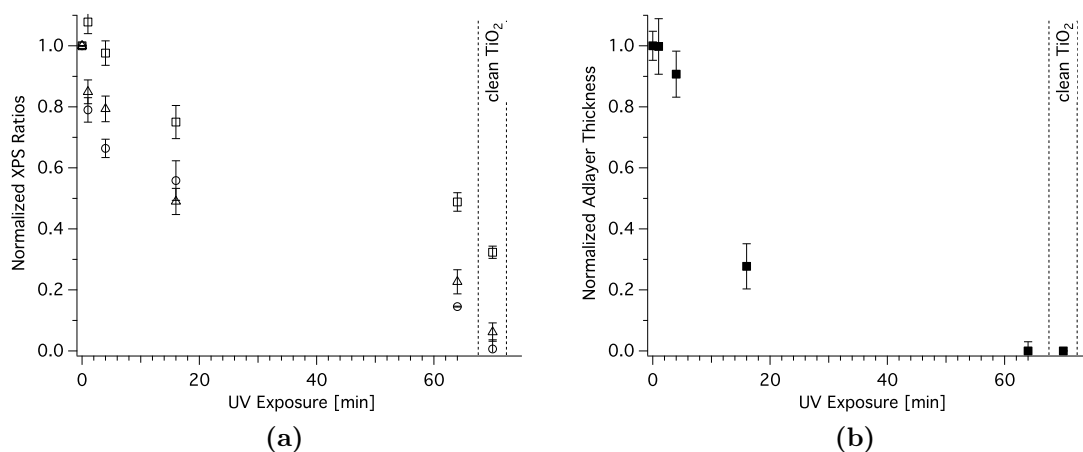


Figure 4.10: Remaining adlayer as function of UV exposure time: Left normalized XPS ratios C/Ti (□), N/Ti (△), and F/Ti (○); Right: normalized adlayers thickness as measured with VASE (■).

systems where the anchor group usually cannot be removed by UV photocatalysis and remains on the TiO₂ surface. [30] It is thus reasonable to assume that catechol-based direct UV photolithography systems (on TiO₂ or Nb₂O₅) are ideal for creating binary structures since adlayers can be completely and selectively (through masks) removed.

4.1.1.3 Considerations for VASE measurements of (PFA)ND adlayers

VASE measurements reveal a thickness of 1.3 - 1.4 nm for densely packed monolayers of PFAND. The difference between molecular length (≈ 2.1 nm when stretched) and measured adlayer thickness is attributed to three considerations: i) relaxed PFAND molecules are most likely not straight, but helical and bent as in the case of fluorinated alkyl thiols, [173] ii) adsorbed PFAND molecules, as fluorinated alkyls, might be tilted with respect to the surface normal by 30°-35° to optimize packing and intermolecular interactions, [173,250] iii) VASE-determined thickness is systematically underestimated by the layer model that was employed, because of adventitious carbon/contamination, which is constantly replaced by PFAND during adsorption (see Figure 4.12) - a process referred to as “self-cleaning” by Buck et al. for thiols on gold. [251] Comparison of C 1s XP spectra allows an estimation of the replacement

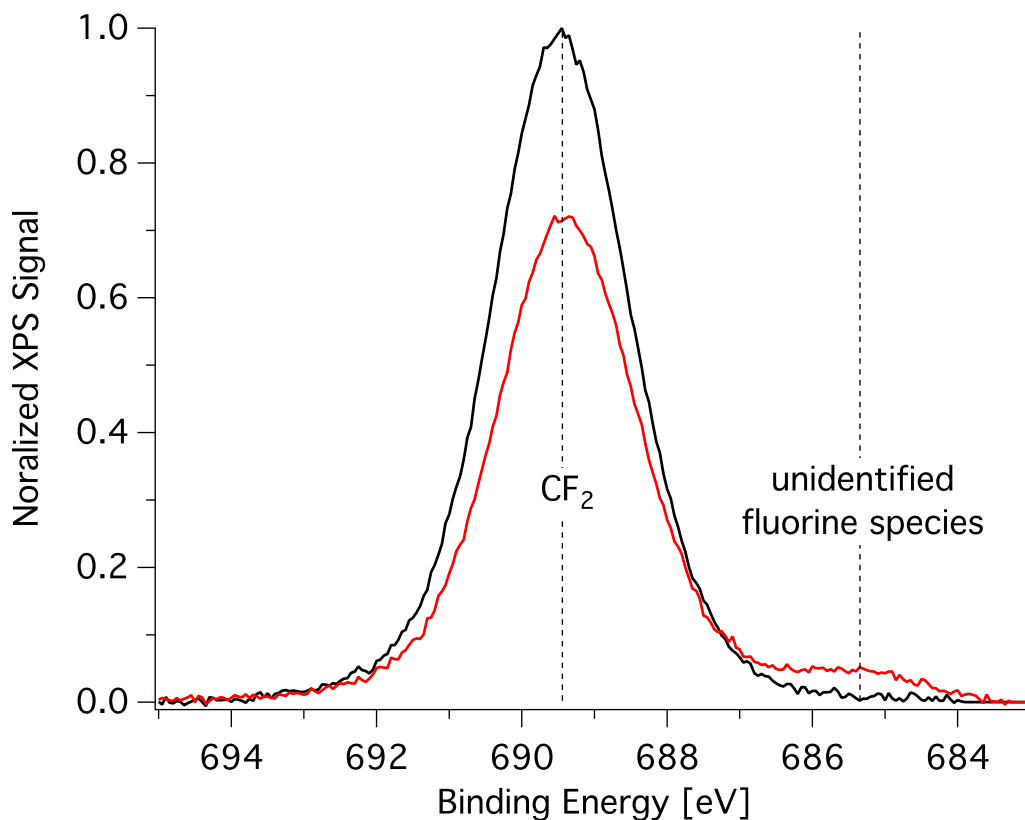


Figure 4.11: F1s XPS spectra of PFAND monolayer on TiO₂ before (black) and after 16 min of UV exposure. Side peak (unidentified fluorine species) appears at around 685.5 eV next to PFAND CF₂ peak at \approx 689.5 eV. Spectra are normalized to maximum intensity of the full monolayer peak.

of surface contamination: the amount of contamination on clean TiO_2 surfaces is equivalent to a fraction (20-25%) of what is measured on adlayers. The good agreement between stoichiometry and XPS C 1s data for PFAND (Table 4.2) indicate (complete) replacement of this contamination during (PFAND) adlayer formation. As a function of adlayer thickness the slope of F/Ti is higher than of C/Ti (PFAND static and one-component gradient samples) in Figure 4.12a. This difference and the fact that C/Ti for a clean wafer (0 nm) is 0.3 and thus about 25% of that of a full PFAND monolayer (1.2) affirm the assumption. Hence, VASE-measured thickness of a PFAND monolayer might be compensated by 25% yielding 1.7 nm. We assume that the packing of PFAND and ND is mainly governed by the adsorption kinetics of catechols on TiO_2 surfaces, which have been addressed extensively in the literature, as well as the interaction between the perfluoro-alkyl chains. [106, 178, 249, 252] While it is not clear how much the different properties of perfluoro-alkyl and hydrocarbon alkyl chains (the radius of $-\text{CF}_2-$ links is about 0.04 nm larger than that of CH_2) [253] influence ordering, an average tilt angle of $\approx 32^\circ$ is assumed for a densely packed PFAND monolayer in analogy to thiol-gold [163] and phosphate-metal-oxide [171, 172] systems.

4.1.2 Adsorption on Cr/CrOx

For reasons of comparison, PFAND was also adsorbed on Cr/CrOx. The same conditions as for TiO_2 experiments were applied, even though they might be inadequate and leave room for improvement (solvents, pH, (oxidation) state of substrate). Figure 4.13 shows XP spectra recorded for PFAND adlayers adsorbed for 48 h from 440 μM 1:2 2-propanol: H_2O solutions on Cr coated Si wafers (Cr forms a native oxide layer (CrOx) when exposed to air). The C 1s spectra indicate that the layer's quality is lower than for those observed on TiO_2 - the intensity of the C1 peak is considerably higher than that of C6, implying a higher degree of remaining contamination on CrOx than on TiO_2 . It is also noticeable that the nitrogen 1s spectrum contains only one major peak at 400.4 eV and only a minute one at 405.9 eV in contrast to PFAND layers on TiO_2 . While the sum of their ratios amounts to about 2, in agreement with stoichiometry, it is not clear why the nitro peak is considerably smaller. Within the UV and X-radiation degradation experiments of PFAND adlayers on TiO_2 it was

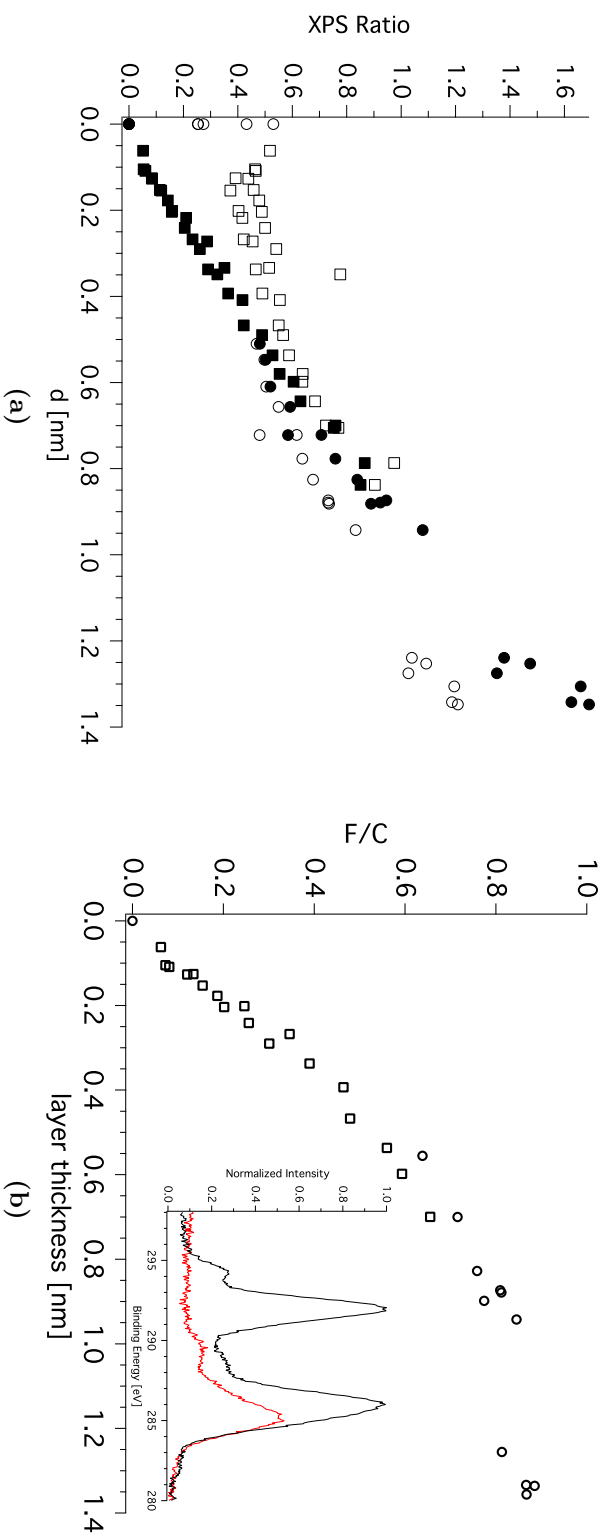


Figure 4.12: Correlation between adlayer thickness (VASE) and elemental composition (XPS) measurements for PFAND on TiO₂ reveals continuous replacement of adventitious carbon/contamination by adsorbed PFAND: a) F/Ti (filled shapes) and C/Ti (open shapes) for gradient (circles) and static samples (squares), b) F/C ratio for static (○) and one-component gradient (□) samples (see Section 5.1), inset shows C 1s spectra of PFAND monolayer (black) versus a clean TiO₂ substrate (normalized to maximum intensity of PFAND spectrum).

noticed that the nitro peak disappears faster, leaving a major peak at about 400 eV. Hence, it might be that the XPS measurement itself causes the same observation on Cr/CrO_x substrates.

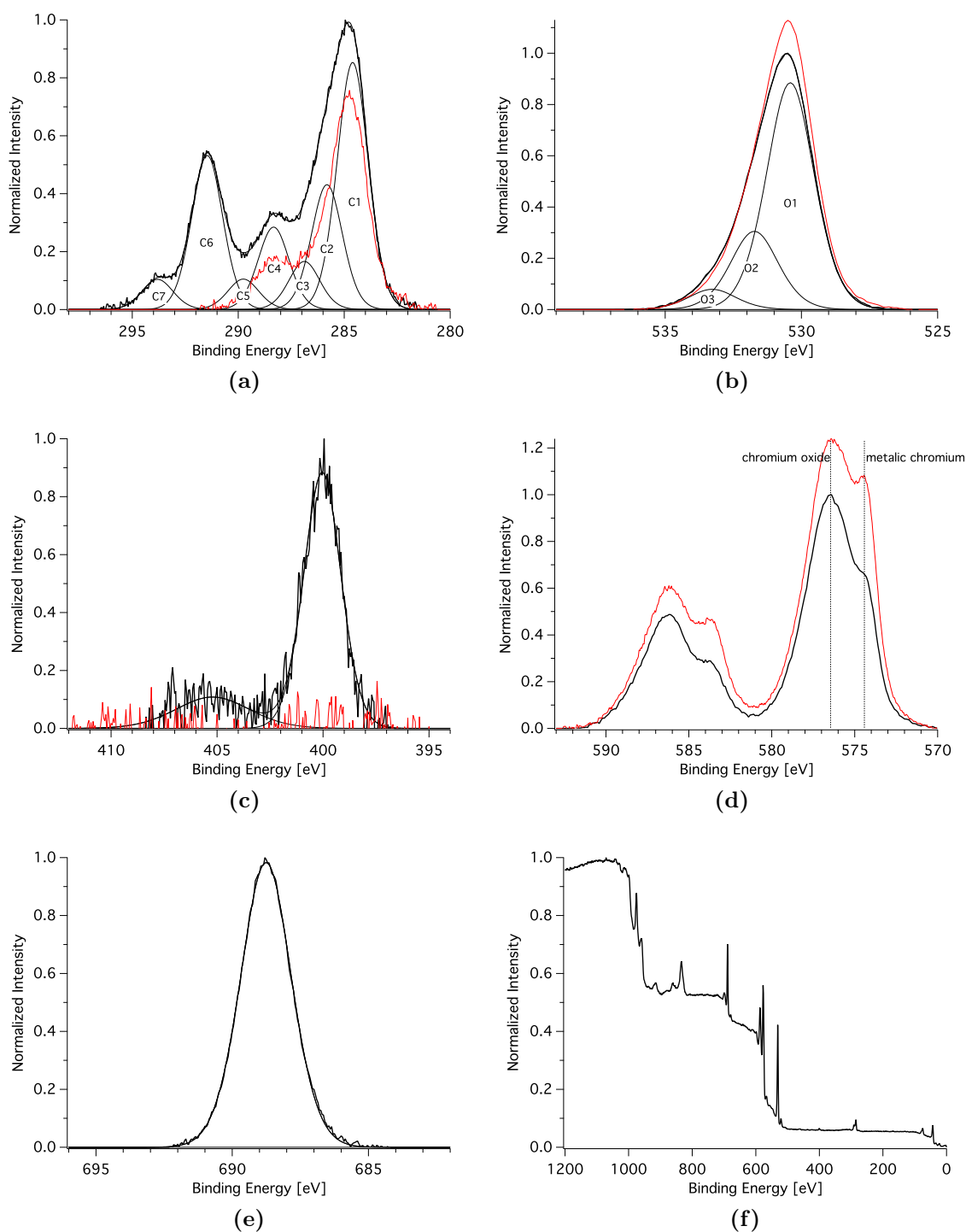


Figure 4.13: XP (Sigma2) spectra of PFAND monolayers adsorbed on Cr/CrOx normalized to maximum intensity value: (a) carbon 1s, (b) oxygen 1s, (c) nitrogen 1s, (d) chromium 2p, (e) fluorine 1s, (f) survey. C 1s, N 1s, O 1s components are listed in Table 4.2. Red lines are the respective spectra of the clean Cr/CrOx surface (see Section 3.2).

Table 4.4: Binding energies, full width at half maximum (FWHM), assignment and measured areas for a homogeneous PFAND film on Cr/CrOx relative to the carbon area of the CF₃ group. Comparison between experimental and stoichiometrically calculated intramolecular ratios, non-monochromatic X-rays (Sigma2 Probe).

Element	Peak	Binding energy [eV] ^a	FWHM [eV] ^a	Assignment (atoms)	Area ^b relative to CF ₃ = 15
	C1	285.0	1.7 ± 0.1	C-C-C (4)	13.2 ± 2.2
	C2	286.2 ± 0.1	=FWHM(C1)	C-O; C-N; C-CON; C-CF ₂ - (5)	6.9 ± 0.8
Carbon (1s)	C3	287.4 ± 0.2	=FWHM(C1)	-C(=O)-N (1)	2.6 ± 0.2
	C4	288.8 ± 0.1	=FWHM(C1)	-C-NO ₂ (1)	1.9 ± 0.3
	C5	290.4 ± 0.2	=FWHM(C1)	C-CF ₂ -CF ₂ (1)	1.3 ± 0.0
	C6	291.9 ± 0.1	=FWHM(C1)	CF ₂ -CF ₂ -CF _x (6)	5.7 ± 0.2
	C7	294.1 ± 0.1	=FWHM(C1)	CF ₂ -CF ₃ (1)	1.0 ± 0.0
Nitrogen (1s)	N1	400.4 ± 0.1	2.1 ± 0.1	-C(=O)-NH ₂ (1)	1.6 ± 0.1
	N2	405.9 ± 0.3	3.8 ± 0.4	-C-NH ₃ ⁺ (II) (1)	0.5 ± 0.0
Fluorine (1s)		689.2 ± 0.1	2.2 ± 0.1	-CF _x (17)	17.5 ± 1.5
	O1	530.4 ± 0.0	2.1 ± 0.0	Cr ₂ O ₃	52.9 ± 8.6
Oxygen (1s)	O2	531.8 ± 0.0	=FWHM(O1)	C-O-H; C-O-Cr; -C(=O)-N	17.9 ± 3.4
	O3	533.3 ± 0.0	=FWHM(O1)	-C-NO ₂ ; Cr-OH	3.5 ± 0.5

^aSigma2, ^bR.S.F. corrected

4.2 Polyelectrolytes

Two variations of each of the polymers poly(L-lysine)-*graft*-poly(ethylene glycol) (PLL-*g*-PEG), and poly(L-lysine)-*graft*-poly(2-methyl-2-oxazoline) (PLL-*g*-PMOXA) were used for direct UV photolithography studies in this work. The structural configurations of the polymers are given in Section 3.3.3. Preliminary work included the characterization of homogeneous layers (see Section 4.2.1) and their resistance to X-radiation (see Section 4.2.2) as well as UV light (see Section 4.2.3).

4.2.1 Homogeneous layers

Protein resistant coatings were obtained on TiO_2 and Nb_2O_5 substrates by adsorption of PLL-*g*-PEG and PLL-*g*-PMOXA from their respective 1 g/l and 0.1 g/l HEPES2 buffer solutions. [254,255] The resulting homogeneous adlayers have been characterized by VASE, XPS, and with respect to bio-passivity before. [120,121,126,254,255] Figures 4.14 - 4.17 show detailed XP spectra of adlayers of the polymers on Nb_2O_5 and TiO_2 used throughout this work. Individual peaks are labeled C1-C3 (C 1s), O1 and O2 (O 1s), N1 and N2 (N 1s) and identified in Table 4.5 and 4.6. Stoichiometries match well with measured peak-area ratios (relative to N1), with opposing discrepancies for the peaks associated to aliphatic carbon (285.0 eV) and C-N (286.3 eV), which can be explained by carbon species within the polymers whose binding energies are between 285.0 and 286.0 and cannot be associated clearly to either peak. All spectra were shifted by ≈ -0.6 eV (calibrated to 530.1 eV for oxygen 1s in TiO_2 , and 530.2 eV for Nb_2O_5 to correct for charging effects of the adlayer). The intensity of O2 generally exceeds calculated values due to free hydroxyl groups and water present on the surfaces. Both corresponding signals are found at around 532 eV. The O 1s peak at 533 eV is essentially solely associated to C-O-C bonds (only present in PEG). [169,256]

4.2.2 Degradation under X-ray

PLL-*g*-PEG is known to degrade under X-radiation. [125] It is possible that PLL-*g*-PMOXA also degrades when exposed to X-rays (during XPS measurements). Correct quantification of XPS data of polymer adlayers requires the evaluation of magni-

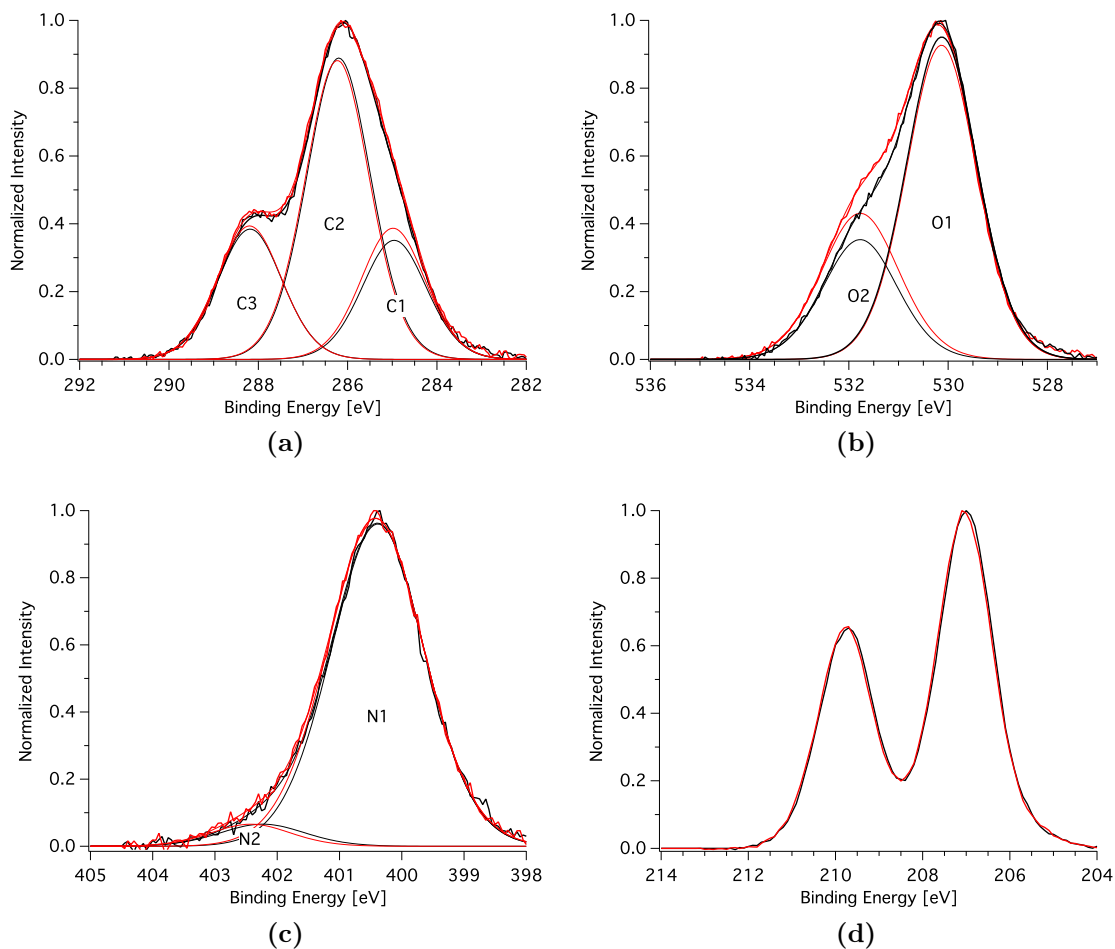


Figure 4.14: Normalized XP spectra of PLL-*g*-PMOXA PMOXA8 (red) and PMOXA4 (black) adsorbed on Nb₂O₅: (a) carbon 1s, (b) oxygen 1s, (c) nitrogen 1s, (d) niobium 3d.

Table 4.5: Binding energies, full width at half maximum (FWHM), assignment and measured areas for a homogeneous PLL-*g*-PMOXA films on Nb₂O₅ relative to the area of -NH₂ peak (N1). Comparison between experimental and stoichiometrically calculated intramolecular ratios, measured using non-monochromatic X-rays (Sigma2 Probe).

Element	Peak	Binding energy [eV]	FWHM [eV]	Assignment (stoichiometry)	Area [†] relative to N1
Carbon(1s)	C1	285.0 ± 0.2	1.7 ± 0.1	C-C-C, C-C=O (1.2)	0.8 ± 0.0
	C2	286.3 ± 0.2	=FWHM(C1)	C-N (1.9)	2.2 ± 0.0
	C3	288.2 ± 0.2	=FWHM(C1)	-C(=O)-N (0.9)	0.9 ± 0.0
Nitrogen (1s)	N1	400.4 ± 0.1	1.8 ± 0.2	-C(=O)-NH ₂ (1.0)	1.0 ± 0.0
	N2	402.4 ± 0.3	1.6 ± 0.2	-C-NH ₃ ⁺ (0.1)	0.1 ± 0.0
Oxygen (1s)	O1	530.1 ± 0.1	1.7 ± 0.1	TiO ₂ / Nb ₂ O ₅	3.8 ± 0.1
	O2	531.8 ± 0.1	1.8 ± 0.2	O-C=O, O-H, C=O; H ₂ O (1.0)	1.5 ± 0.1
Carbon (1s)	C1	285.1 ± 0.1	1.7 ± 0.1	C-C-C, C-C=O (1.1)	0.9 ± 0.0
	C2	286.3 ± 0.1	=FWHM(C1)	C-N (2.0)	2.2 ± 0.0
	C3	288.3 ± 0.1	=FWHM(C1)	-C(=O)-N (1.0)	0.9 ± 0.0
Nitrogen (1s)	N1	400.4 ± 0.1	1.8 ± 0.2	-C(=O)-NH ₂ (1.0)	1.0 ± 0.0
	N2	402.4 ± 0.0	1.5 ± 0.2	-C-NH ₃ ⁺ (0.3)	0.0 ± 0.0
Oxygen (1s)	O1	530.2 ± 0.1	1.7 ± 0.1	Nb ₂ O ₅	2.9 ± 0.1
	O2	531.8 ± 0.1	1.8 ± 0.2	O-C=O, O-H, C=O; H ₂ O (1.0)	1.4 ± 0.1

[†]R.S.F. corrected

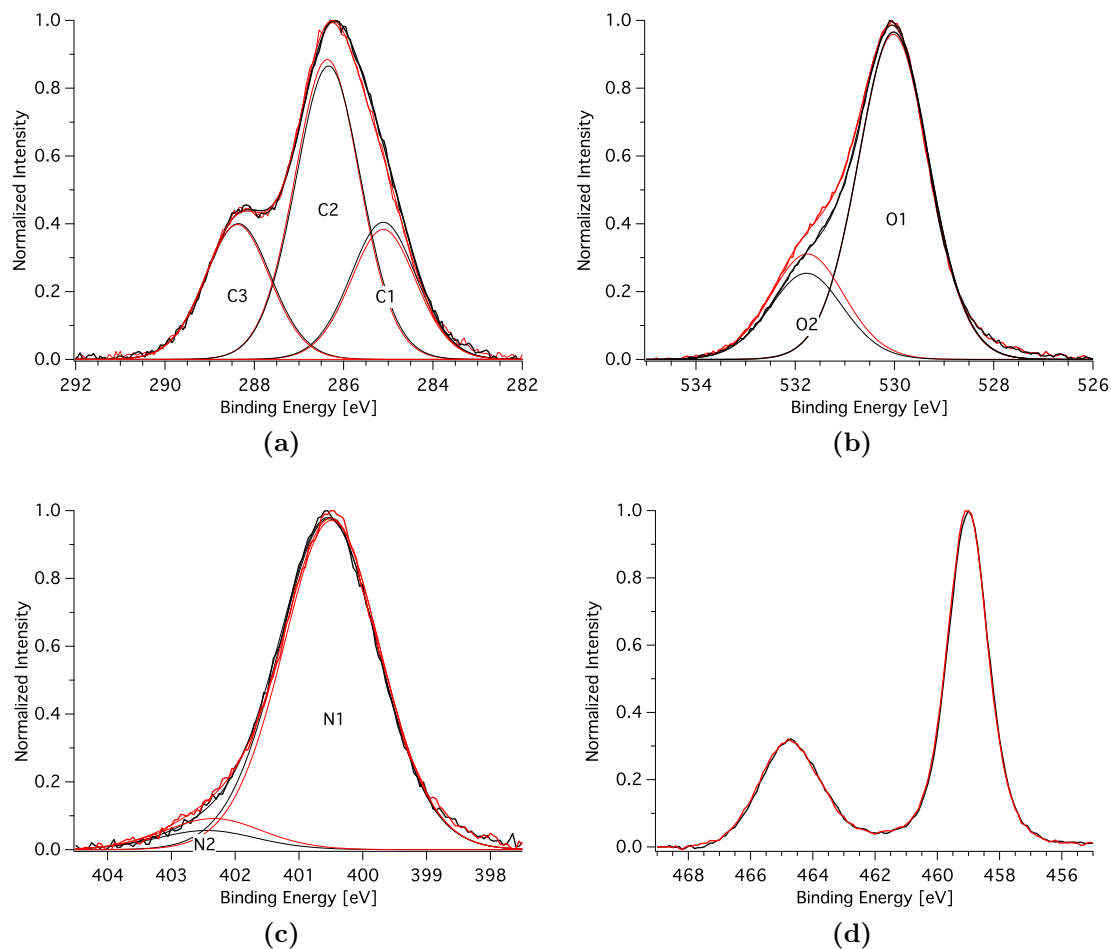


Figure 4.15: Normalized XP spectra of PLL-*g*-PMOXA PMOXA8 (red) and PMOXA4 (black) adsorbed on TiO₂: (a) carbon 1s, (b) oxygen 1s, (c) nitrogen 1s, (d) titanium 2p.

Table 4.6: Binding energies, full width at half maximum (FWHM), assignment and measured areas for a homogeneous PLL-*g*-PMOXA films on TiO₂ relative to the area of -NH₂ peak (N1). Comparison between experimental and stoichiometrically calculated intramolecular ratios, measured using non-monochromatic X-rays (Sigma2 Probe).

Element	Peak	Binding energy [eV]	FWHM [eV]	Assignment (stoichiometry)	Area [†] relative to N1
Carbon (1s)	C1	285.2 ± 0.0	1.7 ± 0.1	C-C-C, C-C=O (1.2)	0.9 ± 0.0
	C2	286.5 ± 0.0	=FWHM(C1)	C-N (1.9)	2.1 ± 0.0
	C3	288.5 ± 0.0	=FWHM(C1)	-C(=O)-N (0.9)	0.9 ± 0.0
Nitrogen (1s)	N1	400.5 ± 0.0	1.8 ± 0.2	-C(=O)-NH ₂ (1.0)	1.0 ± 0.0
	N2	402.5 ± 0.1	1.6 ± 0.2	-C-NH ₃ ⁺ (0.1)	0.1 ± 0.0
Oxygen (1s)	O1	530.1 ± 0.0	1.7 ± 0.1	TiO ₂	5.2 ± 0.1
	O2	531.8 ± 0.0	1.8 ± 0.2	O-C=O, O-H, C=O; H ₂ O (1.0)	1.5 ± 0.1
Carbon (1s)	C1	285.2 ± 0.1	1.7 ± 0.1	C-C-C, C-C=O (1.1)	1.0 ± 0.0
	C2	286.4 ± 0.1	=FWHM(C1)	C-N (2.0)	2.1 ± 0.0
	C3	288.4 ± 0.1	=FWHM(C1)	-C(=O)-N (1.0)	1.0 ± 0.0
Nitrogen (1s)	N1	400.5 ± 0.1	1.8 ± 0.2	-C(=O)-NH ₂ (1.0)	1.0 ± 0.0
	N2	402.3 ± 0.0	1.5 ± 0.2	-C-NH ₃ ⁺ (0.3)	0.1 ± 0.0
Oxygen (1s)	O1	530.1 ± 0.1	1.7 ± 0.1	TiO ₂	4.4 ± 0.1
	O2	531.8 ± 0.1	1.8 ± 0.2	O-C=O, O-H, C=O; H ₂ O (1.0)	1.5 ± 0.1

[†]R.S.F. corrected

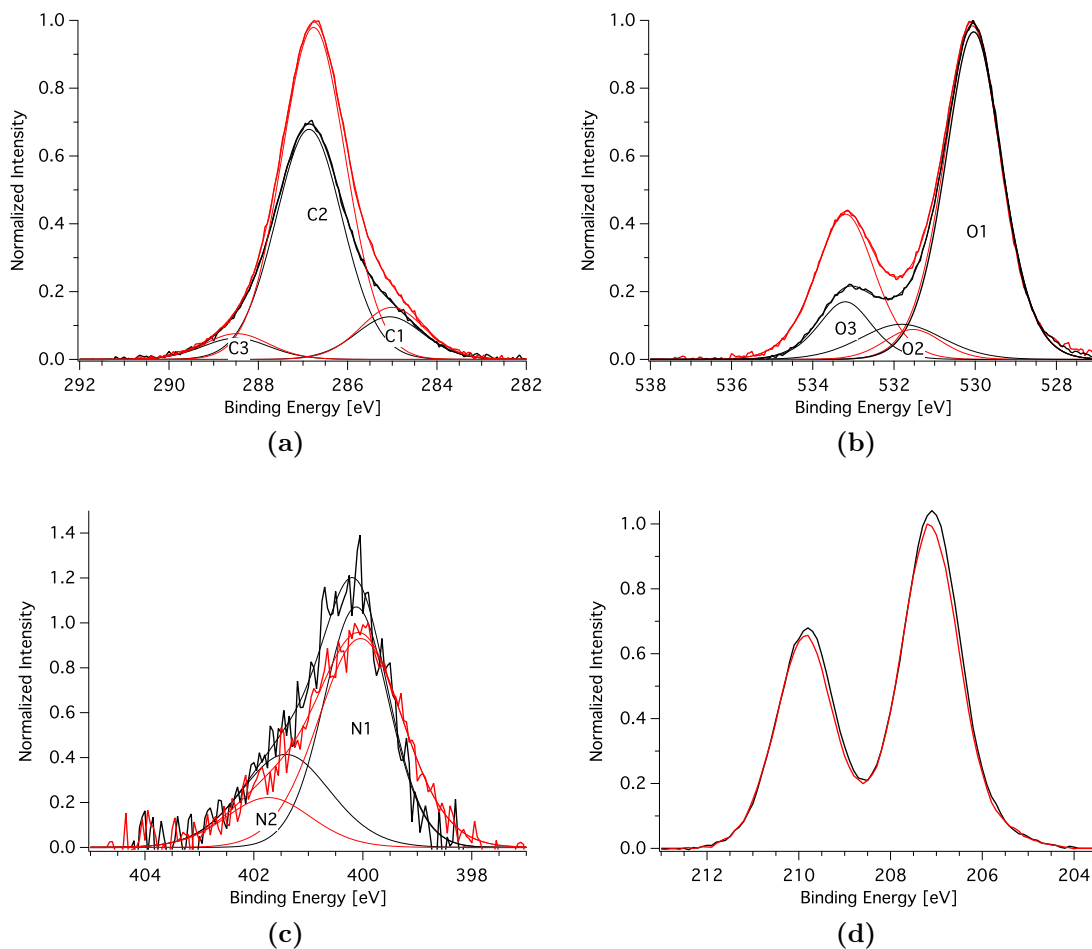


Figure 4.16: Normalized XP spectra of PLL-*g*-PEG PEG5 (red) and PEG2 (black) adsorbed on Nb₂O₅: (a) carbon 1s, (b) oxygen 1s, (c) nitrogen 1s, (d) niobium 3d.

Table 4.7: Binding energies, full width at half maximum (FWHM), assignment and measured areas for a homogeneous PLL-*g*-PEG films on Nb₂O₅ relative to the area of aliphatic carbon peak (C1). Comparison between experimental and stoichiometrically calculated intramolecular ratios, measured using non-monochromatic X-rays (Sigma2 Probe).

Element	Peak	Binding energy [eV]	FWHM [eV]	Assignment (stoichiometry)	Area [†] relative to C1
Carbon (1s)	C1	284.9 ± 0.0	1.7 ± 0.1	C-C-C, C-C=O (1.0)	1.0 ± 0.0
	C2	286.7 ± 0.2	=FWHM(C1)	C-N, C-O (5.2)	5.1 ± 0.4
	C3	288.3 ± 0.2	=FWHM(C1)	-C(=O)-N (0.5)	0.5 ± 0.0
Nitrogen (1s)	N1	399.9 ± 0.1	1.8 ± 0.2	-C(=O)-NH ₂ (0.5)	0.2 ± 0.1
	N2	400.9 ± 0.3	1.6 ± 0.2	-C-NH ₃ ⁺ (0.1)	0.1 ± 0.0
PEG2	O1	530.2 ± 0.1	1.6 ± 0.1	Nb ₂ O ₅	9.4 ± 0.2
	O2	532.2 ± 0.1	1.7 ± 0.2	O-C=O, O-H, C=O; H ₂ O (0.5)	1.0 ± 0.0
	O3	533.0 ± 0.1	1.9 ± 0.2	C-O-C (4.5)	2.9 ± 0.3
Carbon (1s)	C1	284.9 ± 0.1	1.7 ± 0.1	C-C-C, C-C=O (1.1)	1.0 ± 0.0
	C2	286.7 ± 0.1	=FWHM(C1)	C-N, C-O (7.0)	7.4 ± 0.6
	C3	288.4 ± 0.1	=FWHM(C1)	-C(=O)-N (0.5)	0.5 ± 0.0
Nitrogen	N1	400.0 ± 0.1	1.8 ± 0.2	-C(=O)-NH ₂ (0.5)	0.2 ± 0.0
	N2	402.8 ± 0.0	1.5 ± 0.2	-C-NH ₃ ⁺ (0.3)	0.0 ± 0.0
PEG5	O1	530.2 ± 0.1	1.6 ± 0.1	Nb ₂ O ₅	7.1 ± 0.2
	O2	532.2 ± 0.1	1.7 ± 0.2	O-C=O, O-H, C=O; H ₂ O (0.5)	0.8 ± 0.5
	O3	533.0 ± 0.1	1.9 ± 0.2	C-O-C (6.8)	4.5 ± 0.3

[†]R.S.F. corrected

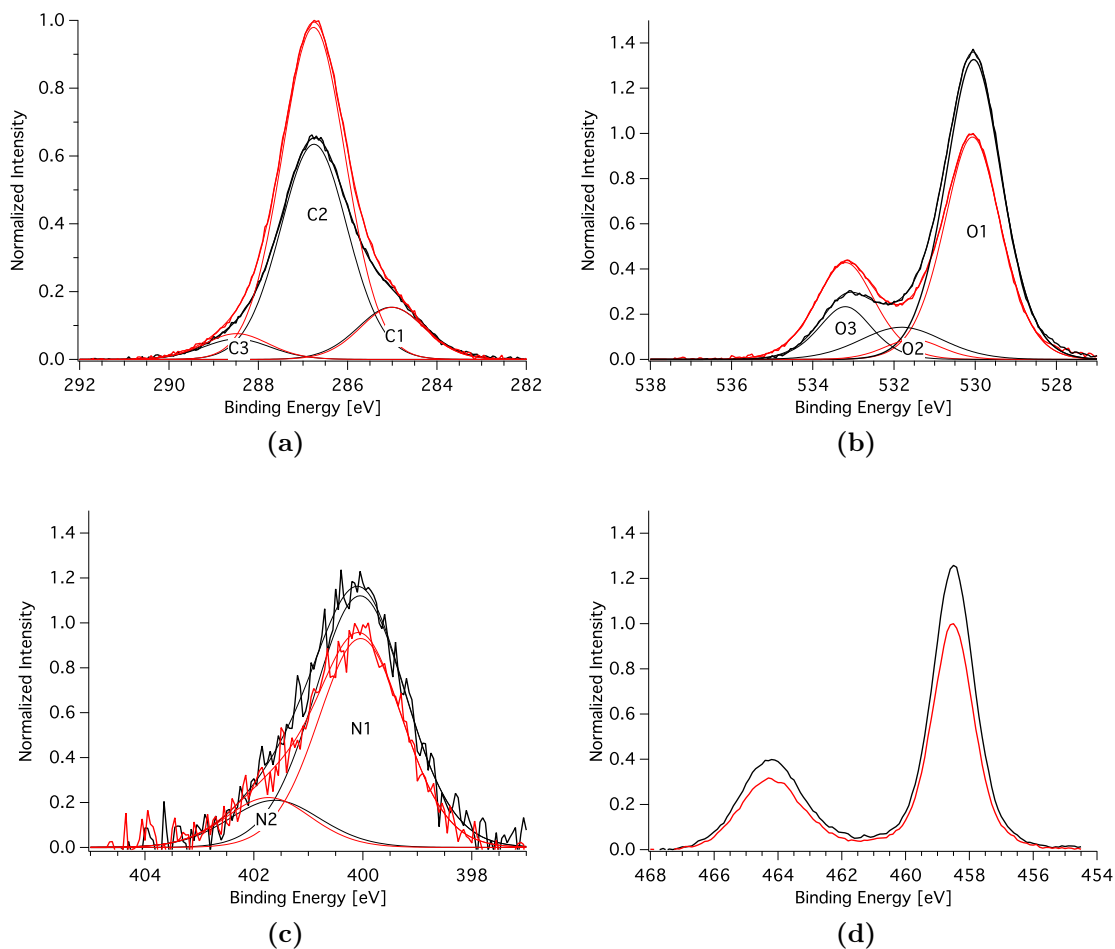


Figure 4.17: Normalized XP spectra of PLL-*g*-PEG PEG5 (red) and PEG2 (black) adsorbed on TiO₂: (a) carbon 1s, (b) oxygen 1s, (c) nitrogen 1s, (d) titanium 2p.

Table 4.8: Binding energies, full width at half maximum (FWHM), assignment and measured areas for a homogeneous PLL-*g*-PEG films on TiO₂ relative to the area of aliphatic carbon peak (C1). Comparison between experimental and stoichiometrically calculated intramolecular ratios, measured using non-monochromatic X-rays (Sigma2 Probe).

Element	Peak	Binding energy [eV]	FWHM [eV]	Assignment (stoichiometry)	Area [†] relative to C1
Carbon (1s)	C1	285.1 ± 0.2	1.7 ± 0.1	C-C-C, C-C=O (1.0)	1.0 ± 0.0
	C2	286.3 ± 0.2	=FWHM(C1)	C-N, C-O (5.2)	4.2 ± 0.1
	C3	288.2 ± 0.2	=FWHM(C1)	-C(=O)-N (0.5)	0.4 ± 0.0
Nitrogen (1s)	N1	400.1 ± 0.1	1.8 ± 0.2	-C(=O)-NH ₂ (0.5)	0.3 ± 0.0
	N2	401.7 ± 0.3	1.6 ± 0.2	-C-NH ₃ ⁺ (0.1)	0.1 ± 0.0
PEG2	O1	530.1 ± 0.1	1.5 ± 0.1	TiO ₂	8.5 ± 0.2
	O2	531.3 ± 0.2	1.8 ± 0.2	O-C=O, O-H, C=O; H ₂ O (0.5)	2.7 ± 0.1
	O3	533.3 ± 0.1	1.5 ± 0.2	C-O-C (4.5)	1.6 ± 0.1
Carbon (1s)	C1	285.0 ± 0.1	1.7 ± 0.1	C-C-C, C-C=O (1.1)	1.0 ± 0.0
	C2	286.3 ± 0.1	=FWHM(C1)	C-N, C-O (7.5)	6.8 ± 0.0
	C3	288.6 ± 0.1	=FWHM(C1)	-C(=O)-N (0.5)	0.5 ± 0.0
Nitrogen (1s)	N1	400.1 ± 0.1	1.8 ± 0.2	-C(=O)-NH ₂ (0.5)	0.3 ± 0.0
	N2	401.8 ± 0.0	1.5 ± 0.2	-C-NH ₃ ⁺ (0.3)	0.1 ± 0.0
PEG5	O1	530.1 ± 0.1	1.7 ± 0.1	TiO ₂	9.0 ± 0.7
	O2	531.6 ± 0.1	1.7 ± 0.2	O-C=O, O-H, C=O; H ₂ O (0.5)	0.6 ± 0.4
	O2	533.2 ± 0.2	1.7 ± 0.2	C-O-C (6.8)	4.0 ± 0.4

[†]R.S.F. corrected

tude and mechanism of any X-ray induced degradation. In order to assess both, monolayers of PMOXA8 and PEG5 were continuously measured with XPS (Sigma2) over 4 hours. XP spectra resulting from the experiments are shown in Figures 4.18 for Nb_2O_5 and 4.19 for TiO_2 . The degradation kinetics are presented through elemental XPS ratios in Figures 4.20 and 4.21. For both polymers and substrates, degradation with time is apparent in Figures 4.18 - 4.21. The degradation kinetics appear to be identical for both types of substrates. The elemental C/substrate and $O_{\text{polymer}}/\text{substrate}$ ratios follow decreasing linear trends over the whole 4 hours. While total carbon and oxygen signals indicate a loss of about 20% of all adlayers during 4 hours of X-ray exposure, the O 1s signal associated to C-O-C decreases by about 60% over the same time. Hence, the PEG part of the polymer is decreasing faster than the whole polymer (that is PEG degrades faster than PLL). Regarding the C 1s spectra of PEG5 in Figure 4.18 and 4.19, the decrease of C2 (associated to EG units and C-N of PLL) can be seen to be the strongest, in the case of TiO_2 additionally accompanied by an increase of aliphatic carbon (C1). This observation does not hold true for PLL-*g*-PMOXA or Nb_2O_5 . Hence, it is apparent that PEG is differently affected by X-ray induced degradation on TiO_2 . PLL-*g*-PMOXA adlayers on TiO_2 and Nb_2O_5 show a higher resistance to X-rays than PLL-*g*-PEG. Keeping measurement times in the range of 10 min per spot can be assumed to be safely in the margin of experimental error (on a Sigma2 instrument). The observation that the aliphatic peak for the PLL-*g*-PEG C 1s spectra does not increase during degradation might imply two things: a) the degradation mechanisms for the two substrates are different (This can also include the removal of one molecular species accompanied by the retention of another, intermittent one.); b) intermittent species that are created during the degradation have a higher affinity for TiO_2 than for Nb_2O_5 surfaces. PLL-*g*-PMOXA on Nb_2O_5 shows the same behavior: the aliphatic peak (C1) does not significantly change during X-ray exposure while the others (C2 and C3) decrease visibly.

4.2.3 Degradation under deep-UV

The usage of PLL-*g*-PEG in biosensors and other bio-chemistry systems where sterilization is necessary and possibly performed using UV requires a deeper understand-

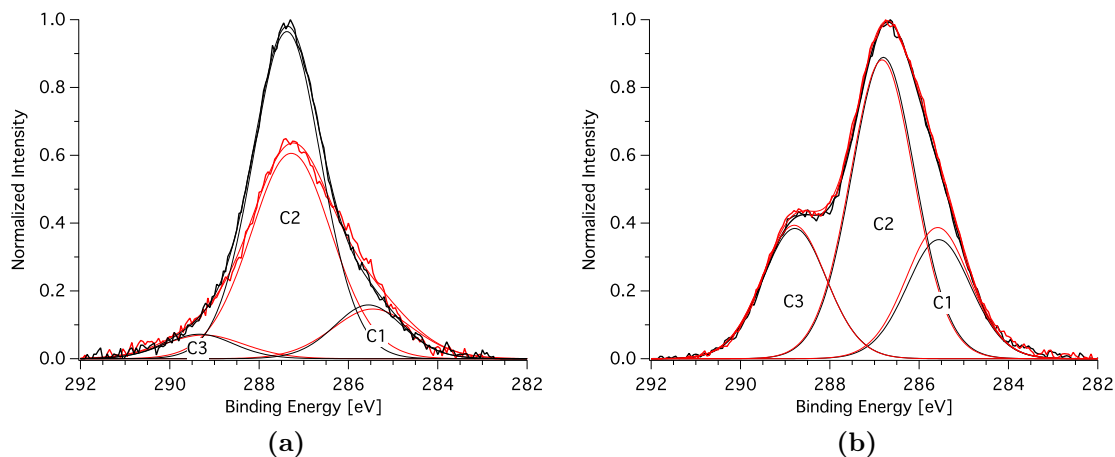


Figure 4.18: Normalized carbon 1s XP spectra of PEG5 (left) and PMOXA8 (right) adsorbed on Nb_2O_5 at the beginning (black) and after 4 hours of XPS measurement (red) .

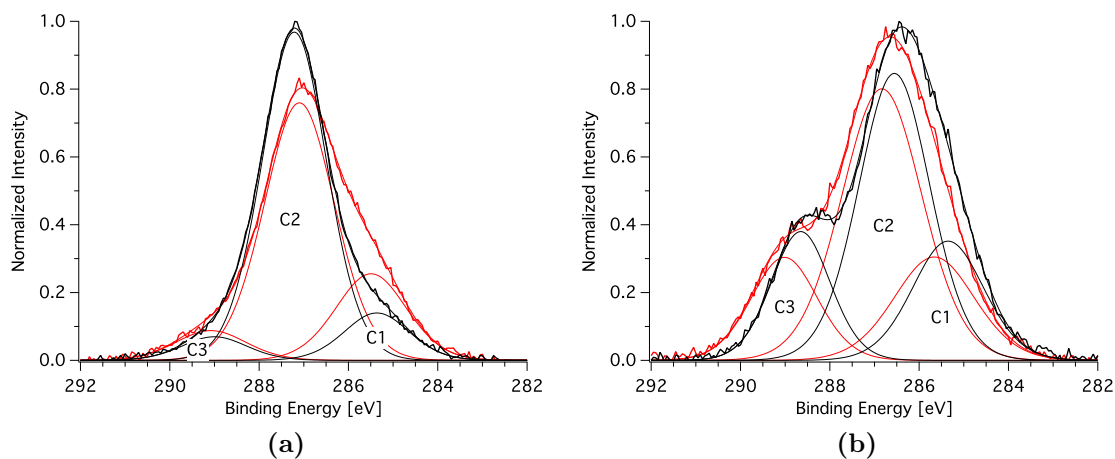


Figure 4.19: Normalized carbon 1s XP spectra of PEG5 (left) and PMOXA8 (right) at the beginning (black) and after 4 hours of XPS measurement (red) adsorbed on TiO_2 .

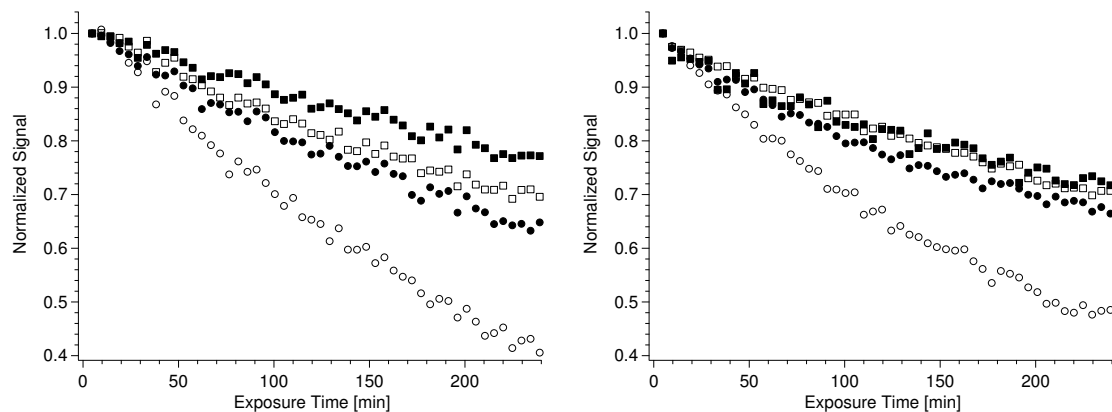


Figure 4.20: XPS C/Ti, C/Nb (■), $O_{polymer}/Ti$, $O_{polymer}/Nb$ (□), (C-O-C)/Ti, (C-O-C)/Nb (○), and (C-O)/Ti, (C-O)/Nb (●) ratios (normalized to initial monolayers) for PLL-*g*-PEG (PEG5) on TiO_2 (left) and Nb_2O_5 (right) during extended X-ray exposure in the Sigma2.

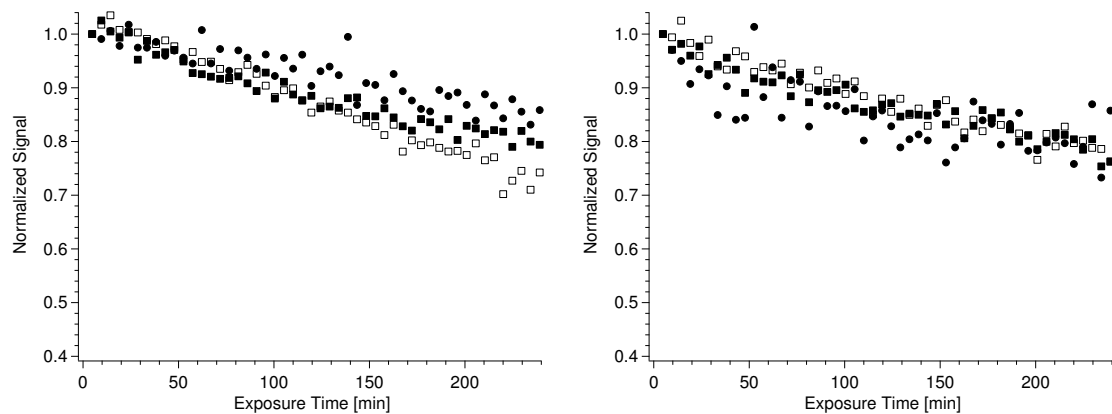


Figure 4.21: XPS C/Ti, C/Nb (■), $O_{polymer}/Ti$, $O_{polymer}/Nb$ (□), and N/Ti, N/Nb (●) ratios (normalized to initial monolayers) for PLL-*g*-PMOXA (PMOXA8) on TiO_2 (left) and Nb_2O_5 (right) during extended X-ray exposure in the Sigma2.

ing of the stability of PLL-*g*-PEG adlayers under UV. Furthermore specific spatially controlled UV induced degradation/removal has been of interest regarding different substrates including TiO₂ and adlayer systems such as alkylsiloxanes [257] and phosphonic acids [30] for example as a basis for the investigation of cellular adhesion and proliferation. [30, 33, 257] In order to assess possibilities to pattern surface adlayers of PLL-based polymers on Nb₂O₅ and TiO₂ substrates it has to be established how effective and complete degradation can be and what the mechanisms are. Figure 4.22 shows C 1s XP spectra of cleaned Nb₂O₅, TiO₂, and SiO₂ substrates, after adsorption of PMOXA8, and after subsequent exposure to deep UV (mainly 365 nm and 254 nm) for 1 h (unprotected). In the case of Nb₂O₅ and TiO₂ the surfaces become even cleaner than they were before adsorption (due to a stronger UV light source used for degradation experiments than the one in the standard UV/O₃ cleaner and longer exposure times. Also, the shortened time of sample exposure to air before insertion into XPS system reduced airborne contamination of samples). The adlayer on SiO₂, however, is seen to only decrease by about 60% in the same time. The differences between the substrate and their respective degradation rates (amount of polymer on substrates after adsorption follows the order: Nb₂O₅ > TiO₂ > SiO₂) is explained by UV-induced photocatalytic activities of Nb₂O₅ and TiO₂ (see Section 2.1.1). SiO₂ has a band gap considerably larger than 3.3 eV and 4.4 eV (365 nm and 254 nm) and hence shows no such photoactivity. The apparent reduction of polymer on SiO₂ is due to direct UV-induced polymer degradation assisted by ozone generation by the UV light.

Preliminary experiments had to establish how fast the different components of the polymer adlayers on Nb₂O₅ and TiO₂ degrade under UV exposure with time and how strong the protein resistance of remaining adlayers is. Figure 4.23 shows the reduction of carbon and nitrogen as determined by XPS as a consequence of degradation during UV exposure (without quartz glass) of the polymers: PLL, PMOXA4, PMOXA8, PEG2, PEG5. All polymers degrade upon exposure to deep UV. The degradation of PLL-*g*-PEG appears faster and dominated by degradation of PEG - C/Nb falls to levels of PLL after 1 min of UV exposure and then follows the trend of PLL. PLL-*g*-PMOXA reaches PLL levels between 8 and 16 min. The main degradational mechanism is thus assumed to be oxidation, primarily supported by oxygen radicals that are generated photocatalytically at the TiO₂ and Nb₂O₅ surfaces. After 16

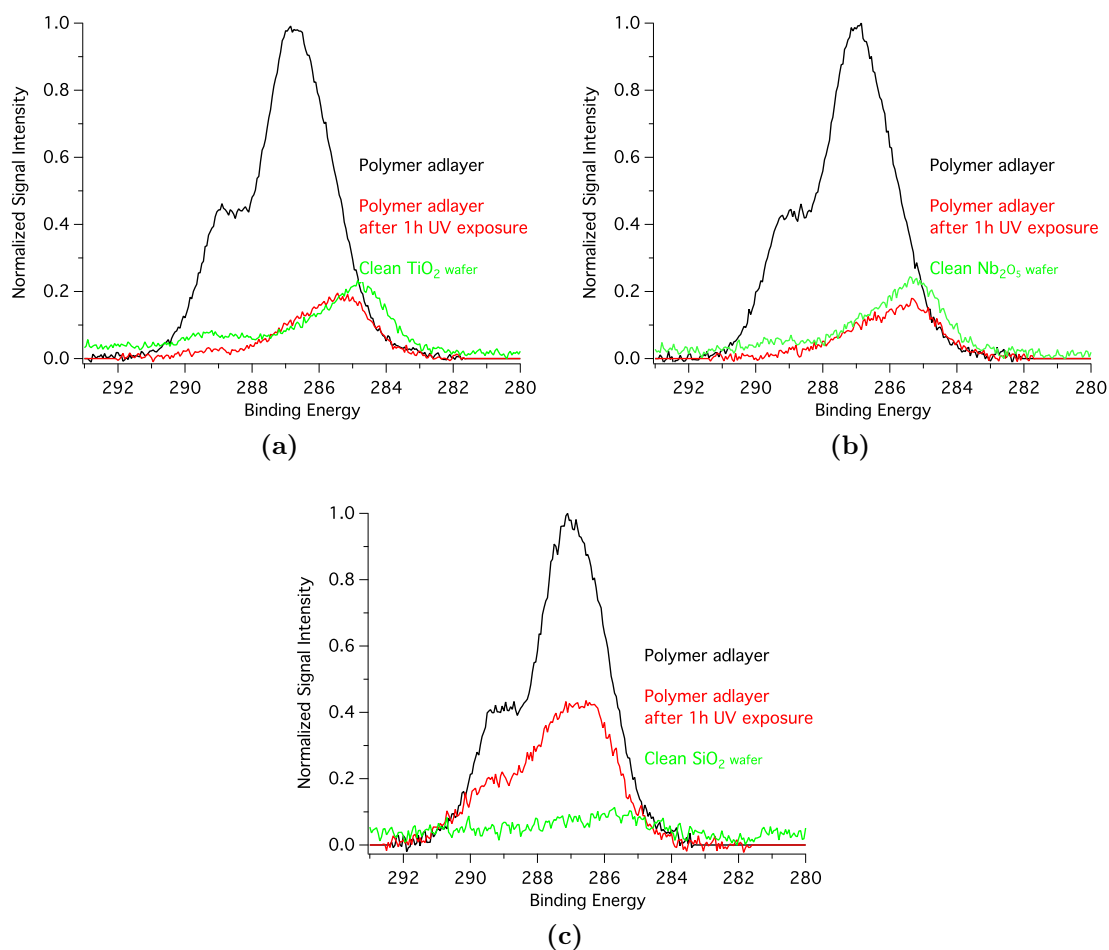


Figure 4.22: Normalized carbon 1s XP spectra of PMOXA8 adlayers on a) TiO₂, b) Nb₂O₅, c) SiO₂ before (black line) and after (red line) 1 h of UV (254 nm) exposure. Green lines are spectra from clean substrates for comparison.

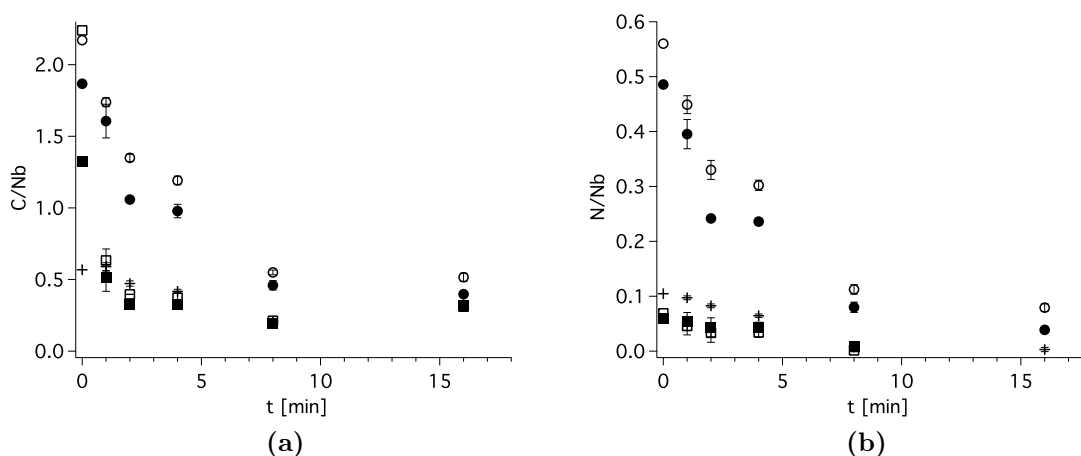


Figure 4.23: XPS (Sigma2) ratios a) C/Nb, b) N/Nb of PLL (+), PLL-*g*-PEG (PEG5 (□), PEG2 (■)), and PLL-*g*-PMOXA (PMOXA8 (○), PMOXA4 (●)) on Nb₂O₅ after different times of exposure to UV.

min of UV exposure only 20%-30% of the polymers' carbon signals remain while VASE measurements show an adlayer thickness of 0 nm (Figure 4.23a) indicating that no polymers remain intact. This is also supported by serum adsorption tests (see Figure 4.23b). While PMOXA-based polymers maintain protein resistance for 2-4 min of UV exposure, PEG-based polymers degenerate from the very beginning (Figure 4.23b) losing their protein resistance almost immediately. The results thus demonstrate that PLL-*g*-PMOXA is also more stable against UV than PLL-*g*-PEG making the polymer a better candidate for surface coatings that could also be used with UV sterilization.

4.3 Alkyl phosphates

Three different types of ω -terminations for alkyl-phosphates were chosen: -CH₃, -OH, and -COOH (see Section 2.2 for details). Homogeneous adlayers were adsorbed onto TiO₂ substrates from 500 μ M either aqueous solutions or a 99.2:0.8 mixtures with n-heptane:2-propanol (molecules were dissolved in 2-propanol first and then diluted with n-heptane) for 48 h. The length of the alkyl chain was 11 (CH₂) links to facilitate solution in water while still maintaining high degrees of order once adsorbed

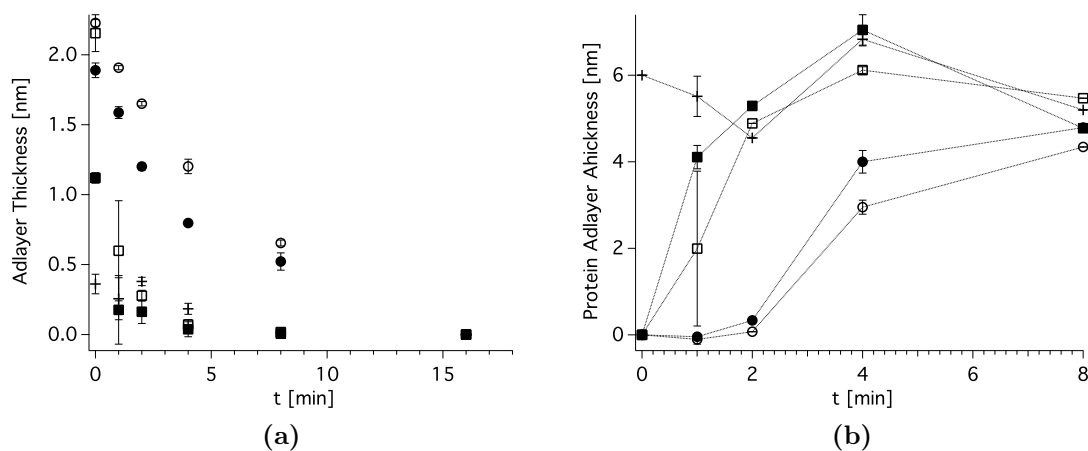


Figure 4.24: a) Surface adlayer thickness and b) remaining protein resistance (VASE) of PLL (+), PLL-*g*-PEG (PEG5 (□), PEG2 (■)), and PLL-*g*-PMOXA (PMOXA8 (○), PMOXA4 (●)) on Nb₂O₅ after different times of exposure to UV light ($\lambda > 250$ nm).

as SAMs on the metal oxide surface. Static water contact angles for surfaces coated with DDPO4 were determined to be $101^\circ \pm 2^\circ$, with OH-DDPO4 $52^\circ \pm 2^\circ$, and for COOH-UDPO4 $63^\circ \pm 3^\circ$. While contact angles for methyl-terminated SAMs are high and in good agreement with the other studies, [20, 23, 50] -OH and -COOH terminated phosphate SAMs do not achieve results [23] of comparable SAM systems such as thiols on gold. [258] The slightly higher sCA for COOH-functionalized SAMs might be due to lower order within the respective SAMs and a higher affinity of -COOH than -OH for TiO₂ and thus stronger exposure of alkyl chains compared to OH-terminated ones. Nevertheless, XPS results imply good SAM formation on TiO₂ substrates for all three DDPO4 derivatives - measured intramolecular ratios are in good agreement with stoichiometric values (see Table 4.9). Only oxygen signals deviate considerably, possibly caused by airborne contamination prone to adsorb on the hydrophilic (OH- and COOH-terminated) surfaces but also by H₂O and free surface hydroxyl groups.

SAM thicknesses were determined by VASE to be 1.6 ± 0.1 nm for DDPO4 and 1.7 ± 0.1 nm for OH-DDPO4 and for COOH-UDPO4 in agreement with previous works. [31]

Table 4.9: Binding energies, full width at half maximum (FWHM), assignment and measured areas for a homogeneous DDP04, OH-DDP04, and COOH-UDDP04 films on TiO₂. “stoichiometry” values are ratios of C1/Peak, C1 being the aliphatic carbon peak. Comparison between experimental and stoichiometrically calculated intramolecular ratios, measured using non-monochromatic X-rays (Sigma2 Probe).

Molecule	Element	Peak	Binding energy [eV]	FWHM [eV]	Assignment (stoichiometry)	Area [†] relative to C1
DDP04	Carbon (1s)	C1	285.0 ± 0.2	1.6 ± 0.1	CH ₂ (1)	1.0 ± 0.0
		C2	286.8 ± 0.2	=FWHM(C1)	C-O-P (11)	11.5 ± 0.2
	Oxygen (1s)	O1	530.2 ± 0.2	1.5 ± 0.1	TiO ₂	0.6 ± 0.1
		O2	531.1 ± 0.2	=FWHM(O1)	C=O, P=O, Ti-O-P (3.3)	3.0 ± 0.2
	Phosphorus (2p)	O3	532.6 ± 0.2	=FWHM(O1)	C-O (11)	6.0 ± 0.1
			135.1 ± 0.1	2.1 ± 0.2	PO ₄ (11)	11.6 ± 0.4
OH-DDP04	Carbon (1s)	C1	285.0 ± 0.2	1.6 ± 0.1	CH ₂ (1)	1.0 ± 0.0
		C2	286.9 ± 0.2	=FWHM(C1)	C-O, C-O-P (5)	6.6 ± 0.3
	Oxygen (1s)	O1	529.9 ± 0.2	1.5 ± 0.1	TiO ₂	0.5 ± 0.1
		O2	530.9 ± 0.2	=FWHM(O1)	C=O, P=O, Ti-O-P (3.3)	3.2 ± 0.6
	Phosphorus (2p)	O3	532.6 ± 0.2	=FWHM(O1)	C-O (5)	5.5 ± 0.3
			133.9 ± 0.2	2.1 ± 0.2	PO ₄ (10)	12.6 ± 0.9
COOH-UDDP04	Carbon (1s)	C1	285.0 ± 0.2	1.6 ± 0.1	CH ₂ (1)	1.0 ± 0.0
		C2	286.8 ± 0.2	=FWHM(C1)	C-O, C-O-P, C-COOH (3)	6.1 ± 1.1
	Oxygen (1s)	C3	289.0 ± 0.2	=FWHM(C1)	COOH (8)	17.9 ± 1.7
		O1	530.0 ± 0.2	1.5 ± 0.1	TiO ₂	0.4 ± 0.1
	Phosphorus (2p)	O2	531.2 ± 0.2	=FWHM(O1)	C=O, P=O, Ti-O-P (2.5)	2.0 ± 0.6
		O3	532.7 ± 0.2	=FWHM(O1)	C-O (10)	2.6 ± 0.3
Phosphorus (2p)		133.8 ± 0.2	2.1 ± 0.2	PO ₄ (10)	10.9 ± 0.9	

[†]R.S.F. corrected

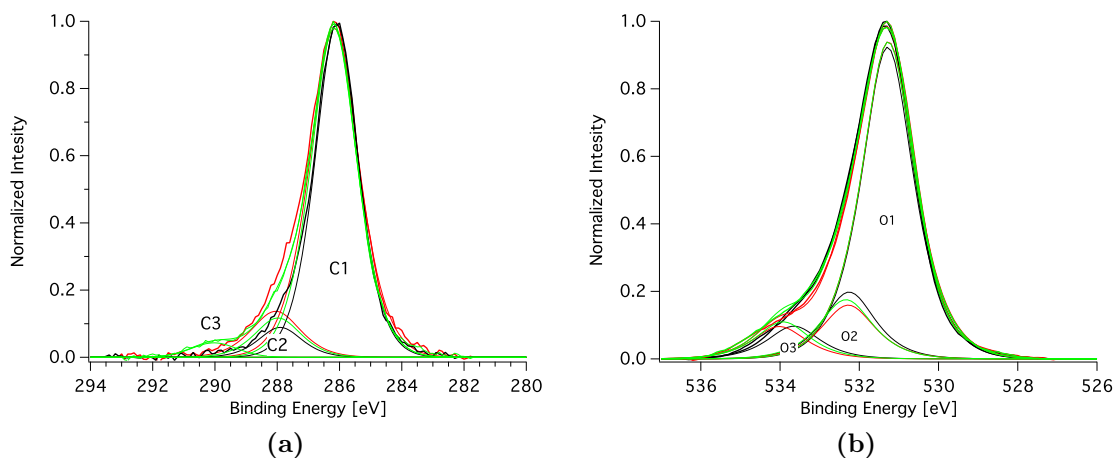


Figure 4.25: Normalized XP spectra of DDPO4 (black), OH-DDPO4 (red) and COOH-UDPO4 (green) adsorbed on TiO₂: (a) carbon 1s, (b) oxygen.

4.4 Conclusion

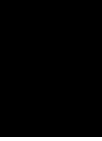
Self-assembled monolayers (SAMs) of catchol derivatives (from aqueous solution), alkyl phosphates (from aqueous solutions and mixtures of organic solvents), and poly(L-lysine)-based copolymers (from buffer solutions) could be fabricated on metal oxide substrates (TiO₂ and Nb₂O₅). Surface coverage was determined by XPS (chemical composition of surface adlayers) and VASE (thickness of surface adlayers) measurements.

SAMs of perfluoro-alkyl nitrodopamine (PFAND) on TiO₂ render the surface hydrophobic. Static water contact angles of $105 \pm 2^\circ$ and dynamic water contact angles of $110 \pm 3^\circ$ (advancing) and $75 \pm 5^\circ$ (receding) were measured on 1.3 nm (1.7 nm with VASE data corrections based on the assumption of contamination replacement during adsorption) thick full coverage adlayers. Surfaces fully covered with nitrodopamine (ND) yielded water contact angles $< 10^\circ$. SAMs of alkyl-phosphates (dodecyl alkyl phosphate, DDPO4) yielded incomplete SAMs (≈ 1.1 nm thickness) when adsorbed from a 2-propanol (0.8 vol.%) n-heptane (99.2 vol.%) mixture. The ammonium salt derivatives of DDPO4 ω -functionalized with -CH₃, -OH, -COOH namely DDPO4(NH₄)₂, OH-DDPO4(NH₄)₂, and COOH-UDPO4(NH₄)₂ adsorbed from water yielded dense SAMs (1.6 - 1.7 nm adlayers thickness) with static wa-

ter contact angle of $101^\circ \pm 2^\circ$, (DDPO4), $52^\circ \pm 2^\circ$ (OH-DDPO4), and $63^\circ \pm 3^\circ$ (COOH-UDPO4). 2 types of PLL-*g*-PEG and of PLL-*g*-PMOXA formed adlayers with thicknesses of 1.3 ± 0.1 nm for a “short” PEG (PEG2), 2.4 ± 0.2 nm for a “long” PEG (PEG5), 2.1 ± 0.2 nm for a “short” PMOXA (PMOXA4), 2.4 ± 0.1 nm for a “long” PMOXA (PMOXA8).

Degradation studies of the catechol derivatives and the PLL-based polymers revealed that PFAND, PLL-*g*-PEG, PLL-*g*-PMOXA SAMs on TiO₂ and Nb₂O₅ can be completely removed with deep UV (450 W, medium pressure Hg-arc lamp with peaks at 254 nm and 365 nm) in a matter of hours (samples placed at a distance of 10 cm from the light sources). (non-monochromatic) X-radiation was found to degrade SAMs of PFAND, PLL-*g*-PEG, PLL-*g*-PMOXA on TiO₂ and Nb₂O₅. Such degradation has to be considered when performing XPS measurements.

CHAPTER 5



Surface-chemical gradients by
immersion

Change in all things is sweet.

Aristotle

Homogeneous surface functionalizations with SAM-based chemistries, comparable to those presented in the previous chapter, have been performed with silanes on silicon and silicon dioxide [52, 127, 143, 259], thiols on gold [49, 50, 150, 151, 155, 161, 163, 204], and phosph(on)ates on metal oxides such as Al_2O_3 [25, 172, 260–262], Ta_2O_5 [51, 167], and TiO_2 [25, 26, 51, 122, 124]. In particular, hydrophobic surfaces were fabricated by using CH_3 -terminated alkyls [50, 155, 156, 177, 226, 263, 264] and CF_3 -terminated perfluoro-alkyls [44, 155, 156, 197] of different chain lengths. Alkyls with $-\text{NH}_2$, $-\text{OH}$ or $-\text{COOH}$ as their functional group are (more) hydrophilic. The ω -termination of alkyl SAM molecules determines the degree of hydrophobicity. It must be noted that the hydrophobicity of a SAM also depends on intermolecular order within a SAM, surface coverage, and alkyl chain length. Similar systems must thus be treated with care when conducting comparisons because even SAMs of the same type of molecule can give different adlayer qualities when formed on different substrates and may thus exhibit different water contact angles (CA). [53, 226] Usually, water contact angles and surface coverage correlate, which means that lower (submonolayer) coverage leads to smaller CAs (for hydrophobic SAM molecules on hydrophilic substrates since clean metal oxide surfaces are usually hydrophilic). It is also possible to create mixed adlayers of, for example, hydrophilic and hydrophobic SAM molecules. The resulting degree of hydrophobicity of such surfaces can be tailored to a value between those of full SAMs of either of the two molecular types by adjusting the ratio of their adsorbed amounts on the surface. Such mixed functionalization can be done either homogeneously across a surface (effective functionalization and thus the CA are the same everywhere) or in the form of a gradient (effective functionalization and CA vary along the surface). Several techniques have been used to create such surface-chemical gradients, e.g. for functional thiols on gold [18, 20, 28, 265] and silanes on silicon/silicon dioxide [14, 19, 205, 266].

Some of the techniques are based on controlling the molecular adsorption kinetics during SAM formation. Thus, much research has been directed at understanding the mechanisms and kinetics during molecular adsorption and layer formation. Several mathematical formulations based on diffusion kinetics as well as adsorption and desorption probabilities have been created to describe monolayer formation. One of the first attempts was that by Langmuir for oil films on water. [267] He described an equilibrium state of the interface of the two substances for the static case of

finished film formation. [267] For the dynamic case of adsorption, quasi-equilibrium assumptions are made and time dependent formulations for the surface coverage θ at any given point in time t are deduced. The result is the classical Langmuir-type adsorption kinetics, [268] which can be written:

$$\theta(t) = (1 - e^{-k_A t^a}) \quad (5.1)$$

where θ describes surface coverage as a function of exposure time t . k_A is the effective adsorption rate (constant, in the case of a classical Langmuir isotherm) which can be influenced by a variety of factors including the substrate, solvents, concentration, and temperature. a is usually set to 1 if there is no diffusion limit, or 0.5 for a diffusion-limited model. [261] Equation 5.1 can be rewritten for adlayer thickness $D(t)$ as a function of time with $D_{ML} = D(\infty)$ as the maximum achievable layer thickness:

$$D(t) = D_{ML}(1 - e^{-k_A t^a}) \quad (5.2)$$

With a possibly being different from 1, k_A can have physically unrealistic units ($M^{-1}s^{-a}$) since the exponent must not have any unit. Equations 5.1 and 5.2 can be rewritten to:

$$\theta(t) = (1 - e^{-(k_A t^a)}) \quad (5.3)$$

and

$$D(t) = D_{ML}(1 - e^{-(k_A t^a)}) \quad (5.4)$$

The formulation of Langmuir-type adsorption implies three assumptions of the interaction between SAM molecules and the surface:

1. adlayer thickness is limited to a monolayer coverage ($\theta \leq 1$)
2. all surface sites are similar
3. there is no interaction taking place with already adsorbed molecules

In a number of cases not all of these conditions are fulfilled. Assumption 1. commonly holds true for simple alkyl phosphates but should be (experimentally) verified as there

have been reports of multilayer formation of phosphate-based SAM molecules. [269] It is unlikely that 2. holds for amorphous substrates and there will also be interaction with already adsorbed molecules (meaning 3. might also be violated). For very low concentrations and short adsorption times 3. can be expected to hold better than for higher concentrations and longer immersion times because slower initial adsorption implies fewer SAM molecules already present. Because of these issues, Dannenberger et al. proposed a modified Langmuir model (for the case of alkyl thiols on gold):

$$\theta(t) = \frac{e^{(1+k_S)ck_A t} - 1}{e^{(1+k_S)ck_A t} + k_S} \quad (5.5)$$

with its equivalent to Equation 5.2:

$$D(t) = D_{ML} \frac{e^{(1+k_S)k_A t} - 1}{e^{(1+k_S)k_A t} + k_S} \quad (5.6)$$

where k_S , additionally to the parameters already given in Equation 5.1, describes adsorption sites within already existing alkanethiol islands.

Morgenthaler [243] investigated both models to describe adsorption kinetics for thiols on gold. She bases her argumentation on the work by Dannenberger et al. [270] for thiols on gold and concludes that thiol adsorption kinetics can be fitted with both functions with the modified model (Equations 5.5 and 5.6) yielding better fits. Koutsioubas et al. [261] made the case for alkyl phosphonic acids from ethanol solution on alumina. They elaborated that initial SAM formation of their alkyls of different lengths from ethanol solution on alumina follow a first order Langmuir kinetic model (Equation 5.1) initially and then second order Langmuir kinetics (Equation 5.7) for longer immersion times: [261]

$$D(t) = D_{ML}(1 - (1 + k_A t)^{-1}) \quad (5.7)$$

where $D(t)$ is the adsorption time dependent adlayer thickness, D_{ML} its maximum value, and k_A the adsorption rate constant. The authors also pointed out that maximum achievable thickness D_{ML} depends on solution concentration and solvent.

If a chosen SAM-substrate system follows the kinetics given by Equations 5.1-5.7, one can easily achieve gradient formation by spatially controlling the molecular adsorption according to the appropriate equation. The two parameters which deter-

mine surface coverage during adsorption, concentration c and time t can be freely adjusted exogenously, as can be seen from Equations 5.1, 5.5, and 5.7.

Morgenthaler introduced a simple dip-and-rinse technique, linear motion drive immersion (LMD), where the solution concentration c is kept constant and the exposure time is varied by controlled and gradual immersion of the substrate. [18,28,243] She described how to utilize adsorption kinetics to fabricate two-component (hydrophobicity) gradients for the case of thiols on gold. Within this thesis, the same approach was chosen to generate surface-chemical gradients with the LMD technique on metal oxides, in particular with phosphate and catechol derivatives as functional SAM molecules. Homogeneous adlayers were discussed in Chapter 4. This chapter describes the fabrication of surface-chemical (hydrophobicity) gradients on TiO_2 substrates by controlled adsorption of catechol- and phosphate-based SAM molecules. On the one hand, presented results introduce both kinds of molecules as valid “gradient chemistries” by investigating their adsorption kinetics. On the other hand, it is demonstrated how the LMD technique can be used with phosphate and catechol chemistries to fabricate cm-long hydrophobicity gradients.

The kinetics of the particular molecules (perfluoro-alkyl nitrodopamine (PFAND), nitrodopamine (ND), dodecyl phosphate (DDPO4), and the phosphate’s ammonium salt $\text{DDPO}_4(\text{NH}_4)_2$) on TiO_2 substrates were determined for different concentrations and solvents. Subsequently, appropriate LMD immersion programs were designed based on fits to the data. Gradients were then fabricated by controlled gradual immersion of $1 \times 4 \text{ cm}^2$ TiO_2 substrates into suitable adsorbate solutions. Altogether, the (linear motion drive) LMD technique of Morgenthaler et al. [18] was adapted by adjusting concentrations, solvents, rinsing procedures, and immersion protocols.

All surfaces were examined with X-ray photoelectron spectroscopy (XPS), variable angle spectroscopic ellipsometry (VASE), and static water contact angle (sCA) measurements.

5.1 Catechol-based

Adsorption kinetics of PFAND (perfluoro-alkyl nitrodopamine) and ND (nitrodopamine) on TiO_2 substrates from their respective solutions were determined from VASE and

XPS data. Static water contact angles were also measured to correlate adlayer thickness and wettability. An LMD immersion program derived from the kinetics of PFAND (ND did not yield reproducible results) was designed and used to fabricate PFAND one-component gradients on $1 \times 4 \text{ cm}^2$ TiO_2 substrates with LMD. All gradient samples were analyzed with XPS, VASE, and sCA. One-component gradients were backfilled with ND to yield two-component gradients. Such gradients were immersed in ultra pure water for 15 hours to test stability in aqueous solutions. Two-component gradient samples were measured before or after water exposure, again with XPS, VASE, and sCA.

5.1.1 PFAND and ND self-assembly kinetics

In order to be able to apply the LMD gradient-deposition protocol, it is required to study and control the kinetics of molecular adsorption. Therefore, it was necessary to determine a concentration that would yield good coverage (with high sCAs, $> 90^\circ$) within several minutes while after a few seconds of immersion coverage would be low enough to obtain low sCAs ($< 30^\circ$). In this way, gradients would be practicably achievable on a scale of a few centimeters. In the case of PFAND dissolved in 1:2 2-propanol: H_2O , clean $1 \times 1 \text{ cm}^2$ TiO_2 substrates were immersed for different times (1 min - 1 day) into solutions of different concentrations (7 - 220 μM). The dependence of surface coverage on assembly time as well as on solution concentration, with standard deviations below 10%, is clearly visible in Figures 5.1 and 5.2. While for a concentration of 7 μM the layer thickness shows no time dependence, values of concentration in the range of 44 μM - 220 μM were deemed suitable for the fabrication of gradients by LMD. XPS data (Figure 5.2b) for the N/Ti and F/Ti ratios of submonolayers confirm the (logarithmic) trend observed by ellipsometry (Figure 5.2a) measured for PFAND layers after different immersion times. The data indicate the presence of about 100% more adsorbed molecules after 1 hour than after 1 min (see Figure 5.2b).

VASE data for PFAND adsorption kinetics on TiO_2 were fit with Equations 5.1 - 5.7. Fits are shown in Figures 5.1 and 5.2. Figure 5.1a shows fits with the first-order Langmuir model (Equation 5.2) using standard deviations for weighting (dashed lines). The exponential parameter is fitted as well to determine how well the

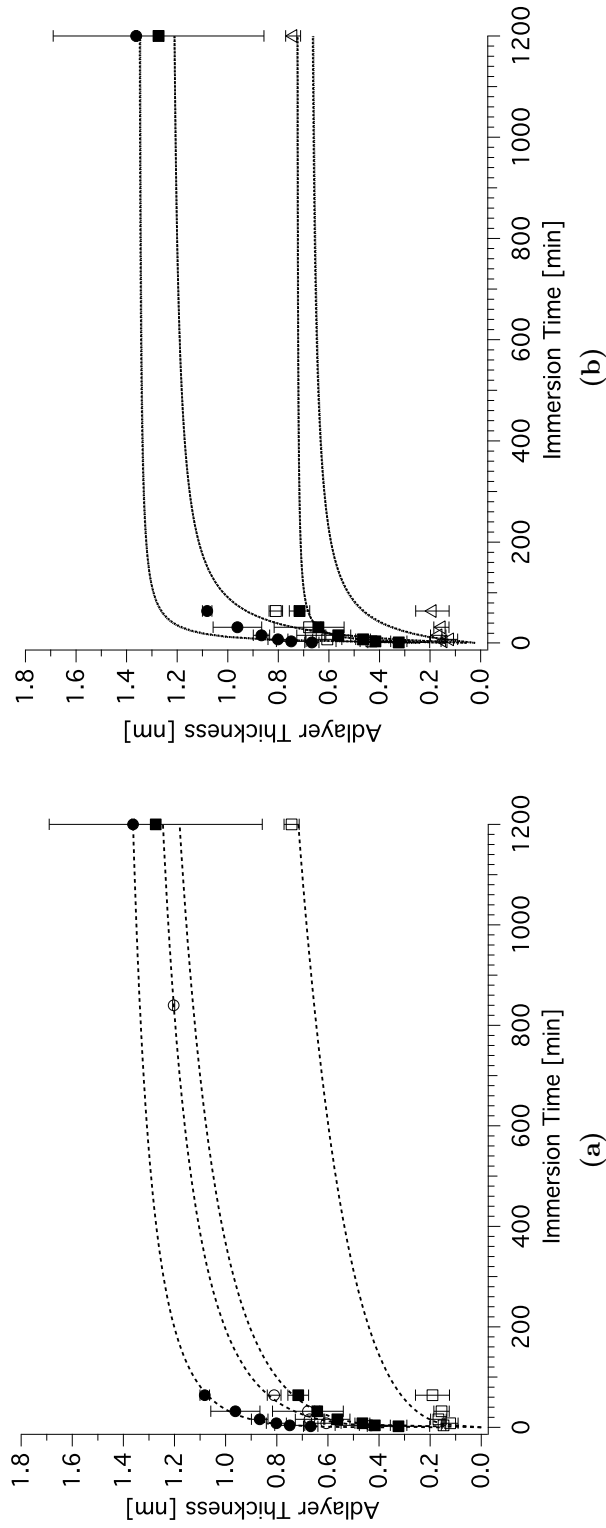


Figure 5.1: Plot of adsorption kinetics of PFAND from 1:2 2-propanol:H₂O, concentrations: 220 μM (\bullet), 110 μM (\circ), 44 μM (\blacksquare), 7 μM (\square). The higher the concentration, the higher the adsorption rate and the higher the "initial coverage" at the short immersion times: a) Fits are Langmuir-type adsorption kinetics (Equation 5.2). b) Fits are from second order (Equation 5.7) and modified (Equation 5.5) Langmuir model.

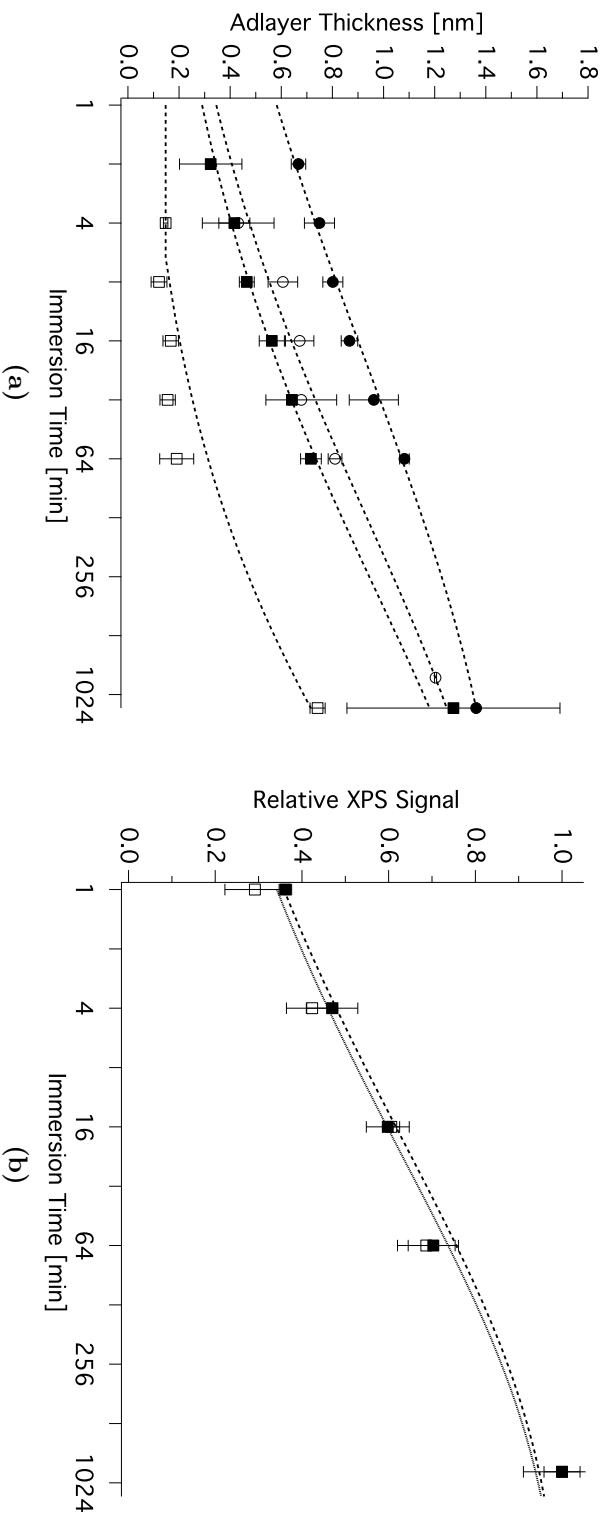


Figure 5.2: Logarithmic plot of adsorption kinetics of PFAND from 1:2 2-propanol:H₂O, concentrations: 220 μM (\bullet), 110 μM (\circ), 44 μM (\blacksquare), 7 μM (\square). The higher the concentration, the higher the adsorption rate and the higher the "initial coverage" at the short immersion times. 220 μM was determined as an ideal concentration for making gradients. Logarithmic plot of normalized F/Ti (\square) and N/Ti (\blacksquare) XPS ratios for PFAND monolayers adsorbed from 220 μM 1:2 2-propanol:H₂O. Time dependence is in agreement with that of the measured surface coverage. Dashed (VASE and N/Ti) and dotted (F/Ti) lines are fits with Equations 5.2 (a) and 5.1 (b) and for eye guidance only (see Table 5.1 for parameter values).

Table 5.1: Fit parameters for PFAND adsorption kinetics on TiO₂ using Langmuir model (Equation 5.2 and 5.4).

c [μM]	D_{ML} [nm]	k_A [min^{-a}]	k_B [min^{-1}]	a
220	1.49 ± 0.05	0.496 ± 0.014	0.0451 ± 0.0013	0.226 ± 0.018
110	1.49 ± 0.18	0.264 ± 0.031	0.0135 ± 0.0011	0.272 ± 0.089
44	1.56 ± 0.68	0.206 ± 0.091	0.0030 ± 0.0013	0.272 ± 0.042
7*	1.6 ± 16.3	0.053447 ± 584	0.0002 ± 2.2	0.34368 ± 137
220, N/Ti	1	0.444 ± 0.022	0.0538 ± 0.0028	0.278 ± 0.027
220, F/Ti	1	0.419 ± 0.069	0.0442 ± 0.0072	0.279 ± 0.058

*7 μM (and concentrations below) solutions demonstrate no reasonable adsorption behavior and are only included for completeness

data can be described by classical or diffusion limited Langmuir models. The model produces good fits for all concentrations. Values of the fit parameters are presented in Table 5.1 for VASE and XPS data. Errors are extreme for parameter values of in the case of 7 μM because adlayer formation does not proceed efficiently. One can see that with increasing concentration c :

- D_{ML} is in the range of 1.5 ± 0.1 nm.
- k_A is of the same order of magnitude. Good agreement between VASE and XPS N/Ti and F/Ti data.
- a is in the range of 0.25 ± 0.03 .

The observation that D_{ML} calculates to about 1.5 nm (1.3 nm is the thickness of a monolayer as determined by VASE) for concentrations higher than 7 μM indicates that these concentrations are suitable to obtain full monolayers (given sufficiently long immersion times). a having a value of 1/4 indicates a deviation from classic theory, according to which $a = 1$ is expected leading to linear contribution of time to the exponential term (for systems not limited by diffusion). For diffusion limited systems $a = 0.5$ is given in some studies. [261,270] The case of $a = 1$ is derived from the assumption that

$$\frac{d\theta}{dt} = 1 - \theta \quad (5.8)$$

Evidently this assumption does not hold. The reasons for this can be manifold:

- Catechols can form different types of bonds with TiO_2 surfaces, in contrast to thiols (on gold or silver) or silanes on silicon surfaces. It is reasonable to assume that the different bonds have different strengths and different adsorption/desorption rates. Such an effect would be even more pronounced on amorphous TiO_2 substrates.
- The desorption rate is not only governed by the binding strength of the molecules to the surface but also the solvent. It was observed that PFAND could not be dissolved in the 2:1 H_2O :2-propanol mixture (it has to be dissolved in 2-propanol first and then diluted with H_2O). Hence, sorption kinetics might not be easily described by a linear combination of adsorption and desorption rate constants.
- Catechols, being aromatic compounds, and especially in conjunction with a perfluoro-alkyl (being an amphiphile), are more complex in their interaction with surfaces and other molecules than (comparable) thiols, silanes, or phosph(on)ates.
- Mixed solvents might influence the conformation and intramolecular interaction of dissolved molecules in solution. Furthermore, adsorbing a hydrophobic adlayer against an aqueous (mixed with an organic) solvent could change adsorption kinetics dynamically. It was observed that increased PFAND surface coverage was accompanied by “2-propanol-phobicity” (only observed qualitatively).
- TiO_2 in contrast to other substrates, for example gold (with thiols as the SAM system), always displays a contamination layer when handled in a normal laboratory environment. The molecular-exchange-adsorption-desorption reactions occurring during SAM formation might thus be considerably more complicated (than for thiols on gold).

Nonetheless, the kinetics follow straight lines on a logarithmic scale (Figure 5.2) and should thus be suitable for LMD using a logarithmic-time-dependent immersion protocol.

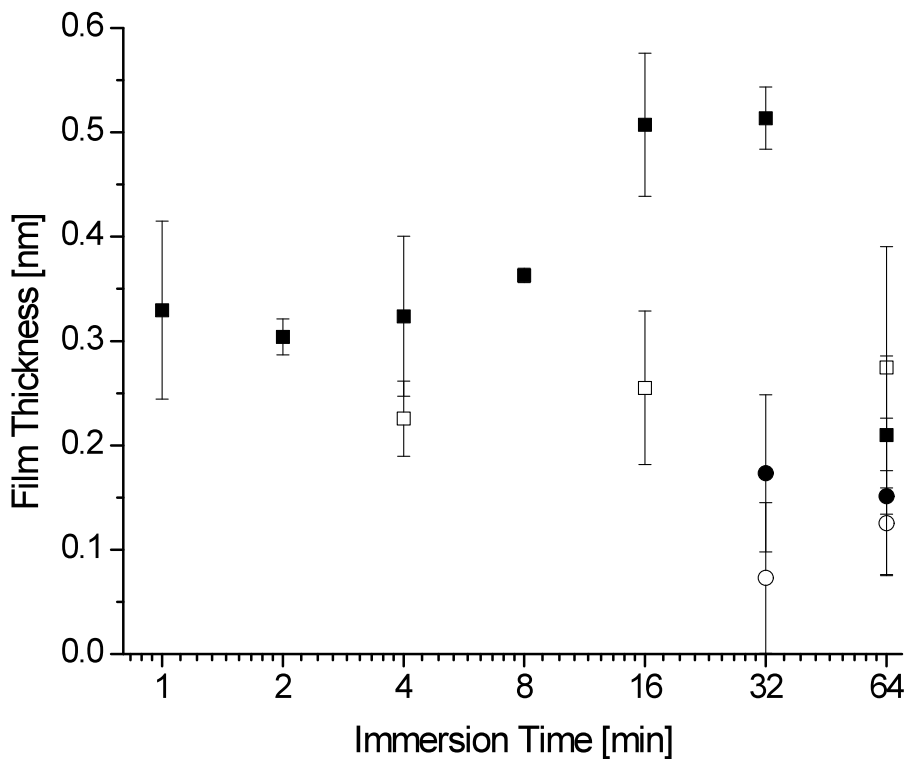


Figure 5.3: Logarithmic plot of adsorption kinetics of ND from H_2O , measured with VASE, concentration: 500 μM (■), 50 μM (□), 5 μM (●), 1 μM (○). No general time dependence is observable.

Figure 5.3 shows the adsorption kinetics of ND on TiO_2 , as determined by VASE. In the case of ND, solutions with concentrations below 10 μM yielded coverages comparable to contamination levels. Higher solution concentrations result in higher coverage. It was not possible to establish a clear dependence between adsorption time and adlayer thickness. The highest thickness measured was about 0.5 nm (48 hours in 500 μM ND) but substantial standard deviations of up to 20% have been recorded

(Figure 5.3), likely due to the hydrophilic nature of ND (static water contact angle $< 10^\circ$, see Table 4.1) resulting in varying degrees of wetting and contamination under ambient laboratory conditions but also due to the resolution of the VASE instrument (± 0.1 nm). High fluctuations in detected layer thickness suggest that ND would not be a good choice as a first component for LMD-fabricated gradients. For backfilling, as described later on, this does not pose a problem, since all surfaces are ultimately completely covered by catechols of either hydrophobic and hydrophilic type.

5.1.2 PFAND and PFAND-ND gradients on TiO_2

PFAND follows Langmuir-type adsorption kinetics when adsorbed onto TiO_2 which can be approximated well with a straight line in a logarithmic plot (see Figure 5.2). Hence, the immersion protocol for 1×4 cm² TiO_2 substrates was adapted to a logarithmic z-position-vs-time program (see Figure 5.4) based on XPS and VASE data shown in Figure 5.2. Bare substrates were thus immersed in PFAND solution in a controlled manner. The following parameters were chosen for the preparation of gradient samples:

1. concentration of PFAND: 220 μM .
2. immersion time at high-coverage end: 1 hour, low coverage end: 4 seconds.
3. logarithmic immersion depth vs. time dependence.
4. immediate sonication of samples for 3 min in 2-propanol after gradual immersion, followed by blow-drying with N_2 gas.
5. Backfilling was carried out by immersing one-component PFAND gradients in ND (500 μM in ultra pure water) solution for one hour, followed by thorough rinsing with ultra pure water blow-drying with nitrogen.

The gradients in surface coverage can be detected by measuring film thickness (VASE), as well as F/Ti and N/Ti XPS signal ratios. While PFAND forms hydrophobic layers, ND results in an amine-terminated hydrophilic surface. Thus, water contact angles should also show gradients in hydrophobicity. The extreme ends of the gradients were tested in the form of homogeneous samples (Table 5.2) with

Table 5.2: Apparent atomic % (at.-%) of mixed PFAND (220 μM) vs. ND (500 μM) layers on TiO_2 as determined by XPS, film thickness as determined using VASE and static water contact angles (sCA).

Sample	XPS apparent at.-% for layers on TiO_2					VASE d [nm]	sCA [°]
	C 1s	N 1s	O 1s	F 1s	Ti 2p		
Clean TiO_2	6.9	0.4	65.5	0.0	27.2	0.0	<10
PFAND 1 h	15.0	1.2	45.8	18.6	19.4	1.1 ± 0.1	90 ± 2
ND 1 h	12.2	1.9	61.4	0.0	24.4	0.4 ± 0.1	<10
PFAND 1 h + ND 1 h	17.7	1.9	49.9	10.7	19.8	1.0 ± 0.1	82 ± 2

different coating steps – different timings and combinations of PFAND adsorption followed by ND backfilling.

Table 5.3: Linear-motion drive immersion program to generate PFAND gradients (from 220 μM solution).

Δt [s]	Δd [mm]
2	-1
1860	-4
900	-4
440	-5
200	-5
100	-5
40	-5
20	-5
4	-5
30	60

It must be noted that ND adsorbs onto and possibly even partially replaces PFAND adlayers, especially for incomplete PFAND monolayers, resulting in higher nitrogen (+60%) and lower fluorine (-40%) apparent at.-% for mixed layers, as outlined in Table 5.2. Such replacement is also observed for gradients, but can readily be compensated for during the fabrication process if deemed necessary.

Figure 5.6 and 5.5 present the film thickness (VASE), relative F/Ti ratio and N/Ti ratio (XPS) and static water contact angles of the gradients immersed in 220 μM PFAND solution, before and after backfilling, as determined by VASE, sCA, and

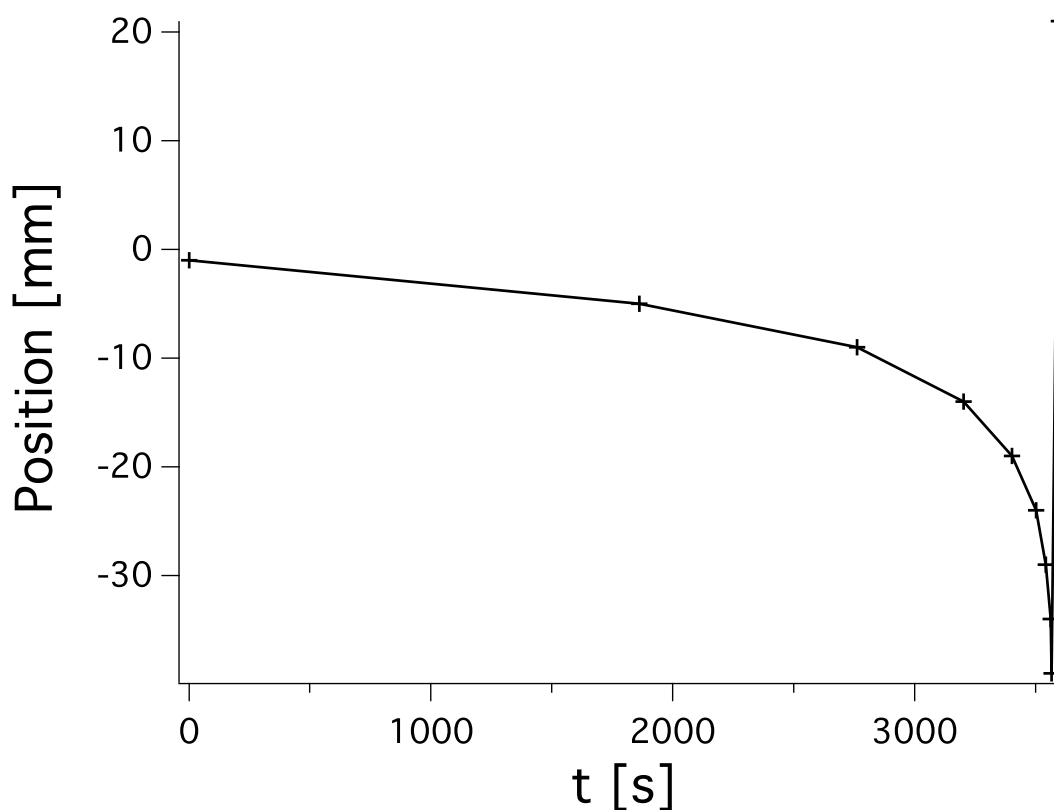


Figure 5.4: Position of substrate relative to PFAND solution – air interface as function of time during one-component gradient fabrication.

XPS. A surface-coverage gradient going from one end to the other end of the sample is observable in all cases. Before backfilling, the measured layer thickness varies in a linear manner by a factor of 7 from 0.15 nm to 1.05 nm (Figure 5.6a). Similar changes and position dependencies are observed for the F/Ti (Figure 5.5a) and N/Ti (Figure 5.5b) ratios measured for the same gradients while contact angles range from 35° to 95° (Figure 5.6b).

After backfilling the gradients with ND for 1 hour, the total surface coverage levels out to be almost homogeneous, with the lower-coverage end of PFAND being about 15% of the high-coverage end. Standard deviation becomes noticeably higher along the whole sample (up to 20%). The same observations hold true for the N/Ti ratio (Figure 5.5b). Additionally, the data show that the N/Ti signal of backfilled gradients is at least 50% higher than the one-component ones, meaning that there

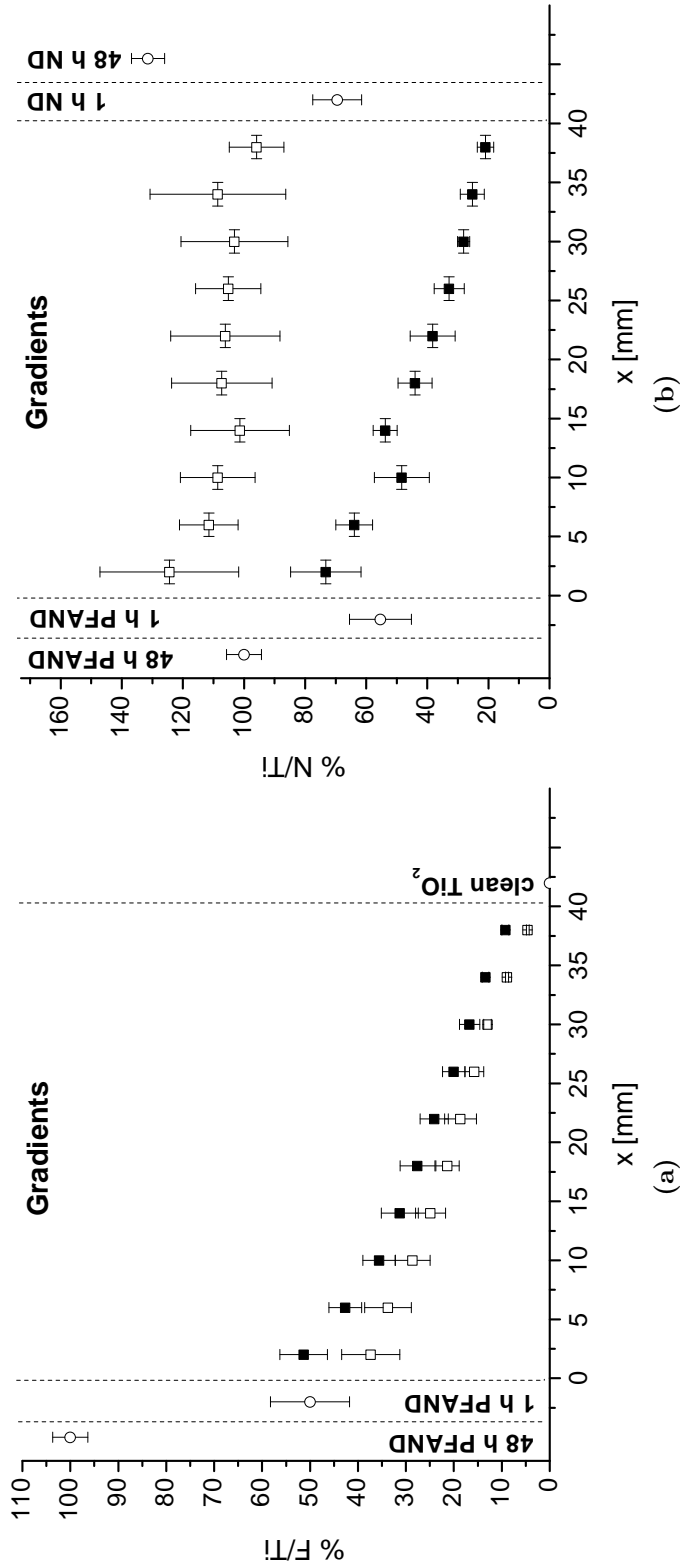


Figure 5.5: a) F/Ti XPS ratios for homogeneous PFAND layers (○) and gradients (■) and PFAND-ND (□) gradients normalized to 48h homogeneous layer. Dependence is linear, as for VASE, along immersion direction. High-PFAND-coverage end (left), and low-coverage end (right) differ by a factor of 5. b) Relative N/Ti XPS ratios for homogeneous PFAND and ND layers (○), PFAND (■) and PFAND-ND (□) gradients. Dependence is linear, as for VASE, along immersion direction. High-PFAND-coverage end (left), and low-coverage end (right) differ by a factor of about 4 for one-component gradients. Two-component gradients show a more homogeneous N/Ti ratio.

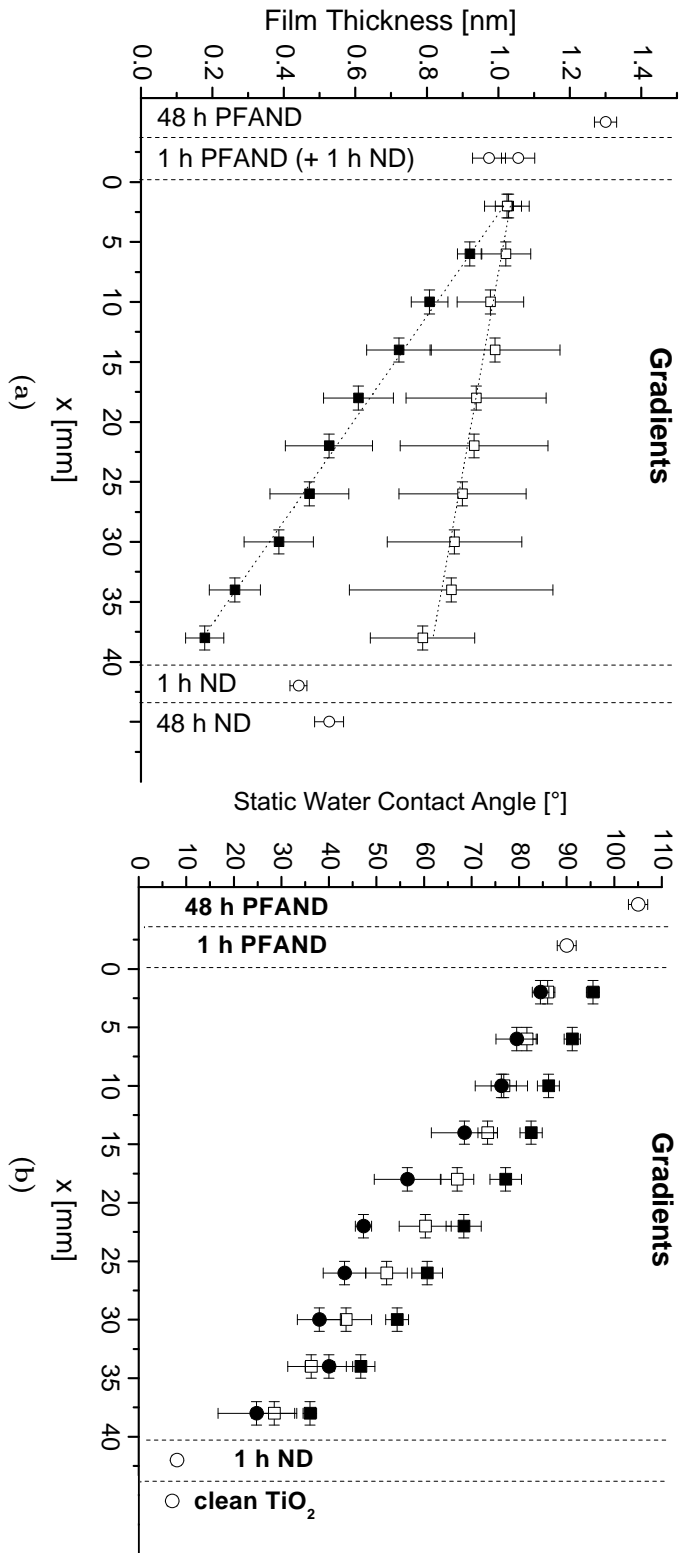


Figure 5.6: a) Film thickness (ellipsometry) depends linearly (dotted lines are linear fits to the data sets) on the position along the PFAND one-component gradient (■). ND backfilled gradients (□) exhibit more homogeneous coverage. ND coverage in two-component (difference to one-component) gradient is also linear (●). b) Static water contact angles for PFAND one-component (■), ND backfilled gradients (□), after their additional immersion in H_2O for 14 h (●). Homogeneous samples (○).

is additional ND adsorbed along the whole gradient, also on the higher PFAND coverage side. This also explains why backfilling PFAND gradients with ND causes a reduction of contact angles for the whole gradient by approximately 10° (Figure 5.6b). On the other hand H_2O conditioning for 14 h does not change the sCA-position dependence significantly, suggesting that the backfilled gradients remain stable in water for this time.

The Langmuir-type adsorption kinetics of perfluoro-alkyl nitrodopamine (PFAND) in combination with the linear-motion-drive technique (LMD) allowed one-component surface-coverage gradients to be fabricated, which, once backfilled with ND, yielded catechol-based hydrophobicity gradients on TiO_2 .

The higher surface density of ND versus PFAND adlayers suggests the presence of unoccupied binding sites within PFAND monolayers. This general abundance of adsorption sites and the sub-monolayer state of PFAND one-component gradients can explain the additional adsorption of ND everywhere within the PFAND gradients, as can be observed for VASE (Figure 5.6a) and N/Ti XPS (Figure 5.5b) data.

From VASE (Figure 5.6a) and XPS (Figure 5.5) results one can see that the two-component gradients apparently consist of complete mixed monolayers. In Figure 5.6a, the difference between the one- and two-component gradient is a linear curve ranging from 0.0 nm to about 0.6 nm (not shown), which essentially represents the adsorbed ND (concentration) in the two-component gradient but also includes contamination and potential replacement of PFAND by ND during backfilling. Yet, one has to be aware that up to 10% of PFAND remains (at the lower end of the gradient), as can be seen in Figure 5.5a. Accordingly, the N/Ti ratio, being equally representative for PFAND and ND, in Figure 5.5b almost reaches the ND monolayer level along the gradient (only slightly attenuated by the lower coverage end PFAND density) indicating complete surface coverage by catechols. The high N/Ti ratios vs. the small ND coverage as measured by VASE can be explained by molecular displacement: The sub-monolayers of PFAND might not be stable with respect to substitution. Yet, most likely the abundance in Ti-OH binding sites allows plentiful ND co-adsorption with airborne contamination, impeding an unambiguous interpretation of the obtained data. Steric hindrance of PFAND molecules might impede formation of strong bonds between molecules and substrate. Subsequent backfilling with ND can lead to replacement of PFAND because ND has easier access to the

surface due to its size, which facilitates optimization of bonding, and possible electrostatic interaction of protonated amines with the negatively charged surface. Both XPS and VASE show that PFAND coverage at the opposing low and high PFAND ends of one- and two-component gradients differ by a factor of 5-7. The high-end coverage, as deduced from XPS (F 1s spectra) data, corresponds to only about 50% of maximum coverage (48 h in 440 μM), while VASE yields about 75%. This difference can be explained by high levels of airborne contamination, as is expected for the long time of sample exposure to air (more than 1.5 hours during adsorption and VASE measurements). The process of immersing the clean TiO_2 substrate in a normal lab environment over an hour and the time for performing VASE measurements allows for contamination of one-component gradients (see Section 3.2). Figure 5.7 shows F/C XPS ratios increasing along the gradient towards the high PFAND coverage end implying less carbon originating from airborne contamination. Yet, the PFAND is still about 20%-25% below that of a monolayer (48 h PFAND immersion). Backfilling one-component PFAND gradients with ND replaces this contamination and creates a well-defined surface-chemical composition. The gradient in hydrophobicity is still intact (Figure 5.6b) after backfilling, since PFAND coverage is only slightly influenced (Figure 5.5a) while the whole sample surface is covered by catechols (Figure 5.5b).

5.2 Phosphate-based

Phosphate-based SAMs have proven to be very versatile and powerful to the easy and efficient functionalization of metal oxide surfaces, as commonly found on medical implants. Al_2O_3 , Nb_2O_5 , Ta_2O_5 , and TiO_2 are only a few examples of surfaces that can be rendered hydrophobic [23, 26, 31, 51, 235], protein resistant [108, 271, 272], or opto-electronically sensitive [273] using phosphate groups as anchors for functional molecules. Depending on the field of application, different types of gradients of such functionalities can facilitate for example the study of protein and cellular interaction with surfaces [33, 34, 36, 205, 274, 275] through parallelized surface analysis. Providing a cost-effective and easily reproducible method to produce such gradients is thus important to facilitate and extend phosphate-SAMs-based applications. This

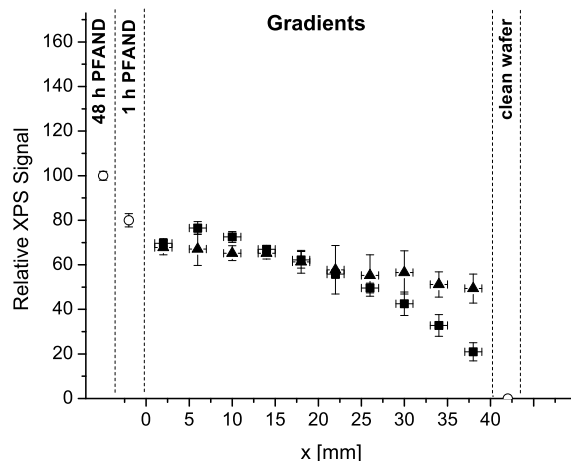


Figure 5.7: Relative XPS signals F/C (■) and F/N of one-component PFAND gradients on TiO_2 in comparison to homogeneous samples (▲) of 48 h PFAND layer and clean wafer. Decrease of F/C ratio indicates increased amount of contamination. High-concentration PFAND end contains also contains carbon which does not belong to the PFAND layer (likely air-borne contamination).

section shows how the adsorption kinetics of dodecyl phosphates (DDPO4) can be used to apply Morgenthaler’s LMD method [18] to fabricate cm-scale one- and two-component hydrophobicity gradients on TiO_2 with phosphate-based SAM molecules. Alkyl phosphates were also chosen because their interaction with surfaces (mainly metal oxides) are well studied and they can be adsorbed from both organic solvents and water. [23, 26, 31, 51, 235] Adsorption of SAMs from aqueous solution is highly preferred for biomedical applications. [23, 26, 51]

The data compiled in this thesis can thus serve to facilitate future works related to phosphate-based surface modification aimed at high-throughput experiments with the help of surface-chemical gradients.

5.2.1 DDPO4 self-assembly kinetics

Adsorption kinetics of $\text{DDPO4}(\text{NH}_4)_2$ (from water) and DDPO4 (from n-heptane:2-propanol (99.2:0.8 vol.%)) and solvent suitability were determined first, to be able to adjust the immersion protocol for the LMD technique to produce the desired

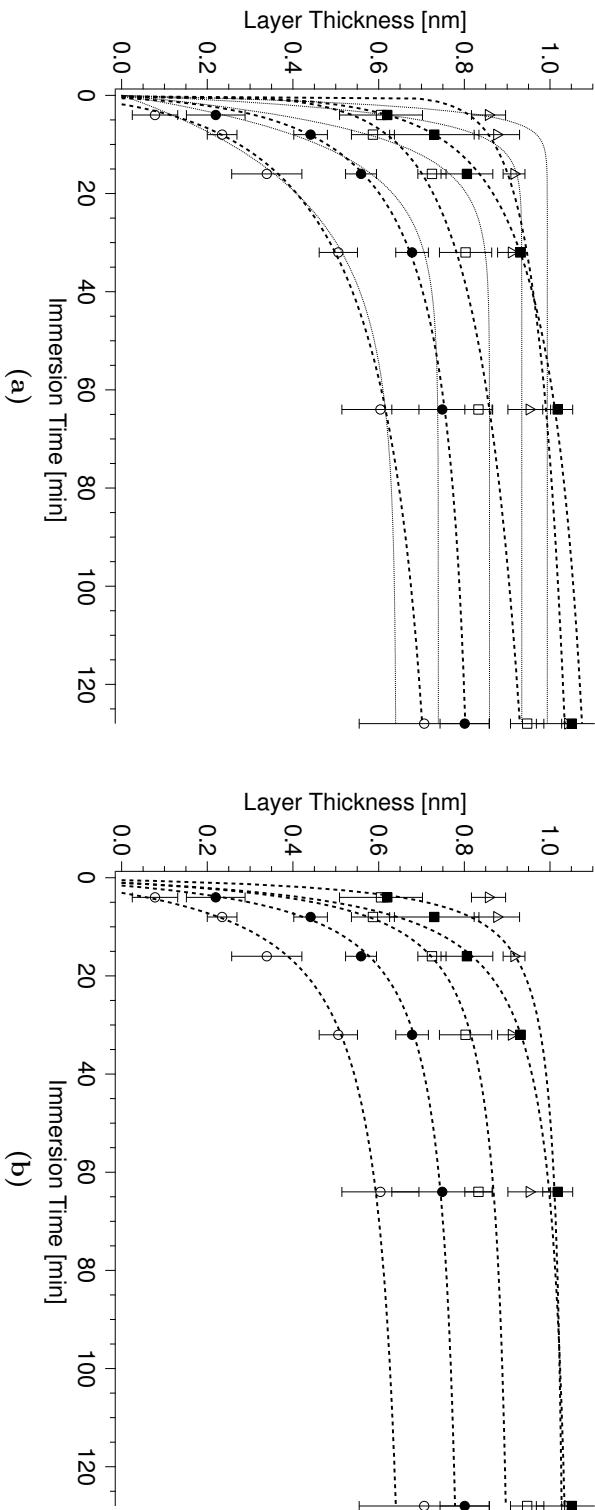


Figure 5.8: Surface adlayer thickness (VASE): adsorption kinetics of 0.5 μM (\circ), 1 μM (\bullet), 10 μM (\square), 50 μM (\blacksquare), and 500 μM (\triangle) DDPO4 solutions in 99.2%:0.8% n-heptane:2-propanol. Lines are for eye guidance: a) Fits are Langmuir-type adsorption kinetics (Equation 5.2). b) Fits are from second order (Equation 5.7) Langmuir model.

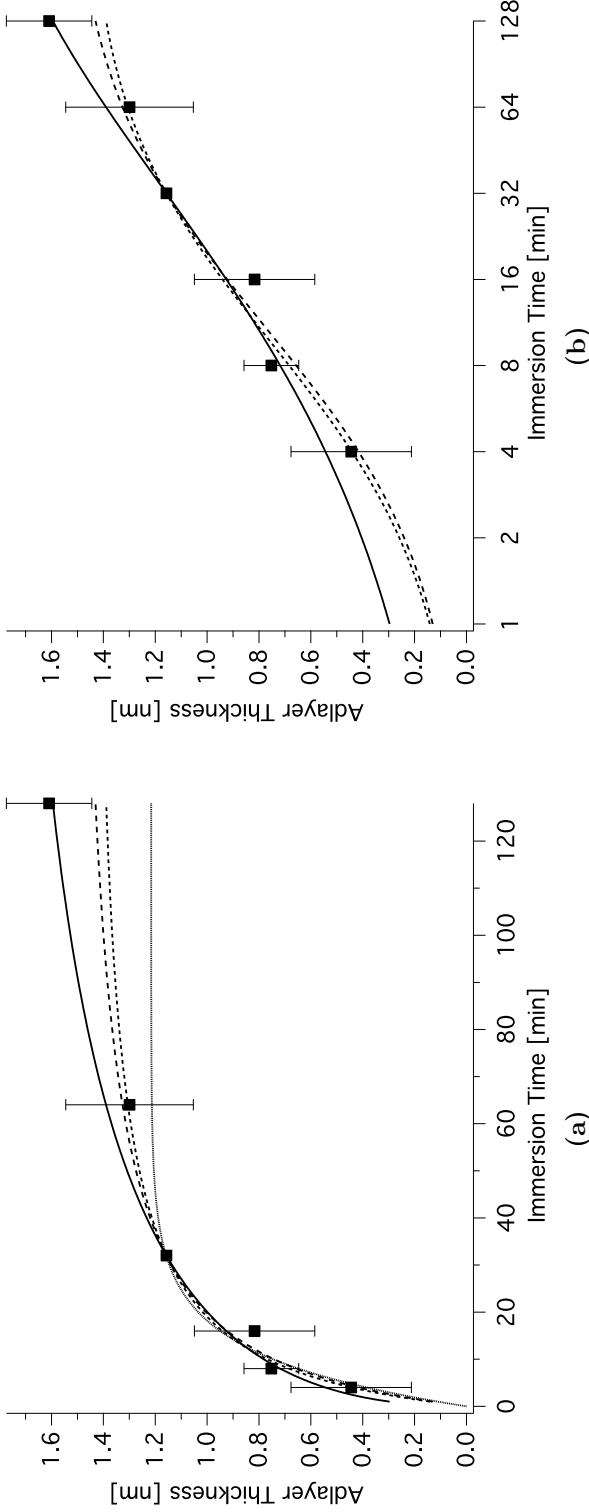


Figure 5.9: Surface adlayer thickness (VASE) for 250 μM (■) DDPO₄(NH₄)₂ dissolved in ultra pure water on linear (a) and logarithmic (b) scale.

Table 5.4: Fit parameters of kinetics of DDPO4 adsorption on TiO₂ using Langmuir model (Equation 5.2)

Langmuir model	c [μM]	D_{ML} [mm]	k_A [min^{-a}]	$k_{A'}$ [min^{-1}]	a	χ^2
first order	500	1.66 ± 5.06	0.61 ± 2.46	$.006 \pm .023$	0.10 ± 0.23	2.59
	50	1.14 ± 0.05	0.471 ± 0.015	0.131 ± 0.001	0.370 ± 0.024	0.35
	10	1.16 ± 0.80	0.439 ± 0.217	0.046 ± 0.019	0.269 ± 0.253	1.89
second order	1	0.79 ± 0.04	0.163 ± 0.043	0.082 ± 0.021	0.727 ± 0.117	0.043
	0.5	0.66 ± 0.08	0.055 ± 0.017	0.047 ± 0.015	0.948 ± 0.149	0.150
	500	$1.34 \pm .016$	0.607 ± 0.134	-	-	8.23
first order*	50	1.37 ± 0.04	0.276 ± 0.085	-	-	1.11
	10	1.23 ± 0.03	0.313 ± 0.064	-	-	2.97
	1	1.11 ± 0.05	0.232 ± 0.050	-	-	0.63
second order	0.5	0.99 ± 0.07	0.141 ± 0.035	-	-	0.64
	500	0.99 ± 0.01	0.461 ± 0.064	$= k_A$	$\cong 1$	31.24
	50	0.93 ± 0.01	0.273 ± 0.004	$= k_A$	$\cong 1$	12.49
first order*	10	0.86 ± 0.02	0.139 ± 0.018	$= k_A$	$\cong 1$	14.04
	1	0.74 ± 0.04	0.097 ± 0.014	$= k_A$	$\cong 1$	3.36
	0.5	0.64 ± 0.08	0.051 ± 0.013	$= k_A$	$\cong 1$	1.21

*fitting was done with first-order-Langmuir model and the restriction of $a=1$.

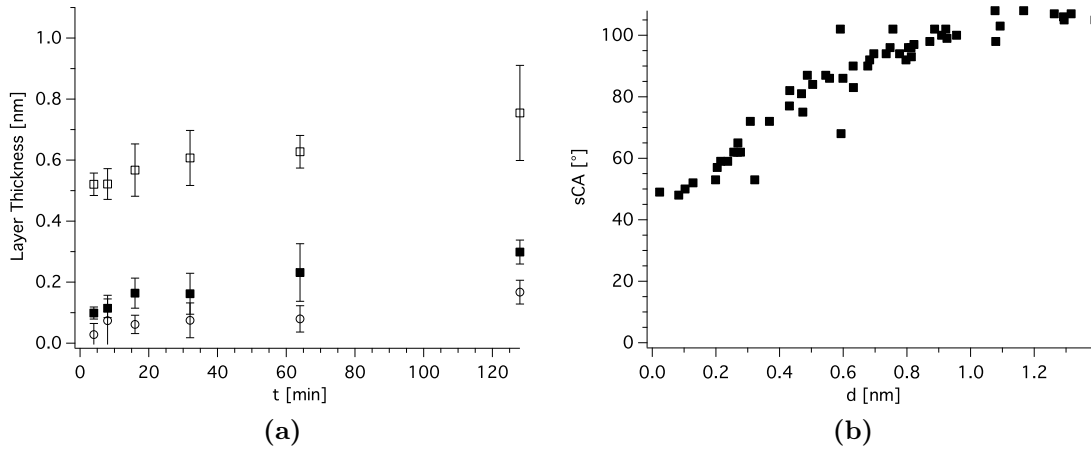


Figure 5.10: a) Surface adlayer thickness (VASE) on clean TiO_2 substrates exposed to n-heptane (\square), rinsed with 2-propanol (\blacksquare) and rinsed with H_2O (\circ). ; b) Static water contact angles correlation with thickness of DDPO4 adlayers on TiO_2 (measured on single samples homogeneously coated from DDPO4 in n-heptane (0.8% 2-propanol) and DDPO4(NH_4)₂ in ultra pure water).

Table 5.5: Fit parameters of kinetics of 250 μM DDPO4(NH_4)₂ adsorption on TiO_2 from water using classical (Equation 5.2), extended (Equation 5.6), and second order (Equation 5.7) Langmuir model. Weighting was done with standard deviations.

Langmuir model	D_{ML} [nm]	k_A [min^{-a}]	a	χ^2
classic	1.87 ± 0.67	0.173 ± 0.062	0.50 ± 0.19	0.65
classic	1.22 ± 0.05	0.095 ± 0.025	$\doteq 1$	7.20
extended*	1.55 ± 23.1	0.097 ± 0.627	-	2.49
second order	1.55 ± 0.14	0.092 ± 0.033	-	2.24

* k_E is -1.0 ± 12.2 and thus a singularity for the fit being responsible for the huge errors.

phosphate-based surface-chemical gradients. Figure 5.8 shows the adsorption kinetics (in adlayer thickness) of DDPO4 on TiO_2 from n-heptane (0.8% 2-propanol) solutions for different concentrations (0.5, 1, 10, and 500 μM) and immersion times (4, 8, 16, 32, 64, 128 min) as assessed by VASE. Samples were completely immersed in 2 ml of solution every time, then rinsed with 2-propanol and ultra pure H_2O , followed by

blow-drying under nitrogen. VASE data for DDPO4 adsorption kinetics on TiO_2 were fitted with Equations 5.1 - 5.7. Figure 5.8a includes plots of fits with the Langmuir model (Equation 5.6) weighted with standard deviations (dotted lines) and without weighting (dashed lines). Both fits appear reasonable and show no significant differences. Figure 5.8b shows the same experimental data but with fits based on the extended (dashed lines, see Equation 5.8b) and the second order (dotted lines, see Equation 5.7) Langmuir models, weighted with standard deviations. In all cases, the models fit well for all concentrations. The values for the fit parameters of the Langmuir model are listed in Table 5.4. It can be seen that with increasing concentration c (from 0.5 μM to 50 μM ; errors for 500 μM solutions are over 300%, meaning that the first-order-Langmuir model cannot describe well adsorption for such high concentrations):

- D_{ML} increases slightly from 0.6 to 1.2 nm (first-order-Langmuir model) and 1.0 to 1.3 (second-order-Langmuir model),
- first-order-Langmuir model: k_A increases by one order of magnitude, $k_{A'}$ remains in the same order of magnitude, second-order-Langmuir model: k_A remains in the same order of magnitude,
- a decreases from 1.0 to 0.4 (first-order-Langmuir model without restriction on a),
- χ^2 (a quantitative measure for the correlation between model (fit) and experimental data) increases, indicating less suitability of the studied models with increasing concentration.

It must be noted that for the case of DDPO4 investigated here, none of the concentrations in the range of 0.5 - 500 μM appears sufficient to generate an adlayer thickness in the range of that of a SAM (1.6 nm) within 1 hour, remaining at least 30% below that value. The data obtained within this work does not suffice to draw a definite conclusion as to why this is the case. Spori et al. made similar observations and argued that short alkyl phosphates form more liquid-like adlayers with less order and more freedom of binding states on the amorphous TiO_2 substrates. Koutsioubas et al. [261], Hauffman et al. [262], and Forget et al. [260] pointed out that adsorption kinetics and total surface coverage are solvent dependent.

A difference in obtainable surface coverage was also observed in this work between the organic solvent mixture and pure water (see below on DDPO4 vs. DDPO4(NH₄)₂). DDPO4 and DDPO4(NH₄)₂ were dissolved in different solvents (2-propanol in n-heptane and water, respectively) because of their different anchor groups: -PO₄H₂ is an acid, -PO₄(NH₄)₂ its corresponding ammonium salt. Hence, direct comparison is not straightforward.

For DDPO4, concentrations feasible for LMD are between 0.5 μM to 10 μM, which would allow the fabrication of surface-chemical gradients in adlayer thickness ranging from 0.1 nm to 1 nm with contact angles from 50° to 100° (see Figure 5.10b). As can be seen from Figure 5.8a, maximum thicknesses and surface coverage along the gradients would be different (as would be the corresponding water contact angles) under otherwise equal conditions (LMD immersion protocol). If gradients on TiO₂ are to be made with n-heptane (with 0.8% 2-propanol) as a solvent for DDPO4, an assessment of (the time dependence of) the contamination brought upon clean substrate surfaces by the pure solvent (n-heptane) itself is mandatory. Figure 5.10a shows measured adlayer thickness (by VASE) on TiO₂ substrates after exposure to pure n-heptane for different amounts of time and subsequent rinsing with 2-propanol and H₂O (followed by nitrogen blow-drying after each solvent step). It is observed that n-heptane causes considerable surface contamination (in the same order of magnitude as a SAM layer) which can be mostly rinsed off with 2-propanol and H₂O. It must be noted, however, that after 2 hours of n-heptane exposure, contamination amounting to ≈ 0.2 nm apparent adlayer thickness cannot be removed by simple solvent rinsing. Such contamination could significantly influence the quality of gradients made by LMD immersion: The rate of evaporation of organic solvents under normal laboratory conditions can cause undesired contamination effects because the differences in surface energy between clean TiO₂ substrates and organic solvents would result in solution evaporating directly on the substrate surface (mainly at the edge of the meniscus) of the sample during the LMD immersion. On the other hand, n-heptane and 2-propanol evaporate at different rates causing changes in solvent composition, possibly leading to uncontrollable adsorption kinetics. Below the depicted range (0.5 μM - 10 μM), SAM formation would take an unnecessarily long time and thus give way to relatively high levels of contamination. Above 500 μM, immersion times for the low coverage end would be too short to handle and induce unnecessarily high

standard deviations.

The aforementioned observation that the maximum achievable thicknesses (within a maximum of 1h for gradients) are about 30% lower than that of a monolayer (see Section 4.3) led to a shift of focus to the ammonium salts of the three types of alkyl phosphates (DDPO4(NH₄)₂, OH-DDPO4(NH₄)₂, and COOH-UDPO4(NH₄)₂) and the exclusive use of water as a solvent. This step is further encouraged by the high preference of aqueous solutions over organic solvents for biomedical applications. The adsorption kinetics for 250 μM DDPO4(NH₄)₂ aqueous solution onto TiO₂ are shown in Figure 5.9.

Layer thickness of DDPO4 adlayers, formed from DDPO4(NH₄)₂ aqueous solution, as a function of time (shown in Figures 5.9) can be fitted well with all three models (modified, first order and second order Langmuir-type adsorption kinetics). For the concentration of 250 μM, the VASE data indicated that a diffusion-limited ($a = 0.5$) first-order Langmuir model reflects the kinetics best (smallest χ^2), especially for longer adsorption times. The data is, however, not sufficient to make a definite judgment how well this observation holds true for other concentrations. Table 5.5 lists the fit parameter values for the classical (Equation 5.2), extended (Equation 5.6), and second order (Equation 5.7) Langmuir models. For all fits k_A is of the same order of magnitude (the extended model shows larger errors because k_E is close to -1, which is a singularity for the model function), D_{ML} is 1.5 ± 0.3 nm which is close to the monolayer value of 1.6 nm. a is 0.5 (for the first-order Langmuir model with no restrictions) which leads to the conclusion that the kinetics actually obey a diffusion-limited Langmuir model. [261, 270] The simple first-order Langmuir model ($a = 1$) is inadequate indicated by the largest χ^2 and obvious deviations of the fit from the experimental data for long immersion times (see Figure 5.9a). Omitting this model gives $D_{ML} = 1.70 \pm 0.15$ nm.

The correlation of sCA and adlayer thickness (see Figure 5.10b) shows that the maximum static water contact angle (sCA) is $105^\circ \pm 2^\circ$, reached at around 1.1 nm DDPO4 layer thickness. The correlation between DDPO4 layer thickness and sCA is not linear. Hence, a simple linear immersion protocol will not suffice to achieve a linear sCA(x) dependence. It is also apparent that for very low surface coverage ($d < 0.1$ nm), static water contact angles are well above 45° . Such high minimum contact angles imply that it would be difficult to obtain high degrees of hydrophilic-

ity on DDPO4 functionalized surfaces without applying short adsorption times or low concentrations, both problematic for LMD-based gradients. This problem is emphasized by the water contact angles of SAMs of the COOH- and OH-terminated alkyl phosphates used for backfilling, which are in the range of 50° - 65° mainly caused by the hydrophobicity of the alkyl spacer group coupled with lack of order. Regarding the kinetics shown in Figure 5.8a a concentration of 0.5 μM can be used to obtain surface-chemical gradients with static water contact angles in the range of 50° - 90° by LMD. Nevertheless, even such gradients would require time scales of up to two hours - unfavorable under ambient laboratory conditions because of airborne contamination of TiO_2 substrates as outlined above (see Section 3.2).

5.2.2 Phosphate-based surface-chemical gradients by LMD

Table 5.6: Linear-motion drive immersion program to generate a) DDPO4 gradients (from 250 μM solution) b) adsorb second component (OH-DDPO4, or COOH-UDPO4) in opposite direction on a).

Δt [s]	Δd [mm]		Δt [s]	Δd [mm]
2	-1		4	-8
930	-4		3000	-8
450	-4		600	-8
220	-5		240	-8
100	-5		27	-7
50	-5		25	45
20	-5			
10	-5			
2	-5			
30	60			

(a)

(b)

Substrates for Phosphate-based surface-chemical gradients by LMD were $4 \times 1 \text{ cm}^2$ pieces of TiO_2 coated silicon wafer. The substrates were cleaned according to the standard protocol given in Section 3.2 and measured with VASE (10 spots distanced at 4 mm starting at ≈ 2 mm from the edge that was to be immersed first). DDPO4 one-component gradients were fabricated by immersing the substrates gradually into 250 μM aqueous solution of $\text{DDPO4}(\text{NH}_4)_2$. The immersion protocol given in Table

5.6a as deduced from the adsorption kinetics in Figure 5.9b was used in a first step with the LMD technique. After immersion, samples were quickly retracted (automatically at 2 mms^{-1} and manually once sample holder could safely be removed from the solution) and rinsed with 2-propanol and H_2O , then dried under a stream of nitrogen. In the second step, samples were inversely immersed into ultrapure H_2O with the LMD according to 5.6b. After retraction, the DDPO4 gradients were rinsed with 2-propanol and H_2O , then dried under a stream of nitrogen and subsequently measured with VASE and either XPS or the static water contact angle goniometer.

Two-component gradients (DDPO4 vs. COOH-UDPO4 or OH-DDPO4) were made by inversely immersing DDPO4 samples after the first step not into water but a second aqueous solution of either OH-DDPO4(NH_4)₂ or COOH-UDPO4(NH_4)₂ with a concentration of 250 μM according to the LMD program given in Table 5.6b. Samples were again rinsed with 2-propanol and H_2O , then dried with nitrogen, immediately followed by VASE and either XPS or sCA measurements. Initial protocols used full immersion in the second component for backfilling but yielded gradients with smaller slopes which led to the adoption of the inverse immersion protocol. The steeper gradients might be explained by higher substitution rates across whole samples when one-component gradients were completely immersed. Using a second gradual immersion step would also cause different amounts of DDPO4 to be replaced by the second component along the gradients.

Figure 5.11 shows the comparison between DDPO4 one-component and either DDPO4 vs. COOH-UDPO4 (Figure 5.11a-c) or vs. OH-DDPO4 (Figure 5.11d-f) two-component gradients by thickness profile (VASE), sCA, and XPS elemental analysis. XPS data (see Table 4.9 for peak assignment) include elemental ratios (normalized to the ratios of a full SAM of the second step phosphate: P/Ti is used to determine presence of any of the three types of alkyl phosphate and can thus show gradient quality of one-component gradients and degree of coverage for two-component gradients, C/Ti is indicative of any organic material on the surface, also including contamination, C2/Ti (for OH-DDPO4) or C3/Ti (for COOH-UDPO4) represent how much of the adlayer at any given point along the gradient can be associated to the second component (see Section 4.3 for XPS peak assignments).

The immersion steps in Table 5.6 were tailored to yield one- and two-component gradients exhibiting linear sCA-position dependence along their surfaces. XPS data

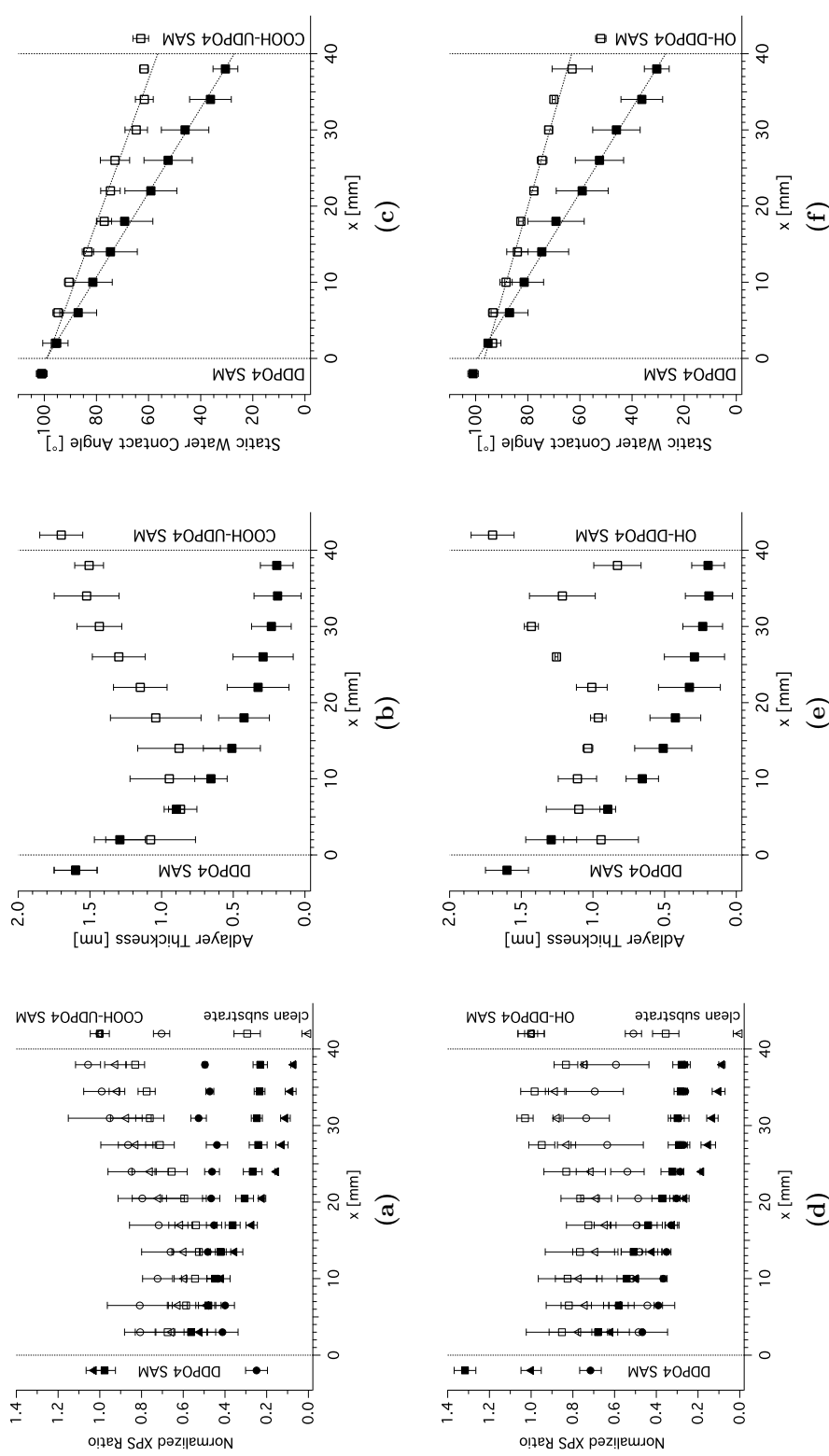


Figure 5.11: COOH-UDPO4 (a-c) and OH-DDPO4 (d-f) two-component (open shapes) compared to DDPO4 (a-f) one-component (filled shapes) gradients: XPS ratios (a, d) for C/Ti (□, ■), P/Ti (△, ▲), and C_{SAM}/Ti (○, ●), VASE adlayers thickness (b, e), and static water contact angle (c, f).

show P/Ti having a factor of about 7 difference between the low and high coverage ends (8.5% and 62% of SAM) while the ratio of C/Ti between both ends is about 2.4. The fact that P/Ti shows a steeper slope than C/Ti for one-component gradients indicates contamination brought upon by extended exposure of the substrate to air during LMD immersion: high P/Ti implies high coverage by DDPO4 thus less space for contamination, while at the low DDPO4 coverage end more contamination can adsorb (exhibiting increased carbon presence). The ratio of layer thicknesses of the two ends is about 6 (0.2 nm and 1.2 nm) while the corresponding static contact angles are 30° and 95°. Adlayer thickness does not depend linearly on position along the gradient, as would be expected from sCA-adlayer-thickness dependence (see Figure 5.10b) while the sCA values show a good linear trend.

Two-component gradients - VASE, XPS, and sCA data - are presented in Figure 5.11. They show slightly increasing adlayer thickness along the samples surface (towards the low DDPO4 coverage end):

For DDPO4 vs. OH-DDPO4 the increase is 10% - 20%. The OH-DDPO4 end shows higher standard deviations and abruptly falling thickness, possibly due to the initial dipping step where material present at the air-water interface might spontaneously adsorb in larger quantities.

For DDPO4 vs. COOH-UDPO4 the increase in adlayer thickness is 50%. -COOH functionality has a higher affinity for TiO₂ than -CH₃ and -OH. Thus, layer formation might proceed more effectively than contamination or OH-DDPO4 adsorption.

XPS data indicate good coverage for all samples: P/Ti is about constant across the surface of OH-vs.-CH₃-gradients while COOH-vs.-CH₃-gradients again show about 50% increase from DDPO4 to COOH-UDPO4 end, C2/Ti and C/Ti show an increase towards the higher OH-DDPO4 coverage end (25% and 10%) as do C3/Ti and C/Ti for the case of COOH-UDPO4 (20% and 25%). Both observations support a gradient surface well covered with alkyl phosphates with a gradient in functionalization from -CH₃ to -OH or -CH₃ to -COOH. Backfilling of DDPO4 one-component gradients with COOH-DDPO4 leads to complete coverage of sample surfaces with alkyl phosphate derivatives and linearly position-dependent static water contact angles (60° - 95°). Contact angles range from 65° (high OH-DDPO4 coverage end) to 95° (high DDPO4 coverage end) for OH-vs.-CH₃ gradients. Static water contact angles for both two-component gradients are higher than for the DDPO4 one-component

ones because of the considerably higher degree in hydrophobicity of COOH-UDPO4 and OH-DDPO4 covered TiO₂ surfaces in comparison to clean TiO₂ substrates. The increase can be ascribed to the alkyl spacer group, which impairs the hydrophilic nature of the -COOH and -OH functional groups and is exposed because of the lack of molecular order within the adlayers.

5.3 Conclusion for phosphate- and catechol-based SAM molecules: adsorption kinetics and surface-chemical gradients by LMD

The adsorption kinetics of two types of catechols and alkyl phosphates on TiO₂ were analyzed with VASE and XPS. No reproducible kinetics could be established for nitrodopamine (ND). Perfluoro-alkyl nitrodopamine (PFAND) showed Langmuir-type adsorption kinetics which could be fit well with a time dependent description of surface coverage during surface adlayer formation (Equations 5.1 and 5.2). Second-order Langmuir-type kinetics and an extended Langmuir model [243,261,270] yielded worse fits. The reason for the better fit of the first-order kinetics is that the immersion time is not linear in the exponential part but rather in the range of $t^{0.2} - t^{0.3}$, indicating a more complex evolution of SAM formation of catechols on TiO₂ than for thiols on gold [243,270]. Reasons could be that PFAND, adsorbed from a mixture of two solvents (water and 2-propanol), is not soluble in the actual mixture, thus exhibiting more complex desorption statistics, additionally increased by the fact that the amphiphile molecule renders the metal oxide surface hydrophobic upon adsorption causing dynamic changes in interaction and diffusion kinetics between solution and surface. Furthermore, catechols can form bonds of different strength with TiO₂ [106,178]. Thus, adsorption kinetics with different adsorption and desorption constants might occur in parallel on the same surface. The exact nature of the more complex adsorption kinetics, however, will require more research regarding different solvents and variation of other parameters such as temperature and substrates. With decreasing solution concentration, the maximum adlayer thickness remained roughly constant around 1.5 nm (with about 10% higher values for lower concentrations)

while the adsorption rate constants remained in the same order of magnitude.

Adsorption kinetics of PFAND (220 μM) were plotted against time yielding a straight line on a logarithmic scale. An LMD immersion program was designed accordingly. 4 cm long one-component surface-chemical gradients were fabricated on TiO_2 substrates, backfilled with ND, and then tested for stability against water. The catechol derivatives PFAND and ND can be adsorbed onto TiO_2 from aqueous solutions to produce either a hydrophobically ($\text{sCA} = 105^\circ$) or a hydrophilically ($\text{sCA} < 10^\circ$) functionalized surface. The adlayers formed in this way are stable for at least 14 hours of water exposure, as confirmed by XPS and VASE. Static water contact-angle measurements show that the adlayer functionality is maintained after the exposure. The fact that PFAND adsorption onto TiO_2 follows clearly reproducible Langmuir-type adsorption kinetics, allows for PFAND-based one- and (ND-backfilled) two-component hydrophobicity gradients on TiO_2 to be produced by utilizing the LMD technique. [18] This is the first example of catechol-based surface-chemical gradients. XPS and VASE data show that surface coverage on the opposing ends of such gradients differs by a factor of 5-7. Static water contact angles are linearly dependent on the position along the gradients over a range of $35^\circ - 95^\circ$ when a logarithmic time-dependence immersion protocol is employed. The adsorption of catechol-bound self-assembled monolayers appears to be a powerful approach to the fabrication of water-stable surface-chemical gradients. Of particular technological significance is the compatibility of these systems with oxide substrates, such as titanium dioxide. Catechol derivatives were chosen because of their strong adhesive properties to a variety of substrates including metals (Ag, Au) [152, 276] native oxide surfaces (on Ti, Cu, Fe) [192, 277, 278] semiconductors (Si) [279] and polymers such as polystyrene [27]. Results from this thesis can serve future studies because of the versatility of catechols and the LMD method to produce stable surface-chemical gradients based on catechol derivatives.

DDPO4 adlayers were formed on TiO_2 by adsorbing DDPO4 from n-heptane:2-propanol (99.2:0.8 vol.%) solutions and $\text{DDPO4}(\text{NH}_4)_2$ from pure water. The kinetics were also analyzed with the first order, second order and the extended Langmuir models. It was found that the data could be fit with all three models. For the case of DDPO4, it was found that decreasing concentration was accompanied by decreasing maximum adlayer thickness (with values of 0.6 - 1.3 nm), an increase in adsorption

rate by one order of magnitude, and an increase in linearity of exponential time dependence (indicating that adsorption from lower concentrations is better described by classical first-order Langmuir-type kinetics). It was not possible to achieve monolayer thickness with DDPO4 but only with DDPO4(NH₄)₂, indicating different adsorption behaviors of the two systems possibly caused by the different solvents used. Fitting the first-order Langmuir model (Equation 5.2) for DDPO4(NH₄)₂ kinetics returned an $a = 0.5$ for t^a (meaning time appeared in the form $t^{0.5}$ in the exponential function), which is equivalent to a diffusion-limited Langmuir-type model. [261] The adsorption rate constants are in the same range as those determined by Koutsioubas et al. for alkyl phosphates adsorbed from ethanol solutions onto alumina.

Clean TiO₂ substrates tended to be contaminated upon extended exposure to the solvent used for DDPO4 (n-heptane). Such an effect would become elevated at the air-liquid interface during the LMD procedure because of solvent evaporation. This situation, the preference of biomedical applications for the use of aqueous solutions, and easier handling when working with water led to the usage of (DDPO4(NH₄)₂) dissolved in ultrapure H₂O as a first component for the phosphate-based hydrophobicity gradients on TiO₂. A concentration of 250 μM (DDPO4(NH₄)₂ in H₂O) was determined to yield reasonable adlayers thicknesses within 1 hour of immersion and was thus chosen.

The adsorption kinetics of DDPO4(NH₄)₂ allowed the design of a suitable LMD program to produce one-component phosphate (DDPO4) based gradients by a logarithmic-versus-time dependent immersion using Morgenthaler's LMD method [243] with a sCA range of 30° - 95° for adlayer thicknesses ranging from 0.2 to 1.2 nm. Two-component gradients OH-DDPO4 versus DDPO4 and COOH-UDPO4 versus DDPO4 showed comparable linear static water contact angles (65° - 95° and 60° - 95°, respectively) while surface coverage was about flat for OH-vs.-CH₃ gradients (with high standard deviations at the ends indicating worse adsorption during second step immersion) and increasing towards low DDPO4 coverage for COOH-vs.CH₃ gradients. VASE data is well supported by XPS measurements in all three cases.

While phosphate-based surface-chemical gradients on TiO₂ can be fabricated using the LMD technique, it is apparent that the range of functionality of obtained adlayers is limited when using simple ω-functionalized alkyls. Stability assessment was not explicitly performed for the phosphate-based gradients in this work. It is

seen from contact angle and P 2p XPS measurements of one- and two-component gradients that (gradient) functionality is preserved after second-component exposure. Long term stability was not assessed because application-specific environments are decisive for such tests. High stability can be advantageous if several experiments are to be conducted on the same gradient surface. In other cases, the promotion of protein or cell adhesion by the presence of a certain surface functionality is investigated and the functional layer should be (easily) degradable to obtain a “clean” interface between protein or cell and the substrate, *e.g.* osteointegration.

The LMD technique is well suitable to fabricate one- and two- component surface-chemical gradients on TiO₂ with phosphate- or catechol-based SAM molecules. The composition and spatial distribution of the gradients was confirmed by VASE, XPS, and static water contact angle (sCA) measurements.

CHAPTER 6

Surface adlayer modification through
deep-UV

As I never tire of saying, heat is
not the antithesis of light but
rather the source of it.

Christopher Hitchens

In recent years, controlled fabrication of surface patterns and structures has seen its ultimate trend towards the nm range. [280,281] This specific surface manipulation is usually achieved by controlled removal, degradation, or transformation of parts of the surface by lithographic techniques. Downscaling efforts for electronic circuits have seen an increased need for thin (nm-range) functional structures and layers. Self-assembled monolayers (SAMs) have seen increasing application in the design of nano devices and surface structuring because of their inherent features of easy transfer of functionality to a surface by specific and spatially controllable adsorption during adlayer formation. [7, 61, 159, 282]

Combining the two approaches: top-down (lithography) and bottom-up (SAMs) offers the possibility to alter the surface(-chemical) functionality of a SAM via (photo, X-ray, or electron beam) lithography also on large scales, potentially yielding nm-size 3D structures. First studies have been successful with this combination for thiols on gold and silanes on silicon surfaces. [30, 283, 284] While electron beam lithography is a viable route, it is desirable to establish cost-effective patterning techniques to form nm-scale systems by self-assembly in order to improve overall efficiency and ease of application. Thus, laboratories without the means of extreme UV (EUV) or electron beam systems would have access to nanometer-scale functional surface patterns. This possibility would encourage downscaling surface patterns to the nm-range and allow the investigation of phenomena already well studied for macro- and microscale structures such as cell and bacterial interactions with surfaces, protein adsorption, or wetting of surfaces.

Well-established techniques for the creation of surface patterns with focus on SAMs include electron beam lithography, photolithography, micro Contact Printing (μ CP), Molecular Assembly Patterning by Lift-off (MAPL), and Selective Molecular Assembly Patterning (SMAP). [29, 30, 128, 211, 283–285] Photolithographic methods such as extreme ultraviolet interferometric lithography [283, 284], which have been shown to be applicable to create patterns of sub 50 nm size, rely on photoresists during processing. Others demand expensive equipment such as vacuum chambers and electron beam sources. It is thus desirable to reduce equipment costs by substituting or eliminating parts of the fabrication process. Tizazu et al. demonstrated that it is possible to use a simple scanning near field optical microscope (SNOM), which is far less expensive than an electron beam setup and can be implemented in

any laboratory environment, to achieve sub micrometer structures in SAMs of phosphonic acids. [30] Such nanopatterned SAM-based substrates can serve as platforms for the epitaxial growth of other self assembly systems. [284] It is thus desirable and feasible to pattern SAMs (down to the nanoscale) and use such structures as platforms for nanostructure studies or further development of 3D systems. Another prerequisite for the success of such an endeavor is the cleanliness of surfaces throughout the fabrication process in order to obtain (chemically) well defined 2D structures after patterning. Hence, a patterning process which inherently can produce small (micro- or nanometer-size) patterns (2D and 3D) while being “self-cleaning”¹ and cost-efficient is highly advantageous.

The first step into the direction of the outlined demands is to establish a chemical system which can serve as a general platform: a collection of SAM system plus a substrate that is “self-cleaning” during the patterning process. The excellent properties of Nb₂O₅ and TiO₂ responsible for the photocatalytically driven degradation of many organic materials under UV exposure as described make the materials ideal candidates as substrates. UV-based lithography assisted by photocatalytic processes to degrade surface adlayers would be used for direct patterning, eliminating the need for photoresists. In combination with SAM chemistries such as catechols or PLL-based polymers, appropriate adlayers could be systematically degraded on the metal oxide surfaces in a controlled manner. [286–290] This is achieved by utilizing UV masks. Such masks can be either binary (Cr/CrOx on a quartz glass where areas are either completely transparent for or blocking UV light) or gray-scale masks (Cr/CrOx is coated on the quartz glass in such a way that the intensity of transmitted UV light (depending on Cr layer thickness) is position dependent in a continuous manner).

This chapter presents the direct photolithographic approach to patterning functional SAMs of perfluoro-alkyl nitrodopamine (PFAND) and the PLL-based copolymer poly(L-lysine)-*graft*-poly(ethylene glycol) (PLL-*g*-PEG) and poly(L-lysine)-*graft*-poly(2-methyl-2-oxazoline) (PLL-*g*-PMOXA) on TiO₂ and Nb₂O₅. In order to understand the inherent processes of surface alteration under UV in the presences of TiO₂ and Nb₂O₅ substrates and to verify that clean target SAM structures can be made, the UV induced and photocatalytically assisted degradation kinetics were in-

¹“self-cleaning” means that every component that is removed during the patterning is completely removed and leaves no (undesired) residues which would compromise the final result.

investigated first. The results serve three purposes: establishing the illumination-time-degradation dependence which can then be used to make surface-chemical gradients, determining the amount of UV irradiation sufficient to completely remove the surface adlayers, and propose a description of degradational processes. The two given example systems yielded surfaces with patterns in protein resistance and in hydrophobicity. The advantage is complete removal of the adlayers leaving residues only below the detection limits of used analysis techniques. The metal oxide substrates used for this part of the thesis were always amorphous (as determined within the scope of included X-ray diffraction (XRD) data - see Section 3.2.1). Other crystallographic forms would likely not show any substantial differences to the substrates used within this work. UV degradation kinetics were assessed with X-ray photoelectron spectroscopy (XPS) and variable angle spectroscopic ellipsometry (VASE). Imaging of perfluoro-alkyl nitrodopamine (PFAND) patterns was done with the microdroplet density technique (MDD). Patterns of PLL-based polymers were imaged indirectly with fluorescence microscopy (FM) after exposure to fluorescently labeled proteins.

6.1 Degradation kinetics

SAMs of perfluoro-alkyl nitrodopamine (PFAND) and the PLL-based copolymers poly(L-lysine)-*graft*-poly(ethylene glycol) (PLL-*g*-PEG) and poly(L-lysine)-*graft*-poly(2-methyl-2-oxazoline) (PLL-*g*-PMOXA) on TiO₂ and Nb₂O₅ are not stable against UV (see Chapter 4). Reactive groups created on the metal oxide surface at different stages during UV illumination as given in Table 6.1 include O₂⁻, H₂O₂ and •OH which are highly reactive and oxidizing. [291] Ethylene glycol can be oxidized (in particular catalytically in the presence of metal oxides) [292, 293] while catechols, perfluoro-alkyls and amide groups are also prone to degradation by O₂⁻ and •OH.

Degradation kinetics for PEG2, PEG5, PMOXA4, and PMOXA8² under deep-UV (with a medium pressure Hg-arc lamp, main peaks at 365 nm and 254 nm) were determined by XPS and VASE. For each data point, one of the polymers was adsorbed onto three 1×1 cm² pieces of Nb₂O₅ or TiO₂ coated silicon wafers each as

²The architectures of PEG2, PEG5, PMOXA4, and PMOXA8 are outlined in Section 3.3.3: PEG2: PLL(20 kDa)-*g*(3.2)-PEG(2 kDa), PEG5: PLL(20 kDa)-*g*(3.6)-PEG(5 kDa), PMOXA4: PLL(20 kDa)-*g*(3)-PMOXA(4 kDa), PMOXA8: PLL(20 kDa)-*g*(3)-PMOXA(8 kDa).

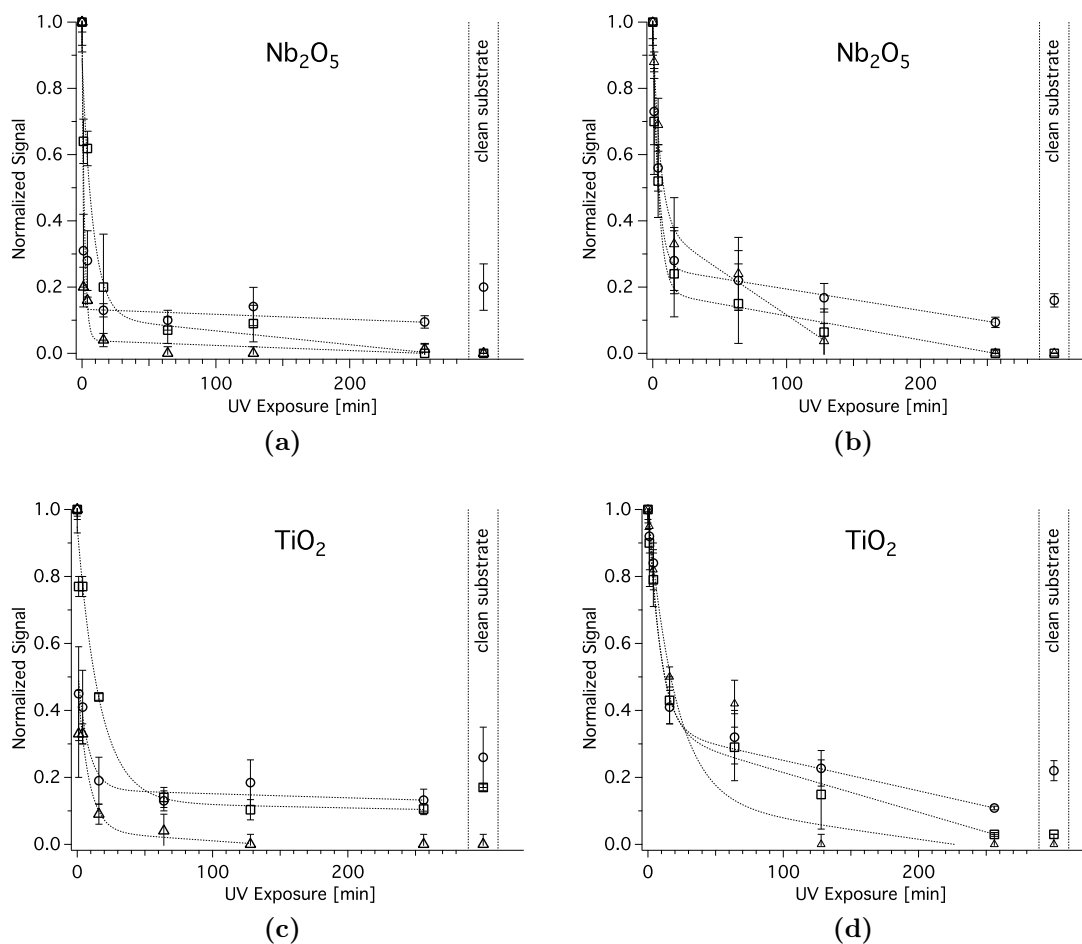
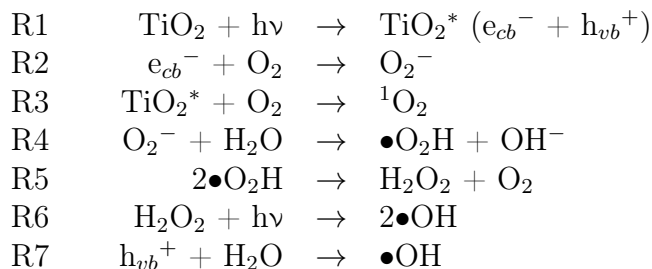


Figure 6.1: VASE thickness (Δ), XPS signals (C/Nb (a,b) or C/Ti (c,d) (\circ) and N/Nb (a) or N/Ti (b) (\square) of PLL-*g*-PEG (left side) and PLL-*g*-PMOXA (right side) on Nb_2O_5 (top) and TiO_2 (bottom) substrates for different times of UV-exposure (deep-UV medium pressure Hg-arc lamp with peak intensities at 254 nm and 365 nm), normalized to values of respective monolayers (1 at $t = 0$). Dashed lines are fits with Equation 6.1. Values found for fit parameters are given in Table 6.2.

Table 6.1: Processes generating radicals by photoinduced reactions in TiO₂ (as given by Cho et al. [291]).



described in Section 3.5. Since the goal is to fabricate patterns by UV lithography where UV-masks have to be placed in close contact with the surface, in order to achieve sharp edges and corners of SAM patterns during exposure, samples were placed on a home-built sample holder. The holder consists of three parts: a metal plate (5 mm thick) on which samples are placed, a quartz glass plate (5 mm thick), and a metal frame with 8 screws to press the quartz glass (with the mask) onto the samples and ensure close contact. Samples were then exposed for different time (1, 4, 16, 64, 128, and 256 min) at a distance of 10 cm. After exposure, samples were thoroughly rinsed with 50% ethanol:H₂O solutions to remove any physisorbed residues and dried under a stream of nitrogen. Samples were then measured with VASE, immediately followed by XPS. An analysis for UV degradation in the setup (without a mask) is given here (see Section 3.5.3 for the UV patterning protocol). During UV exposure, the quartz glass is pressed onto the sample resulting in a very tight and almost sealed system. In contrast to a freely exposed surface, where diffusion and exchange of air and radicals is much freer, the degradation kinetics are expected to be different.

Polyethylene glycol (PEG) is more likely to degrade by oxidation than PMOXA (2-methyl-2-oxazoline) because ethylene glycol is more likely to oxidize in environments of oxygenic radicals such as H₂O₂ or superoxide and the amide group has a stabilizing affect on the PMOXA against oxidation/radicalization. Hence, it is expected that adlayers of PLL-*g*-PEG on TiO₂ or Nb₂O₅ degrade faster than those of PLL-*g*-PMOXA under UV exposure. Figure 6.1 shows the degradation kinetics of both polymers in terms of XPS signal intensities (C 1s and N 1s) and remaining

surface layer thickness as determined by VASE. While VASE is indiscriminate of chemical composition, XPS signals can reveal which parts of the molecules (polymer adlayers) are degraded at what rate. Comparing N and C for PLL-*g*-PEG shows that nitrogen (only present in PLL) decreases considerably more slowly than carbon, which means that PEG degrades faster than PLL. This observation is confirmed when assessing PMOXA (the monomer units of PMOXA and PLL are chemically very similar and indistinguishable with XPS): C and N disappear from the surfaces at about the same rate. After 2 hours in the closed system, surfaces can be considered clean (VASE and XPS signals are essentially identical to those of bare substrates after the standard cleaning protocol) and only slightly more material is removed afterward (measurements were done for up to 4 hours of UV exposure). It is possible that the surfaces after 4 hours of UV exposure are cleaner than they appear under XPS and VASE because airborne contamination readily adsorbs on UV cleaned surfaces of both metal oxides under normal laboratory conditions.

The UV degradation data shown in Figure 6.1 was fitted with a linear plus an exponential function:

$$f(t) = a + bt + A \exp\left(\frac{t}{-\tau}\right) \quad (6.1)$$

with a and A representing initial signal intensities and b and τ^{-1} the corresponding degradation rates of an initial (0-16 min) fast exponential decay and second (up to 4 hours) prolonged step. t is the exposure time. A first attempt to fit the data with one exponential decay function:

$$S(t) = S_0 \exp(-t/\tau) \quad (6.2)$$

derived from the assumption that the surface adlayer degradation rate and remaining surface coverage represented by either the XPS or the VASE signals ($S(t)$) relate in the form:

$$-\frac{dS(t)}{dt} \sim S(t) \quad (6.3)$$

was only successful for the initial part of degradation ($t = 0 - 16$ min) but increasingly deviated for longer exposure times. Hence, a second, linear term, was introduced and sufficed to correct for the deviation yet missing an explicit identification of the

physical/chemical process and might not be linear but rather a second exponential of a slower degradation or adsorption of contamination. Possible explanations for the deviation could be:

- the actual degradation kinetics change due to the formation of different intermediate products (adsorbing on the surface) which are less prone to further degradation, being less reactive
- different parts of the adlayers degrade by different mechanisms and thus with different speeds and kinetics
- measurements are not performed *in situ*. Exposure of samples after UV exposure facilitates (subsequent) adsorption of air-borne contamination, thus skewing adlayer thickness (VASE) and chemical composition (XPS) measurements, especially after longer exposure times because the samples are cleaner.

All data could be fit rather well with Equation 6.1. Table 6.2 shows values found for the fit parameters of Equation 6.1 (actual fits are presented by dashed lines in Figure 6.1). For all signals, τ is greater for TiO_2 than for Nb_2O_5 as substrate, indicating that degradation of all polymers proceeds more slowly on TiO_2 . For PLL-*g*-PMOXA there is no noticeable difference for τ between the carbon and nitrogen indicating that the polymer degrades rather homogeneously. For PLL-*g*-PEG $\tau(\text{N } 1\text{s})$ is 3 - 10 times $\tau(\text{C } 1\text{s})$ emphasizing the earlier observation that PEG (containing no nitrogen) degrades considerably faster than PLL (containing nitrogen). Furthermore, all $\tau(\text{C } 1\text{s})_{T_i}$ values are higher for PMOXA than PEG indicating that PMOXA is generally more stable against UV than PEG.

6.2 Patterning

Based on the observation that the polymers are completely removed from the surfaces within the UV setup after sufficiently long exposure because of UV-induced and photocatalytically assisted degradation, masked direct UV lithography could be used to fabricate patterns of the SAMs on TiO_2 than for Nb_2O_5 substrates. Binary structures would be easily made visible with fluorescently labeled proteins that would only adsorb on cleaned areas and not on those with intact protein resistant

Table 6.2: Fitting coefficients (according to Equation 6.1) of UV degradation kinetics of PEG2/PEG5 and PMOXA4/PMOXA8 adlayers on TiO₂ and Nb₂O₅ as shown in Figure 6.1. The kinetics are detailed into adlayer thickness (VASE) and C 1s and N 1s (XPS) signals (normalized to those of a full monolayer before UV exposure). a and A represent initial signal intensities with b and τ^{-1} the corresponding degradation rates of an initial (0-16 min) fast exponential decay and second (up to 4 hours) prolonged step.

Polymer	Substrate	Signal	a / 10 ⁻³	b / 10 ⁻⁶ min ⁻¹	A / 10 ⁻³	τ [min]
PLL- <i>g</i> -PMOXA	Nb ₂ O ₅	C/Nb	259.0 ± 62.7	-648 ± 261	713 ± 88	4.3 ± 1.4
		N/Nb	185.8 ± 90.4	-728 ± 357	786 ± 127	4.44 ± 2.01
		VASE	390 ± 160	-2720 ± 1390	602 ± 157	5.41 ± 2.83
	TiO ₂	C/Ti	342.2 ± 72.7	-913 ± 286	733 ± 112	8.39 ± 3.17
		N/Ti	333 ± 111	-1185 ± 437	666 ± 148	9.68 ± 5.35
		VASE	129.9 ± 63.1	-573 ± 315	861.5 ± 67.4	20.55 ± 3.07
PLL- <i>g</i> -PEG	Nb ₂ O ₅	C/Nb	133.2 ± 18.4	-153 ± 109	865.8 ± 91.8	0.650 ± 0.256
		N/Nb	109.7 ± 49.5	-418 ± 243	777.7 ± 74.1	8.1 ± 2.3
		VASE	39.4 ± 15.9	-154 ± 102	919.5 ± 32.9	1.867 ± 0.139
	TiO ₂	C/Ti	163.3 ± 71.2	-120 ± 280	371 ± 115	7.73 ± 6.04
		N/Ti	88.0 ± 65.4	70 ± 280	756.3 ± 68.3	21.01 ± 2.84
		VASE	39.1 ± 97.5	-286 ± 856	459 ± 88	8.15 ± 5.55

polymer coatings. Either one-component patterns (one type of polymer/molecule vs. bare substrate) or two component structures (one type of polymer/molecule against another one) can be generated. It would be expected that the latter would not show any protein adsorption. UV-initiated degradation of surface adlayers on Nb₂O₅ and TiO₂ is expected to be localized to UV exposed areas and not to spread considerably, for example through air, by long-living radicals. The idea has been used by other groups to create patterns of SAMs of phosphonic acids on TiO₂. [30] As done by Tizazu, TEM grids were used as masks to create patterns of the PLL-based polymers. Results are presented here. The advantage of the TEM grids is their well-defined microstructures (the two types used in this work: 120×120 μm² with edge-to-edge distance of 30 μm and 30×30 μm² with edge-to-edge distance of 20 μm). Such patterned surfaces can eventually be used for studies of cell and bacterial adhesion or proliferation. Downscaling to sub-micrometer scales can yield more insights into reactions of cells to patterned structures smaller than their own size. One advantage of the presented method is that the areas where the surface adlayer is removed is very clean (based on the XPS measurements from the degradation kinetics) only leaving minimal amounts of contamination, which are inevitable when working under normal laboratory conditions.

6.2.1 PLLs

Homogeneous adlayers of either PEG5, FITC labeled PEG5, or PMOXA8 on Nb₂O₅ and TiO₂ were exposed through UV masks (TEM grid with 30×30 μm² squares, edge-to-edge spacing of 20 μm) to deep-UV (medium pressure Hg-arc lamp) at a distance of 3 cm for 1 hour. After exposure, samples were rinsed with 50% ethanol:H₂O solutions to remove any physisorbed residues and dried under a stream of nitrogen. Samples were then exposed to protein solution of AlexaFluor488 labeled fibrinogen for 20 min, then rinsed with ultra pure water and dried under a stream of nitrogen. Samples were imaged directly using either the fluorescently (FITC) labeled polymers (Figure 6.2 shows PEG5 patterns) or indirectly by imaging the treated polymer surfaces with adsorbed labeled proteins. Protein only adsorbs where the protein resistant polymers (PLL-*g*-PEG or PLL-*g*-PMOXA) have been sufficiently removed/degraded. It is observable that corners and square edges (show gradient shape of ≈ 8 μm length)

are not sharp, which could be either due to diffraction or diffusion of polymer after processing. Labeled polymer and protein patterns show the same shape features, indicating that the problem is already caused during the fabrication process and not after protein adsorption. The reason for this pattern softening is not clear. If it is of optical nature (diffraction) it could be improved by using a better mask system - instead of a TEM grid pressed onto the samples, a tailor-made Cr-coated quartz glass mask might be used. No difference between patterns based on PLL-*g*-PEG or PLL-*g*-PMOXA were observable indicating that both polymers are valid systems for this patterning technique.

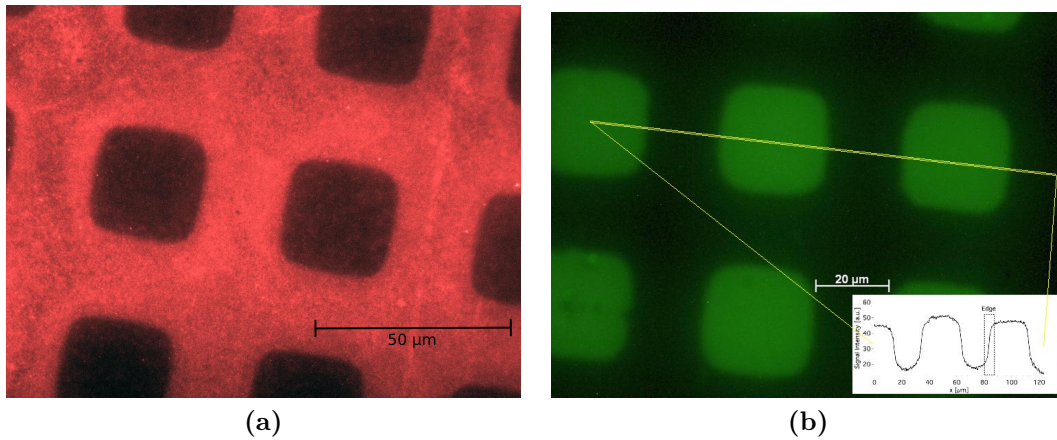


Figure 6.2: FM images of a) FITC labeled PLL-*g*-PEG after UV patterning (metal strip with $30 \times 30 \mu\text{m}^2$ squares at distanced by $20 \mu\text{m}$) and b) UV-patterned (metal strip with $30 \times 30 \mu\text{m}^2$ squares at distanced by $20 \mu\text{m}$) PLL-*g*-PMOXA on Nb_2O_5 followed by adsorption of AlexaFluor488 labeled fibrinogen. Proteins only adsorb in cleared areas (squares). Square edge have the shape of gradients (about $8 \mu\text{m}$ long).

6.2.2 PFAND

The high degree of hydrophobicity of PFAND facilitates the visualization of UV-photolithography induced patterns by MDD. Patterns of PFAND were generated by direct UV-photolithography similar to the case off PLL-based polymers: PFAND was adsorbed from $440 \mu\text{M}$ 2:1 H_2O :2-propanol solutions for 2 days and patterned (UV masks (TEM grid with $120 \times 120 \mu\text{m}^2$ squares, edge-to-edge spacing of $30 \mu\text{m}$)

to deep-UV (medium pressure Hg-arc lamp) at a distance of 3 cm for 1 hour) after rinsing with 2-propanol and drying with nitrogen. Patterned samples were immersed in 2-propanol and sonicated for 3 min then dried under a stream of nitrogen. Figure 6.3 shows an MDD image of a pattern of PFAND produced by using a S160 TEM UV-mask after 1 h of UV exposure a PFAND SAM on TiO_2 . Areas that were covered by grid lines of the mask remain dark because the unexposed PFAND retained its hydrophobicity and water is more likely to go to the squares which were exposed to UV. Such areas, where PFAND had been degraded/removed by UV, show droplet formation due to nucleation sites and increased hydrophilicity. Some droplets form on the ring which is wider than the inner structure and water cannot flow as easily as within the grid. Nevertheless, droplet formation is considerably higher on the squares than on the ring.

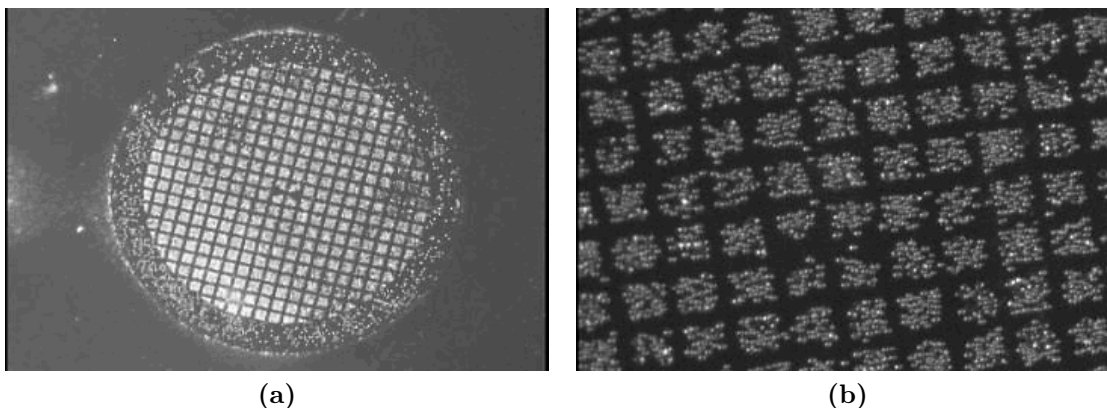


Figure 6.3: a) photo of a pattern (TEM grid as UV mask) of PFAND on TiO_2 with MDD. b) zoom of center of a). Squares are 120 μm , edge-to-edge distance between squares is 30 μm .

6.2.3 Backfilled patterns

It is also possible to backfill UV patterned adlayers with another type of SAM molecules to fabricate heterogeneous SAMs. This can be useful to create patterns with localized areas that exhibit specific protein affinity. Samples with patterns of either PFAND or PLL-based polymer were backfilled with either of the PLL-based polymers by immersing samples for 2 hours in the respective solution then rinsing

thoroughly with ultra pure water followed by drying with nitrogen. Samples fabricated in this way were exposed to solutions of AlexaFluor488 labeled fibrinogen for 20 min then rinsed with ultra pure water and dried with nitrogen.

It was observed that backfilling patterns of one type of protein resistant polymer (PLL-*g*-PEG or PLL-*g*-PMOXA) with either the same or the other kind rendered surfaces completely resistant again (no patterns were visible anymore). Patterns of PFAND that were backfilled with a protein-resistant polymer demonstrated an inverse structure (Figure 6.4b shows the case of PLL-*g*-PEG backfilled PFAND TEM-grid pattern on TiO₂) compared to direct patterning (Figure 6.4a) shows the TEM grid pattern of a PLL-*g*-PMOXA adlayer on TiO₂).

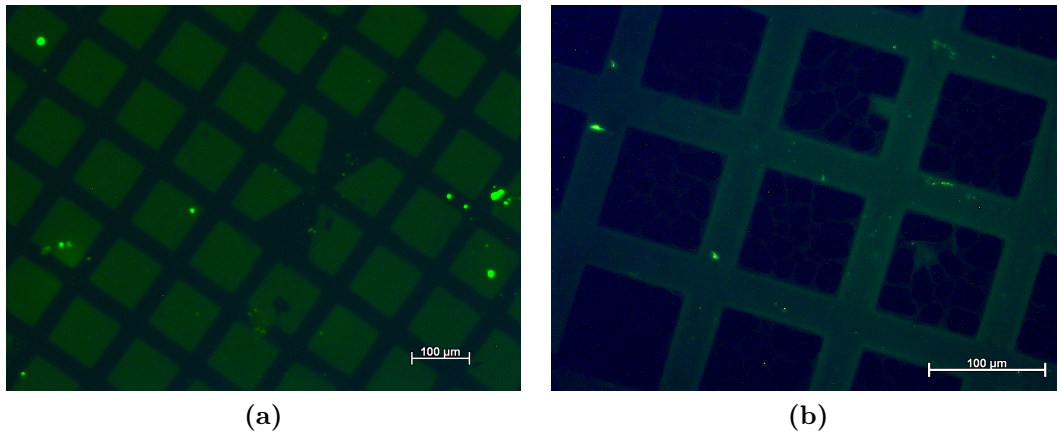


Figure 6.4: FM images of a) AlexaFluor488 labeled fibrinogen adsorbed on UV patterned PLL-*g*-PMOXA adlayer on TiO₂, in comparison of the inverse pattern generated by b) AlexaFluor488 labeled fibrinogen adsorbed on a UV patterned PFAND adlayer backfilled with PLL-*g*-PEG on TiO₂. Proteins only adsorb on PFAND which is not protein resistant.

6.3 Conclusion

Degradation kinetics of PLL-*g*-PEG or PLL-*g*-PMOXA adlayers on TiO₂ or Nb₂O₅ were determined by VASE and XPS measurements. The studies showed that PLL, PMOXA, and PEG degrade at different rates (PMOXA being roughly equivalent to PLL, and PEG degrading at rate 3-10 times faster than PMOXA). Complete removal

of adlayers is successful on both kinds of substrates used in this work (amorphous TiO_2 and Nb_2O_5) leaving clean substrate surfaces. Degradation is slightly faster on Nb_2O_5 than on TiO_2 . The complete degradation was used to create micrometer scale patterns of PEG5, PMOXA, and PFAND. The patterns were visualized with FM by using labeled polymers and labeled proteins. Both reflect the same 2D surface adlayer structures of protein resistance. PFAND patterns were successfully visualized using MDD with higher degrees of hydrophobicity in areas of blocked UV exposure. Backfilling of PFAND patterns with protein-resistant polymers yielded inverse structures, compared to the case of directly patterning the polymers. Backfilling patterns of either protein-resistant polymer with another yielded completely resistant surfaces, implying that patterns of polymers can be successfully generated allowing for specific protein or cell adhesion patterns.

The presented technique is limited by the fact that it will work best with very flat surfaces (depending on the roughness of the SAM adlayer and substrate) because the UV mask has to be in close contact with the SAM and a SAM thickness of only a few nanometers would not allow for much flexibility. This disadvantage could be overcome by using a SNOM instead of the TEM grid or chromium mask setup as Tizazu did for phosphonic acids on TiO_2 , with the additional benefit of creating patterns on the submicrometer scale. [30]

CHAPTER 7

Conclusions and Outlook

The only positive finding which could be drawn from the first series, was the conclusion that the relationships obviously had a more complicated lay-out than had been thought, for the effects were so varied that no obedience to any law could be discovered.

Walter Rudolf Hess

This chapter presents conclusions to be drawn from the findings regarding catechol- or phosphate-based surface functionalizations and surface-chemical gradients on metal oxides within this thesis. It also covers how (photocatalytically assisted) direct UV photolithography can be used to create surface-chemical patterns and potentially gradients. As part of the cooperative work with other laboratories and people within the group of LSST during the course of this thesis, other projects were undertaken or have been started. Their initial promising results are shown here.

7.1 Conclusions

The catechols perfluoro-alkyl nitrodopamine (PFAND) and nitrodopamine (ND) form self-assembled monolayers on the metal oxides TiO_2 and Nb_2O_5 when adsorbed from appropriate solutions. For PFAND it was shown by X-ray photoelectron spectroscopy (XPS), variable spectroscopic ellipsometry (VASE) and static water contact angle measurements (sCAs) that full monolayers can be adsorbed from a $440 \mu\text{M}$ solution in a 2:1 2-propanol: H_2O solvent mixture, ND from a $500 \mu\text{M}$ solution in ultra pure water. PFAND replaces contamination initially present on cleaned TiO_2 and Nb_2O_5 surfaces and forms hydrophobic surface adlayers (static water contact angle $(105 \pm 3)^\circ$, dynamic water contact angles: advancing $(110 \pm 3)^\circ$, receding $(75 \pm 5)^\circ$), with thickness of 1.7 nm implying a tilt angle of about 30° of PFAND molecules when densely packed in a SAM. PFAND follows Langmuir-type adsorption kinetics on TiO_2 with (concentration-dependent) deviations from classical descriptions regarding the dependence on time. This deviation is possibly due to the usage of a mixture of organic solvents during adsorption causing more complex adsorption-desorption dynamics. Reproducible kinetics could not be established for ND due to the molecule's hydrophilicity, increasing the likelihood of surface contamination under normal laboratory conditions and thus causing higher standard deviations for VASE and XPS experiments.

The adsorption kinetics of PFAND from a $220 \mu\text{M}$ solution were used to design a gradual immersion program that was used in combination with Morgenthaler's linear motion drive technique (LMD) [18] to produce cm-long surface-chemical PFAND-ND gradients with sCAs ranging from 95° to 35° that are stable against prolonged

immersion in ultra pure water.

The SAM molecule alkyl phosphate dodecyl phosphate (DDPO4, dissolved in n-heptane with 0.8% 2-propanol) and its ammonium salt DDPO4(NH₄)₂ also follow Langmuir-type adsorption kinetics when adsorbed onto TiO₂. DDPO4 shows (concentration dependent) deviations in time dependence similar to PFAND, supporting the possible cause being the use of a mixture of organic solvents. DDPO4(NH₄)₂, when adsorbed from ultra pure water, shows a time dependence of \sqrt{t} in the exponential part of the Langmuir function (see Equation 5.1) implying diffusion limited adsorption, as described by Koutsioubas et al. for alkyl phosphates on Al₂O₃. [261] DDPO4 adsorbed from organic solvents did not form full monolayers (as already discussed by Spori et al. [171]) in contrast to its ammonium salt (adlayer thickness of ≈ 1.6 nm), both observations being supported by Langmuir-type curve fits against VASE data. 250 μ M aqueous solution of DDPO4(NH₄)₂ was used in combination with LMD to fabricate one-component gradients which were backfilled by reversed immersion into a second-component aqueous solution of either the hydroxyl terminated alkylphosphate OH-DDPO4(NH₄)₂ or the carboxyl terminated variant COOH-UDPO(NH₄)₂. In both cases two-component phosphate-based surface-chemical gradients could be fabricated on 1×4 cm² TiO₂ substrates with contact angles in the range of 60°-95°.

PFAND and ND were tested for the stability of their respective SAMs on TiO₂ against X-radiation. Both molecules degrade under prolonged (continuously for 20 h) exposure to X-rays (300 W source of Sigma2 XPS instrument). PFAND's degradation appears stronger (higher loss of functionality) as was shown with iterative XPS measurements of the remaining chemical elements present on the surface. The degradational process is thought to be multifold (different reactions with different intermediate products) based on direct damage by the electromagnetic radiation as well as secondary electrons that are emitted from samples. The amount of carbon is only reduced during the first 3 hours, while the fluorine signal continuously decreases, indicating that the CF₂-chain is degraded via several steps but only fluorine is effectively removed. Prolonged X-ray exposure also leads to transformation of the catechols' nitro group observed by the disappearance of the corresponding N 1s peak. The polymers poly(L-lysine)-*graft*-poly(ethylene glycol) (PLL-*g*-PEG), and poly(L-lysine)-*graft*-poly(2-methyl-2-oxazoline) (PLL-*g*-PMOXA) also degrade during XPS

measurements, mainly destroying the PEG functional unit at a greater speed than the PMOXA. The given observations emphasize that X-ray induced degradation has to be considered during XPS measurements to guarantee correct quantification of the chemical composition of surface adlayers.

SAMs of all molecules discussed in this work were observed to be unstable against (deep) UV-light (alkyl phosphates have already been discussed by Tizazu et al. [30]). Exposure to a medium pressure 450 W Hg-arc lamp for less than 10 minutes completely eliminates the protein-resistant properties of both types of PLL-based polymers (for PLL-*g*-PEG adlayers already after about 2 min). Continued exposure for about 1 hour leads to complete removal of all of the molecules, leaving clean TiO₂ or Nb₂O₅ surfaces. Comparison of PLL-*g*-PMOXA and PLL-*g*-PEG adlayers on TiO₂ or Nb₂O₅ with those on SiO₂ proved that the photocatalytic properties play an important role in the degradational process during UV exposure. Although the polymers form high-coverage layers on TiO₂ or Nb₂O₅ (PLL-based polymers adsorb with higher affinity to the metal oxides), they are completely degraded after exposure times that would lead to only partial removal for full-coverage layers on SiO₂ (judged by the respective C 1s XP spectra). PLL-*g*-PMOXA is more stable than PLL-*g*-PEG and degradation proceeds faster on Nb₂O₅ than on TiO₂.

The circumstance that SAMs of the described molecules and polymers can be completely removed led to the application of direct UV-photolithography supported by the UV initiated photocatalytic activity of TiO₂ and Nb₂O₅. Masked exposure of complete adlayers on either of the metal oxides to deep UV leads to a transfer of the mask pattern to patterns in functionality on the surfaces. PFAND patterns result in patterns of hydrophobicity while those of PLL-*g*-PMOXA and PLL-*g*-PEG result in 2D protein resistance patterns (demonstrated by patterning of labeled polymers and adsorption of labeled proteins on the 2D structures).

7.2 Applications

The applications of and need for surfaces with 2D structures and gradients in hydrophobicity and protein resistance (and SAMs in general) have been outlined by several authors: Kennedy et al. demonstrated that fibronectin coated gradients in

surface energy ranging from 23 to 62mN/m (water contact angles ranging from 25° to 95°) allowed the parallel study of osteoblast adhesion and proliferation as a function of surface energy/hydrophobicity. [33] Lehnert et al. described the adaptation of cells to extracellular matrix patterns on surfaces. [294] Fink et al. provided a comparative study of different micropatterning techniques elaborating on advantages and disadvantages of microcontact printing (μ CP) on different substrates and UV patterning techniques emphasizing the need of biology research labs for(cost-)efficient substrate fabrication methods with high quality and precision. [32] Dibbell et al. used SAM forming mercaptoalkanoic acids in combination with UV patterning for the spatially controlled deposition of quantum dots on TiO_2 . [63] Kim et al. fabricated nanopatterns of SAMs with different wettability on Si_3N_4 and showed the differential epitaxial self-assembly of block copolymers on the structures. [284]

From such examples it seems worthwhile to provide new methods for the fabrication of patterned surface-functionalities. Direct UV patterning of PLL- and catechol-based adlayers on Nb_2O_5 or TiO_2 is a very promising route because it will eventually allow generating clear 2D structures on the metal oxide surfaces on submicrometer scales. [30]

7.2.1 Surface-chemical gradients by direct UV-photolithography

An advance from binary patterns is to utilize UV initiated and photocatalytically assisted degradation kinetics of surface adlayers on Nb_2O_5 or TiO_2 substrates to create gradients in surface functionality. In order to generate such surfaces, the amount of UV light impinging on the surface during exposure has to be a function of position along the substrate. One way to achieve this is by using gradients in thickness of a chromium layer (and thus optical transmittivity) deposited on a quartz glass.

Blondiaux et al. [285] demonstrated how such gradient masks can be made and applied for the case of thiols on gold with an additional nanometer-thick layer of TiO_2 to generate radicals which would then degrade the thiol SAM. Using TiO_2 or Nb_2O_5 as a substrate as done in this work would eliminate the need for an additional photoactive layer and thus simplify the setup. The gradient shape/design can be

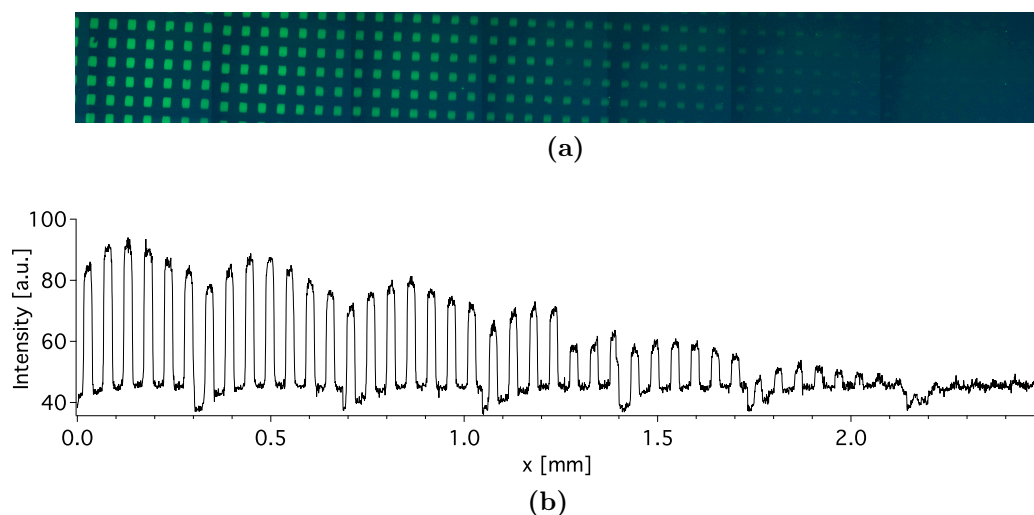


Figure 7.1: Surface-chemical gradient in protein resistant produce by illuminating a monolayer of PLL-*g*-PEG through a gray scale gradient Cr/CrOx mask on top of a metal strip with $30 \times 30 \mu\text{m}^2$ square with $20 \mu\text{m}$ edge-to-edge distance. Full length of the gradient (maximum contrast to no contrast) is about 2.5 mm. a) FM image and b) intensity profile along the gradient.

transferred to surface-chemical gradients directly by illuminating a SAM on either TiO_2 or Nb_2O_5 with UV through the mask.

A first presentation of such a surface functional gradient (in protein resistance) is given in Figure 7.1: A monolayer of PLL-*g*-PEG was adsorbed from 1 mg/ml HEPES2 solution onto a $1 \times 1 \text{ cm}^2$ TiO_2 substrate. The samples was then illuminated through a grey-scale mask (gradient in surface coverage of Cr/CrOx on quartz glass) with the standard UV setup described above at a distance of 10 cm for 20 min. In order to ease imaging, the same kind of TEM grid as it was used to obtain Figure 6.2 ($30 \times 30 \mu\text{m}^2$ squares with $20 \mu\text{m}$ edge-to-edge spacing) was placed between grey-scale mask and sample. The intensity profile (Figure 7.1b) was recorded by taking several conjunctive fluorescence (FM) images and subsequently joining them. Protein resistance decreases towards the end of higher UV exposure (lower Cr coverage on the quartz glass). The position dependence of fluorescence signal intensity is roughly linear along the gradient, as is protein coverage/resistance (assuming it correlates linearly with fluorescence signal intensity). The total length of

the presented gradient is about 2.5 mm. Smaller gradients could be fabricated but would be more challenging to image.

7.2.2 Controlled localization of cellular adhesion

A first application for the photocatalytically enhanced direct UV photolithography patterning method was given by Thomas von Erlach in his master thesis. As part of the work here, square patterns ($120 \times 120 \mu\text{m}^2$ with $30 \mu\text{m}$ edge-to-edge spacing) of the protein resistant polymers PEG5 and PMOXA8 (see Section 3.3.3) were fabricated on Nb_2O_5 coated silicon wafers ($1 \times 1 \text{ cm}^2$). The patterned surfaces were then exposed to fibronectin labeled with AlexaFluor488 for 20min and subsequently rinsed with ultra pure water and dried under a stream of nitrogen. Thomas incubated the samples in cell cultures of human foreskin fibroblasts (hff) for up to 1 month to compare the stability of both polymers under cell culture conditions. Results can be found in his work: cells spread faster on PEG5 patterns than PMOXA8. After 2 hours, cells still adhere to the square shapes, only residing on protein-covered areas. After 2 days, cells spread over the whole sample for the case of PEG5. PMOXA8 patterns were still intact after 1 month. Sample FM images to demonstrate the applicability as part of such cell adhesion and proliferation studies are given here (taken by Thomas von Erlach): Figure 7.2 shows hff cells on the protein patterns (a), their red labeled cytoskeletons (b), and blue labeled cell nuclei (c). Cells adhere very well to the protein structures and usually refrain from adhering to the protein-resistant, polymer-(PLL-*g*-PMOXA-)covered areas (grids between squares). Within his work, Thomas also performed comparison between structures made by direct UV photolithography and microcontact printing (μCP) of the same polymers. He noted that fibronectin disappeared in a considerably shorter time on the μCP -samples than UV-patterned ones albeit polymer patterns remaining intact on both kinds of samples (assessed by cellular adhesion tests). This observation could be due to stronger binding of the proteins to the surfaces that were UV-cleaned during the photolithography procedure. The UV cleaning would strongly reduce and avoid contamination, which could weaken protein-surface bonds. Details on the comparison can be found in Thomas's thesis. [295]

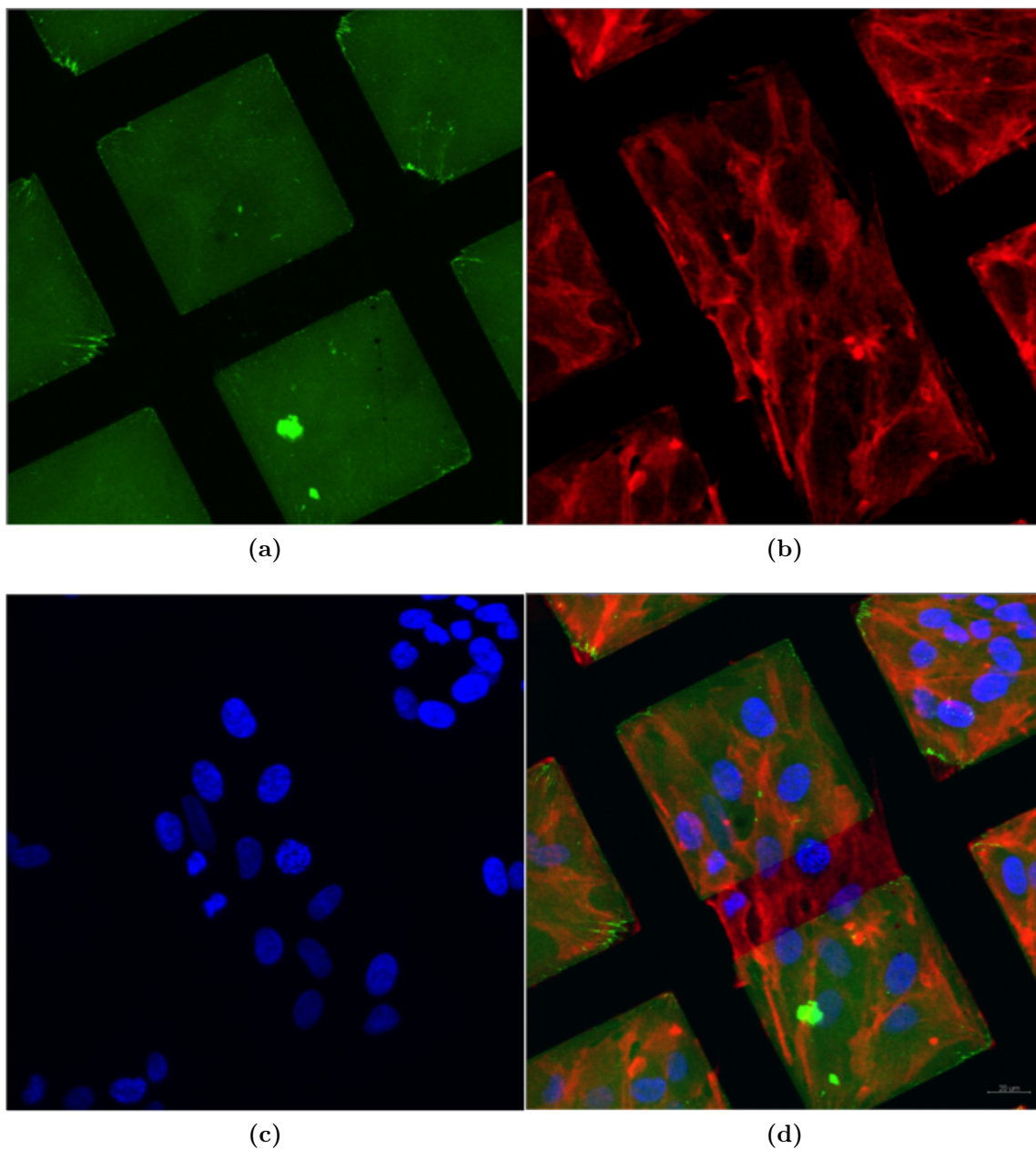


Figure 7.2: Fluorescent images of human foreskin fibroblasts (hff) adsorbed on PLL-*g*-PMOXA structures created by direct UV patterning and back-filled with fibronectin. a) fibronectin square structure, b) hff cytoskeletons, c) hff nuclei, d) overlay of a)-c).

7.3 Outlook

Various pathways have been laid out within this work regarding the fabrication of surface-chemical gradients and patterns on metal oxide surfaces (TiO_2 and Nb_2O_5 in particular). Further development can go into the direction of using other catechol derivatives such as PLL-catechol-PEG introduced by Saxer et al. [202] and possibly PLL-catechol-PMOXA (because of considerably higher stability of PMOXA against oxidizing environments, in cell cultures, and against radiation) to form stable surface-chemical gradients with different functionality also on other substrates such as polymers. Given the possibilities of fabricating (hydrophobicity) gradients on TiO_2 for high-throughput experiments of cellular interactions with surfaces of different surface energies can be performed as demonstrated by Kennedy et al. on silicon substrates. [33]

First examples of direct UV patterning of polymer- and catechol-based adlayers on TiO_2 and Nb_2O_5 substrates can be extended further to more complex 2-D and 3-D structures and also richer gradient structures in combination with other catechol-based surface functionalizations. Further downscaling can be achieved by applying other surface modification methods such as extreme UV interference or scanning near-field optical microscopy with UV light sources. Controlled surface photopolymerization without photoinitiators can yield simple and cost-efficient routes to potentially tailor tribological but also bacterial and cell adhesion properties (using appropriate monomer building blocks) of surfaces of titanium alloys. The fact that UV photolithography is well established should greatly facilitate the spread of surface-modification methods such as those presented here.

Nomenclature

Nb_2O_5 Niobium pentoxide

TiO_2 Titanium dioxide

FM fluorescence microscopy

ND nitrodopamine

PFAND perfluoro-alkyl nitrodopamine

PLL-g-PEG Poly(L-lysine)-g-poly(ethylene glycol)

PLL-g-PMOXA Poly(L-lysine)-g-poly-2-methyl-2-oxazoline)

VASE Variable-angle spectroscopic ellipsometry

XPS X-ray photoelectron spectroscopy

XRD X-ray diffraction

Bibliography

- [1] A. Nakajima, K. Hashimoto, T. Watanabe, K. Takai, G. Yamauchi, and A. Fujishima. Transparent superhydrophobic thin films with self-cleaning properties. *Langmuir*, 16(17):7044–7047, 2000.
- [2] R. Blossey. Self-cleaning surfaces - virtual realities. *Nat Mater*, 2(5):301–306, 2003.
- [3] M. Heydari, H. Hasuda, M. Sakuragi, Y. Yoshida, K. Suzuki, and Y. Ito. Modification of the titan surface with photoreactive gelatin to regulate cell attachment. *J Biomed Mater Res A*, 83A(4):906–914, 2007.
- [4] C. Trepanier, M. Tabrizian, L. Yahia, L. Bilodeau, and D. Piron. Effect of modification of oxide layer on NiTi stent corrosion resistance. *J Biomed Mater Res*, 43(4):433–440, 1998.
- [5] M. Mottaghi, P. Lang, F. Rodriguez, A. Romyantseva, A. Yassar, G. Horowitz, S. Lenfant, D. Tondelier, and D. Vuillaume. Low-operating-voltage organic transistors made of bifunctional self-assembled monolayers. *Advanced Functional Materials*, 17(4):597–604, 2007.
- [6] J. C. Love, L. A. Estroff, J. K. Kriebel, R. G. Nuzzo, and G. M. Whitesides. Self-Assembled Monolayers of Thiolates on Metals as a Form of Nanotechnology. *Chem Rev*, 105:1103–1170, 2005.
- [7] G. Tulevski, Q. Miao, M. Fukuto, R. Abram, B. M. Ocko, R. Pindak, M. Steigerwald, C. Kagan, and C. Nuckolls. Attaching organic semiconductors to gate oxides: In situ assembly of monolayer field effect transistors. *J Am Chem Soc*, 126(46):15048–15050, 2004.
- [8] I. M. Hutchings. *Tribology: friction and wear of engineering materials*. Elsevier Limited, 1992.
- [9] P. O. Brown and D. Botstein. Exploring the new world of the genome with DNA microarrays. *Nature Genetics*, 21:33–37, 1999.

-
- [10] J. Genzer and R. R. Bhat. Surface-Bound Soft Matter Gradients. *Langmuir*, 24(6):2294–2317, 2008.
- [11] S. Morgenthaler, C. Zink, and N. D. Spencer. Surface-chemical and -morphological gradients. *Soft Matter*, 4(3):419–434, 2008.
- [12] N. L. Jeon, H. Baskaran, S. K. W. Dertinger, G. M. Whitesides, L. V. D. Water, and M. Toner. Neutrophil chemotaxis in linear and complex gradients of interleukin-8 formed in a microfabricated device. *Nat. Biotechnol.*, 20:826–830, 2002.
- [13] C. A. Parent and P. N. Devreotes. A Cell’s Sense of Direction. *Science*, 284:765–770, 1999.
- [14] M. K. Chaudhury and G. M. Whitesides. How to Make Water Run Uphill. *Science*, 256:1539–1541, 1992.
- [15] S.-W. Lee and P. E. Laibinis. Directed Movement of Liquids on Patterned Surfaces Using Noncovalent Molecular Adsorption. *J Am Chem Soc*, 122(22):5395–5396, 2000.
- [16] K. Ichimura, S.-K. Oh, and M. Nakagawa. Light-Driven Motion of Liquids on a Photoresponsive Surface. *Science*, 288:1624–1626, 2000.
- [17] R. Terrill, K. Balss, Y. Zhang, and P. Bohn. Dynamic Monolayer Gradients: Active Spatiotemporal Control of Alkanethiol Coatings on Thin Gold Films. *J Am Chem Soc*, 122:988–989, 2000.
- [18] S. Morgenthaler, S. Lee, S. Zürcher, and N. D. Spencer. A Simple, Reproducible Approach to the Preparation of Surface-Chemical Gradients. *Langmuir*, 19:10459–10462, 2003.
- [19] S.-H. Choi and B. min Zhang Newby. Micrometer-Scaled Gradient Surfaces Generated Using Contact Printing of Octadecyltrichlorosilane. *Langmuir*, 19:7427–7435, 2003.
- [20] B. Liedberg and P. Tengvall. Molecular Gradients of ω -Substituted Alkanethiols on Gold: Preparation and Characterization. *Langmuir*, 11:3821–3827, 1995.
- [21] Y. S. Lin and V. Hlady. The desorption of ribonuclease A from charge density gradient surfaces studied by spatially-resolved total internal reflection fluorescence. *Colloid Surface B*, 4:65–75, 1995.

- [22] S. Guerin and B. Hayden. Physical vapor deposition method for the high-throughput synthesis of solid-state material libraries. *J Comb Chem*, 8(1):66–73, 2006.
- [23] S. G. P. Tosatti, R. Michel, M. Textor, and N. D. Spencer. Self-Assembled Monolayers of Dodecyl and Hydroxy-dodecyl Phosphates on Both Smooth and Rough Titanium and Titanium Oxide Surfaces. *Langmuir*, 18(9):3537–3548, 2002.
- [24] J. T. Woodward, A. Ulman, and D. K. Schwartz. Self-Assembled Monolayer Growth of Octadecylphosphonic Acid on Mica. *Langmuir*, 12(15):3626–3629, 1996.
- [25] W. Gao, L. Dickinson, C. Grozinger, F. G. Morin, and L. Reven. Self-Assembled Monolayers of Alkylphosphonic Acids on Metal Oxides. *Langmuir*, 12:6429–6435, 1996.
- [26] M. Zwahlen, S. G. P. Tosatti, M. Textor, and G. Hahner. Orientation in Methyl- and Hydroxyl-Terminated Self-Assembled Alkanephosphate Monolayers on Titanium Oxide Surfaces Investigated with Soft X-ray Absorption. *Langmuir*, 18:3957–3962, 2002.
- [27] H. Lee, S. M. Dellatore, W. M. Miller, and P. B. Messersmith. Mussel-Inspired Surface Chemistry for Multifunctional Coatings. *Science*, 318(5849):426–430, 2007.
- [28] S. Morgenthaler, S. Lee, and N. D. Spencer. Submicrometer Structure of Surface-Chemical Gradients Prepared by a Two-Step Immersion Method. *Langmuir*, 22:2706–2711, 2006.
- [29] J. P. Bearinger, G. Stone, A. L. Hiddessen, L. C. Dugan, L. Wu, P. Hailey, J. W. Conway, T. Kuenzler, L. M. Feller, S. Cerritelli, and J. A. Hubbell. Photocatalytic Lithography of Poly(propylene sulfide) Block Copolymers: Toward High-Throughput Nanolithography for Biomolecular Arraying Applications. *Langmuir*, 25(2):1238–1244, 2009.
- [30] G. Tizazu, A. M. Adawi, G. J. Leggett, and D. G. Lidzey. Photopatterning, Etching, and Derivatization of Self-Assembled Monolayers of Phosphonic Acids on the Native Oxide of Titanium. *Langmuir*, 25(18):10746–10753, 2009.
- [31] S. G. P. Tosatti. *Functionalized titanium surfaces for biomedical applications*. PhD thesis, ETH Zurich, 2003.

- [32] J. Fink, M. Thery, A. Azioune, R. Dupont, F. Chatelain, M. Bornens, and M. Piel. Comparative study and improvement of current cell micro-patterning techniques. *Lab Chip*, 7(6):672–680, 2007.
- [33] S. Kennedy, N. Washburn, C. Simon, and E. Amis. Combinatorial screen of the effect of surface energy on fibronectin-mediated osteoblast adhesion, spreading and proliferation. *Biomaterials*, 27(20):3817–3824, 2006.
- [34] T. G. Ruardy, J. M. Schakenraad, H. C. van der Mei, and H. J. Busscher. Preparation and characterization of chemical gradient surfaces and their application for the study of cellular interaction phenomena. *Surf Sci Rep*, 29:3–30, 1997.
- [35] P. van Wachem, A. Hogt, T. Beugeling, J. Feijen, A. Bantjes, J. Detmers, and W. van Aken. Adhesion of cultured human endothelial cells onto methacrylate polymers with varying surface wettability and charge. *Biomaterials*, 8(5):323–328, 1987.
- [36] H. Elwing, S. Welin, A. Askendal, U. Nilsson, and I. Lundstrom. A wettability gradient method for studies of macromolecular interactions at the liquid/solid interface. *Journal of Colloid and Interface Science*, 119(1):203–210, 1987.
- [37] S. Sun and G. J. Leggett. Micrometer and nanometer scale photopatterning of self-assembled monolayers of phosphonic acids on aluminum oxide. *Nano Lett*, 7(12):3753–3758, 2007.
- [38] C. Dulcey, J. Georger, V. Krauthamer, D. Stenger, T. L. Fare, and J. M. Calvert. Deep UV photochemistry of chemisorbed monolayers: patterned coplanar molecular assemblies. *Science*, 252:551–554, 1991.
- [39] K. W. Krosley, D. M. Collard, J. Adamson, and M. A. Fox. Degradation of organophosphonic acids catalyzed by irradiated titanium dioxide. *J Photoch Photobio A*, 69:357–360, 1993.
- [40] H. Ohsaki, Y. Tachibana, A. Mitsui, T. Kamiyama, and Y. Hayashi. High rate deposition of TiO_2 by DC sputtering of the TiO_{2-x} target. *Thin Solid Films*, 392(2):169–173, 2001.
- [41] Y. Sato, A. Uebayashi, N. Ito, T. Kamiyama, and Y. Shigesato. High rate deposition of photocatalytic TiO_2 films by dc magnetron sputtering using a TiO_{2-x} target. *J Vac Sci Technol A*, 26(4):903–907, 2008.
- [42] P. Stefanov, M. Shipochka, P. Stefchev, Z. Raicheva, V. Lazarova, and L. Spassov. XPS characterization of TiO_2 layers deposited on quartz plates. *Journal of Physics: Conference Series*, 100:012039, 2008.

- [43] K. Schenk-Meuser, D. Velten, E. Eisenbarth, V. Biehl, H. Duschner, and J. Brems. XPS analysis of sol-gel-generated mixed-oxide layers for biomedical application. *Surf. Interface Anal.*, 34(1):59–62, 2002.
- [44] S. Frey, K. Heister, M. Zharnikov, and M. Grunze. Modification of semifluorinated alkanethiolate monolayers by low energy electron irradiation. *Phys Chem Chem Phys*, 2(9):1979–1987, 2000.
- [45] T. Geldhauser, P. Leiderer, J. Boneberg, S. Walheim, and T. Schimmel. Generation of Surface Energy Patterns by Single Pulse Laser Interference on Self-Assembled Monolayers. *Langmuir*, 24(22):13155–13160, 2008.
- [46] W. Geyer, V. Stadler, W. Eck, M. Zharnikov, A. Golzhauser, and M. Grunze. Electron-induced crosslinking of aromatic self-assembled monolayers: Negative resists for nanolithography. *Appl Phys Lett*, 75(16):2401–2403, 1999.
- [47] T. P. Kunzler, T. Drobek, C. M. Sprecher, M. Schuler, and N. D. Spencer. Fabrication of material-independent morphology gradients for high-throughput applications. *Appl Surf Sci*, 253(4):2148–2153, 2006.
- [48] L. Eng, M. Abplanalp, and P. Guner. Ferroelectric domain switching in triglycine sulphate and barium-titanate bulk single crystals by scanning force microscopy. *Appl Phys A-Mater*, 66:S679–S683, 1998.
- [49] R. G. Nuzzo, B. R. Zegarski, and L. H. Dubois. Fundamental studies of the chemisorption of organosulfur compounds on gold(111). Implications for molecular self-assembly on gold surfaces. *J Am Chem Soc*, 109(3):733–740, 1987.
- [50] E. B. Troughton, C. D. Bain, G. M. Whitesides, R. G. Nuzzo, D. L. Allara, and M. D. Porter. Monolayer films prepared by the spontaneous self-assembly of symmetrical and unsymmetrical dialkyl sulfides from solution onto gold substrates: structure, properties, and reactivity of constituent functional groups. *Langmuir*, 4(2):365–385, 1988.
- [51] R. Hofer, M. Textor, and N. D. Spencer. Alkyl Phosphate Monolayers, Self-Assembled from Aqueous Solution onto Metal Oxide Surfaces. *Langmuir*, 17(13):4014–4020, 2001.
- [52] S. Wasserman, G. M. Whitesides, I. M. Tidswell, B. M. Ocko, P. Pershan, and J. D. Axe. The structure of self-assembled monolayers of alkylsiloxanes on silicon: a comparison of results from ellipsometry and low-angle X-ray reflectivity. *J Am Chem Soc*, 111(15):5852–5861, 1989.

- [53] A. Ulman. Formation and Structure of Self-Assembled Monolayers. *Chem Rev*, 96:1533–1554, 1996.
- [54] K. Kanazawa, A. Diaz, W. Gill, P. Grant, G. Street, G. Gardini, and J. Kwak. Polypyrrole: An electrochemically synthesized conducting organic polymer. *Synthetic Met*, 1(3):329–336, 1980.
- [55] H. Luo, S. Park, H. Chan, and M. Weaver. Surface oxidation of platinum-group transition metals in ambient gaseous environments: Role of electrochemical versus chemical pathways. *J Phys Chem B*, 104(34):8250–8258, 2000.
- [56] S. S. Kocha, M. W. Peterson, A. J. Nelson, Y. Rosenwaks, D. J. Arent, and J. A. Turner. Investigation of chemical wet-etch surface modification of $\text{Ga}_{0.5}\text{In}_{0.5}\text{P}$ using photoluminescence, X-ray photoelectron spectroscopy, capacitance measurements, and photocurrent-voltage curves. *J Phys Chem*, 99(2):744–749, 1995.
- [57] B. Bhushan, Y. C. Jung, and K. Koch. Micro-, nano- and hierarchical structures for superhydrophobicity, self-cleaning and low adhesion. *Philos T R Soc A*, 367(1894):1631–1672, 2009.
- [58] E. S. Gawalt, M. J. Avaltroni, M. Danahy, B. Silverman, E. L. Hanson, K. Midwood, J. Schwarzbauer, and J. Schwartz. Bonding Organics to Ti Alloys: Facilitating Human Osteoblast Attachment and Spreading on Surgical Implant Materials. *Langmuir*, 19(1):200–204, 2003.
- [59] S. Nishiguchi, H. Kato, H. Fujita, H. Kim, F. Miyaji, T. Kokubo, and T. Nakamura. Enhancement of bone-bonding strengths of titanium alloy implants by alkali and heat treatments. *J Biomed Mater Res*, 48(5):689–696, 1999.
- [60] J. Morgado, N. Barbagallo, A. Charas, M. Matos, L. Alcacer, and F. Cacialli. Self-assembly surface modified indium-tin oxide anodes for single-layer light-emitting diodes. *J Phys D Appl Phys*, 36(5):434–438, 2003.
- [61] C. Ganzorig, K. Kwak, K. Yagi, and M. Fujihira. Fine tuning work function of indium tin oxide by surface molecular design: Enhanced hole injection in organic electroluminescent devices. *Appl Phys Lett*, 79(2):272–274, 2001.
- [62] A. Vilan, A. Shanzer, and D. Cahen. Molecular control over Au/GaAs diodes. *Nature*, 404(6774):166–168, 2000.
- [63] R. S. Dibbell, G. R. Soja, R. M. Hoth, and D. F. Watson. Photocatalytic patterning of monolayers for the site-selective deposition of quantum dots onto TiO_2 surfaces. *Langmuir*, 23(6):3432–3439, 2007.

- [64] J. Moser, S. Punchihewa, P. Infelta, and M. Grätzel. Surface complexation of colloidal semiconductors strongly enhances interfacial electron-transfer rates. *Langmuir*, 7(12):3012–3018, 1991.
- [65] S. Kinoshita and S. Yoshioka. Structural colors in nature: The role of regularity and irregularity in the structure. *ChemPhysChem*, 6(8):1442–1459, 2005.
- [66] M. Quinten. The color of finely dispersed nanoparticles. *Applied Physics B: Lasers and Optics*, 73(4):317–326, 2001.
- [67] J. D. Debord, S. Eustis, S. B. Debord, M. T. Lofye, and L. A. Lyon. Color-tunable colloidal crystals from soft hydrogel nanoparticles. *Adv. Mater.*, 14(9):658–662, 2002.
- [68] K. Cai, M. Frant, J. Bossert, G. Hildebrand, K. Liefeth, and K. Jandt. Surface functionalized titanium thin films: Zeta-potential, protein adsorption and cell proliferation. *Colloid Surface B*, 50(1):1–8, 2006.
- [69] D. M. Spori, T. Drobek, S. Zürcher, M. Ochsner, C. M. Sprecher, A. Muehlebach, and N. D. Spencer. Beyond the lotus effect: Roughness, influences on wetting over a wide surface-energy range. *Langmuir*, 24(10):5411–5417, 2008.
- [70] T. P. Kunzler, T. Drobek, M. Schuler, and N. D. Spencer. Systematic study of osteoblast and fibroblast response to roughness by means of surface-morphology gradients. *Biomaterials*, 28(13):2175–2182, 2007.
- [71] R. Heeb, R. M. Bielecki, S. Lee, and N. D. Spencer. Room-Temperature, Aqueous-Phase Fabrication of Poly(methacrylic acid) Brushes by UV-LED-Induced, Controlled Radical Polymerization with High Selectivity for Surface-Bound Species. *Macromolecules*, 42(22):9124–9132, 2009.
- [72] R. Heeb, S. Lee, N. V. Venkataraman, and N. D. Spencer. Influence of Salt on the Aqueous Lubrication Properties of End-Grafted, Ethylene Glycol-Based Self-Assembled Monolayers. *Acs Appl Mater Inter*, 1(5):1105–1112, 2009.
- [73] Z. Yoshimitsu, A. Nakajima, T. Watanabe, and K. Hashimoto. Effects of surface structure on the hydrophobicity and sliding behavior of water droplets. *Langmuir*, 18:5818–5822, 2002.
- [74] R. Contreras, H. Sahlin, and J. A. Frangos. Titanate biomaterials with enhanced antiinflammatory properties. *J Biomed Mater Res A*, 80A(2):480–485, 2007.

- [75] J. Guo, R. J. Padilla, W. Ambrose, I. J. D. Kok, and L. F. Cooper. The effect of hydrofluoric acid treatment of TiO₂ grit blasted titanium implants on adherent osteoblast gene expression in vitro and in vivo. *Biomaterials*, 28(36):5418–5425, 2007.
- [76] C. Xu, P. H. Shin, L. Cao, J. Wu, and D. Gao. Ordered TiO₂ Nanotube Arrays on Transparent Conductive Oxide for Dye-Sensitized Solar Cells. *Chem Mater*, 22(1):143–148, 2010.
- [77] J. Xia, N. Masaki, K. Jiang, and S. Yanagida. Sputtered Nb₂O₅ as a novel blocking layer at conducting Glass/TiO₂ interfaces in dye-sensitized ionic liquid solar cells. *J Phys Chem C*, 111(22):8092–8097, 2007.
- [78] D. Rosenfeld, P. E. Schmid, S. Szeles, F. Levy, V. Demarne, and A. Grisel. Electrical transport properties of thin-film metal-oxide-metal Nb₂O₅ oxygen sensors. *Sensor Actuat B-Chem*, 37(1-2):83–89, 1996.
- [79] G. Puma and P. Yue. Effect of the radiation wavelength on the rate of photocatalytic oxidation of organic pollutants. *Ind Eng Chem Res*, 41(23):5594–5600, 2002.
- [80] C. Karunakaran and R. Dhanalakshmi. Selectivity in photocatalysis by particulate semiconductors. *Cent Eur J Chem*, 7(1):134–137, 2009.
- [81] C. Damm and G. Israel. Photoelectric properties and photocatalytic activity of silver-coated titanium dioxides. *Dyes and Pigments*, 75(3):612–618, 2007.
- [82] A. Fujishima, T. N. Rao, and D. A. Tryk. Titanium dioxide photocatalysis. *Journal of Photochemistry and Photobiology C: Photochemistry Reviews*, 1:1–21, 2000.
- [83] H. Kim, F. Miyaji, T. Kokubo, S. Nishiguchi, and T. Nakamura. Graded surface structure of bioactive titanium prepared by chemical treatment. *J Biomed Mater Res*, 45(2):100–107, 1999.
- [84] A. Ashrafizadeh and F. Ashrafizadeh. Structural features and corrosion analysis of thermally oxidized titanium. *J Alloy Compd*, 480(2):849–852, 2009.
- [85] Y. Zhang, X. Ma, P. Chen, and D. Yang. Crystallization behaviors of TiO₂ films derived from thermal oxidation of evaporated and sputtered titanium films. *J Alloy Compd*, 480(2):938–941, 2009.
- [86] D. S. R. Krishna, Y. L. Brama, and Y. Sun. Thick rutile layer on titanium for tribological applications. *Tribology International*, 40(2):329–334, 2007.

- [87] F. Borgioli, E. Galvanetto, A. Fossati, and G. Pradelli. Glow-discharge and furnace treatments of Ti-6Al-4V. *Surf Coat Tech*, 184(2-3):255–262, 2004.
- [88] F. Borgioli, E. Galvanetto, F. Iozzelli, and G. Pradelli. Improvement of wear resistance of Ti-6Al-4V alloy by means of thermal oxidation. *Mater Lett*, 59(17):2159–2162, 2005.
- [89] M. A. Khan, H.-T. Jung, and O.-B. Yang. Opto-electronic properties of titania nanotubes. *Chem Phys Lett*, 458(1-3):134–137, 2008.
- [90] M. Grätzel. Photoelectrochemical cells. *Nature*, 414(6861):338–344, 2001.
- [91] J. Fendler. Chemical self-assembly for electronic applications. *Chem Mater*, 13(10):3196–3210, 2001.
- [92] A. Ennaoui, B. Sankapal, V. Skryshevsky, and M. Lux-Steiner. TiO₂ and TiO₂-SiO₂ thin films and powders by one-step soft-solution method: Synthesis and characterizations. *Solar Energy Materials and Solar Cells*, 90(10):1533–1541, 2006.
- [93] R. Ahuja and L. Dubrovinsky. High-pressure structural phase transitions in TiO₂ and synthesis of the hardest known oxide. *J Phys-Condens Mat*, 14(44):10995–10999, 2002.
- [94] R. Romero, J. Ramos-Barrado, F. Martin, and D. Leinen. Nb₂O₅ thin films obtained by chemical spray pyrolysis. *Surf. Interface Anal.*, 36(8):888–891, 2004.
- [95] M. Radecka, K. Zakrzewska, H. Czternastek, T. Stapiński, and S. Debrus. The influence of thermal annealing on the structural, electrical and optical properties of TiO_{2-x} thin films. *Appl Surf Sci*, 65-6:227–234, 1993.
- [96] M. Kuo, C. Chen, C. Hua, H. Yang, and P. Shen. Density functional theory calculations of dense TiO₂ polymorphs: Implication for visible-light-responsive photocatalysts. *J Phys Chem B*, 109(18):8693–8700, 2005.
- [97] G. Brauer. Die Oxyde des Niobs. *Zeitschrift für anorganische und allgemeine Chemie*, 248(1):1–31, 1941.
- [98] H. Schäfer, R. Gruehn, and F. Schulte. Die Modifikationen des Niobpentoxids. *Angewandte Chemie*, 78(1):28–41, 1970.
- [99] D. Cromer and K. Herrington. The Structures of Anatase and Rutile. *J Am Chem Soc*, 77(18):4708–4709, 1955.

- [100] W. Baur. Atomabstände und Bindungswinkel im Brookit, TiO_2 . *Acta Cryst.*, 14(3):214–216, 1961.
- [101] A. Pawlicka, M. Atik, and M. Aegerter. Synthesis of multicolor Nb_2O_5 coatings for electrochromic devices. *Thin Solid Films*, 301(1-2):236–241, 1997.
- [102] M. Hoffmann, S. Martin, W. Choi, and D. Bahnemann. Environmental Applications of Semiconductor Photocatalysis. *Chem Rev*, 95(1):69–96, 1995.
- [103] S. Livraghi, K. Elghniji, A. M. Czoska, M. C. Paganini, E. Giamello, and M. Ksibi. Nitrogen-doped and nitrogen-fluorine-codoped titanium dioxide. Nature and concentration of the photoactive species and their role in determining the photocatalytic activity under visible light. *J Photoch Photobio A*, 205(2-3):93–97, 2009.
- [104] X. Chen, T. Yu, X. Fan, H. Zhang, Z. Li, J. Ye, and Z. Zou. Enhanced activity of mesoporous Nb_2O_5 for photocatalytic hydrogen production. *Appl Surf Sci*, 253(20):8500–8506, 2007.
- [105] V. Stone and R. Davis. Synthesis, characterization, and photocatalytic activity of titania and niobia mesoporous molecular sieves. *Chem Mater*, 10(5):1468–1474, 1998.
- [106] S.-C. Li, J.-G. Wang, P. Jacobson, X.-Q. Gong, A. Selloni, and U. Diebold. Correlation between Bonding Geometry and Band Gap States at Organic-Inorganic Interfaces: Catechol on Rutile $\text{TiO}_2(110)$. *J Am Chem Soc*, 131:980–984, 2009.
- [107] S.-C. Li, L.-N. Chu, X.-Q. Gong, and U. Diebold. Hydrogen Bonding Controls the Dynamics of Catechol Adsorbed on a $\text{TiO}_2(110)$ Surface. *Science*, 328(5980):882–884, 2010.
- [108] M. Gnauck, E. Jaehne, T. Blaettler, S. G. P. Tosatti, M. Textor, and H.-J. P. Adler. Carboxy-Terminated Oligo(ethylene glycol)-Alkane Phosphate: Synthesis and Self-Assembly on Titanium Oxide Surfaces. *Langmuir*, 23:377–381, 2007.
- [109] D. Mardare and P. Hones. Optical dispersion analysis of TiO_2 thin films based on variable-angle spectroscopic ellipsometry measurements. *Mat Sci Eng B-Solid*, 68(1):42–47, 1999.
- [110] G. J. Babonas. Spectroscopic ellipsometry of TiO_2/Si . *Proc. SPIE*, 5122:50–55, 2003.

- [111] J. Masse, H. Szymanowski, O. Zabeida, A. Amassian, J. Klembersapieha, and L. Martinu. Stability and effect of annealing on the optical properties of plasma-deposited Ta₂O₅ and Nb₂O₅ films. *Thin Solid Films*, 515(4):1674–1682, 2006.
- [112] J. Martinez-Anton and E. Bernabeu. Simultaneous determination of film thickness and refractive index by interferential spectrogoniometry. *Opt Commun*, 132(3-4):321–328, 1996.
- [113] W. Lukosz and P. Pliska. Determination of thickness and refractive index of SiO₂ films on silicon wafers using an Abbe refractometer. *Opt Commun*, 85(5-6):381–384, 1991.
- [114] B. von Blanckenhagen, D. Tonova, and J. Ullmann. Application of the Tauc-Lorentz Formulation to the Interband Absorption of Optical Coating Materials. *Applied Optics*, 41(16):3137–3141, 2002.
- [115] R. I. Bickley, T. Gonzalez-Carreno, J. S. Lees, L. Palmisanod, and R. J. D. Tilley. A structural investigation of titanium dioxide photocatalysts. *J Solid State Chem*, 92(1):178–190, 1991.
- [116] S. Lenfant, C. Krzeminski, C. Delerue, G. Allan, and D. Vuillaume. Molecular rectifying diodes from self-assembly on silicon. *Nano Lett*, 3(6):741–746, 2003.
- [117] N. Park, T. Kim, and S. Park. Band gap engineering of amorphous silicon quantum dots for light-emitting diodes. *Appl Phys Lett*, 78(17):2575–2577, 2001.
- [118] S. Heike, Y. Wada, S. Kondo, M. Lutwyche, K. Murayama, and H. Kuroda. Evaluation of Thin Silicon Dioxide Layers by Beam Assisted Scanning Tunneling Microscope. *Jpn J Appl Phys 1*, 34(2B):1376–1380, 1995.
- [119] G. Tan, M. Lemon, D. Jones, and R. French. Optical properties and London dispersion interaction of amorphous and crystalline SiO₂ determined by vacuum ultraviolet spectroscopy and spectroscopic ellipsometry. *Phys Rev B*, 72(20):205117, 2005.
- [120] G. Kenausis, J. Voros, D. L. Elbert, N. Huang, R. Hofer, L. A. Ruiz-Taylor, M. Textor, J. Hubbell, and N. D. Spencer. Poly(L-lysine)-*g*-poly(ethylene glycol) layers on metal oxide surfaces: Attachment mechanism and effects of polymer architecture on resistance to protein adsorption. *J Phys Chem B*, 104(14):3298–3309, 2000.

- [121] N. Huang, R. Michel, J. Voros, M. Textor, R. Hofer, A. Rossi, D. L. Elbert, J. Hubbell, and N. D. Spencer. Poly(L-lysine)-*g*-poly(ethylene glycol) layers on metal oxide surfaces: Surface-analytical characterization and resistance to serum and fibrinogen adsorption. *Langmuir*, 17(2):489–498, 2001.
- [122] E. S. Gawalt, M. J. Avaltroni, N. Koch, and J. Schwartz. Self-Assembly and Bonding of Alkanephosphonic Acids on the Native Oxide Surface of Titanium. *Langmuir*, 17:5736–5738, 2001.
- [123] K. Shafi, A. Ulman, X. Yan, N. Yang, M. Himmelhaus, and M. Grunze. Sonochemical preparation of silane-coated titania particles. *Langmuir*, 17(5):1726–1730, 2001.
- [124] R. Helmy and A. Fadeev. Self-assembled monolayers supported on TiO₂: Comparison of C₁₈H₃₇SiX₃ (X = H, Cl, OCH₃), C₁₈H₃₇Si(CH₃)₂Cl, and C₁₈H₃₇PO(OH)₂. *Langmuir*, 18(23):8924–8928, 2002.
- [125] L. Feuz. *On the conformation of graft-copolymers with polyelectrolyte backbone in solution and adsorbed on surfaces*. PhD thesis, ETH Zurich, 2006.
- [126] R. Konradi, B. Pidhatika, A. Muehlebach, and M. Textor. Poly-2-methyl-2-oxazoline: A peptide-like polymer for protein-repellent surfaces. *Langmuir*, 24(3):613–616, 2008.
- [127] J. Sagiv. Organized monolayers by adsorption. 1. Formation and structure of oleophobic mixed monolayers on solid surfaces. *J Am Chem Soc*, 102(1):92–98, 1980.
- [128] R. Michel, J. W. Lussi, G. Csucs, I. Reviakine, G. Danuser, B. Ketterer, J. A. Hubbell, M. Textor, and N. D. Spencer. Selective Molecular Assembly Patterning: A New Approach to Micro- and Nanochemical Patterning of Surfaces for Biological Applications. *Langmuir*, 18:3281–3287, 2002.
- [129] O. Carp, C. Huisman, and A. Reller. Photoinduced reactivity of titanium dioxide. *Progress in Solid State Chemistry*, 32:33–177, 2004.
- [130] U. Diebold. The surface science of titanium dioxide. *Surf Sci Rep*, 48(5-8):53–229, 2003.
- [131] V. S. Santana and N. R. C. F. Machado. Photocatalytic degradation of the vinasse under solar radiation. *Catal Today*, 133:606–610, 2008.
- [132] A. G. S. Prado, L. B. Bolzon, C. P. Pedroso, A. O. Moura, and L. L. Costa. Nb₂O₅ as efficient and recyclable photocatalyst for indigo carmine degradation. *Applied Catalysis B*, 82(3-4):219–224, 2008.

- [133] L. Zhou, S. Yan, B. Tian, J. Zhang, and M. Anpo. Preparation of TiO₂-SiO₂ film with high photocatalytic activity on PET substrate. *Mater Lett*, 60(3):396–399, 2006.
- [134] H. Kominami, K. Oki, M. Kohno, S. Onoue, Y. Kera, and B. Ohtani. Novel solvothermal synthesis of niobium(v) oxide powders and their photocatalytic activity in aqueous suspensions. *Journal of Materials Chemistry*, 11(2):604–609, 2001.
- [135] A. Mills and S. LeHunte. An overview of semiconductor photocatalysis. *J Photoch Photobio A*, 108(1):1–35, 1997.
- [136] A. Fujishima, X. Zhang, and D. A. Tryk. TiO₂ photocatalysis and related surface phenomena. *Surf Sci Rep*, 63(12):515–582, 2008.
- [137] T. Essam, M. Alyamin, O. Eltayeb, B. Mattiasson, and B. Guieysse. Solar-based detoxification of phenol and p-nitrophenol by sequential TiO₂ photocatalysis and photosynthetically aerated biological treatment. *Water Research*, 41(8):1697–1704, 2007.
- [138] N. Serpone, J. Martin, S. Horikoshi, and H. Hidaka. Photocatalyzed oxidation and mineralization of branched and oxidized C4 and C5 aliphatic acids in UV-irradiated aqueous titania dispersions adsorption and degradation dynamics. *J Photoch Photobio A*, 170(1):51–60, 2005.
- [139] Y. Shen, T. Xiong, J. Shang, and K. Yang. Preparation of Nb₂O₅ and N co-doped TiO₂ photocatalysts and their enhanced photocatalytic activities under visible light. *Res Chem Intermediat*, 34(4):353–363, 2008.
- [140] U. Akpan and B. Hameed. Parameters affecting the photocatalytic degradation of dyes using TiO₂-based photocatalysts: A review. *Journal of Hazardous Materials*, 170(2-3):520–529, 2009.
- [141] D. Elbert and J. Hubbell. Self-assembly and steric stabilization at heterogeneous, biological surfaces using adsorbing block copolymers. *Chemistry & Biology*, 5(3):177–183, 1998.
- [142] M. Pomerantz, A. Segmüller, L. Netzer, and J. Sagiv. Coverage of Si substrates by self-assembling monolayers and multilayers as measured by IR, wettability and X-ray diffraction. *Thin Solid Films*, 132(1-4):153–162, 1985.
- [143] I. M. Tidswell, B. M. Ocko, P. Pershan, S. Wasserman, G. M. Whitesides, and J. D. Axe. X-ray specular reflection studies of silicon coated by organic monolayers (alkylsiloxanes). *Phys Rev B*, 41(2):1111–1128, 1990.

- [144] I. Turyan and D. Mandler. Selective determination of Cr(VI) by a self-assembled monolayer-based electrode. *Anal Chem*, 69(5):894–897, 1997.
- [145] J. Rodriguez, D. Wheeler, and J. McCusker. Density functional studies of a Heisenberg spin coupled chromium-semiquinone complex and its chromium-catechol analog. *J Am Chem Soc*, 120(46):12051–12068, 1998.
- [146] C. Benelli, A. Dei, D. Gatteschi, H. U. Güdel, and L. Pardi. Large intensity enhancement of the spin-forbidden $^4A_{2g} - ^2E_g$ transition in chromium(III)-semiquinone complexes. *Inorg Chem*, 28(16):3089–3091, 1989.
- [147] P. K. Grzyska and R. P. Hausinger. Cr-II reactivity of taurine/alpha-ketoglutarate dioxygenase. *Inorg Chem*, 46(24):10087–10092, 2007.
- [148] N. V. Venkataraman, S. Zürcher, A. Rossi, and S. Lee. Spatial Tuning of the Metal Work Function by Means of Alkanethiol and Fluorinated Alkanethiol Gradients. *J Phys Chem C*, 113(14):5620–5628, 2009.
- [149] L. M. Feller, S. Cerritelli, M. Textor, J. A. Hubbell, and S. G. P. Tosatti. Influence of Poly(propylene sulfide-block-ethylene glycol) Di- and Triblock Copolymer Architecture on the Formation of Molecular Adlayers on Gold Surfaces and Their Effect on Protein Resistance: A Candidate for Surface Modification in Biosensor Research. *Langmuir*, 38:10503–10510, 2005.
- [150] C. D. Bain and G. M. Whitesides. Depth sensitivity of wetting: monolayers of ω -mercapto ethers on gold. *J Am Chem Soc*, 110(17):5897–5898, 1988.
- [151] R. G. Nuzzo, F. A. Fusco, and D. L. Allara. Spontaneously organized molecular assemblies. 3. Preparation and properties of solution adsorbed monolayers of organic disulfides on gold surfaces. *J Am Chem Soc*, 109(8):2358–2368, 1987.
- [152] P. A. Brooksby, D. R. Schiel, and A. D. Abell. Electrochemistry of Catechol Terminated Monolayers with Cu(II), Ni(II) and Fe(III) Cations: A Model for the Marine Adhesive Interface. *Langmuir*, 24(16):9074–9081, 2008.
- [153] H. A. Biebuyck, C. D. Bain, and G. M. Whitesides. Comparison of Organic Monolayers on Polycrystalline Gold Spontaneously Assembled from Solutions Containing Dialkyl Disulfides or Alkanethiols. *Langmuir*, 10(6):1825–1831, 1994.
- [154] M. Browne and P. Gregson. Surface modification of titanium alloy implants. *Biomaterials*, 15(11):894–898, 1994.
- [155] R. G. Nuzzo and D. L. Allara. Adsorption of bifunctional organic disulfides on gold surfaces. *J Am Chem Soc*, 105(13):4481–4483, 1983.

- [156] A. Hozumi, B. Kim, and T. J. McCarthy. Hydrophobicity of Perfluoroalkyl Isocyanate Monolayers on Oxidized Aluminum Surfaces. *Langmuir*, 25(12):6834–6840, 2009.
- [157] C. Loppacher, U. Zerweck, D. Koehler, M. Rodenstein, E. Jaehne, R. Luther, H.-J. P. Adler, and L. M. Eng. Physical vapour deposition of alkyl phosphonic acid on mica and HOPG investigated by NC-AFM. *Nanotechnology*, 18(8):084003, 2007.
- [158] P. Hoffmann, M. Stelzle, and J. Rabolt. Vapor phase self-assembly of fluorinated monolayers on silicon and germanium oxide. *Langmuir*, 13(7):1877–1880, 1997.
- [159] B. Kippelen. Optical materials - Self-assembly reaches new heights. *Nat Mater*, 3(12):841–843, 2004.
- [160] F. Löffler and C. Siewert. Homogeneous coatings inside cylinders. *Surf Coat Tech*, 177:355–359, 2004.
- [161] C. D. Bain, E. B. Troughton, Y.-T. Tao, J. Evall, G. M. Whitesides, and R. G. Nuzzo. Formation of monolayer films by the spontaneous assembly of organic thiols from solution onto gold. *J Am Chem Soc*, 111(1):321–335, 1989.
- [162] C. D. Bain and G. M. Whitesides. Formation of two-component surfaces by the spontaneous assembly of monolayers on gold from solutions containing mixtures of organic thiols. *J Am Chem Soc*, 110(19):6560–6561, 1988.
- [163] C. E. D. Chidsey and D. Loiacono. Chemical functionality in self-assembled monolayers: structural and electrochemical properties. *Langmuir*, 6(3):682–691, 1990.
- [164] H.-B. Liu, N. V. Venkataraman, N. D. Spencer, M. Textor, and S.-J. Xiao. Structural evolution of self-assembled alkanephosphate monolayers on TiO₂. *ChemPhysChem*, 9(14):1979–1981, 2008.
- [165] J. Lahann, S. Mitragotri, T.-N. Tran, H. Kaido, J. Sundaram, I. S. Choi, S. Hoffer, G. Somorjai, and R. Langer. A Reversibly Switching Surface. *Science*, 299(5605):371–374, 2003.
- [166] R. G. Nuzzo, L. H. Dubois, and D. L. Allara. Fundamental studies of microscopic wetting on organic surfaces. 1. Formation and structural characterization of a self-consistent series of polyfunctional organic monolayers. *J Am Chem Soc*, 112(2):558–569, 1990.

- [167] M. Textor, L. Ruiz, R. Hofer, A. Rossi, K. Feldman, G. Hahner, and N. D. Spencer. Structural chemistry of self-assembled monolayers of octadecylphosphoric acid on tantalum oxide surfaces. *Langmuir*, 16(7):3257–3271, 2000.
- [168] M. Wagner, S. Pasche, D. Castner, and M. Textor. Characterization of poly(L-lysine)-graft-poly(ethylene glycol) assembled monolayers on niobium pentoxide substrates using time-of-flight secondary ion mass spectrometry and multivariate analysis. *Anal Chem*, 76(5):1483–1492, 2004.
- [169] L. A. Ruiz-Taylor, T. L. Martin, F. Zaugg, K. Witte, P. Indermuhle, S. Nock, and P. Wagner. Monolayers of derivatized poly(L-lysine)-grafted poly(ethylene glycol) on metal oxides as a class of biomolecular interfaces. *P Natl Acad Sci Usa*, 98(3):852–857, 2001.
- [170] R. N. Kapoor, S. Prakash, and P. N. Kapoor. Organic derivatives of niobium and tantalum. Reactions of Niobium and Tantalum Pentaethoxides with catechol. *Zeitschrift für anorganische und allgemeine Chemie*, 353:109–112, 1966.
- [171] D. M. Spori, N. V. Venkataraman, S. G. P. Tosatti, F. Durmaz, N. D. Spencer, and S. Zürcher. Influence of alkyl chain length on phosphate self-assembled monolayers. *Langmuir*, 23(15):8053–8060, 2007.
- [172] M. Pellerite, T. Dunbar, L. Boardman, and E. Wood. Effects of fluorination on self-assembled monolayer formation from alkanephosphonic acids on aluminum: Kinetics and structure. *J Phys Chem B*, 107(42):11726–11736, 2003.
- [173] D. Barriet and T. R. Lee. Fluorinated self-assembled monolayers: composition, structure and interfacial properties. *Current Opinion in Colloid & Interface Science*, 8(3):236–242, 2003.
- [174] C. Naud, P. Calas, and A. Commeyras. Critical influence of the fluorinated chain length in the self-assembly of terminally perfluorinated alkanethiol monolayers on gold surfaces. An electrochemical study. *Langmuir*, 17(16):4851–4857, 2001.
- [175] J. Park, A. Smith, and T. Lee. Loosely packed self-assembled monolayers on gold generated from 2-alkyl-2-methylpropane-1,3-dithiols. *Langmuir*, 20(14):5829–5836, 2004.
- [176] J. Park, A. Vo, D. Barriet, Y. Shon, and T. Lee. Systematic control of the packing density of self-assembled monolayers using bidentate and tridentate chelating alkanethiols. *Langmuir*, 21(7):2902–2911, 2005.

- [177] G. Lecollinet, N. Delorme, M. Edely, A. Gibaud, J.-F. Bardeau, F. Hindre, F. Boury, and D. Portet. Self-Assembled Monolayers of Bisphosphonates: Influence of Side Chain Steric Hindrance. *Langmuir*, 25(14):7828–7835, 2009.
- [178] U. Terranova and D. R. Bowler. Adsorption of Catechol on TiO₂ Rutile (100): A Density Functional Theory Investigation. *J Phys Chem C*, 114:6491–6495, 2010.
- [179] G. Guerrero, P. Mutin, and A. Vioux. Anchoring of Phosphonate and Phosphinate Coupling Molecules on Titania Particles. *Chem Mater*, 13(11):4367–4373, 2001.
- [180] B. Malisova, S. G. P. Tosatti, M. Textor, K. Gademann, and S. Zürcher. Poly(ethylene glycol) Adlayers Immobilized to Metal Oxide Substrates Through Catechol Derivatives: Influence of Assembly Conditions on Formation and Stability. *Langmuir*, 26(6):4018–4026, 2010.
- [181] M. Schmidt and S. G. Steinemann. XPS studies of amino acids adsorbed on titanium dioxide surfaces. *Fresenius J Anal Chem*, 341(5-6):412–415, 1991.
- [182] M. Nooney, T. Murrell, J. Corneille, E. Rusert, L. Hossner, and D. Goodman. A spectroscopic investigation of phosphate adsorption onto iron oxides. *J Vac Sci Technol A*, 14(3):1357–1361, 1996.
- [183] N. Adden, L. J. Gamble, D. G. Castner, A. Hoffmann, G. Gross, and H. Menzel. Phosphonic Acid Monolayers for Binding of Bioactive Molecules to Titanium Surfaces. *Langmuir*, 22:8197–8204, 2006.
- [184] C. Viornerly, Y. Chevolut, D. Leonard, B. Aronsson, P. Pechy, H. Mathieu, P. Descouts, and M. Gratzel. Surface modification of titanium with phosphonic acid to improve bone bonding: Characterization by XPS and ToF-SIMS. *Langmuir*, 18(7):2582–2589, 2002.
- [185] E. Cavalieri, K. Li, N. Balu, M. Saeed, P. Devanesan, S. Higginbotham, J. Zhao, M. L. Gross, and E. G. Rogan. Catechol ortho-quinones: the electrophilic compounds that form depurinating DNA adducts and could initiate cancer and other diseases. *Carcinogenesis*, 23(6):1071–1077, 2002.
- [186] E. Eldrup. Significance and origin of DOPA, DOPAC, and dopamine-sulphate in plasma, tissues and cerebrospinal fluid. *Dan Med Bull*, 51(1):34–62, 2004.
- [187] A. M. Krstulovic. Investigations of catecholamine metabolism using high-performance liquid chromatography : Analytical methodology and clinical applications. *J Chromatogr*, 229(1):1–34, 1982.

- [188] A. Napolitano, M. Dischia, C. Costantini, and G. Protà. A New Oxidation Pathway of the Neurotoxin 6-Aminodopamine. Isolation and Characterisation of a Dimer with a Tetrahydro[3,4a]iminoethanophenoxazine Ring System. *Tetrahedron*, 48(39):8515–8522, 1992.
- [189] Y. Itou, S. Okada, and M. Murakami. Two structural isomeric siderophores from the freshwater cyanobacterium *Anabaena cylindrica* (NIES-19). *Tetrahedron*, 57(44):9093–9099, 2001.
- [190] S. Zürcher, D. Wäckerlin, Y. Bethuel, B. Malisova, M. Textor, S. G. P. Tosatti, and K. Gademann. Biomimetic Surface Modifications Based on the Cyanobacterial Iron Chelator Anachelin. *J Am Chem Soc*, 128(4):1064–1065, 2006.
- [191] M. Weinhold, S. Soubatch, R. Temirov, M. Rohlfing, B. Jastorff, F. S. Tautz, and C. Doose. Structure and bonding of the multifunctional amino acid L-DOPA on Au(110). *J Phys Chem B*, 110(47):23756–23769, 2006.
- [192] J. L. Dalsin, L. Lin, S. G. P. Tosatti, J. Voros, M. Textor, and P. B. Messersmith. Protein resistance of titanium oxide surfaces modified by biologically inspired mPEG-DOPA. *Langmuir*, 21(2):640–646, 2005.
- [193] J.-Y. Wach, B. Malisova, S. Bonazzi, S. G. P. Tosatti, M. Textor, S. Zürcher, and K. Gademann. Protein-Resistant Surfaces through Mild Dopamine Surface Functionalization. *Chem-Eur J*, 14(34):10579–10584, 2008.
- [194] A. Rosenheim and E. Roehrich. Innerkomplexe Verbindungen des fünfwertigen Niobs und Tantals. *Zeitschrift für anorganische und allgemeine Chemie*, 204:342–350, 1932.
- [195] Y. Xu, W.-K. Chen, S.-H. Liu, M.-J. Cao, and J.-Q. Li. Interaction of photoactive catechol with TiO₂ anatase (101) surface: A periodic density functional theory study. *Chem. Phys.*, 331(2-3):275–282, 2007.
- [196] S. D. Evans, T. Flynn, A. Ulman, and G. Beamson. XPS imaging of patterned self-assembled monolayers containing perfluorinated alkyl chains. *Surf. Interface Anal.*, 24(3):187–192, 1996.
- [197] R. Wallace, P. Chen, S. Henck, and D. Webb. Adsorption of perfluorinated n-alkanoic acids on native aluminum oxide surfaces. *J Vac Sci Technol A*, 13(3):1345–1350, 1995.
- [198] T. Blättler, S. Pasche, M. Textor, and H. Griesser. High salt stability and protein resistance of poly(L-lysine)-*g*-poly(ethylene glycol) copolymers covalently immobilized via aldehyde plasma polymer interlayers on inorganic and polymeric substrates. *Langmuir*, 22(13):5760–5769, 2006.

- [199] W. Hartung, T. Drobek, S. Lee, S. Zürcher, and N. D. Spencer. The influence of anchoring-group structure on the lubricating properties of brush-forming graft copolymers in an aqueous medium. *Tribol Lett*, 31(2):119–128, 2008.
- [200] M. Muller, S. Lee, H. Spikes, and N. D. Spencer. The influence of molecular architecture on the macroscopic lubrication properties of the brush-like copolyelectrolyte poly(L-lysine)-*g*-poly(ethylene glycol) (PLL-*g*-PEG) adsorbed on oxide surfaces. *Tribol Lett*, 15(4):395–405, 2003.
- [201] S. Lee, M. Muller, M. Ratoi-Salagean, J. Voros, S. Pasche, S. D. Paul, H. Spikes, M. Textor, and N. D. Spencer. Boundary lubrication of oxide surfaces by Poly(L-lysine)-*g*-poly(ethylene glycol) (PLL-*g*-PEG) in aqueous media. *Tribol Lett*, 15(3):231–239, 2003.
- [202] S. Saxer, C. Portmann, S. G. P. Tosatti, K. Gademann, S. Zürcher, and M. Textor. Surface Assembly of Catechol-Functionalized Poly(l-lysine)-graft-poly(ethylene glycol) Copolymer on Titanium Exploiting Combined Electrostatically Driven Self-Organization and Biomimetic Strong Adhesion. *Macromolecules*, 43:1050–1060, 2010.
- [203] S. Plummer, Q. Wang, P. Bohn, R. Stockton, and M. Schwartz. Electrochemically derived gradients of the extracellular matrix protein fibronectin on gold. *Langmuir*, 19(18):7528–7536, 2003.
- [204] S. D. Evans and A. Ulman. Surface potential studies of alkyl-thiol monolayers adsorbed on gold. *Chem Phys Lett*, 170(5-6):462–466, 1990.
- [205] H. Elwing and C.-G. Gölander. Protein and detergent interaction phenomena on solid surfaces with gradients in chemical composition. *Advances in Colloid and Interface Science*, 32:317–339, 1990.
- [206] N. L. Jeon, S. K. W. Dertinger, D. T. Chiu, I. S. Choi, A. D. Stroock, and G. M. Whitesides. Generation of Solution and Surface Gradients Using Microfluidic Systems. *Langmuir*, 16:8311–8316, 2000.
- [207] S. Zhang, L. Yan, M. Altman, M. Lasse, H. Nugent, F. Frankel, D. Lauffenburger, G. M. Whitesides, and A. Rich. Biological surface engineering: a simple system for cell pattern formation. *Biomaterials*, 20(13):1213–1220, 1999.
- [208] J. Liu and V. Hlady. Chemical pattern on silica surface prepared by UV irradiation of 3-mercaptopropyltriethoxy silane layer: Surface characterization and fibrinogen adsorption. *Colloid Surface B*, 8(1-2):25–37, 1996.

- [209] O. Shekhah, H. Wang, T. Strunskus, P. Cyganik, D. Zacher, R. Fischer, and C. Woell. Layer-by-layer growth of oriented metal organic polymers on a functionalized organic surface. *Langmuir*, 23(14):7440–7442, 2007.
- [210] Y. Xia, X. Zhao, and G. M. Whitesides. Pattern transfer: Self-assembled monolayers as ultrathin resists. *Microelectronic Engineering*, 32(1-4):255–268, 1996.
- [211] D. Falconnet, A. Koenig, T. Assi, and M. Textor. A combined photolithographic and molecular-assembly approach to produce functional micropatterns for applications in the biosciences. *Advanced Functional Materials*, 14(8):749–756, 2004.
- [212] M. Zharnikov, W. Geyer, A. Golzhauser, S. Frey, and M. Grunze. Modification of alkanethiolate monolayers on Au-substrate by low energy electron irradiation: Alkyl chains and the S/Au interface. *Phys Chem Chem Phys*, 1(13):3163–3171, 1999.
- [213] M. Zharnikov, S. Frey, K. Heister, and M. Grunze. Modification of alkanethiolate monolayers by low energy electron irradiation: Dependence on the substrate material and on the length and isotopic composition of the alkyl chains. *Langmuir*, 16(6):2697–2705, 2000.
- [214] K. Yoshihara and A. Tanaka. Interlaboratory study on the degradation of poly(vinyl chloride), nitrocellulose and poly(tetrafluoroethylene) by X-rays in XPS. *Surf. Interface Anal.*, 33(3):252–258, 2002.
- [215] A. A. Brown, O. Azzaroni, and W. T. S. Huck. Photoresponsive Polymer Brushes for Hydrophilic Patterning. *Langmuir*, 25(3):1744–1749, 2009.
- [216] K. Critchley, L. Zhang, H. Fukushima, M. Ishida, T. Shimoda, R. J. Bushby, and S. D. Evans. Soft-UV photolithography using self-assembled monolayers. *J Phys Chem B*, 110(34):17167–17174, 2006.
- [217] R. Smith, P. Lewis, and P. Weiss. Patterning self-assembled monolayers. *Progress in Surface Science*, 75(1-2):1–68, 2004.
- [218] M. Himmerlich, V. Yanev, A. Opitz, A. Keppler, J. Schaefer, and S. Krischok. Effects of X-ray radiation on the surface chemical composition of plasma deposited thin fluorocarbon films. *Polymer Degradation and Stability*, 93(3):700–706, 2008.
- [219] R. L. Graham, C. D. Bain, H. A. Biebuyck, and P. E. Laibinis. Damage to trifluoroacetamido-terminated organic self-assembled monolayers (SAMs) on

- aluminum, titanium, copper and gold by aluminum K.alpha. X-rays is due principally to electrons. *J Phys Chem*, 97(37):9456–9464, 1993.
- [220] K. Heister, M. Zharnikov, M. Grunze, L. Johansson, and A. Ulman. Characterization of X-ray induced damage in alkanethiolate monolayers by high-resolution photoelectron spectroscopy. *Langmuir*, 17(1):8–11, 2001.
- [221] A. Azioune, M. Storch, M. Bornens, M. They, and M. Piel. Simple and rapid process for single cell micro-patterning. *Lab Chip*, 9(11):1640–1642, 2009.
- [222] T. Tatsuma, W. Kubo, and A. Fujishima. Patterning of Solid Surfaces by Photocatalytic Lithography Based on the Remote Oxidation Effect of TiO₂. *Langmuir*, 18:9632–9634, 2002.
- [223] T. Tatsuma and W. Kubo. Photocatalytic lithography based on photocatalytic remote oxidation. *J Photopolym Sci Tec*, 20(1):83–86, 2007.
- [224] H. Notsu, W. Kubo, I. Shitanda, and T. Tatsuma. Super-hydrophobic/super-hydrophilic patterning of gold surfaces by photocatalytic lithography. *Journal of Materials Chemistry*, 15:1523–1527, 2005.
- [225] T. Ishida, N. Nishida, S. Tsuneda, M. Hara, H. Sasabe, and W. Knoll. Alkyl chain length effect on growth kinetics of n-alkanethiol self-assembled monolayers on gold studied by X-ray photoelectron spectroscopy. *Jpn J Appl Phys* 2, 35(12B):L1710–L1713, 1996.
- [226] P. E. Laibinis, M. A. Fox, J. Folkers, and G. M. Whitesides. Comparisons of self-assembled monolayers on silver and gold: mixed monolayers derived from HS(CH₂)₂₁X and HS(CH₂)₁₀Y (X, Y = CH₃, CH₂OH) have similar properties. *Langmuir*, 7(12):3167–3173, 1991.
- [227] R. F. Reilman, A. Msezane, and S. T. Manson. Relative intensities in photoelectron spectroscopy of atoms and molecules. *Journal of Electron Spectroscopy and Related Phenomena*, 8(5):389–394, 1976.
- [228] J. H. Scofield. Hartree-Slater subshell photoionization cross-sections at 1254 and 1487 eV. *Journal of Electron Spectroscopy and Related Phenomena*, 8(2):129–137, 1976.
- [229] A. Einstein. Generation and conversion of light with regard to a heuristic point of view. *Ann Phys-Berlin*, 17(6):132–148, 1905.
- [230] P. J. Cumpson and M. P. Seah. Elastic Scattering Corrections in AES and XPS. II. Estimating Attenuation Lengths and Conditions Required for their Valid

- Use in Overlayer/ Substrate Experiments. *Surf. Interface Anal.*, 25:430–446, 1997.
- [231] P. J. Cumpson. Estimation of inelastic mean free paths for polymers and other organic materials: use of quantitative structure-property relationships. *Surf. Interface Anal.*, 31(1):23–34, 2001.
- [232] M. P. Seah and W. Dench. Quantitative electron spectroscopy of surfaces: a standard data base for electron inelastic mean free paths in solids. *Surf. Interface Anal.*, 1(1):2–11, 1979.
- [233] K. Lau, J. Caulfield, and K. Gleason. Variable angle spectroscopic ellipsometry of fluorocarbon films from hot filament chemical vapor deposition. *J Vac Sci Technol A*, 18:2404–2411, 2000.
- [234] K. Postava, M. Aoyama, T. Yamaguchi, and H. Oda. Spectroellipsometric characterization of materials for multilayer coatings. *Appl Surf Sci*, 175:276–280, 2001.
- [235] R. Hofer, M. Textor, and N. D. Spencer. Imaging of surface heterogeneity by the microdroplet condensation technique. *Langmuir*, 17(13):4123–4125, 2001.
- [236] J. Aizenberg, A. Black, and G. M. Whitesides. Controlling local disorder in self-assembled monolayers by patterning the topography of their metallic supports. *Nature*, 394(6696):868–871, 1998.
- [237] C. Frisbie, L. Rozsnyai, A. Noy, M. Wrighton, and C. Lieber. Functional Group Imaging by Chemical Force Microscopy. *Science*, 265(5181):2071–2074, 1994.
- [238] A. Blanchard, R. Kaiser, and L. Hood. High-density oligonucleotide arrays. *Biosens Bioelectron*, 11(6-7):687–690, 1996.
- [239] G. P. López, H. A. Biebuyck, C. Frisbie, and G. M. Whitesides. Imaging of Features on Surfaces by Condensation Figures. *Science*, 260(5108):647–649, 1993.
- [240] W. Bragg and W. Bragg. The reflection of X-rays by crystals. *P R Soc Lond A-Conta*, 88(604):428–428, 1913.
- [241] W. L. Bragg. The structure of some crystals as indicated by their diffraction of X-rays. *P R Soc Lond A-Conta*, 89(610):248–277, 1913.
- [242] A. Hull. A new method of chemical analysis. *J Am Chem Soc*, 41:1168–1175, 1919.

- [243] S. Morgenthaler. *Surface Chemical Gradients*. PhD thesis, ETH Zurich, 2007.
- [244] W.-J. Kim, S. Kim, B. S. Lee, A. Kim, C. S. Ah, C. Huh, G. Y. Sung, and W. S. Yun. Enhanced Protein Immobilization Efficiency on a TiO₂ Surface Modified with a Hydroxyl Functional Group. *Langmuir*, 25(19):11692–11697, 2009.
- [245] M. Rodenstein, S. Zürcher, S. G. P. Tosatti, and N. D. Spencer. Fabricating Chemical Gradients on Oxide Surfaces by Means of Fluorinated, Catechol-Based, Self-Assembled Monolayers. *Langmuir*, 28:in press, 2010.
- [246] S. G. P. Tosatti and S. Zürcher. ULTRA-THIN HYDROPHOBIC AND OLEOPHOBIC LAYER, ITS METHOD OF MANUFACTURE AND USE IN MECHANICS AS A BARRIER FILM, Patent Appl. PCT/CH2007/000603, 2007.
- [247] B. Beard. X-ray radiation decomposition of cyclo-1,3,5-trimethylene-2,4,6-trinitramine (RDX), at low temperature: Initial reaction steps. *Propellants*, 16(2):81–87, 2004.
- [248] P. Mendes, M. Belloni, M. Ashworth, C. Hardy, K. Nikitin, D. Fitzmaurice, K. Critchley, S. D. Evans, and J. Preece. A Novel Example of X-Ray-Radiation-Induced Chemical Reduction of an Aromatic Nitro-Group-Containing Thin Film on SiO₂ to an Aromatic Amine Film. *ChemPhysChem*, 4(8):884–889, 2003.
- [249] R. Rodriguez, M. Blesa, and A. Regazzoni. Surface complexation at the TiO₂ (anatase) aqueous solution interface: Chemisorption of catechol. *Journal of Colloid and Interface Science*, 177:122–131, 1996.
- [250] H. Schonherr and H. Ringsdorf. Self-assembled monolayers of symmetrical and mixed alkyl fluoroalkyl disulfides on gold. 1. Synthesis of disulfides and investigation of monolayer properties. *Langmuir*, 12:3891–3897, 1996.
- [251] M. Buck, F. Eisert, J. Fischer, M. Grunze, and F. Träger. Investigation of self-organizing thiol films by optical second harmonic generation and X-ray photoelectron spectroscopy. *Appl Phys A-Mater*, 53(6):552–556, 1991.
- [252] D. Vasudevan and A. Stone. Adsorption of catechols, 2-aminophenols, and 1,2-phenylenediamines at the metal (hydr)oxide/water interface: Effect of ring substituents on the adsorption onto TiO₂. *Environ Sci Technol*, 30(5):1604–1613, 1996.
- [253] R. Geer, D. Stenger, M. Chen, J. M. Calvert, R. Shashidhar, Y. Jeong, and P. Pershan. X-ray and Ellipsometric Studies of Self-Assembled Monolayers of Fluorinated Chlorosilanes. *Langmuir*, 10(4):1171–1176, 1994.

- [254] B. Pidhatika, J. Moeller, V. Vogel, and R. Konradi. Nonfouling surface coatings based on poly(2-methyl-2-oxazoline). *CHIMIA*, 62(4):264–269, 2008.
- [255] S. Pasche, S. D. Paul, J. Voros, N. D. Spencer, and M. Textor. Poly(L-lysine)-graft-poly(ethylene glycol) assembled monolayers on niobium oxide surfaces: A quantitative study of the influence of polymer interfacial architecture on resistance to protein adsorption by ToF-SIMS and in situ OWLS. *Langmuir*, 19(22):9216–9225, 2003.
- [256] L. A. Ruiz-Taylor, T. L. Martin, and P. Wagner. X-ray photoelectron spectroscopy and radiometry studies of biotin-derivatized poly(L-lysine)-grafted-poly(ethylene glycol) monolayers on metal oxides. *Langmuir*, 17(23):7313–7322, 2001.
- [257] J. Lee, H. Kim, C. Park, G. Park, H. Kwak, S. Koo, and M. Sung. Photocatalytic decomposition of alkylsiloxane self-assembled monolayers on titanium oxide surfaces. *J Phys Chem B*, 107(34):8997–9002, 2003.
- [258] D. Kisailus, Q. Truong, Y. Amemiya, J. Weaver, and D. Morse. Self-assembled bifunctional surface mimics an enzymatic and templating protein for the synthesis of a metal oxide semiconductor. *P Natl Acad Sci Usa*, 103(15):5652–5657, 2006.
- [259] L. Netzer, R. Iscovici, and J. Sagiv. Adsorbed monolayers versus Langmuir-Blodgett monolayers—Why and how? I: From monolayer to multilayer, by adsorption. *Thin Solid Films*, 99(1-3):235–241, 1983.
- [260] L. Forget, F. Wilwers, J. Delhalle, and Z. Mekhalif. Surface modification of aluminum by n-pentane phosphonic acid: XPS and electrochemical evaluation. *Appl Surf Sci*, 205(1-4):44–55, 2003.
- [261] A. G. Koutsioubas, N. Spiliopoulos, D. L. Anastassopoulos, A. A. Vradis, and G. D. Priftis. Formation of alkane-phosphonic acid self-assembled monolayers on alumina: an in situ SPR study. *Surf. Interface Anal.*, 41(11):897–903, 2009.
- [262] T. Hauffman, O. Blajiev, J. Snauwaert, C. van Haesendonck, A. Hubin, and H. Terryn. Study of the Self-Assembling of n-Octylphosphonic Acid Layers on Aluminum Oxide. *Langmuir*, 24(23):13450–13456, 2008.
- [263] P. E. Laibinis, J. Hickman, M. Wrighton, and G. M. Whitesides. Orthogonal Self-Assembled Monolayers: Alkanethiols on Gold and Alkane Carboxylic Acids on Alumina. *Science*, 245(4920):845–847, 1989.

- [264] M. Calistri-Yeh, E. Kramer, R. Sharma, W. Zhao, M. Rafailovich, J. Sokolov, and J. Brock. Thermal stability of self-assembled monolayers from alkylchlorosilanes. *Langmuir*, 12:2747–2755, 1996.
- [265] B. Liedberg, M. Wirde, Y. Tao, P. Tengvall, and U. Gelius. Molecular gradients of ω -substituted alkanethiols on gold studied by X-ray photoelectron spectroscopy. *Langmuir*, 13(20):5329–5334, 1997.
- [266] H. Elwing. Adsorption of fibrinogen as a measure of the distribution of methyl groups on silicon surfaces. *Journal of Colloid and Interface Science*, 123(1):306–308, 1988.
- [267] I. Langmuir. Oil lenses on water and the nature of monomolecular expanded films. *J Chem Phys*, 1(11):756–776, 1933.
- [268] S. Mckee and D. Swales. On the derivation of the Langmuir isotherm for adsorption kinetics. *J Phys A-Math Gen*, 24(4):L207–L209, 1991.
- [269] E. L. Hanson, J. Schwartz, B. Nickel, N. Koch, and M. F. Danisman. Bonding Self-Assembled, Compact Organophosphonate Monolayers to the Native Oxide Surface of Silicon. *J Am Chem Soc*, 128:16074 –16080, 2003.
- [270] O. Dannenberger, M. Buck, and M. Grunze. Self-Assembly of n-Alkanethiols: A Kinetic Study by Second Harmonic Generation. *J Phys Chem B*, 103:2202–2213, 1999.
- [271] V. Zoulalian, S. Monge, S. Zürcher, M. Textor, J. J. Robin, and S. G. P. Tosatti. Functionalization of Titanium Oxide Surfaces by Means of Poly(alkylphosphonates). *J Phys Chem B*, 110:25603 –25605, 2006.
- [272] V. Zoulalian. *Functionalization of titanium oxide surfaces by means of poly(alkyl-phosphonate) polymers*. PhD thesis, ETH Zurich, 2008.
- [273] P. Bonhote, J. Moser, R. Humphry-Baker, N. Vlachopoulos, S. Zakeeruddin, L. Walder, and M. Gratzel. Long-lived photoinduced charge separation and redox-type photochromism on mesoporous oxide films sensitized by molecular dyads. *J Am Chem Soc*, 121(6):1324–1336, 1999.
- [274] M. Wahlgren, S. Welin-Klintström, T. Arnebrant, A. Askendal, and H. Elwing. Competition between fibrinogen and a non-ionic surfactant in adsorption to a wettability gradient surface. *Colloid Surface B*, 4:23–31, 1995.
- [275] Y. S. Lin, V. Hlady, and J. Janatova. Adsorption of complement proteins on surfaces with a hydrophobicity gradient. *Biomaterials*, 13(8):497–504, 1992.

- [276] T. Kawabata. Iron coordination by catechol derivative antioxidants. *Biochemical Pharmacology*, 51(11):1569–1577, 1996.
- [277] P. Z. Araujo, P. J. Morando, and M. A. Blesa. Interaction of Catechol and Gallic Acid with Titanium Dioxide in Aqueous Suspensions. 1. Equilibrium Studies. *Langmuir*, 21(8):3470–3474, 2005.
- [278] C. Creutz and M. H. Chou. Binding of catechols to mononuclear titanium(IV) and to 1-and 5-nm TiO₂ nanoparticles. *Inorg Chem*, 47(9):3509–3514, 2008.
- [279] J. Lambert and S. Singer. Self-assembled macrocycles with pentavalent silicon linkages. *Journal of Organometallic Chemistry*, 689(14):2293–2302, 2004.
- [280] J. Fujita, Y. Ohnishi, Y. Ochiai, and S. Matsui. Ultrahigh resolution of calixarene negative resist in electron beam lithography. *Appl Phys Lett*, 68(9):1297–1299, 1996.
- [281] C. Vieu, F. Carcenac, A. Pepin, Y. Chen, M. Mejias, A. Lebib, L. Manin-Ferlazzo, L. Couraud, and H. Launois. Electron beam lithography: resolution limits and applications. *Appl Surf Sci*, 164:111–117, 2000.
- [282] I. Campbell, S. Rubin, T. Zawodzinski, J. Kress, R. Martin, D. Smith, N. Barashkov, and J. Ferraris. Controlling Schottky energy barriers in organic electronic devices using self-assembled monolayers. *Phys Rev B*, 54(20):14321–14324, 1996.
- [283] H. Solak, C. David, J. Gobrecht, V. Golovkina, F. Cerrina, S. Kim, and P. Nealey. Sub-50 nm period patterns with EUV interference lithography. *Microelectronic Engineering*, 67-8:56–62, 2003.
- [284] S. Kim, H. Solak, M. Stoykovich, N. Ferrier, J. de Pablo, and P. Nealey. Epitaxial self-assembly of block copolymers on lithographically defined nanopatterned substrates. *Nature*, 424(6947):411–414, 2003.
- [285] N. Blondiaux, S. Zürcher, M. Liley, and N. D. Spencer. Fabrication of Multiscale Surface-Chemical Gradients by Means of Photocatalytic Lithography. *Langmuir*, 23(7):3489–3494, 2007.
- [286] J. Zita, J. Krysa, and A. Mills. Correlation of oxidative and reductive dye bleaching on TiO₂ photocatalyst films. *J Photoch Photobio A*, 203(2-3):119–124, 2009.
- [287] W. Tang and H. An. Photocatalytic degradation kinetics and mechanism of acid blue 40 by TiO₂/UV in aqueous solution. *Chemosphere*, 31(9):4171–4183, 1995.

- [288] A. L. Linsebigler, G. Lu, and J. T. J. Yates. Photocatalysis on TiO_n Surfaces: Principles, Mechanisms, and Selected Results. *Chem Rev*, 95:735–758, 1995.
- [289] C.-Y. Kuo. Convenient dye-degradation mechanisms using UV/ TiO_2 /carbon nanotubes process. *Journal of Hazardous Materials*, 163(1):239–244, 2009.
- [290] U. Cernigoj, U. L. Stangar, P. Trebse, and M. Sarakha. Determination of catalytic properties of TiO_2 coatings using aqueous solution of coumarin: Standardization efforts. *J Photoch Photobio A*, 201(2-3):142–150, 2009.
- [291] S. Cho and W. Choi. Solid-phase photocatalytic degradation of PVC- TiO_2 polymer composites. *J Photoch Photobio A*, 143(2-3):221–228, 2001.
- [292] F. Kawai, T. Kimura, M. Fukaya, Y. Tani, K. Ogata, T. Ueno, and H. Fukami. Bacterial oxidation of polyethylene glycol. *Appl Environ Microb*, 35(4):679–684, 1978.
- [293] D. Mantzavinos, R. Hellenbrand, A. Livingston, and I. Metcalfe. Catalytic wet air oxidation of polyethylene glycol. *Appl Catal B-Environ*, 11(1):99–119, 1996.
- [294] D. Lehnert, B. Wehrle-Haller, C. David, U. Weiland, C. Ballestrem, B. Imhof, and M. Bastmeyer. Cell behaviour on micropatterned substrata: limits of extracellular matrix geometry for spreading and adhesion. *J Cell Sci*, 117(1):41–52, 2004.
- [295] T. von Erlach. The role of cell cycle on polymer mediated gene transfer in different cell types and Long-term stability of micropatterns under cell culture conditions using either PLL-*g*-PEG or PLL-*g*-PMOXA as passivation materials. Master’s thesis, ETH Zurich, 2010.

Curriculum Vitae

Personal

Name: Mathias Rodenstein
Date of birth: December 15, 1980
Address: Thomas-Müntzer-Str. 1
3600 Halberstadt
DDR

Education

2006-2010 PhD student at the Laboratory for Surface Science and Technology, Department of Materials, Swiss Federal Institute of Technology (ETH) Zurich.

2000-2005 Studies of Physics at the Technical University Dresden, Dresden, Germany. Graduation with the degree Dipl. Physiker

2003-2004 Exchange semester at Saint Petersburg State University, St. Petersburg , Russia

2002-2003 Exchange year at Ecole Polytechnique Federale de Lausanne, Lausanne, Switzerland